

A 3D model of a human brain, rendered in a light yellow/gold color, showing a large, irregular mass on the left side, possibly representing a tumor. The model is set against a black background.

COMPUTATIONAL MODELING IN NEURO-ONCOLOGY

JANA LIPKOVÁ





Computational Modeling in Neuro-Oncology

Jana Lipková

Vollständiger Abdruck der von der Fakultät für Informatik der Technischen Universität München zur Erlangung des akademischen Grades einer

Doktorin der Naturwissenschaften (Dr. rer. nat.)

genehmigten Dissertation.

Vorsitzender:

Prof. Dr. Julien Gagneur

Prüfende der Dissertation:

1. Prof. Dr. Bjoern H. Menze
2. Prof. John Lowengrub

Die Dissertation wurde am 28.10.2019 bei der Technischen Universität München eingereicht und durch die Fakultät für Informatik am 20.01.2020 angenommen.



“ I almost wish I hadn’t
gone down that rabbit-hole
—and yet—and yet—
it’s rather curious, you know,
this sort of life ! ”

—Alice

ABSTRACT

Computational oncology is an emerging discipline devoted to improving medical care by a synergy of computational modeling and clinical oncology. The computational models can be used to identify the underlying mechanisms of cancer, provide complementary information to medical scans, and predict disease progression. Moreover, treatment procedures can be harmlessly tested in an *in-silico* environment to find the most suitable treatment configuration for each patient.

Despite its enormous potential, an application of computational oncology into clinical practice is still in its infancy. One of the crucial challenges is a calibration of computational models to patient-specific conditions, which stands on the triad of i) strategies enabling the model calibration from incomplete data; ii) computational models describing disease progression and critical conditions; iii) robust automated methods for processing patient medical data. Moreover, to sustain the high pace required by clinical practice, high-performance implementations of tumor models as well as open-source software packages are required.

This thesis addresses the translation of computational models into clinical practice. We design automated methods for the detection and segmentation of tumors from medical scans. We develop a computational model of tumor progression in the patient-specific brain anatomy, which accounts for the most critical symptoms; namely tumor-induced brain deformations and increased intracranial pressure. We design strategies for calibration of tumor models from patient structural and metabolic scans. The calibrated models provide the patient-specific predictions about the tumor infiltration pathways, which are used to design personalized radiotherapy plans. A pilot clinical study showed that the proposed plans reduce radiation toxicity while yielding comparable accuracy with standard radiotherapy protocols. To further improve the quality of model calibrations, identification of novel imaging strategies is of crucial importance. In this direction, we present a clinical study investigating the diagnostic and prognostic potential of novel imaging marker for brain lymphomas.

Last but not least, we develop scalable software for tumor modeling and a platform for processing and segmenting medical scans of patients with brain lesions. The developed software packages are publicly released to facilitate their translation into clinical and scientific practice.

ZUSAMMENFASSUNG

Die computergestützte Onkologie ist eine aufstrebende Disziplin, die sich der Verbesserung der medizinischen Versorgung durch eine Synergie aus computergestützter Modellierung und klinischer Onkologie widmet. Die Berechnungsmodelle können verwendet werden, um die zugrunde liegenden Mechanismen von Krebs zu identifizieren, ergänzende Informationen zu medizinischen Scans bereitzustellen und den Krankheitsverlauf vorherzusagen. Darüber hinaus können die mögliche Behandlungsverfahren risikofrei in einer *In-Silico*-Umgebung getestet werden, um für jeden Patienten einen optimierten Behandlungsansatz bereitzustellen.

Trotz ihres enormen Potenzials steckt eine Anwendung der computergestützten Onkologie in der klinischen Praxis noch in den Kinderschuhen. Eine der bedeutendsten Herausforderungen ist die Kalibrierung der Berechnungsmodelle auf die patientenspezifischen Bedingungen, welche sich auf drei Säulen stützt: i) den Strategien zur Modellkalibrierung aus unvollständigen Daten; ii) den Berechnungsmodellen zur Beschreibung des Krankheitsverlaufs und kritischer Zustände; iii) automatisierte Verfahren zur Verarbeitung klinischer Daten. Um das hohe Tempo der klinischen Praxis aufrechtzuerhalten, sind zudem leistungsfähige Implementierungen von Tumormodellen und öffentlich Softwareprodukte erforderlich.

Diese Arbeit befasst sich mit der Anwendung von der Berechnungsmodelle in die klinische Praxis. Wir entwickeln automatisierte Methoden zur Detektion und Segmentierung von Tumoren aus den medizinischen Scans der Patienten. Wir designen und implementieren ein Computermodell zur Vorhersage von Tumorprogressionen, das patientenspezifische Gehirnanatomie sowie die kritischsten Symptome, insbesondere die tumorinduzierte Hirnverformung und die Erhöhung des intrakraniellen Drucks berücksichtigt. Wir entwickeln Strategien zur Kalibrierung der Tumormodelle aus den Patientenstruktur- und metabolischen Scans. Die kalibrierten Modelle liefern patientenspezifische Vorhersagen über die Tumorinfiltrationswege, mit denen personalisierte Strahlentherapiepläne erstellt werden. Eine klinische Pilotstudie zeigt, dass die vorgeschlagene Pläne die Strahlentoxizität reduzieren wobei gleichzeitig die Genauigkeit der Standardprotokolle erhalten bleibt. Um die Qualität der Modellkalibrierungen weiter zu verbessern, ist die Identifizierung neuartiger Abbildungsstrategien von entscheidender Bedeutung. In dieser Richtung stellen wir eine klinische Studie vor, die das prognostische und diagnostische Potenzial eines neuartigen bildgebenden Markers für Hirnlymphome untersucht.

Zur Bearbeitung dieser vielfältigen Themengebiete der computergestützten Onkologie entwickeln wir eine skalierbare Software für die Tumormodellierung und eine Plattform zur Verarbeitung und Segmentierung von medizinischen Scans von Patienten mit Hirntumoren. Die entwickelten Softwareprodukte sind öffentlich zugänglich, um ihre Umsetzung in die klinische und wissenschaftliche Praxis zu erleichtern.

ACKNOWLEDGEMENTS

First of all, I want to thank the three gentlemen of my research life — my supervisors: Bjoern Menze, John Lowengrub, and Petros Komoutsakos. To Petros, for initiating my Ph.D. journey, triggering my interests in computational science, challenging me and pushing me towards something better. To John — who welcomed me in his lab in California — for sharing his interests in cancer research, the inspiring discussions, the mentoring and motivation to continue with the doctorate. Special thanks to Bjoern, for providing me with guidance, advices, and freedom to learn and play with things that thrill me, and for making my Ph.D. possible.

Since my Ph.D. journey was quite long, the best would be to express the remaining gratitude chronologically. It all started in Oxford with Radek Erban and Kostas Zygalakis; whom I owe a lot for their kind mentoring and for inspiring me to proceed with a Ph.D. in the first place.

I wish to thank the members of the CSElab for teaching me a myriad of things and making my stay in Zurich so joyful. Thanks to: Panos-- (for his guidance and special sense of humor), Panos++ (for all the kind words and soccer events), Diego (for VP, MRAG and for providing prayers instead of comments in the code), Stephen (for all the discussions, kobe beef and other culinary experiences), George (for the late-night skype calls) and finally to my special Zurich-buddies: Angeliki, Christian, Guillem, Gerardo and Rajdeep (it was all those swims, sledges and trips that helped me to recharge and keep my sanity).

I want to express my gratitude to the members of the IBBM Lab, former and past, that all contributed to this work in their own special ways. Many thanks to those who walked the Ph.D. path with me: Esther, Marie, Markus, and Cagdas — thank you for sharing the struggle, joy, and beer. And also to the new kids in the block — for the kicker matches and for making the atmosphere in the lab enjoyable. I also wish to thank my lovely students: Christine, Stevica, Enes, Yusuf, Mohak and Phillipp. Further, I wish to extend my thanks to the members of the Klinikum Rechts Der Isar — for sharing their time and expertise — particularity to Benedikt Wiestler, Christian Diehl, Peter Herhaus, Thomas Pyka, Christine Preibisch, Ulrich Keller, and Stephanie Combs.

Last but not least, I am grateful to my family and friends for providing a healthy balance to my doctorate life. Thanks to (alphabetically): Adam, Alex, Ina, Joanna, Marcel, Mark, Mata, Michal, Ondrej — thanks for all those trips, slopes, drinks, and talks. To my family: d'akujem babka, dedko, ocino a bobo. Finally, to Luca, who changed my life to better; thank you for your support, patience, love and lasagne.

TABLE OF CONTENTS

	Page
1 Introduction	1
1.1 The vision	2
1.2 This thesis	4
2 Background	9
2.1 Biology of cancer	9
2.1.1 Hallmarks of cancer	10
2.1.2 Cancer classification	13
2.1.3 Glioma and glioblastoma	14
2.1.4 Central nervous system lymphoma	15
2.2 Fundamentals of medical imaging	16
2.2.1 X-ray computed tomography	16
2.2.2 Positron emission tomography	18
2.2.3 Magnetic resonance imaging	21
2.3 Imaging in neurooncology	26
2.4 Summary	30
3 Medical Image Segmentation	31
3.1 Introduction	31
3.2 Segmentation methods	35
3.2.1 Atlas-guided methods	35
3.2.2 Skull-stripping and brain tissue segmentation	38
3.2.3 Convolutional neural networks	46
3.2.4 Whole-body multiple myeloma bone lesion detection	51
3.3 Segmentation challenges	58
3.3.1 Liver Tumor Segmentation Challenge (LiTS)	59
3.3.2 Brain Tumor Segmentation Challenge (BraTS)	65
3.4 Summary	71

TABLE OF CONTENTS

4	Image-Based Tumor Modelling	73
4.1	Tumor growth modelling	74
4.2	Tumor-induced brain deformations	78
4.2.1	Method	80
4.2.2	Numerical implementation	83
4.2.3	Results	86
4.3	Summary	91
5	Personalized Medicine	93
5.1	Standard radiotherapy	93
5.2	Bayesian model calibration	95
5.2.1	Image-based model calibration	96
5.2.2	Parameters estimation and uncertainty propagation	99
5.2.3	Sensitivity study	100
5.3	Personalized radiotherapy	103
5.3.1	Patient-specific predictions	103
5.3.2	Clinical study	104
5.4	Summary	107
6	Clinical Study of CXCR4-directed PET	109
6.1	Motivation	109
6.2	Patient cohort	110
6.3	Specificity of CXCR4-PET	111
6.4	Prognostic value of CXCR4-PET	113
6.5	Summary	116
7	Stochastic Simulation Methods	117
7.1	Introduction	118
7.1.1	The Gillespie algorithm	118
7.1.2	The τ -leaping algorithm	119
7.1.3	The R -leaping algorithm	124
7.2	The S -leaping algorithm	125
7.3	Numerical results	129
7.4	Summary	137
8	Scientific Software	139
8.1	Glioma solver	140
8.2	Brain tumor processing pipeline	147
8.3	Stochastic simulation methods software	154

9 Gallery	159
10 Conclusion & Outlook	167
Appendix A Personalised Radiotherapy Planning	171
Appendix B Cahn-Hilliard Image Filtering	175
List of Publications	183
List of Tables	186
List of Figures	186
List of Acronyms	191
Bibliography	195

INTRODUCTION

We live in a truly amazing world shaped by science and technology. New discoveries, that improve our way of living or contribute to great innovations of the future, are made every day. In the 21st century, we have already witnessed the scientific breakthroughs like a detection of gravitational waves [1], the proof of existence of a dark matter [36], evidence of liquid water on Mars [60], discovery of Higgs Boson [9] or synthesis of water and carbon dioxide into fuel [136]. Moreover, self-driving vehicles are already emerging on the roads. In the field of medicine, we are celebrating advances such as sequencing of the cancer genome [168] or the discovery of induced pluripotent stem cells [196], which open a way to grow human organs in the labs. Furthermore, we have already seen two successfully cured HIV/AIDS patients: in 2007 Timothy Brown [6] and the "London patient" in March 2019 [62]. It is impossible to know for sure what the next great discovery will be and how it will impact our lives. Nevertheless, by envisioning future improvements we can shape the course of science.

In comparison to the high speed of technical advancements, their application into medical care is proceeding at a much slower pace. The standard-of-care management of patients did not change much over the last two decades, providing opportunities for future innovations. To identify the potential sources for improvement, let us look at the following example from the current clinical practice. Imagine that it is the summer 2019 and you are not feeling yourself recently. You are experiencing severe headaches, nausea and overall weakness. You decide to visit your family doctor, who recommends medical scans. Once your scans are acquired, they have to be inspected by a certified neuroradiologist who identifies a brain tumor. To prepare the treatment plan, the lesion has to be segmented along with all its subcomponents. It means that the neuroradiologist has to assign a label specifying the tumor component to each pixel in each of your scans (most likely you received at least four different scans). The segmentation task is performed manually

and – depending on the tumor size and the resolution of the scan – it can take between 2-5 hours per scan. The segmented tumor is used to design your treatment plan, which usually involves surgery combined with radio- and chemotherapy.

Once the scans are processed, you meet with your neurooncologist who informs you about the diagnosis and the treatment plan. You might feel confused by all the new terms like *temozolomide* and *stereotactic biopsy*, but you believe in the science and so you proceed with the treatment, assuming that it is the best possible approach designed for you. What you might not know, is that your treatment is derived from large population studies and most likely does not account for your specific conditions. There exists a large variation even among the official radiotherapy guidelines, which means that you can get very different treatment with respect to the hospital or country where you are treated. Moreover, neither you nor your neurooncologist might be fully aware of all the 293 359¹ clinical trials that have started this year and thus it is possible that your treatment plan does not account for all the possible options.

This description reveals few possibilities for improvement, which we tackle in this thesis. To pinpoint the directions of the improvements, let us first envision a better scenario.

1.1 The vision

An improved scenario can look like this. Once your scans are acquired, the clinical personnel sends them to your *Medical Human Avatar*, which is basically a virtual version of you, containing your whole medical history, genetic profile and all information collected from your previous medical checks as well as from your body sensors like a fit-watch. During the night, the software automatically inspects the new scans, detects and segments the tumor and sets the diagnosis. It performs a wide range of virtual surgeries, radiotherapies, and chemotherapies to find the most suitable treatment configuration tailored for your specific conditions.

The next day you meet with your doctor who loads your *Medical Human Avatar*, which might look like as the illustration shown in Fig. 1.1. The software presents you with the diagnosis together with the processed medical scans. It provides you with a list of all suitable treatment options designed for your individual conditions, including prognosis, statistics and recommended dietary restrictions. It informs you that in the absence of the treatment you might experience impairment of vision, resulting from increased intracranial pressure. It warns your clinician about a possible allergy to corticosteroids detected in your family. It also lists all the clinical trials you are eligible to enrol in. Based on your genetic profile and low PET uptake values, it recommends as the most suitable treatment the novel theranostic approach currently tested in a hospital in Munich and provides you with the enrolment documents. You might still be a bit confused, but you can download the avatar to your phone, where you get the full explanation of each term simply by clicking on it. Since your doctor was liberated from the image processing tasks, she/he has

¹As of June 27, 2019 (based on ClinicalTrials.gov)

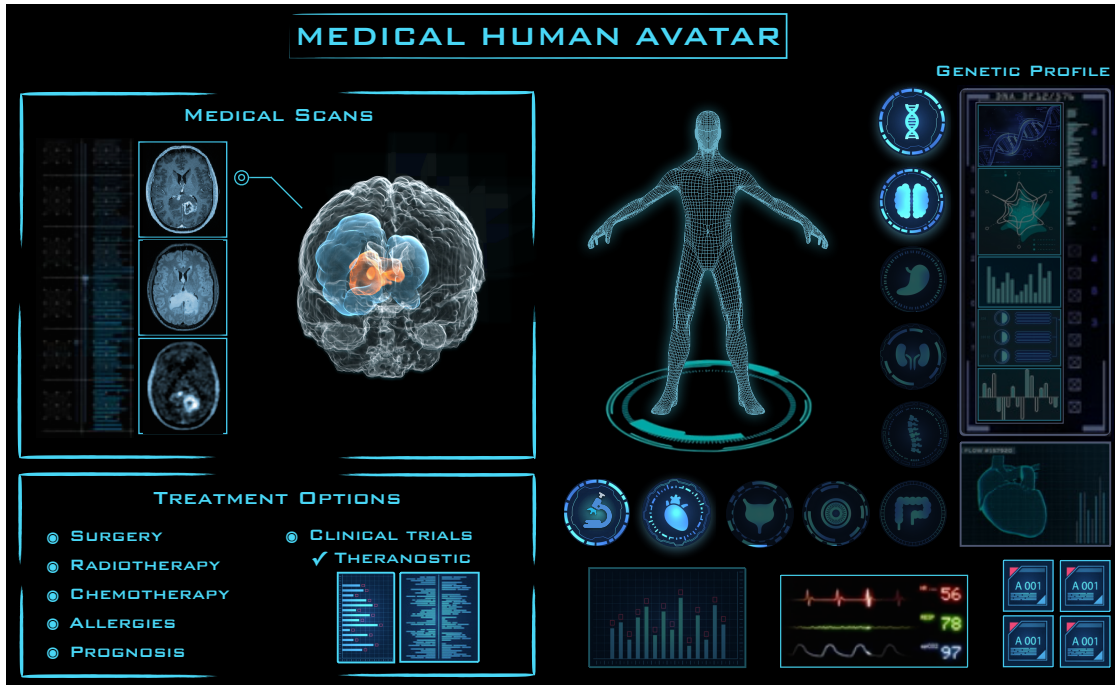


Figure 1.1: An illustration of *Medical Human Avatar*. The avatar is a virtual version of a patient, storing a complete medical history, genetic profile and all relevant health information. The software automatically processes medical scans, detects and segments pathologies, and sets the diagnosis. It tests multiple treatment procedures in the *in-silico* environment, to identify the most optimal treatment configuration for each patient.

more time to answer all your questions and to evaluate with you all the treatment options. As a consequence, you proceed with treatment with a reassurance that you a made well-informed decision. Moreover, the software asks if you are willing to participate in a pilot clinical study investigating the prognostic potential of a novel medical imaging marker, to further contribute to the advancements in medical care.

It can sound a bit like a scene from a distant future, but reality may not be so far off after all. To fulfill this vision we need to put effort into 1) the development of image processing methods for automated, reliable detection and segmentation of pathologies; 2) the identification of novel diagnostic and imaging modalities; 3) the design of computational models describing disease progression and the related critical conditions; 4) the development of the strategies for the calibration of the computational models enabling the patient-specific predictions; 5) the design of high-performance software allowing an efficient computation of the real-world systems.

In this thesis, we address the aforementioned points with a humble wish to contribute a tiny bit to the large picture of personalized medicine.

1.2 This thesis

This thesis presents image-based computational modelling of brain cancer, including image processing methods and models for tumor dynamics. Special emphasis is placed on calibration strategies of the computational models that enable the patient-specific predictions in the presence of incomplete data and uncertainties. The software developed in this work allows for parallel execution on multi-core and multi-processor architectures and hence enables the efficient simulation of realistic large systems. Herein, the following contributions were made:

- We propose a convolutional neural network approach for segmenting multiple myeloma lesions from multimodal medical scans. We present a strategy for skull-stripping and brain tissue segmentation. We contribute to the organization of benchmarks for an unbiased evaluation of the segmentation methods for brain and liver lesions.
- We develop a computational model for tumor dynamics in a patient-specific anatomy accounting for the tumor-induced brain deformations and the elevation of the intracranial pressure, as the two most crucial symptoms. The model provides realistic predictions about disease progression and onset of critical conditions. The efficient implementation of the model is achieved through a combination of the state-of-the-art numerical methods with the high-performance parallelization strategies.
- We present a Bayesian machine learning framework for the calibration of computational tumor models from multimodal medical scans of patient acquired at a single time point. The calibrated models provide robust predictions about the patient-specific tumor infiltration pathways, which are in turn used to design personalized radiotherapy plans. A pilot clinical study shows that the personalized plans spare more healthy tissue thereby reducing radiation toxicity while yielding comparable accuracy with standard radiotherapy protocols. Moreover, the inferred regions of high tumor cell densities coincide with the tumor radioresistant areas, providing guidance for personalized dose-escalation.
- We present a proof-of-concept study suggesting the diagnostic and prognostic potential of a novel imaging marker for lymphomas of the central nervous system.
- We develop an adaptive accelerated stochastic simulation algorithm for modelling well-stirred chemical reactions, which provides an optimal fusion of state-of-the-art methods. Moreover, in the case of large and stiff systems, the proposed algorithm outperforms existing methods.

Furthermore, the following softwares were developed and publicly released:

- High-performance software for simulating tumor dynamics in patient anatomy reconstructed from the medical scans. The software supports several tumor models. Moreover, it provides a fully automated computation of personalized radiotherapy plans.

- Software for automated processing and segmenting head MRI scans of patients with brain lesions. The software is designed in a modular way, that employs the high pace with which new segmentation methods are developed. It supports use of any tumor segmentation method available in the docker library, which ensures software compatibility with state-of-the-art methods (including methods developed in future). Moreover, it provides a graphical user interface for an easy and fast correction of the segmentations through a supervoxels discretization.
- Software for simulating chemical reaction of well-stirred systems, which supports multiple state-of-the-art stochastic methods.

The thesis is organized as follows:

Chapter 2: Background

This chapter provides a concise overview of the essentials relevant to the rest of the thesis. It starts with an overview of the underlying principles of cancer and the classification of the cancer types. Afterwards, the fundamentals of medical imaging are presented together with an overview of standard and novel imaging modalities. Instructions on how to interpret information from the different imaging modalities in terms of pathologies are also provided. A special focus is devoted to brain cancer, as a central topic of this thesis.

Chapter 3: Medical Image Segmentation

The focus of this chapter is on the segmentation of the medical images. The chapter starts with a summary of basic assumptions and terminology used in the image segmentation field. Afterwards, two segmentation methods developed in this thesis are presented. The first one is an atlas-guided method for skull-stripping and brain tissue segmentation. The second method uses convolutional neural networks to detect and segment multiple myeloma lesions from whole-body multimodal scans. Finally, the chapter presents two segmentation benchmarks for an unbiased evaluation of the segmentation methods, namely: the liver lesion segmentation challenge (LiTS) and the brain tumor segmentation challenge (BraTS).

Chapter 4: Image-Based Tumor Modelling

This chapter is devoted to computational tumor modelling in the patient brain anatomy reconstructed from the medical scans. First, the essential concepts of the image-based tumor modelling are illustrated on a simple model describing the basic tumor behavior: proliferation and infiltration. The basic model is then extended to account for the tumor-induced brain deformations and the corresponding elevation of the intracranial pressure. To ensure high efficiency of the computations, the state-of-the-art numerical methods are employed together with multi-core and multi-processor parallelization strategies. Synthetic and clinical data are used to illustrate

the capability of the proposed model to produce realistic brain deformations and accompanying pathological conditions.

Chapter 5: Personalized Medicine

This chapter presents a Bayesian machine learning framework for calibration of the computational tumor models from the patient multimodal scans. The calibrated models provide robust, patient-specific predictions about tumor infiltration pathways, even beyond the tumor outlines visible on the medical scans. The model predictions are utilized to design personalized radiotherapy plans. A pilot clinical study is used to assess the benefits of the personalised plans over the standard radiotherapy protocols, in terms of dose-distribution and dose-escalation.

Chapter 6: Clinical Study of the CXCR4-directed PET

In this chapter, we present a pilot clinical study that investigates a diagnostic and prognostic potential of novel imaging marker, called CXCR4-directed PET, in patients with the central nervous system lymphoma. This work also illustrates how an interplay between medical imaging and image processing can contribute to clinical advancements.

Chapter 7: Stochastic Simulation Methods

This chapter is devoted to stochastic simulation algorithms of well-stirred chemically reacting systems. First, the basic theory of the stochastic simulations is explained, followed by an overview of the state-of-the-art methods, including Gillespie algorithm and its accelerated versions, namely τ -leaping and R -leaping methods. Afterwards, a novel, adaptive, accelerated algorithm, called S -leaping, is introduced. The proposed method is an optimal fusion of the two aforementioned accelerated methods, which allows the scheme to maintain high efficiency under various conditions. Moreover, in the case of large and stiff systems, it outperforms both methods. The performance and the accuracy of the S -leaping are tested together with the τ -leaping and R -leaping methods on a number of benchmark systems involving biological reaction networks.

Chapter 8: Scientific Software

This chapter presents the developed scientific software. First, high-performance software for tumor modelling, called *GliomaSolver*, is introduced. The software supports various tumor models, including the Bayesian framework for personalized radiotherapy design presented in Chapter 5. Then, the platform for processing and segmenting head MRI scans of patients with brain lesions is presented. The software can be used with any segmentation method available in the docker library. This modular architecture ensures software compatibility with the state-of-the-art methods, including the algorithms that will be added to the library in the future. A

graphical user interface allows easy inspection and correction of the segmentations. Finally, the software for stochastic simulations of chemically reacting systems is presented.

Chapter 9: Gallery

This chapter displays a selection of scientific visualizations created as a part of different projects using various visualization techniques. A brief description of each visualisation and the underlying study is presented.

Appendix

The appendix presents additional technical details along with preliminary results on image filtering of the medical scans with liver lesions.

BACKGROUND

Medical imaging represents one of the main pillars of comprehensive cancer care. Imaging plays an essential role in all phases of cancer management, ranging from tumor detection to therapy planning and treatment response monitoring. Novel imaging techniques allow detection of potentially malignant changes in cell metabolism, even before a tumor mass is formed. Early tumor detection through imaging screening, in turn, contributes to reducing mortality for certain cancer types. Moreover, the development of cancer-specific imaging markers has opened doors to novel, minimally invasive treatment procedures. In particular, imaging markers – special molecules designed to accumulate inside the tumor – can be utilized to deliver a high dose of chemotherapeutic drugs directly inside the tumor, while sparing healthy tissue. Medical imaging and cancer biology also constitute the key elements of this thesis. This chapter provides a concise overview of the essential components of cancer and medical imaging. We start with a summary of underlying principles of cancer, followed by classification of the cancer types. Then, the fundamentals of medical imaging are presented together with an overview of the standard and novel imaging modalities. Interpretation of medical images in terms of pathologies is also provided. A special focus is devoted to brain cancer, which is the central topic of this thesis.

2.1 Biology of cancer

Cancer – the emperor of all maladies – is a collection of diseases involving abnormal cell growth with a potential to invade and spread to other parts of the body. There are more than 100 distinct types of cancer, with a myriad of subtypes. Despite such large complexity, it is believed that all cancers share the same underlying principles that govern a transformation of a normal cell to a malignant one. Hitherto, eight such principles, referred to as *hallmarks of cancer*, have been identified [69, 70]. This section presents the cancer hallmarks along with a concise description

of cancer dynamics. We conclude with a classification of cancer types, where a special focus is devoted to brain cancer. The goal of this section is to provide a basic understanding of cancer principles studied in this thesis; more details can be found in [190].

2.1.1 Hallmarks of cancer

Cancer cells, in order to survive and prosper, have to acquire multiple alternations in their DNA which allow them to bypass control mechanism responsible for healthy growth and homeostasis. Hanahan and Weiberg [69] identified eight such alternations shared by all cancer cells, namely: (1) self-sufficiency in growth signals; (2) insensitivity to anti-growth signals; (3) evading apoptosis; (4) limitless replicative potential; (5) sustained angiogenesis; (6) tissue invasion and metastasis; (7) reprogramming of energy metabolism and (8) evading immune destruction. An illustration of all hallmarks is shown in Fig. 2.1. Each of these hallmarks contributes to essential alternations in the cell physiology required for malignant growth. Or in other words, each of these hallmarks represents an essential target for cancer detection and treatment.

Self-Sufficiency in Growth Signals: Normal cells can grow and proliferate only in the presence of external growth signals. These signals ensure that the proliferation takes place only under suitable microenvironment conditions and in a controlled manner. This is in strong contrast with cancer cells which learn to mimic normal growth signals and thus significantly reduce their dependence on the microenvironment. This liberation from external signals allows the cancer cells to bypass control the mechanisms ensuring homeostasis, leading to increased growth and proliferation.

Insensitivity to Anti-Growth Signals: Regular cells have internal mechanisms that prevent their growth and proliferation. These mechanisms are orchestrated by proteins called *tumor suppressor genes*. These proteins monitor the state of the cell and prevent its division if the cell's DNA is damaged. Cancer cells acquire mutations in the tumor suppressor genes, which allows them to divide despite severe abnormalities. Another mechanism preventing excessive cell division is called *contact inhibition*. It prevents cells from further division once they fill up space and experience compressive stresses from other cells. Cancer cells lack this inhibition and continue to grow and divide regardless of their surroundings.

Evading Apoptosis: The ability of cancer cells to expand is determined not only by the increased growth and proliferation but also by their capability to evade programmed cell death – a process termed as *apoptosis*. Normal cells have intracellular sensors that monitor cell's well-being and activate cell death in response to detected abnormalities, such as DNA damage, signaling imbalance, or hypoxia. Cancer cells bypass these control mechanisms and do not undergo apoptosis despite serious abnormalities.

Limitless Replicative Potential: The first three hallmarks liberate the cancer cells from environmental signals. However, this alone is not sufficient for cell expansion that constitutes a macroscopic, life-threatening tumor. Normal cells have intracellular mechanisms that limit the amount of their multiplications. Once a cell has progressed through a certain number of doublings, around 60-70 doublings for a mammalian cell, it becomes unable of further division – a process named *senescence*. This process is controlled by DNA at the end of the chromosomes, known as telomeres. The length of the telomeres is shortened with each division and once the telomers are too short, the cell is prevented from further division. Cancer cells escape this limit by manipulating enzymes that increase the length of their telomeres. This allows indefinite growth and division, making cancer cells immortal.

Sustained Angiogenesis: With a growing tumor size also its demand for nutrient and oxygen increase. Tumor cells with insufficient nutrient and oxygen supplies release vascular endothelial growth factor (VEGF), which binds to the receptors on the endothelial cells (i.e. the cells of the blood vessels). The endothelial cells respond by a formation of new blood vessels – a process called angiogenesis. The newly formed vessels follow the gradient of the VEGF directly towards the tumor. The blood vessels produced by chronically activated tumor angiogenesis are marked by excessive vessel branching, distorted and enlarged vessels, erratic blood flow, leakiness and abnormal levels of endothelial cell proliferation and apoptosis. These factors also impair successful drug delivery inside the tumor.

Tissue Invasion and Metastasis: At some point during the development, most cancer types invade surrounding tissue and spread to distant body parts. These distant settlements of tumor cells – metastases – are responsible for the majority of cancer deaths [166]. Invasion and metastasis consist of multiple steps, starting with a local invasion of the cells into the surrounding tissue, entrance of the cells into a nearby blood vessel, transportation of the cancer cells through the circulatory system, followed by their escape from the vasculature, settlement into the distant tissue, and finally the growth of the cells to macroscopic tumors.

Reprogramming of Energy Metabolism: To sustain excessive, chronic growth and proliferation, cancer cells perform adjustments in their energy metabolism. Tumors differentiate to constitute two symbiotic populations of cells with different energy metabolisms. The first population consists of hypoxic cells, which use glucose for fuel and secrete lactate as a waste – a process known as Warburg-effect. The lactate is in turn used as a fuel by the second population of better-oxygenated cells. This cooperation between lactate-secreting and lactate-utilizing cells enables the tumors to support their increased metabolic demands and maintain excessive proliferation.

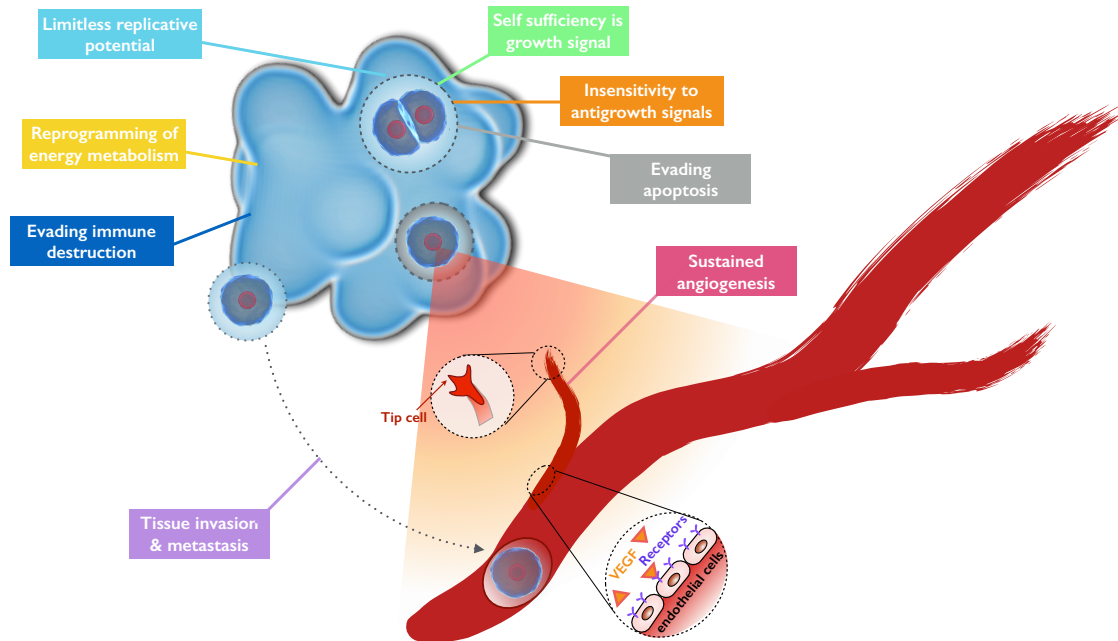


Figure 2.1: An illustration of the hallmarks of cancer. Individual hallmarks are listed in the boxes. The orange-red gradient represents VEGF secreted by a hypoxic tumor cell (shown in a gray circle). The endothelial cells respond to the VEGF by the initiation of the angiogenesis. The cell at the tip of the newly formed vessel senses the VEGF gradient and guides the vessels growth towards the tumor. At the same time, the vessels in the tumor proximity provide migration pathways for the tumor metastasis (as indicated by the gray dashed line).

Evading Immune Destruction: The cells and tissues are constantly monitored by the immune system, which is responsible for recognizing and eliminating the majority of cancer cells. An onset of tumor in the body thus inevitable implies that the cancer cells managed to avoid the surveillance of the immune system or have limited the extent of immunological killing.

Dynamics of cancer

The hallmarks of cancer represent the main components of the tumor dynamics. Cancer starts as a series of mutations that enhance the cell's capability to bypass the control mechanisms of the body. The acquired alterations in the DNA of the cancer cells, such as growth signal autonomy, insensitivity to antigrowth factors, resistance to apoptosis and immune system, and limitless replications enable the uncontrolled growth and proliferation of tumor cells. Tumor growth consists of two main phases: avascular and vascular. In the avascular phase, the tumor gets nutrients and oxygen from the surrounding tissue. This supply becomes insufficient once the tumor reaches a size of 2 – 3 mm. Consequently, the cells in the central part of the tumor become nutrient and oxygen-deprived, which lead to a formation of the necrotic core. The deprived cells

secret pro-angiogenic factors, such as VEGF, that binds to the receptors at the endothelial cells, which respond by forming new vessels. To further sustain the excessive growth and proliferation, cancer cells upgrade their energy metabolism, allowing symbiotic energy utilization between hypoxic and normoxic cells. The cells at the tumor periphery further invade the surrounding tissue to increase their nutrient and space resources. Some cancer cells can even detach from the primary tumor and travel through the vascular or lymphatic circulatory system to the remote parts of the body, where they start new colonies. The metastatic tumor consists of similar cells as the original lesion. It means that metastatic breast tumor found in the liver is made of abnormal breast and not the liver cells.

2.1.2 Cancer classification

Cancer is a class of diseases including many subtypes with diverse physiological and pathological properties. Due to the large variations, it is unlikely that there will ever be a "silver bullet" treatment applicable to all cancers, same as there is not a single universal treatment to all infectious diseases [186]. Different cancer types require distinct treatment procedures accounting for their specific properties. To group cancers by their underlying properties, tumors are classified based on the type of cells from which they originate, resulting in the following classes:

- **Carcinoma:** arises from the epithelial cells. Since the epithelial tissue is the most abundant tissue in the human body, present in the skin, lining of organs, and internal passageways, such as the gastrointestinal tract, carcinomas account for 80 to 90 % of all cancer cases
- **Sarcoma:** originates in supportive and connective tissues such as bones (osteosarcoma), cartilage (chondrosarcoma), muscles (rhabdomyosarcoma), fat (liposarcoma), and neurogenic connective tissue found in the brain (glioma).
- **Myeloma:** is a type of blood cancer that develops in the bone marrow and affects plasma cells. It accumulates in the bone marrow and evades the surrounding bone tissue.
- **Leukemia:** is a type of blood cancer, which originates in the bone marrow but it affects leukocytes (a type of white blood cells). In contrast to multiple myeloma, leukemia does not accumulate in a specific site, instead, it circulates in the bloodstream.
- **Lymphoma:** arise from lymphocytes, a type of white blood cells. It accumulates in lymph nodes or other parts of the lymphatic system. Unlike leukemia and multiple myeloma, which are sometimes called "liquid cancers," lymphomas are "solid cancers." Lymphomas may also occur in specific organs such as stomach, breast or brain.
- **Mixed types:** constitute of two or more types of cancer. This includes cancers derived from pluripotent cells, most often presented in the testicle or the ovary (seminoma and dysgerminoma, respectively) as well as cancer derived from embryonic tissue (blastoma).

This thesis addresses four types of cancer, in particular: liver cancer, multiple myeloma, glioma, and brain lymphoma. Since brain cancer plays a central role in this thesis, additional details about this malignancy are presented in the following two subsections.

2.1.3 Glioma and glioblastoma

Glioma is the most common type of primary brain tumors. It originates from the glial cells, which surround and support neurons in the brain. The World Health Organization (WHO) separates the gliomas into four grades as follows:

- *Grade I* - slowly growing tumors; most common in children and young adults; related with good prognosis; rarely causes death [66]
- *Grade II* - known as low-grade diffuse astrocytoma; slowly growing tumors with low mitotic activity; no necrotic core; most common in young adults; median survival 12 years [66]
- *Grade III* - known as anaplastic astrocytoma; fast-growing tumors with increased mitotic activity; no necrosis or vascular proliferation; median survival 3 years [169]
- *Grade IV* - termed as glioblastoma; highly infiltrative tumor with high mitotic rate; with necrosis and microvascular proliferation; most common type of gliomas; median survival 12-18 months [169]

The grade *II* gliomas are also refereed as *low grade gliomas (LGGs)*, whereas grade *III* and *IV* are termed *high grade gliomas (HGGs)*. Almost all LGGs evolve to the HGGs over time. Gliomas are characterized by infiltrative growth into the surrounding tissue, instead of forming solid tumors with a well-defined boundary. As a consequence, tumor cells can be found even a few centimeters beyond the tumor border visible on medical scans. This invisible tumor infiltration pose many challenges in the treatment and is also the most likely cause of the glioma recurrence – present in almost all cases despite the treatment.

Treatment

The standard-of-care treatment consists of surgery followed by combined radio- and chemotherapy. However, complete tumor resection is rarely possible, due its infiltrative nature and the proximity of vital centers like optical nerves. The residual tumor is targeted by chemotherapeutic drugs, such as temozolomide and bevacizumab, along with radiotherapy. The efficiency of radiotherapy is however impaired by the invisible tumor infiltration and increased radioresistance of the hypoxic tumor cells, which both are likely to contribute to tumor recurrence. We address the question of improved radiotherapy design in Chapter 5.

2.1.4 Central nervous system lymphoma

Central nervous system lymphoma (CNSL) is rare neoplasia in the central nervous system (CNS). Its highest incidence is in the elderly and the immunocompromised subjects, including HIV patients. In contrast to gliomas, CNSLs originate from lymphocytes (white blood cells), instead of the brain glial cells. The CNSL can arise as primary or secondary lymphoma. The primary central nervous system lymphoma (PCNSL) is confined to the CNS at first diagnosis and constitutes 2 – 4% of all primary brain tumors [131, 159]. The secondary central nervous system lymphoma (SCNSL) appears as simultaneous involvement of the CNS next to systemic (peripheral) lymphoma at first diagnosis or as central nervous system relapse [93]. Both entities most commonly occur as diffuse large B-cell lymphoma [112].

Treatment

There is no evidence-based standard therapy established in CNSL yet. First-line treatment for CNSL is systemic chemotherapy consisting of drugs that pass the blood-brain barrier. High-dose methotrexate, as the most effective single agent, is the backbone for treatment of PCNSL [78]. Consolidation therapy¹ with high dose polychemotherapy and autologous stem cell transplantation has further improved overall survival [93]. However, it is not well established which patients profit from such intense treatment. For patients that relapse on first-line treatment, there is nowadays no established salvage therapy and whole-brain radiotherapy – that comes along with severe neurotoxicity – often remains the only possible treatment option [81, 129]. We present a clinical study investigating diagnostic and prognostic potential of a novel imaging modality for CNSL in Chapter 6.

¹Consolidation therapy is a therapy used to kill residual cancer cells that may be left in the body after the first-line treatment.

2.2 Fundamentals of medical imaging

Medical imaging is a noninvasive technique of creating images of the interior of a body for clinical analysis and medical interventions. It started with a discovery of X-rays by Wilhelm Röntgen in 1895 and since then several imaging techniques have been developed. The imaging procedures use different kinds of physical processes to generate the image signal, including:

- *X-ray transmission,*
- *γ -ray emission from radioisotopes,*
- *Spin precession in magnetic fields.*

In this sense, medical imaging can be seen as a solution to an inverse problem, where the cause (the properties of living tissue) is inferred from effects (the observed signal). Based on the used imaging technique, the medical scans can provide either *structural* (i.e. anatomical) or *functional* (i.e. metabolic) description. The following subsections explain the basic principles of the main imaging techniques used in oncology, namely *X-ray computed tomography*, *positron emission tomography*, and *magnetic resonance imaging*. The aim is to provide a basic understanding of the imaging modalities used in this thesis, while deep technical details can be found in [172].

2.2.1 X-ray computed tomography

An X-ray computed tomography (CT) is a structural imaging method using X-rays to generate 3D anatomical images. The CT scanner consists of a source (X-ray tube) and detectors, as illustrated in Fig. 2.2. The source emits X-rays which traverse the scanned object. The X-rays are attenuated by the object depending on its composition; the denser the material, the more attenuation. The X-ray energy transmitted through the object is then measured by the detectors on the opposite side of the source. The X-ray transformation is used to convert the measured values into the material densities. The source and detectors rotate around the object, while the object is translated through the scanner. This allows a 3D image reconstruction, where the image values reflect the material densities reported in the Hounsfield units (HU). An example of a slice from the abdominal CT scan is shown in Fig. 2.2. The typical Hounsfield values of different tissues, shown in Fig. 2.3, allow detection of the distinct anatomies as well as pathologies represented by a deviation from the standard values. Figure 2.4 shows the 3D reconstruction of the skeletal system, inner organs together with surrounding bones, and musculature obtained just by restricting the range of HU values in the CT scan shown in Fig. 2.2.

CT is a widely used imaging technique, which main advantages include low acquisition time, high resolution, and high contrast mainly in dense materials like bones. However, as CT uses ionizing radiation, exposure should be kept at a minimum, particularly to sensitive organs such as optical nerves, spinal cord, and endocrine glands.

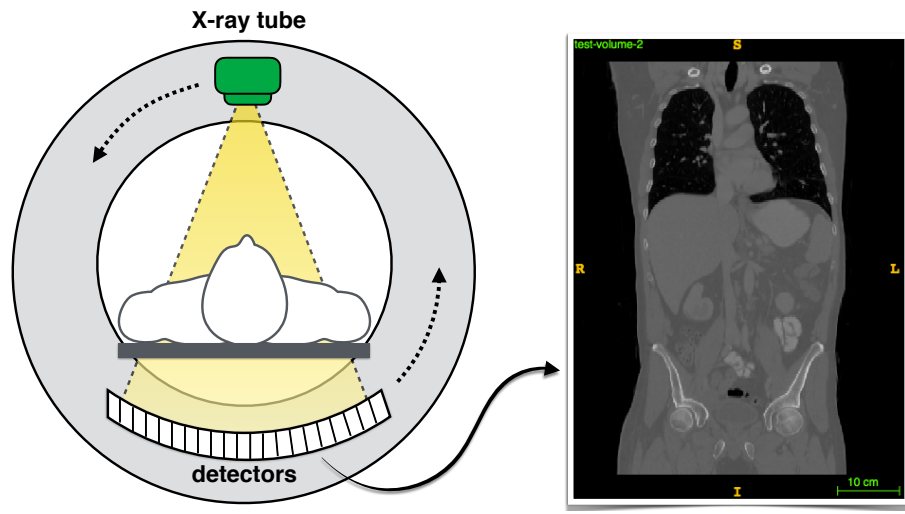


Figure 2.2: A schematic representation of a CT scanner and a slice from an abdominal CT scan. The X-ray tube emits the X-rays, which traverse through the scanned object and are measured by the detectors. Since bones have a higher density than soft tissue, they absorb more X-rays and thus appear brighter on a gray-scaled CT scan.

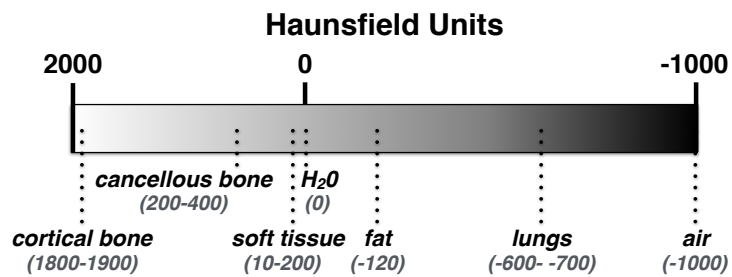


Figure 2.3: Approximate Hounsfield values of tissues commonly found in a CT scan.

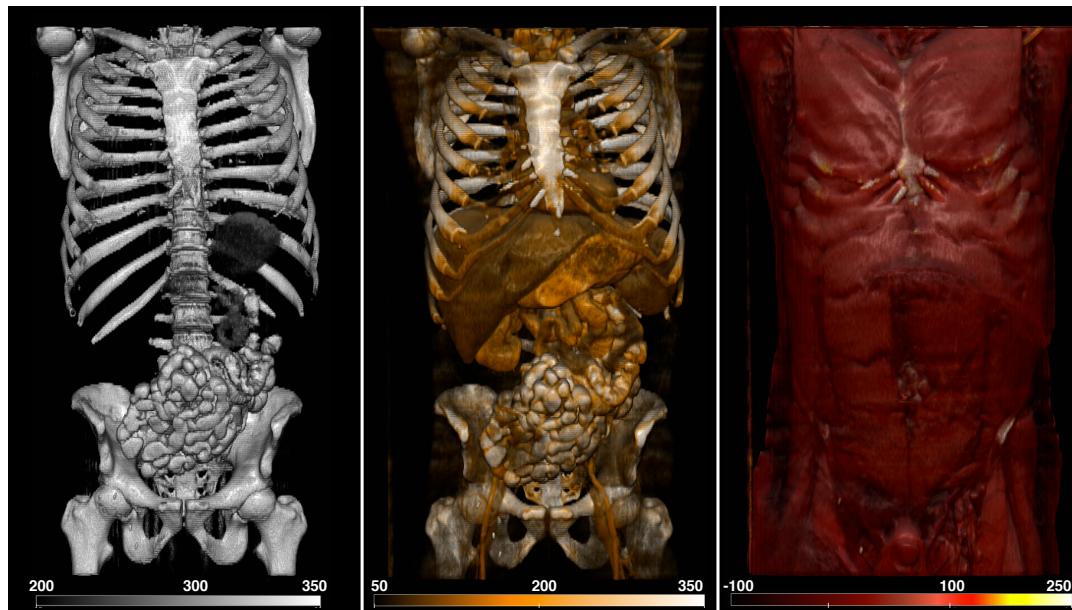


Figure 2.4: A 3D rendering of anatomies reconstructed from the CT scan shown in Fig. 2.2. The skeletal system (left), inner organs and surrounding bones (middle), and musculature (right) are obtained by restricting the range of Hounsfield values in the CT scan. It can be also seen that the HU values of different organs overlap partially.

2.2.2 Positron emission tomography

Positron-emission tomography (PET) is a functional imaging technique used to visualize metabolic processes in the body. The PET imaging uses radioactive tracers that are injected to the patient prior to the scanning. A tracer consists of carrier molecules labeled with radioactive atoms called isotopes. The isotope is a variant of particular chemical element that has modified number of neutrons and thus is unstable. The carrier molecules are designed to accumulate inside cells with high metabolic activity or to bind to specific proteins presented in certain cells. The most commonly used radiotracer is ^{18}F -fluorodeoxyglucose (FDG), a molecule similar to glucose labeled with an ^{18}F isotope of fluorine². Since cancer cells absorb glucose at a higher rate than normal cells, they accumulate a higher amount of the FDG radiotracer. The isotopes trapped inside the cells decay over time. During the decay, one proton of the isotope is converted into one neutron, and at the same time, one positively charged particle, called a positron e^+ , is emitted. A positron is an antimatter to an electron e^- . When a positron collides with an electron, which appears everywhere inside the human body, they annihilate each other. The energy carried by both particles is emitted in the form of two photons (γ -rays), traveling in exactly opposite directions. This process is called antimatter annihilation and is depicted in Fig. 2.5. The released photons

² Fluorine (^{19}F) has 9 electrons and 10 neutrons, while its isotope ^{18}F has the same amount of electrons but only 9 neutrons, which makes it unstable.

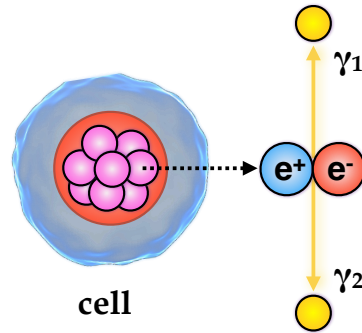


Figure 2.5: Positron emission and antimatter annihilation. A cell takes-up the tracer carrying the isotopes (depicted as purple spheres). Over time, each isotope decays and emits a positron e^+ (shown as a blue sphere). The positron travels $1 - 2\text{mm}$ till it collides with an electron e^- (shown as a red sphere). The electron and positron annihilate each other and their energy is emitted in the form of two photons γ_1 and γ_2 (shown as yellow spheres) in exactly opposite directions. The emitted photons are detected by the PET scanner.

are detected by the detectors inside the PET scanner. The time difference between the detection of two photons in the opposite directions is used to estimate a location from where the two photons were emitted. The PET scanner converts the detected photons to a 3D image of the tracer distribution in the body. Figure 2.6 shows a schematic representation of a PET scanner and a slice of a PET scan obtained with FDG tracer. Since brain, kidney, bladder, and tumor cells have higher glucose uptake, they appear bright on the FDG-PET scan.

The PET scan is characterized by high sensitivity, however, the localization of the abnormal metabolic activities is often complicated by the intrinsic low resolution of the scan. Therefore, the PET scan is often acquired in a combination with a structural scan like CT. If the images are acquired at different scanners, the movement of the patient between the machines creates a misalignment between the scans and hinders the image analysis. To overcome this issue, hybrid PET/CT scanners have been designed. These machines simultaneously acquire both scans, without the necessity to move the patient, making the images naturally aligned. Figure 2.7 shows scans acquired by hybrid PET/CT scanner. Here, the PET scan was performed with PSMA tracer, which binds to a specific protein presented in the prostate cells. By overlaying the CT and the PET scans, as shown in Figure 2.7, the anatomical locations of the high PSMA uptake values can be easily identified, which in turn simplifies the detection of the prostate metastatic lesions inside the spine. In the CT scan alone, the lesions can be indirectly identified as regions with reduced bone density (since the metastatic prostate tumors erode the surrounding bone tissue). However, other factors like increased age or osteoporosis, also reduce the bone density. Moreover, in the early stages of the disease, the tumor-induced changes in the bone density might not yet be visible on the structural CT scan. On the other hand, since the PET scan visualizes the presence of specific cells, it is possible to detect even small lesions without visible bone erosion. The PET

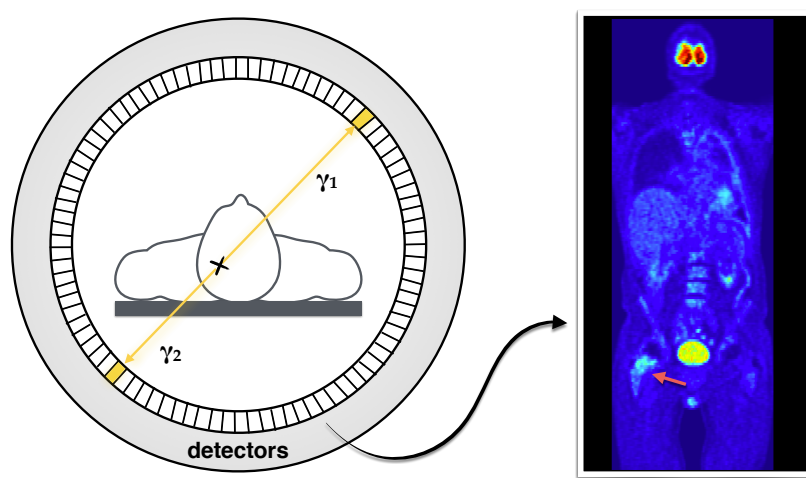


Figure 2.6: A schematic representation of a PET scanner and a slice from a FDG-PET scan. A radioactive tracer, injected to the patient prior to the scanning, accumulates in the cells with high glucose uptake. The unstable isotopes, delivered to the cells with the tracer, decay over time. During this process, a pair of photons, here denoted as γ_1 and γ_2 , is emitted from each isotope. The scanner detects the emitted photons and computes the heat-map of the tracer distribution in the body (shown in the right). Organs that accumulate high amount of glucose, such as brain and bladder, appear brighter on the FDG-PET. The red arrow indicates high tracer uptake in the pelvic bone, caused by a bone lesion.

uptake values can be further used to discriminate between malignant and benign lesions, to estimate patient's prognosis (higher PET uptake values are usually related with more active tumors and worse prognosis), and to monitor tumor response to treatment.

Moreover, the combination of the tracers' ability to accumulate predominantly in cancer cells and the capability of the PET imaging to visualize this accumulation has created novel therapeutic opportunities. The carrier molecules, coated with chemotherapeutic drugs, can be used to deliver a high dose of the drug directly inside the tumor while reducing the treatment effect in the healthy tissue. Recent clinical trials suggested that this targeted treatment – referred to as theranostics – has the potential to become a new milestone in the management of cancer patients [18, 19]. Thus the identification of novel imaging markers plays an essential role in enabling application of the theranostic treatment into mainstream health care. An evaluation of the clinical potential of a novel imaging marker is presented in Chapter 6.

Despite its huge potential, PET imaging also comes with a few limitations. These include low spatial resolution, high acquisition time and cost. Moreover, the measured PET uptake values are affected by various factors such as patient weight and other metabolic processes in the body. Thus for the intra-patient comparison, the PET uptake values have to be normalized by subtracting the signal from healthy tissue of each patient. In comparison with CT imaging, the risks associated with the use of radioactive tracer are very minimal due to small dosage and fast decay.

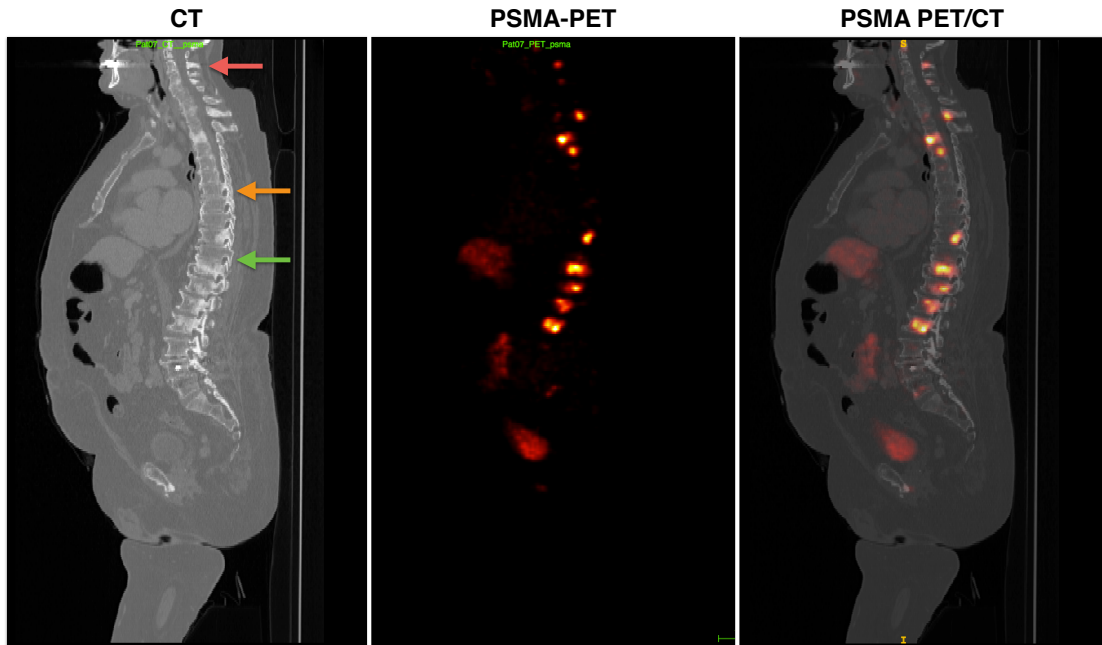


Figure 2.7: A hybrid PSMA-PET/CT scan. The CT scan (left) provides high-resolution anatomical information, while PET scan (middle) highly-specific metabolic description. Since the scans were acquired at the same scanner, they are naturally aligned. An overlay of the CT and PET scans (right) simplifies localization of regions with high tracer uptake, highlighting prostate metastatic lesions inside the spine. The metabolic information enables to discriminate between malignant (green arrow) and benign lesions (orange arrow), although both are manifested by reduced bone density in the CT scan. Moreover, the small tumor in the cervical spine (red arrow) did not yet alter the bone density significantly and thus it might be missed in the CT scan.

2.2.3 Magnetic resonance imaging

Magnetic resonance imaging (MRI) is a structural imaging technique using a strong magnetic field to polarize and excite hydrogen atoms to generate 3D anatomical images. Hydrogen is the most abundant atom in the human body, appearing mainly in water and fat molecules. As the simplest chemical element, hydrogen contains only one proton, which is a positively charged particle with an own magnetic field. In a nutshell, the MRI works as follows. The MRI scanner emits radio frequency (RF) pulses with a resonance frequency specific to hydrogen protons, making the protons to align with the main magnetic field of the MRI scanner. When the RF pulse is turned off, the protons "relax" back to their natural state and emit radio-waves in the process. The MRI scanner detects these radio-waves and transforms them into a 3D anatomical image.

A 3D image consists of voxels (i.e. 3D pixels), where each voxel corresponds to a small volume of tissue, as illustrated in Fig. 2.8. To explain the MRI physics, we look at a single voxel. For simplicity, we will assume that the voxel contains 8 hydrogen protons, as illustrated in Fig. 2.8.

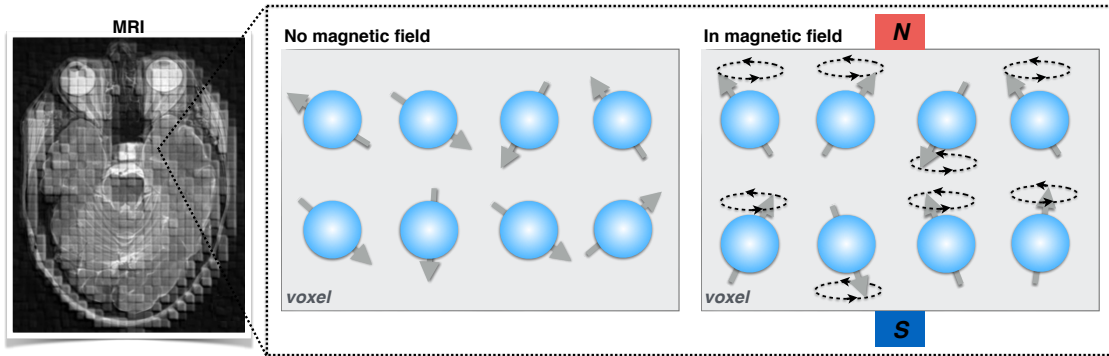


Figure 2.8: The principle of MRI physics inside a voxel. The illustration shows a selected voxel with 8 hydrogen protons. Under normal conditions (the middle plot), the protons are oriented randomly. Once the protons are exposed to a strong magnetic field (left plot), they align parallel or antiparallel with the main magnetic field and precess around it. Majority of the protons get oriented parallel with the main magnetic field and they are assumed in a low energy state, while the antiparallel-oriented protons are assumed in a high energy state.

Under normal conditions, the hydrogen protons are oriented randomly. Once the protons are exposed to a strong external magnetic field, they align in such a way, that majority of the protons is oriented parallel with the main magnetic field, while the rest is antiparallel to it. The orientation of the protons' alignment depends on the protons' energy, where the protons parallel with the main field are assumed to be in low energy state, while those aligned antiparallel are considered to be in high energy state. Moreover, these protons also precess around the main magnetic field. For demonstration purposes, we place all the protons in a common origin, as shown in Fig. 2.9 (A). The net magnetisation, given as a sum of the magnetic fields of all protons, is oriented in the same direction as the main magnetic field. The magnetisation in this direction is called longitudinal and is depicted as a green arrow in Fig. 2.9 (A). Since this magnetisation has the same direction as the main magnetic field, it can not be measured directly. To overcome this, the MRI scanner emits radio frequency (RF) pulses at the resonant frequency of the hydrogen atoms which cause two things:

- I.) The protons absorb the energy from the pulses and flip to the high energy state, reducing the longitudinal magnetisation, since the opposing forces cancel each other out (Fig. 2.9 I.).
- II.) The protons synchronize and start to spin together, making the net magnetisation to point in the direction perpendicular to the main magnetic field. The magnetisation in this direction – termed transversal magnetisation – can be detected (Fig. 2.9 II.).

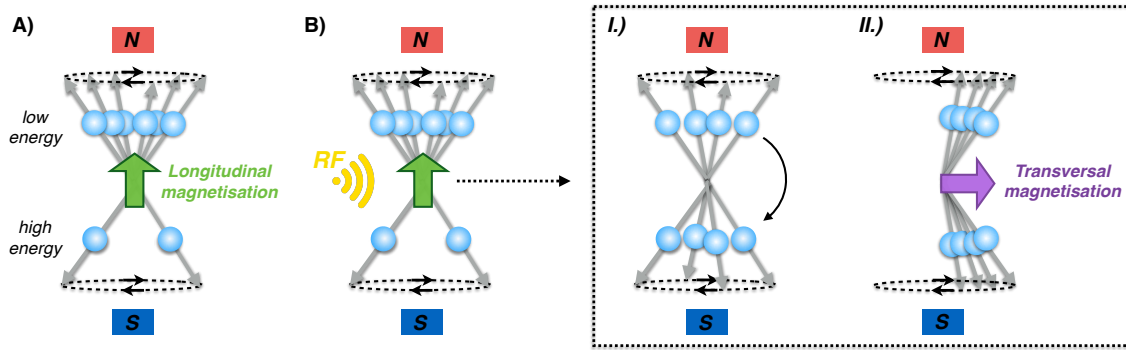


Figure 2.9: Polarization and excitation of protons in a magnetic field. **A)** Polarization: the protons in a magnetic field (shown in a common origin) orient themselves with the main magnetic field. The net magnetisation is oriented in the direction of the main magnetic field and is referred to as longitudinal (green arrow). **B)** By emitting radio frequency (RF) pulses, the protons undergo excitation, which includes two processes: *I.)* Some low energy protons flip to a high energy state, reducing the longitudinal magnetization to zero. *II.)* The protons synchronize and spin together, changing the orientation of the net magnetisation to a direction perpendicular to the main magnetic field, referred to as a transversal magnetisation (purple arrow).

After the RF pulses are switched off, as shown in Fig. 2.10, the protons relax back to their baseline positions through two distinct processes:

- 1) **T2-Relaxation:** The protons, being positively charged will repel each other and move apart, reducing the transversal magnetisation to zero.
- 2) **T1-Relaxation:** The high energy protons fall back to the low energy state while restoring the original longitudinal magnetisation.

This allows to obtain two types of MRI scans, so called T1-weighted (T1w) and T2-weighted (T2w) MRI. Each tissue has own T1 and T2-relaxation. Figure 2.10 shows the T1 and T2-relaxation of water and soft tissue. Since water relaxes the transversal magnetisation slower than tissue, the transversal magnetisation in water is higher and thus water appear brighter (whiter) than tissue on a T2w scan. On the other hand, since water has larger T1-relaxation time than tissue, the longitudinal magnetisation in water is smaller than in tissue, which in turn cause water to appear darker than tissue on the T1w MRI scan.

By changing the frequency of the on/off-modes of the RF pulses, it is possible to suppress a signal from a certain tissue. For instance, in Fluid-attenuated inversion recovery (FLAIR) scan, the signal from free water is suppressed. Alternatively, it is possible to inject a contrast agent to change ferromagnetic properties of tissues that absorb it, reducing their T1-relaxation time and so enhancing their signal. Often Gadolinium (Gd) contrast agent is used to enhanced the vascularised parts of the tissues, producing so called Gadolinium-enhanced T1-weighted (T1Gd) scan. Figure 2.11 shows a slice of a brain scan acquired with different MRI modalities.

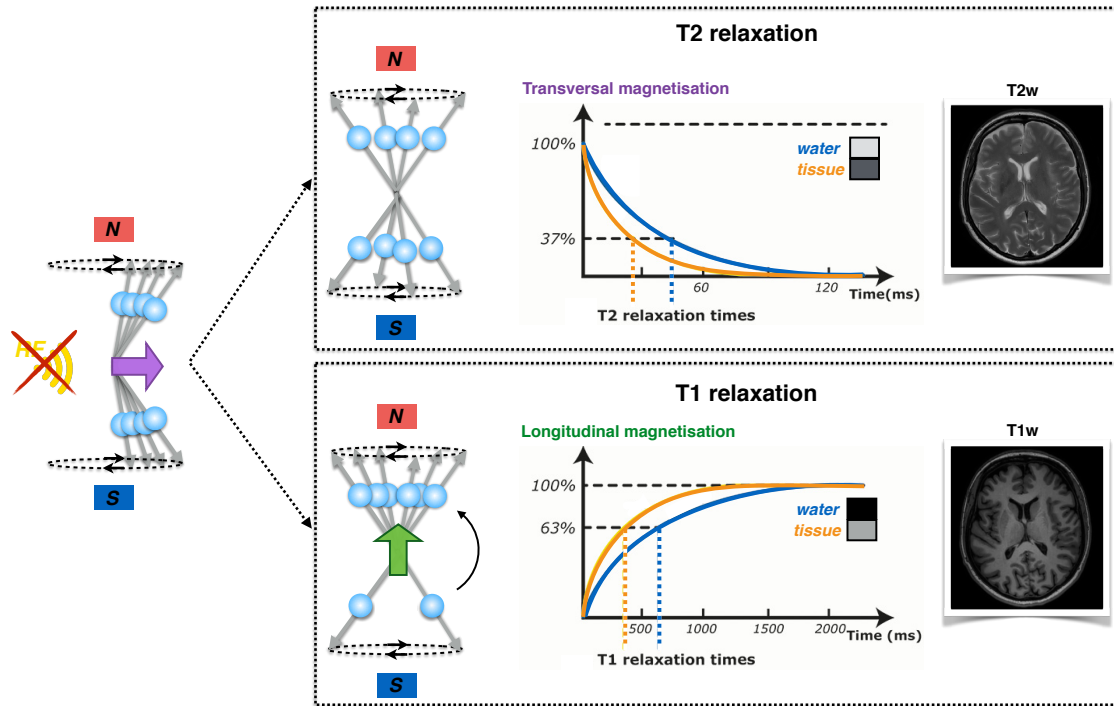


Figure 2.10: T1 and T2 relaxation. After turning off the RF pulses, the protons relax back to their original position through two processes: **T2-relaxation**: The protons that were spinning together repulse each other, which in turn reduces the transversal magnetisation; **T1-relaxation**: The excited protons fall back to the low energy state, restoring the longitudinal magnetisation. Each tissue has different T1 and T2-relaxation, leading to a different representation of distinct tissues on the T1w and T2w MRI scans.

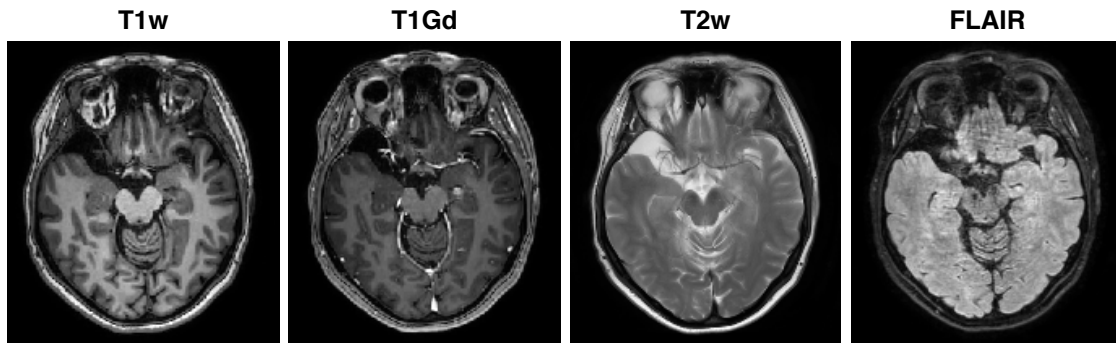


Figure 2.11: A slice of a brain scan acquired with four different MRI modalities. The T1w scan shows a good contrast between white and gray matter, while the T1Gd scan enhances the vasculature. The T2w scan enhances fluid, while a signal from free water is suppressed in the FLAIR scan.

MRI scans have superior soft tissue contrast, in comparison with CT, making it suitable imaging tool for brain, spine, joints and other soft tissue body parts. Moreover, MRI does not use ionizing radiation and thus there is no limit on the number of scans a subject can be exposed to. This makes it especially suitable for cases where frequent imaging is required for diagnosis or therapy. On the other hand, MRI has a significantly higher acquisition time than a CT scan, which might prohibit its usage in emergency cases, e.g. in case of stroke patients. Moreover, MRI can not be used in the presence of non-removable metal implant devices, such as pacemakers, insulin pumps, cochlear implants or bone screws.

2.3 Imaging in neurooncology

The primary role of neuroimaging is the detection and localization of brain lesions together with the estimation of the tumor mass effect on the brain tissue, nerves, and vasculature. Consequently, medical scans are used to identify the target area for biopsy, surgical planning and radiation intervention, and to assess tumor progression and treatment outcome. The fundamentals of the medical imaging were described in the previous section, while here we focus on the interpretation of the scans in the terms of neurooncology. Herein, only scans used in this thesis are presented, while more detailed information, as well as other modalities can be found in [28, 43, 114, 185]. First, we describe the four MRI modalities used in standard-of-care management of patients with brain lesions, in particular: T1w, T1Gd, T2w, and FLAIR scans. Afterward, two novel PET markers used in glioma and brain lymphoma imaging are presented. Figure 2.12 shows an overview of the multimodal MRI and PET scans of a patient with glioblastoma, while scans of a patient with brain lymphoma are shown in Fig. 2.13.

T1w MRI

In the T1w MRI scan, the image contrast is based predominantly on the T1-relaxation time. It is especially suitable for visualizing brain anatomies, providing a clear separation of white matter, gray matter and cerebrospinal fluid (CSF). The lesions appear dark on the T1w MRI scan, however, their complex internal structures usually can not be distinguished.

Description:

- *bright*: fat, muscles, paramagnetic substances
- *gray*: lesions, edema, gray matter, white matter, inflammation, infection
- *dark*: air, calcification, CSF, hemorrhage

Notes:

- Gray matter appears darker than white matter
- Similar intensities in tumor and gray matter impede their distinction
- Less sensitive to tumor internal structures

T1Gd MRI

It is a T1w scan acquired after intravenous administration of the Gd contrast agent. The T1Gd scan enhances vascular and extravascular Gd. Since the tumors have increased vasculature, the Gd accumulates mainly in the vascularised (i.e. active) parts of the tumor. The necrotic core, if presented, appears as a dark region enclosed by the enhancing halo. The T1Gd-enhancement is also used in tumor grading. The LGGs do not show T1Gd-enhancement nor a necrotic core, while the HGGs are characterised by Gd enhancement and often presented necrotic core. However, the final tumor grade is estimated by PET scan and biopsy.

Description:

- *bright*: active tumor, vasculature
- *dark*: necrotic core (enclosed by the enhancing halo)

Note:

- Like the T1w scan but with bright vascularized regions

T2w MRI

The image contrast is based mainly on T2-relaxation time. T2w MRI is particularly suitable for visualizing fluid-rich structures like edema or CSF, but it is less sensitive to soft tissues like white and gray matter.

Description:

- *bright*: lesions, edema, CSF, inflammation, infection, hemorrhage
- *gray*: gray matter, white matter
- *dark*: air, calcification, fat, paramagnetic materials like iron

Notes:

- White matter appears darker than gray matter
- Similar intensities in tumor and CSF hinder lesion delineation near the ventricles
- Less sensitive to the tumor internal structures

FLAIR MRI

Is similar to T2w MRI but the signal from CSF is suppressed. It is particularly useful for the distinction between lesions and CSF. The contrast between white and gray matter is less pronounced.

Description:

- *bright*: lesion, edema, multiple sclerosis lesions, hemorrhage
- *dark*: CSF, ventricles

Note:

- Especially good for lesions near ventricles
- Often bright areas appear around ventricles

FET-PET

It is a PET scan obtained with ^{18}F -fluoro-ethyl-tyrosine (FET) tracer, which is an amino acid exhibiting high uptake by tumor cells but low uptake by healthy cells. The FET is a promising marker in glioma imaging, suitable for visualization of both low and high-grade gliomas. It has a wide application in detection and management of glioma patients.

Description:

- Enhances active parts of the tumor
- Necrotic core and non-active tumor appear dark
- The uptake values significantly correlate with tumor cell density [83, 167]

Usage:

- Early detection of tumor recurrence after therapy [41, 95]
- Differentiation of tumor recurrence from radiotherapy-induced changes [144, 164]
- Localisation of hot-spots that should be targeted by biopsy [95, 167]
- High uptake values are correlated with worse prognosis [83]
- The potential prognostic factor for response to the treatment [41, 142]

CXCR4-PET

The C-X-C motif receptor 4 (CXCR4) is a chemokine receptor that plays an important role in embryonic development, hematopoiesis and immunity. Multiple malignancies have been identified to express CXCR4 on their cell surface, including hematologic cancer like multiple myeloma, lymphoma, and leukemia as well as solid tumors in lungs, prostate, and brain. Overexpression of CXCR4 represents a negative prognostic factor and is a potential target for therapy [90, 96]. Recently, molecular agents targeting CXCR4 receptors have been developed, with [^{68}Ga]Pentixafor being the most prominent imaging trace and [^{68}Ga]Pentixafor its therapeutic twin [51, 90]. Despite the novelty of this approach, the preliminary studies have already suggested a great potential of CXCR4-directed imaging and therapy.

Description:

- Enhances regions with overexpression of CXCR4 receptors
- High uptake values are associated with poor prognosis [74, 90]

Usage:

- Differentiation of brain lymphomas from other brain-derived lesions like glioblastoma
- Better lesion detection in multiple myeloma patients than FDG-PET [90, 96]
- Better contrast than FDG-PET for lymphomas in the central nervous system [74]
- Potential prognostic value for treatment response for brain lymphomas (see Chapter 6)
- CXCR4-directed theranostics for lymphoma and multiple myeloma [76, 90]

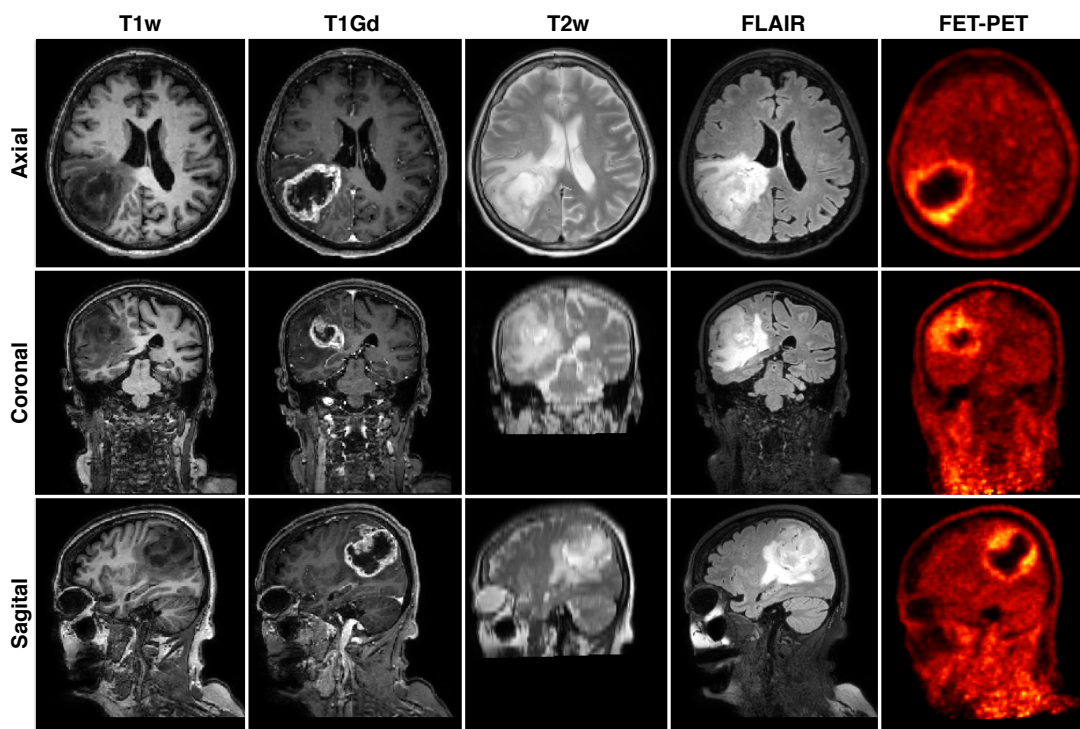


Figure 2.12: The multimodal scans of a patient diagnosed with glioblastoma. The T1w scan shows a good contrast between brain anatomies, while the tumor appears relatively dark. The T1Gd scan enhances active parts of the tumor, while the dark region enclosed by the enhancing tumor corresponds to the necrotic core. The T2w scan enhances fluid-rich structures. Similar intensities in the edema and CSF complicates delineation of the tumor close to the ventricles. The signal from the CSF is suppressed in the FLAIR scan, allowing a clear differentiation between the edema and ventricles. The FET-PET scan enhances active parts of the tumor. The necrotic core appears dark since the dead cells do not take up the tracer.

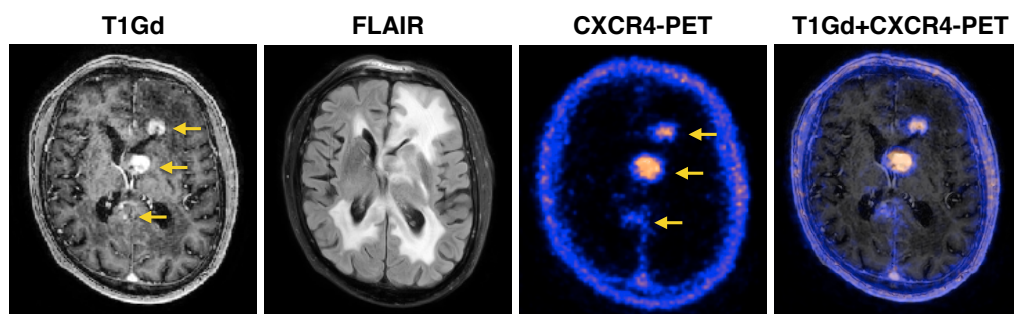


Figure 2.13: The multimodal scans of a patient with brain lymphoma. The CXCR4 directed PET identifies three lesions (marked by yellow arrows) with different level of progression. The smallest lesion is not yet visible on the T1Gd MRI scan, but it can be identified by PET enhancement.

2.4 Summary

Cancer is an aggressive disease capable to invade any part of the human body. Its morphological and physiological manifestations vary significantly for different types of cancer, underlying the complexity of the disease. Medical imaging provides a non-invasive tool to detect, localize, and diagnose tumors as well as to assist treatment procedures. The increasing amount of cancer incidences goes hand-in-hand with a growing demand for tools for processing and extracting information from medical scans. In Chapter 3 we focus on the development of image processing tools in oncology. Once the tumor information is extracted, it has to be evaluated in terms of prognosis and treatment options. Here, mathematical modelling can provide a helping hand, as we show in Chapters 4 to 6.

MEDICAL IMAGE SEGMENTATION

The increasing number and size of medical scans have necessitated the use of computer methods to automatize and facilitate image processing and analysis [138]. In particular, computer algorithms are used to detect and delineate structures of interest, such as organs and pathologies. This process is referred to as image segmentation since it partitions the image into different meaningful segments. Image segmentation plays a vital role in multiple biomedical applications, including localization of pathologies, treatment planning, computer-guided surgery and evaluation of treatment responses. Moreover, image segmentation is an essential part of personalized tumor modelling, where mathematical tumor models are solved in the patient-specific anatomy reconstructed from the medical scans.

This chapter focusses on the medical image segmentation. First, we provide a summary of basic concepts and terminology used in image segmentation field. Then, two segmentation methods developed in this thesis are presented. The first method is an atlas-guided approach for skull-stripping and brain tissue segmentation. The second method uses convolutional neural networks to detect and segment multiple myeloma lesions in multimodal full-body scans. The chapter concludes with two segmentation benchmarks for objective evaluation of the tumor segmentation methods, mainly: the liver lesion segmentation challenge (LiTS) and the brain tumor segmentation challenge (BraTS).

3.1 Introduction

A *digital image* is a collection of measurements on a two-dimensional (2D) or three-dimensional (3D) regular grid. As we saw in Section 2.2, the particular meaning of these measurements (i.e. image intensities) at each location depends on the imaging modality. For instance, in the CT

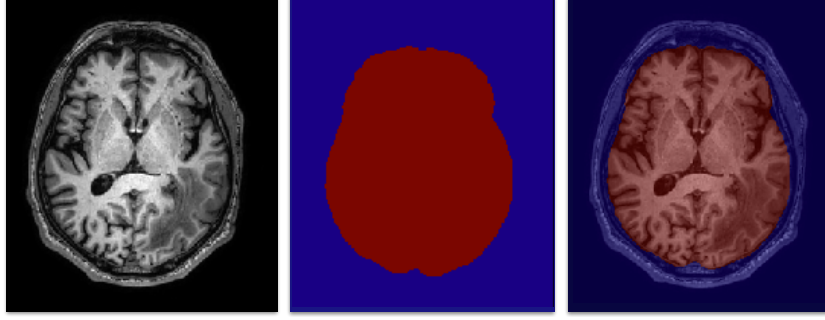


Figure 3.1: Illustration of image segmentation task. The input image (left), the binary image segmentation with two labels: brain and background (middle), and the input image overlaid with the segmentation (right).

scan, the image intensities represent radio-sensitivity, while in PET scan it is a concentration of the tracer. The location of each measurement is called a pixel in a 2D image and a voxel in a 3D image. Mathematically, image I can be defined as a mapping from 2D or 3D space to the space of image intensities, i.e. $I(i_x, i_y)$ in 2D space and $I(i_x, i_y, i_z)$ in 3D space, where $i_x = 1, \dots, N_x$, $i_y = 1, \dots, N_y$ and $i_z = 1, \dots, N_z$, denote spatial coordinates and N_x, N_y, N_z the image resolution in each dimension. For simplicity, we often denote the image I as a vector of all image intensities i.e. $I = \{I_i\}_{i=1}^N$, where i is index across all $N = N_x \times N_y \times N_z$ voxels.

The *image segmentation* S is an image of the same resolution as the input image I , which partitions the image I into constituent non-overlapping segments $S^k \in I$ such that:

$$I = \bigcup_{k=1}^K S^k, \quad (3.1)$$

where $S^k \cap S^j = \emptyset$ for $k \neq j$ and K is the total number of the segments. In the case of discrete image segmentation, each segment is represented by a different integer number, often called a label. Fig. 3.2 shows an example of an image and its segmentation with 2 labels.

Performance evaluation

To evaluate the quality of a segmentation method, its results have to be compared with the ground truth segmentation. In medical imaging, the ground truth segmentation is usually not known, since it would require a biopsy or surgery. Instead, a manual segmentation created by a trained expert or consensus of segmentations from multiple experts is used. The correctness of the segmentation is quantified by various similarity measures. Here, we describe the similarity measures used in this thesis, while an overview of other measures can be found in [176].

For illustration, let us consider a binary tumor segmentation, i.e a segmentation that assigns a value 1 to each voxel with a lesion and 0 otherwise. Figure 3.2 shows a sketch of two binary tumor segmentations. We will denote the ground truth segmentation as T and the predicted

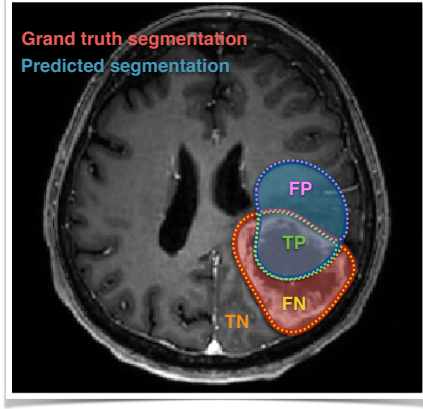


Figure 3.2: Illustration of two binary tumor segmentations: ground truth segmentation (red) and the predicted segmentation (blue). The dashed lines mark regions used for the segmentation evaluation: the true positive (TP) region is shown in green, the false positive (FP) in pink, the false negative (FN) in yellow, while all the rest corresponds to the true negative (TN) region.

segmentation as P . A value of each segmentation at voxel i is then denoted as T_i and P_i , respectively. Then following terms: true positive (TP), true negative (TN), false positive (FP) and false negative (FN) can be defined by so called **confusion matrix** as:

	$P_i = 0$	$P_i = 1$
$T_i = 0$	true negative (TN)	false positive (FP)
$T_i = 1$	false negative (FN)	true positive (TP)

The confusion matrix is used for the computation of the following performance measures:

Sensitivity: This measure, sometimes called a true positive rate, computes a proportion of voxels with the tumor that was correctly identified:

$$\text{Sens}(T, P) = \frac{\sum_{i=1}^N TP}{\sum_{i=1}^N TP + \sum_{i=1}^N FN}. \quad (3.2)$$

In other words, it measures how sensitive the segmentation is to the tumor.

Specificity: This measure, also known as a true negative rate, computes a proportion of voxels without tumor that was identified as such:

$$\text{Spec}(T, P) = \frac{\sum_{i=1}^N TN}{\sum_{i=1}^N TN + \sum_{i=1}^N FP}. \quad (3.3)$$

Thus, it measures how sensitive the segmentation is to the tumor-free regions.

Precision: This score computes a proportion between the correctly estimated voxels with tumor and the number of all voxels estimated as tumor:

$$\text{Prec}(T, P) = \frac{\sum_{i=1}^N TP}{\sum_{i=1}^N TP + \sum_{i=1}^N FP}. \quad (3.4)$$

Dice score: This measure, also called as F-score, is defined as a harmonic mean of sensitivity and precision:

$$\text{Dice}(T, P) = \frac{\sum_{i=1}^N 2TP}{\sum_{i=1}^N 2TP + \sum_{i=1}^N FP + \sum_{i=1}^N FN}. \quad (3.5)$$

Hausdorff distance: This measure computes a maximum overall surface distances between two segmentations. Let us denote ∂T_1 and ∂P_1 the surface of the ground truth and the predicted tumor segmentation, respectively. The Hausdorff measure computes for all points t on the surface of ∂T_1 a shortest distance $d(t, p)$ to points p at the surface of ∂P and vice versa. The final score is then given as:

$$\text{Haus}(T, P) = \max \left\{ \sup_{p \in \partial P_1} \inf_{t \in \partial T_1} d(p, t), \sup_{t \in \partial T_1} \inf_{p \in \partial P_1} d(t, p) \right\}. \quad (3.6)$$

Sensitivity, specificity, precision and Dice scores compute voxel-wise overlap of the segmented regions. In the case of very small structures, the voxel-wise scores can be relatively low, even if the predicted segmentation is relatively close to the ground truth. In such case, it might be more informative to compute the surface distance between the segmentations. On the other hand, since the Hausdorff measure computes the maximum distance, even a single outlier voxel significantly reduces the overall score. Since each measure captures different properties of the segmentation, usually multiple scores are reported.

Partial-volume effect

The partial-volume effect occurs when multiple tissue types contribute to a single voxel, resulting in a blurry interface between the tissues [138]. It is a relatively common artifact in medical imaging, mainly in data with low or anisotropic resolution. Figure 3.3 shows a head MRI scan, where the interface between the white and gray matter is blurred due to the partial-volume effect, which complicates precise delineation of these structures. The most common approach for dealing with the partial-volume effect is to allow an overlap of the segmented regions, so called *soft segmentations*. In such case, the segmentation represents a percentage of a certain structure at each voxel. In comparison with the binary segmentation, the soft segmentation retains more information from the original image by accounting for uncertainties in the boundaries of the objects. A soft segmentation can be translated to a *hard segmentation* (i.e. binary) by assigning each voxel a label of the tissue with the highest percentage.

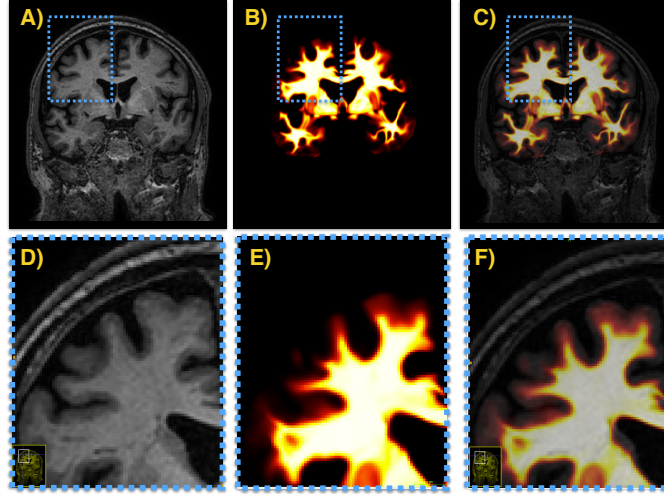


Figure 3.3: Illustration of the partial volume effect. The top row shows axial view of a head scan, while the zoomed view to the region marked by the dashed blue rectangle is shown at the bottom. The partial-volume effect can be seen in the interface between the white and gray matter in A) and D). A soft segmentation of the white matter is shown in B) and E). An overlay of the input scan and the soft segmentation is displayed in C) and F).

3.2 Segmentation methods

Hitherto a cornucopia of segmentation methods was developed. An overview of the methods used for medical image segmentation can be found in review articles such as [42, 138, 161]. In this section, we present two segmentation methods, which are employed in this thesis. The first one is an *atlas-guided method*, while the second approach is based on *conventional-neural networks*. We start with a basic theoretical description of each method, followed by its application to specific tasks. The first method is used for extracting brain anatomies from head MRI scans, while the second one for detecting multiple myeloma lesions from multi-modal full-body scans.

3.2.1 Atlas-guided methods

Atlas-guided segmentation methods are based on a registration of an atlas to a subject scan. The *atlas*, also called template, is an annotated scan of selected anatomy. To capture anatomical variability across the population, the atlas is usually constructed by a fusion of annotated scans from multiple subjects, as illustrated in Fig. 3.4. There exist several fusing strategies, as described in [50, 116], which lead to a different level of specificity along with discrete or probabilistic segmentations. A common feature of most atlases is that the anatomy of interest, which is typically similar across all subjects, is well resolved, while the subject-specific features, like face, are usually blurred due to the fusion process. Figure 3.5 shows T1w and T2w MRI atlas of the healthy adult human brain together with tissue probability maps provided by ICM

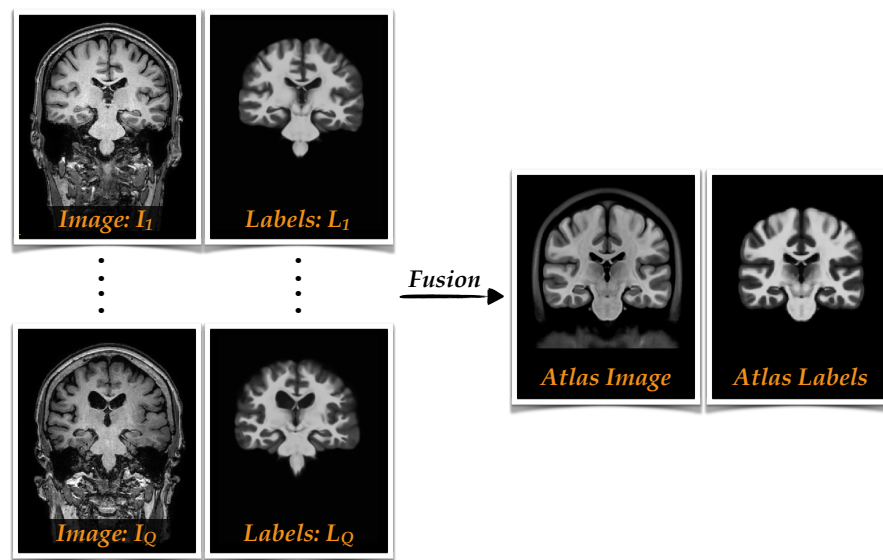


Figure 3.4: An illustration of brain MRI atlas construction. To account for the anatomical variability across the population, the atlas is constructed by fusion of annotated scans from multiple subjects.

multichannel atlas [50]. By deforming the atlas to match the subject scan, one can use the atlas annotation to describe the anatomies in the subject scan.

A transformation that maps one image into a target image is called *registration*. The image that is being transformed is referred to as the moving image, while the target image is called fixed. The transformation can be either rigid (non-deformable) or non-rigid (deformable). The first one consists of linear operations like rotation, translation, and affine transformations, while the latter one allows to deform the image through physical deformation models. Registration is an optimization problem searching for transformation that minimizes the difference between the two images. After successful registration, the resulting image has the same resolution and one-to-one correspondence with the input image. Rigid registration is sufficient for aligning scans of the same patient if the considered anatomy does not deform (i.e. due to breathing, body posture or disease). Non-rigid transformation is required for registration of scans from different subjects or the same subject at different stages of disease or body development. In many cases, a sequential application of rigid and non-rigid transformations is used. Figure 3.6 shows a rigid transformation that maps the brain atlas to the subject scan. The same transformation can be applied to map the atlas annotations to the subject scan to obtain the subject-specific tissue segmentations.

Atlas-guided methods are particularly suitable for segmenting anatomies that are relatively similar across the population, like abdominal organs [132] or brain structures [21, 111]. Often they are fully automated, without input parameters, and can be easily applied for segmenting

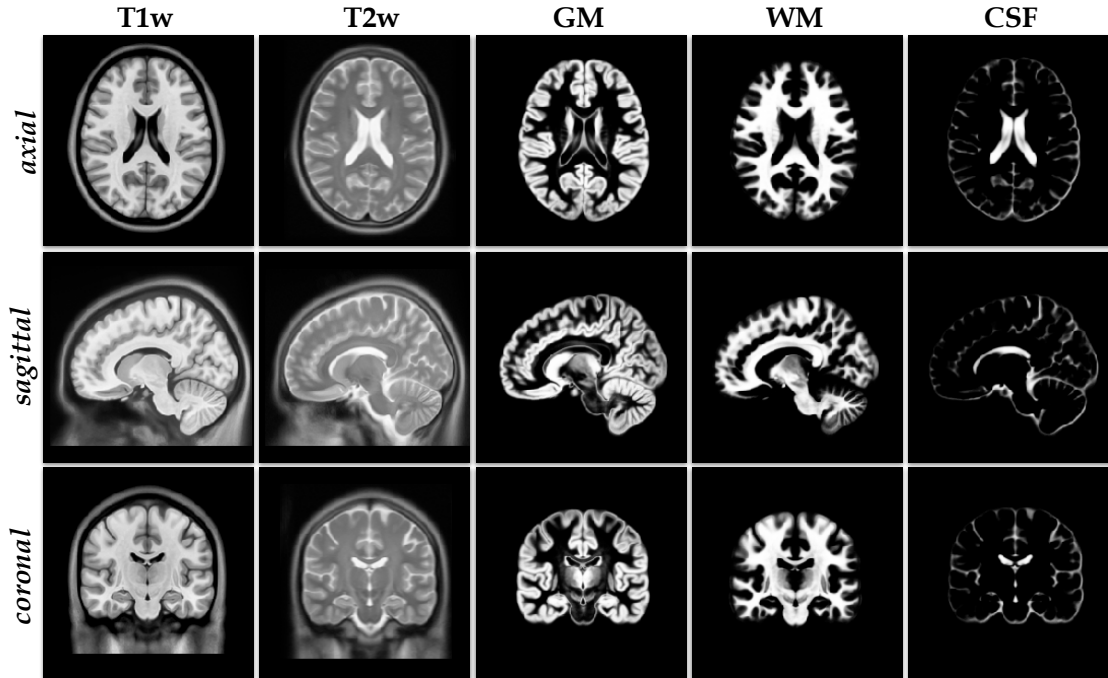


Figure 3.5: The T1w and T2w MRI atlas of the healthy adult human brain together with tissue probability maps provided by [50]. A subject-specific structures like face are usually blurred while structures similar across subjects, like brain tissues, are more clearly pronounced.

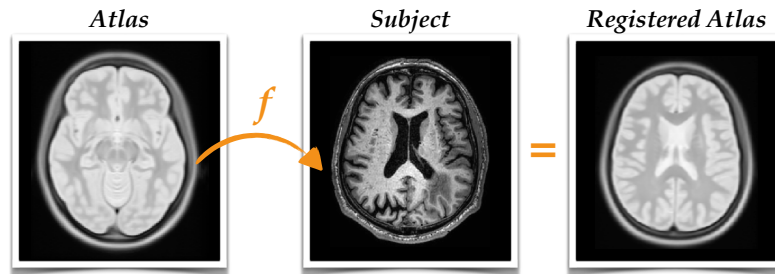


Figure 3.6: An illustration of a rigid registration of an atlas to a subject scan. A rigid transformation f is sufficient to align the scans but it can not capture tissue deformations as seen in the ventricles.

any structure available in the atlas. On the other hand, they are not suitable for segmenting pathologies like tumors, which vary significantly in shape and location. The performance of atlas-guided methods depends on the quality of the registration, which can be prone to errors in patients with significant pathological deformations since the atlas is constructed from a population of healthy subjects. For instance, registration of atlas to a scan with a resection cavity is still an unresolved task, since the current registration methods can not replace a tissue by a resection cavity. Moreover, a choice of atlas also influences the accuracy of the results [5]. A review of the atlas segmentation methods can be found in [85].

3.2.2 Skull-stripping and brain tissue segmentation

Herein, we present a simple atlas-guided method for extracting brain tissue from MRI scans of patients with brain lesions. We wish to point out that this method was developed predominantly for the purpose of the tumor growth modelling presented in Chapters 4 and 5. However, since the method yields promising results, we provide it as open-source code¹. This section presents a theoretical base, while the software details are described in Chapter 8.

Motivation

Presence of non-brain tissues in the head MRI scans hinders the performance of most brain image processing methods. The process of extracting brain tissue from the scan is referred to as a skull-stripping. It is a primary step for most image processing algorithms and its accuracy directly influences the performance of the consequent image analysis methods.

In the past, several skull stripping algorithms were developed. A recent review [87] provides a detailed summary of the existing methods. However, all these methods are designed either for healthy brains or cases with pathologies that do not significantly alter brain anatomy. The accuracy of these methods drops significantly in the presence of brain lesions or resection cavities, usually leading to significant under or over-segmentation. Similarly, most brain tissue segmentation methods are designed for healthy anatomies and underperform in the presence of lesions. Moreover, these methods are not able to estimate the brain tissue below the visible tumor. The reduced performance of the standard skull-stripping and brain tissue segmentation methods in the presence of lesions poses a significant issue not only for clinical application but also for computational models simulating tumor growth in the patient-specific anatomy.

To overcome these issues, we present an automated and robust method for extracting brain tissue from scans with and without brain pathologies. Due to its simplicity, the method is referred to as simple skull stripping (S3) method and it belongs to a family of atlas-guided algorithms. In addition to skull-stripping, S3 estimates the brain tissue segmentations even in the presence of lesions, which can be used for computational tumor modelling as well as for evaluating the

¹ <https://github.com/JanaLipkova/s3>

extent of neurodegenerative diseases. For instance, Alzheimer and dementia diseases manifest their progression by a decreased volume of gray matter and increased volume of ventricles. The next section provides a description of the S3 method, followed by its comparison with two state-of-the-art skull stripping methods, namely Brain Extraction Tool (BET) [162] and Robust Learning-based Brain Extraction System (ROBEX) [84]. The tissue segmentations computed by S3 method are compared with the results obtained by a generative Expectation-Maximization (EM) algorithm [122, 127].

Simple Skull Stripping (S3) method

The S3 method uses a multi-step atlas-guided approach to skull-strip and to segment the brain tissues in the input head MRI scan. The used atlas is the T1w MRI atlas with probabilistic tissue segmentations shown in Fig. 3.5. An overview of the S3 method is depicted in Fig. 3.7 and the algorithm is described in Algorithm 1.

Algorithm 1 Simple Skull-Stripping (S3) Algorithm

- 1: *Input*: Head MRI scan (shown in the light blue frame in Fig. 3.7)
 - 2: Compute a rigid registration f that maps the brain atlas to the subject (Fig. 3.7: blue box)
 - 3: Apply f to map the atlas brain mask and tissue segmentations to the subject scan (purple box). The registered mask provides a coarse approximation of the subject brain mask.
 - 4: Use the coarse brain mask to skull-strip the subject and the atlas scan (yellow box).
 - 5: Compute a non-rigid registration g that maps the masked atlas to the masked subject, accounting for the subject-specific brain morphology (green box).
 - 6: Apply g to map the atlas tissue segmentations to the subject anatomies (orange box).
 - 7: Fuse the subject tissue segmentations to create a refined brain mask (orange box). Compute a 95% percentile of the sum of all tissue segmentations and exclude values smaller than the lower bound of the 95% percentiles.
 - 8: Apply the refined brain mask to the input MRI scan (orange box).
 - 9: *Output*: Coarse and refined brain mask, skull-stripped input scan and tissue segmentations.
-

The reason for using a rigid registration in the first step is that the atlas and subject scan can constitute of different structures (e.g. face, neck). These discrepancies would result in artificial deformations if non-rigid registration would be used. On the other hand, once the atlas and subject scan are masked by the coarse mask, a non-rigid registration can be applied to locally deform the atlas to mimic the subject-specific brain morphology. The non-rigid transformation g could be eventually used to deform the coarse brain mask, however, a fusion of the brain tissues segmentations provides a more refined result. The reasoning is as follows. Since the probabilistic tissue segmentations are used, their sum should be one in the brain region. As a result of the registration, the actual sum might be slightly smaller than one. However, the regions where the sum of all tissues is very small can be assumed as non-brain tissue, and thus they are excluded from the brain mask during the fusion step.

The S3 method can be used to skull-strip any head scan. However, if the tissue segmentations

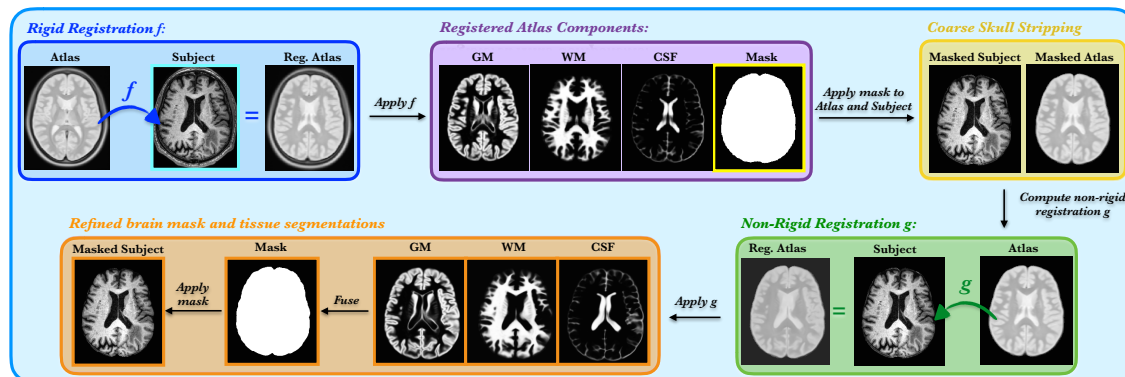


Figure 3.7: An overview of the S3 algorithm. The method takes as input the head MRI scan (marked by the cyan frame) and as output provides brain mask, skull-stripped input MRI scan, and the brain tissue segmentations (shown in the orange box).

are desired, then the T1w is the preferred modality. The reason is twofold: 1) the T1w scan provides better contrast between the brain tissue anatomies than other modalities; 2) the lesions manifestations are least pronounced on the T1w modality.

Results

Skull-stripping. To assess benefits of the S3 skull-stripping method, its performance is compared with two state-of-the-art algorithms, namely BET and ROBEX, on scans without and with pathologies, including lesions and resections cavities. The BET algorithm uses a deformation model to identify brain anatomy. It first estimates a center of gravity of the brain, constrained by the brain tissue, and initializes a small sphere inside it. The sphere is then iteratively inflated until it reaches the edges on the brain. On the other hand, ROBEX uses a random forest classifier to detect the brain boundaries, which are then updated with the use of a generative model. Both BET and ROBEX are fully automated methods and do not require any input parameters.

In the case of a healthy brain scan, all three methods identify the brain mask well, as shown in Fig. 3.8. However, S3 provides a more refined and smoother brain mask than the two standard methods. Moreover, BET and ROBEX slightly over-segment the eye cavity region.

In the presence of morphological pathologies, the performance of the standard methods drops. Figure 3.9 shows the results of all three methods on four scans (A-D) with the brain lesions. The BET brain masks include a significant proportion of non-brain tissue, mainly in the neck and eye cavities. A possible explanation is that in the presence of pathologies, the image intensities inside the brain deviate from the healthy cases. As a consequence, the method misidentifies the center of the brain, which causes the deformation model to include the non-brain tissue. On the other hand, ROBEX tends to over- and under-segment the brain regions in all presented cases. Clinically most crucial errors are presented in cases B) and C), where ROBEX brain mask missed

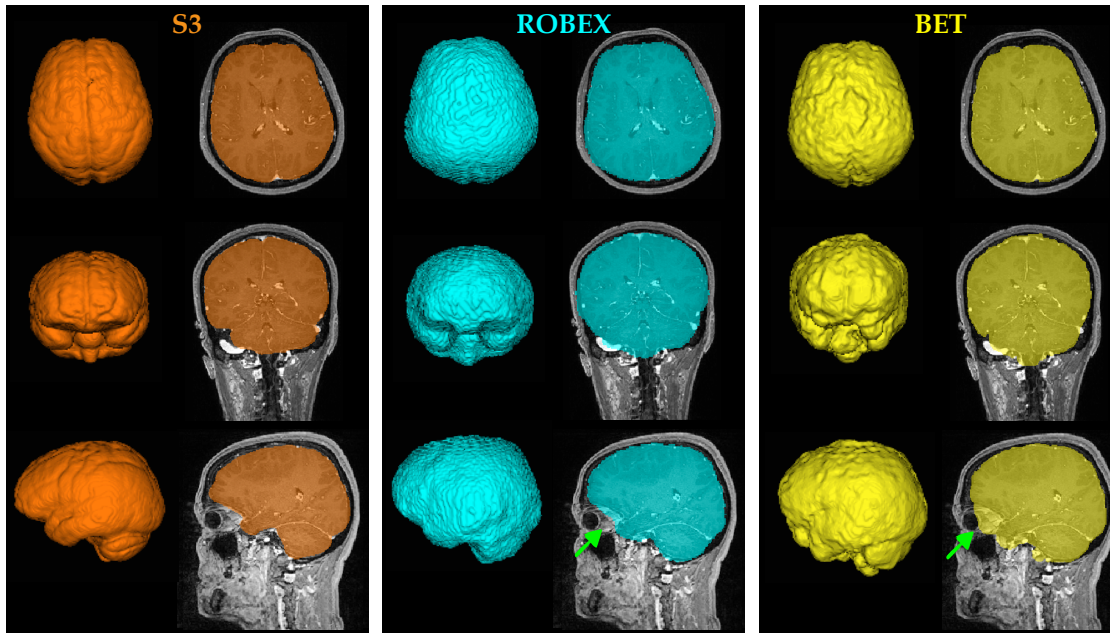


Figure 3.8: A comparison of the brain masks computed by S3 (orange), ROBEX (cyan), and BET (yellow) on a brain scan without a pathology. S3 results in more refined and smooth brain mask than the two standard methods. Moreover, both ROBEX and BET oversegment the region of the eye cavity (green errors).

parts of the tumor. In case D), all three methods suffer from an over-segmentation of eye cavities and under-segmentation of the parental lobe. However, in all cases, the S3 method provides more accurate and refined brain mask than the other two algorithms.

Results of all methods in the presence of resection cavities are shown in Fig. 3.10. The accuracy of the BET method is reduced by over- and under-segmentation arising from non-typical image intensities in the scans with pathologies. ROBEX identified the brain masks relatively well, although in the case B) it includes a non-brain tissue around the eyes. The S3 results show both the coarse and the refined brain mask. As seen in case A), the coarse mask identifies the whole brain region, whereas the refined mask excludes the resection cavity. The S3 solver provides both masks allowing the user to pick the most suitable one for the given application. However, the exclusion of the resection cavity is possible only if the cavity is located at the brain periphery as in case A). If the cavity is embedded in the brain tissue or does not provide sufficient contrast, as in Fig. 3.10 B), then both S3 masks include the cavity.

The presented preliminary results imply that the S3 method provides more refined and accurate brain masks than BET and ROBEX, making it a promising method mainly for the scans with pathologies.

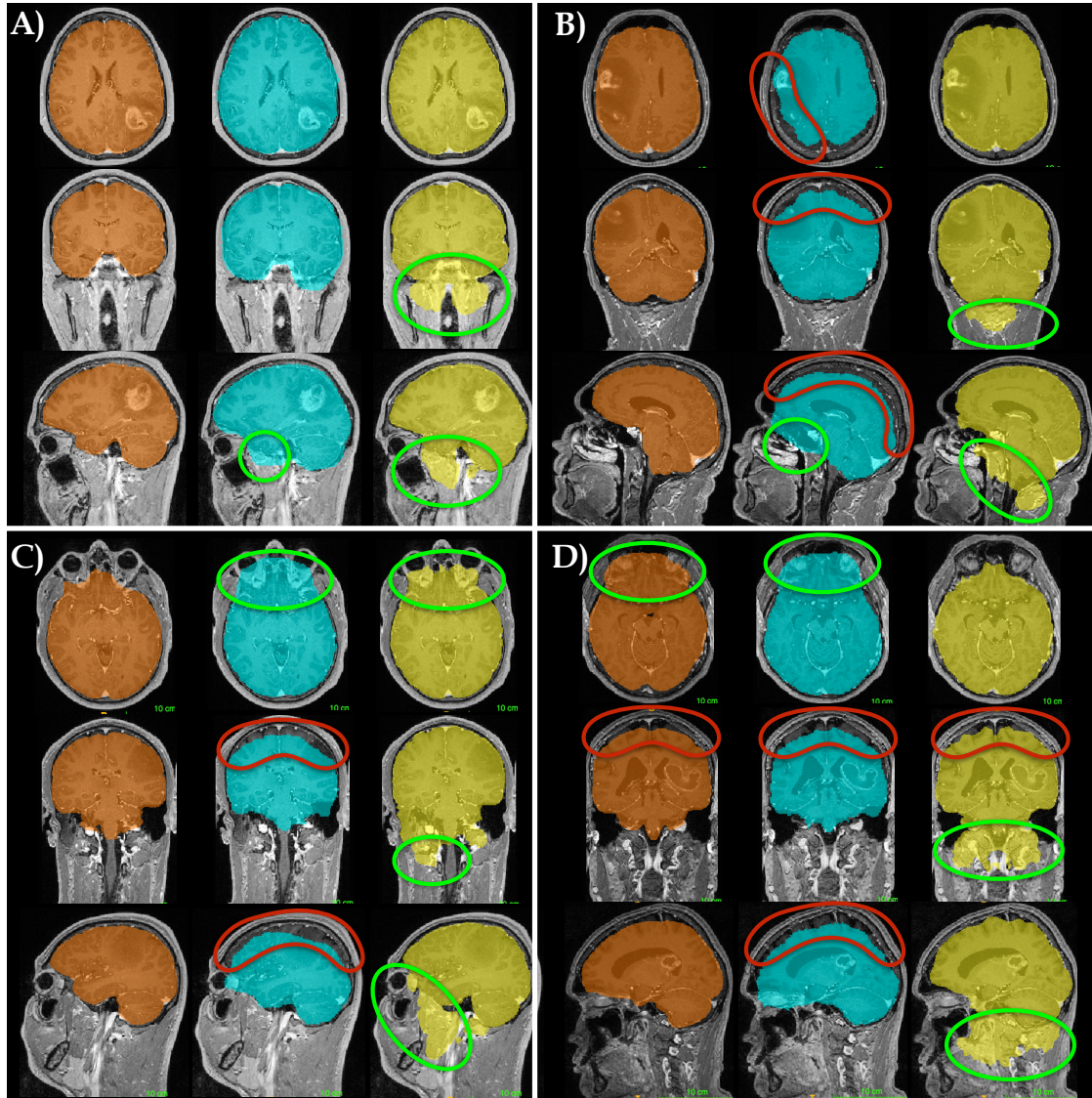


Figure 3.9: Results of the skull-stripping methods: S3 (orange), ROBEX (cyan) and BET (yellow), on scans of four patients (A-D) with brain lesions. The green circles indicate regions with over-segmentations, while under-segmentation is marked in red. BET brain masks include a significant proportion of the non-brain tissue, mainly around neck and eye cavities. ROBEX errors include under and over-segmentation which are present in all four cases. The clinically most crucial errors are in the cases B) and C) where the brain masks missed parts with the brain tumor. Performance of all three methods is reduced in the case of patient D). However, in all cases, S3 provides more accurate and refined brain masks than the two standard methods.

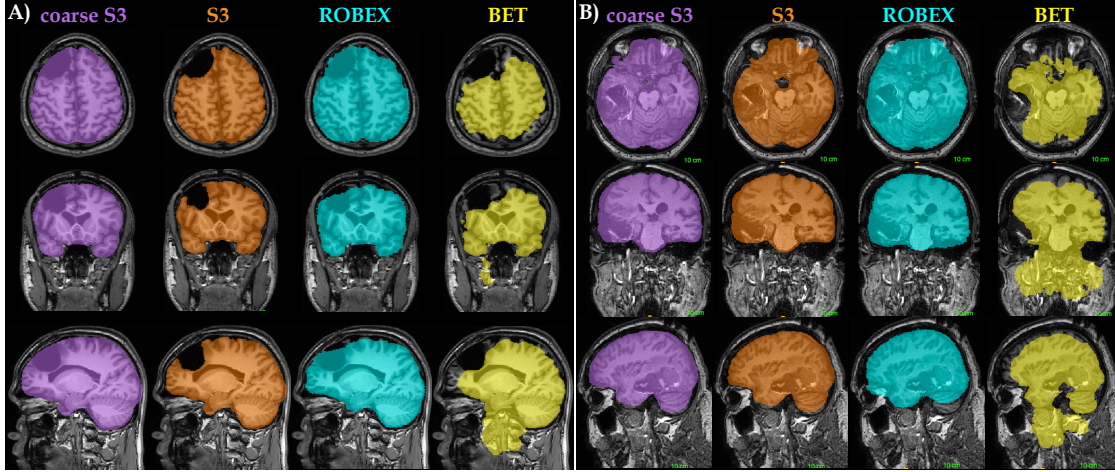


Figure 3.10: Results of the skull-stripping methods on the scans of two patients (A-B) with resection cavities; coarse S3 mask (purple), refined S3 mask (orange), ROBEX (cyan) and BET (yellow). In both cases, S3 masks provide a more accurate and refined solution than BET and ROBEX. As seen in A), the refined S3 mask excludes the resection cavity, while the coarse mask preserves it. However, if the cavity is embedded inside the brain tissue, as in B), then both S3 masks include it.

Tissue segmentation: The S3 tissue segmentation method is compared with the popular EM algorithm [122, 127]. The EM is an iterative method using a Bayesian classifier to segment the brain tissues. It assumes that the MRI intensities of the brain tissues can be represented by a mixture of probability distributions, usually Gaussians. The Bayes rule is then used to assign to each voxel a probability of belonging to each tissue class, based on the distribution of the image intensities and the prior knowledge about the tissues configurations derived from a brain atlas. The tissues segmentations are then obtained by assigning each voxel to the tissue class with the highest probability.

Figure 3.11 shows a comparison of the tissue segmentations computed by the S3 and EM method on scans of five patients (A-E) with brain lesions. The main drawback of EM method is that it estimates the brain lesions as gray matter since they are represented by similar intensities on the T1w scan. Furthermore, the presence of the brain lesions affects the distribution of the image intensities, which can lead to incorrect tissue segmentations as seen in case B). The EM method is very sensitive to noise and intensity inhomogeneities, resulting in relatively noisy segmentations. On the other hand, the atlas driven S3 segmentations are robust against these artifacts, providing smoother segmentations than the EM method.

In general, the estimation of brain tissue below the visible tumor is a complicate task while non-invasive validation of such estimates is even more complicated. However, since the EM method interprets all lesions mainly as gray matter, it is clear that these results are not correct. Contrarily, S3 identifies the tissue segmentations by mimicking the visible anatomies, resulting in more

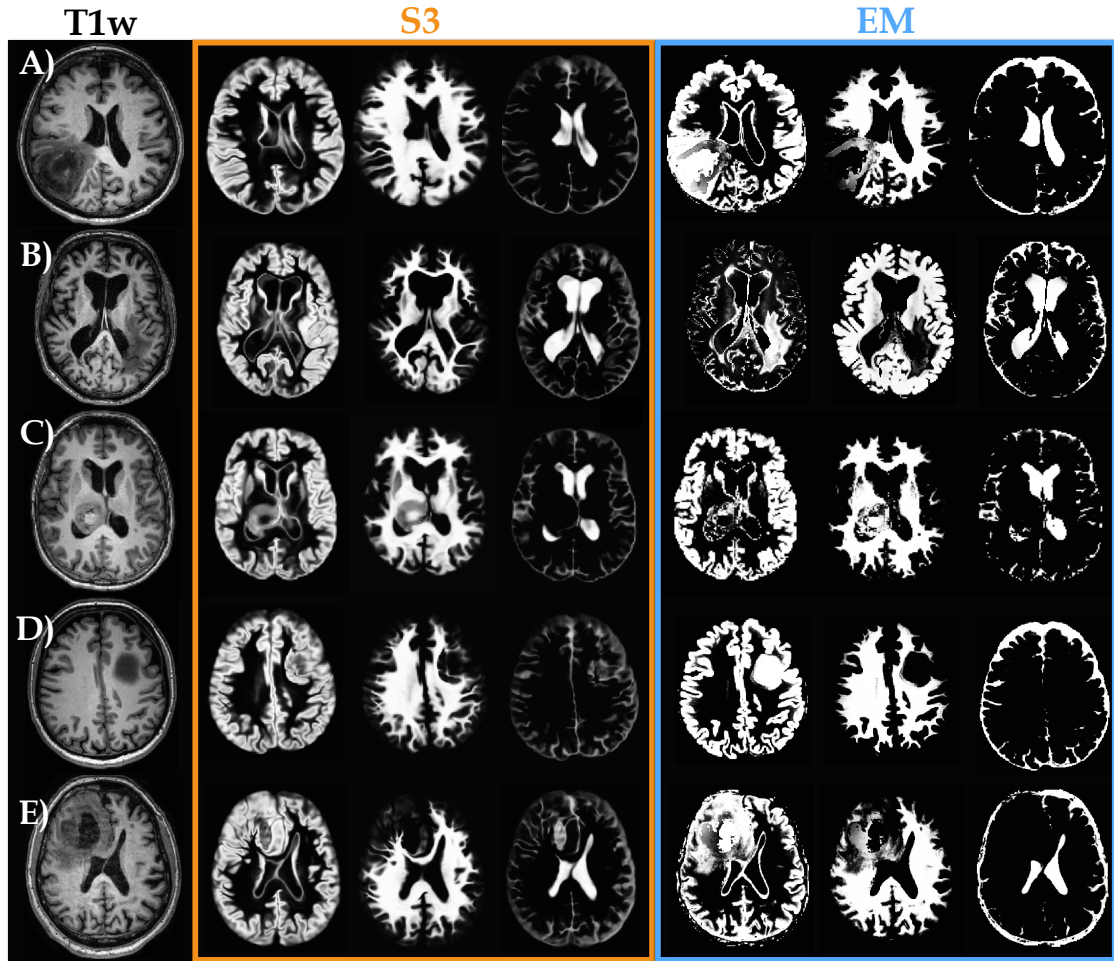


Figure 3.11: A comparison of brain tissue segmentations computed by S3 (orange box) and EM (blue box) on five scans (A-E) with brain lesions. The input T1w MRI scans for each case (A-E) are shown in the first column. EM method is very sensitive to noise and intensity inhomogeneities, resulting in noisy segmentations. Moreover, EM interprets all brain lesions mainly as gray matter due to their similar intensities in the T1w scan. On the other hand, the S3 segmentations are smooth and less prompt to errors. By mimicking the visible brain anatomies, the S3 segmentations can provide visually reasonable estimates about the tissue below the tumor, in the presence of small tumors, as seen in (A-B). However, all estimates below the tumor must be interpreted with caution as seen in (C-E).

reasonable tissue estimates, as seen in (A-B). However, these estimates might be questionable, as in the cases (C-E). Since it is almost impossible to validate such predictions, all tissue segmentations below the tumor have to be interpreted with caution. In general, the S3 method provides less noisy segmentations with a smooth interface between the anatomies, which are particularly suitable for computational tumor modelling, as shown in Chapters 4 and 5.

Conclusion

In this section, we have introduced the S3 algorithm for skull-stripping and segmenting brain tissues from the head MRI scans. The presented preliminary results imply several advantages of the S3 method over the standard approaches. The brain masks computed by the S3 method are more refined, smooth and less prompt to errors than the standard methods, mainly in the scans with pathologies. On the other hand, the tissue segmentations provided by S3 method are particularly suitable for computational tumor modelling, mainly due to smooth interface between the tissues and smaller noise than the EM segmentations. In the case of smaller lesions, the S3 provides reasonable estimates about the anatomies below the tumor, however, they should be interpreted with a caution. To fully assess the potential of S3 method a quantitative comparison is needed. This requires manual segmentations performed by certified radiologist. At the time of writing this thesis, suitable dataset has still been in the preparation. Therefore, we will address the qualitative evaluation in future work.

Disclaimer: The results presented in this section are partially based on a student project co-supervised with Esther Alberts and executed by students Enes Senel, Stevica Bozhinoski, and Yusuf Savran. The S3 algorithm is part of a head MRI processing pipeline presented in Chapter 8.

3.2.3 Convolutional neural networks

Convolutional neural network (CNN) is a type of artificial neural network (ANN) designed predominantly for image processing tasks. We start with an intuitive description of ANN and CNN, followed by their application to image segmentation. The deeper technical details can be found in the excessive amount of literature such as [58, 130].

Artificial Neural Networks

An ANN is a computing system inspired by animal brain architecture. It consists of connected layers of artificial neurons, which loosely resemble biological neurons. Figure 3.12 shows an illustration of an artificial neuron. Each neuron receives inputs x_i from other neurons and combines them together usually through a linear combination such as $\sum_i x_i w_i + b$, where w_i are called *weights* and b is a *bias*. The neuron further processes this information by applying so called *activation function*. The most common forms of the activation function are sigmoid, hyperbolic tangent or rectified linear unit function ($ReLU(x) = \max(0, x)$). The weights reflect the strength of the signal from each input neuron, whereas the bias allows a shift in the activation function. The output of the neuron is then passed to the neurons in the next layer. The layers in the ANN are connected in a way that the input of each neuron in one layer is the output of the neurons in the previous layer, as shown in Fig. 3.13. The signal travels from the first layer (the input layer), through intermediate layers (hidden layers), to the last layer (the output layer). Each hidden layer performs a different kind of transformation to its inputs. If a network has more than one hidden layer it is called *deep neural network*.

The network learns a relation between the input and output. The learning process consists of adjustment of the network parameters, i.e. weights and bias of each neuron, to produce the desired output for a given input. This adjustment is done automatically based on a set of training examples which contains inputs and outputs. The learning is an optimisation problem which minimizes the error in the network predictions. The correctness of the predictions is characterised by a *loss function* and an optimisation algorithm is used to find the parameters that minimize

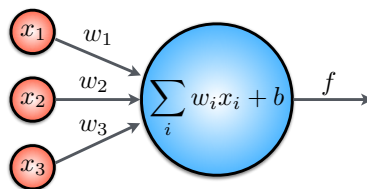


Figure 3.12: An illustration of an artificial neuron. The neuron (shown as a blue circle) takes inputs x_i from the neurons in the previous layer (shown as red circles), combines them together through a linear combination with weights w_i and bias b . The neuron then applies the activation function f to create an output, which is then passed to neurons connected to it.

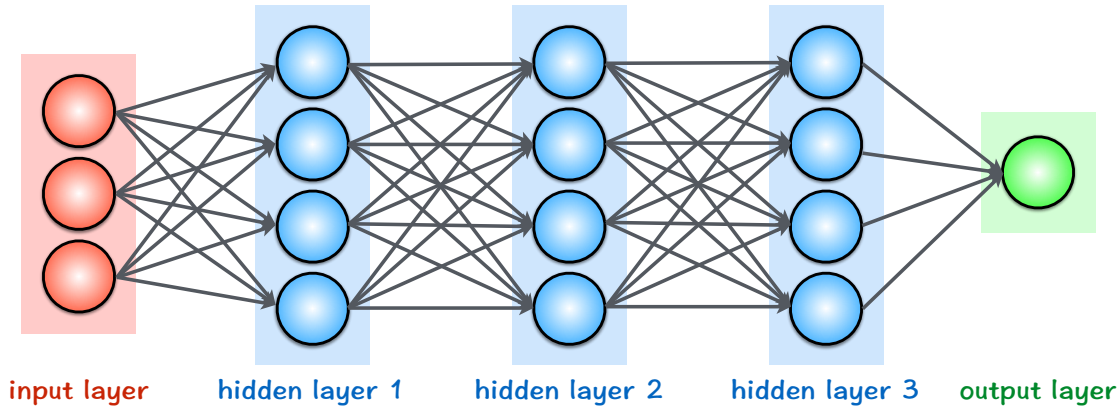


Figure 3.13: An illustration of a deep neural network. The network consists of interconnected layers of artificial neurons. Each layer consists of one or more neurons (depicted as circles), connected such that the input of a neuron in one layer is an output of the previous layer of neurons (after activation).

this loss. Popular optimisation methods used for ANN are a gradient descent method with a back-propagation and Adam-optimiser [89].

The network itself is not an algorithm, but rather a template for many different algorithms. A standard algorithm consists of a series of fixed steps describing relation between the input and the output. On the other hand, a network infers this relation alone by learning the network parameters (i.e. weights and biases). Moreover, the network's architecture is parametrized by the number of layers and the number of neurons in each layer, referred to as *hyper-parameters*. Different network architectures correspond to distinct models. For a given problem, the task is to find the best architecture as well as the best hyper-parameters of the network. Only once the architecture is fixed and the parameters are inferred, the network can be used as an algorithm. The ANNs are particularly suitable for extracting complex relation between input and output. The first few hidden layers usually learn simple features, while the later layers build on these features to extract more complex descriptions. The deeper a network goes, i.e. the more layers it has, the more complex relation it can learn. One of the main advantages is that the network identifies the best features itself without any prior knowledge. This is particularly attractive since often the relation between the input and output is not known or is too complex to be described by standard algorithms. However, the relations and features learned by the network cannot be translated into human-understandable way. This is why the networks are sometimes referred to as non-explainable.

ANNs have found application in various tasks including computer vision [100], speech recognition [59], playing board games [160], and medical diagnosis [7]. The ANNs were also successfully used for image recognition [100], however, only for images of small size (e.g. 64×64). Since the network treats each pixel as a separate neuron, it does not scale well to higher resolutions due to

a curse of dimensionality. For instance, a 1000×1000 RGB image (i.e. 3 color channels) has 3 million input neurons, which is too high for feasible processing at the scale of a fully connected network. Moreover, variations in the location of an object in the image would result in very different features, which all should lead to the similar output. Furthermore, since each pixel is considered separately, the network does not account for a spatial structure of the data. Since the image information is dominated by local spatial patterns, the ANNs alone are not suitable for image recognition. These issues have triggered the development of CNNs.

Convolutional Neural Networks

The CNNs are networks inspired by an animal visual cortex. Each neuron in the visual cortex process only a small region of the visual field – referred to as *receptive field* [82]. The receptive fields of individual neurons partially overlay to cover the whole visual field. Similarly, an artificial convolution neuron receives input only from a small sub-area of the previous layer, defined by the neuron's receptive field. This significantly reduces the dimensionality of the problem in comparison to the fully-connected ANN, where each neuron receives input from every neuron in the previous layers. Each convolutional neuron applies weights and bias to the input coming from its receptive field and applies the activation function to produce the output. The vector of weights and bias – termed *filter* – characterizes certain feature of the input, e.g. presence of an edge. A distinct aspect of CNNs is that each neuron in the same layer applies the same filter (i.e. use the same weights and bias) to the input in its receptive field. It means that all neurons in the same layer response to the same features within their specific receptive field. This reduces the number of parameters and enables a translation invariance since the network can detect the features regardless of their position. The receptive field has usually a square shape (e.g. 5×5 pixels), which allows to exploit spatially local patterns.

CNNs consist of a series of distinct layers including *convolutional layer*, *pooling layer*, and *fully-connected layer*, as depicted in Fig. 3.14.

Convolutional layer: emulates the behaviour of individual neurons in the visual cortex. Each neuron computes a dot product between its input volume and the filter, and applies the activation function. This operation is referred to as convolution in the CNN terminology, although a mathematically more correct term would be a cross-correlation. The parameters of the filter (i.e. weights and bias) are shared among all neurons in the layer. As a result, the network learns a filter that activates when it detects a specific feature at any spatial location in the input. To increase the generality of the network, the convolutional layer consists of multiple of such filters, which are applied by all neurons to identify different features. The convolutional layer is parametrized by the following hyperparameters: width, height, depth, and stride. The *width* and *height* describe the resolution of the receptive field, the *depth* is the number of filters applied by each neuron and *stride* controls the overlay of the receptive fields.

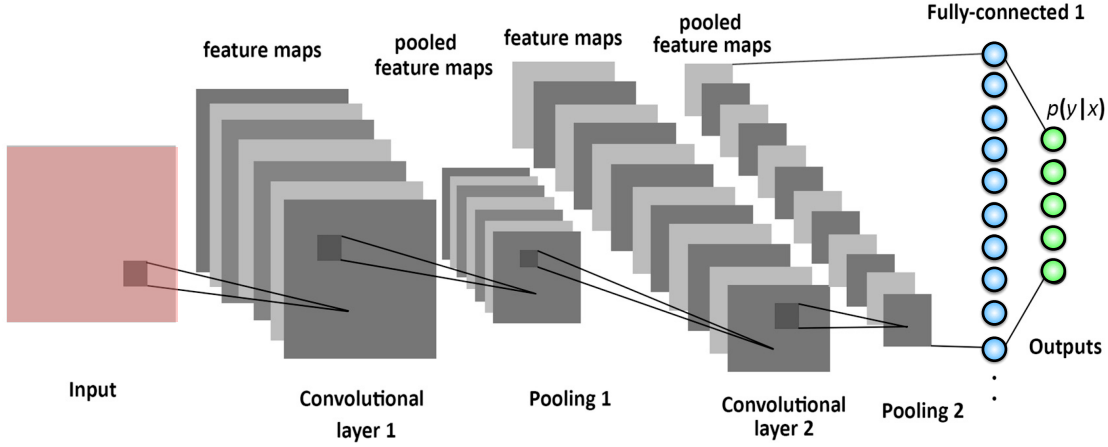


Figure 3.14: An illustration of CNN. The neurons in the convolutional layer extract local features from their preceptive fields, creating the feature maps. The pooling layer extracts the dominant aspects from each feature map and passes them to the next convolutional layer, which learns relations between these features. The fully-connected layer is usually applied at the end and performs a high-level reasoning based on the learned features. Figure modified from [3].

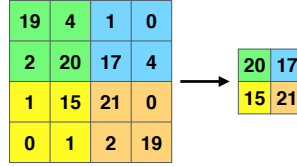


Figure 3.15: An illustration of max-pooling operation. It divides the input into patches (here 2×2 patches) and outputs a maximum of each patch, thus reducing the spatial size of the structure.

Pooling layer: performs non-linear downsampling. Several non-linear functions can be used, among which the *max-pooling* is the most popular. It partitions the input volume into non-overlapping patches and outputs a maximum of each patch, as shown in Fig. 3.15. The pooling is applied independently to the output of each filter from the previous layer. Thus it reduces the spatial size of the feature maps, but it does not decrease the number of the features. The pooling layer reduces the number of parameters and amount of computations, and also controls overfitting. The intuition behind the pooling layer is as follows. It can be assumed that the convolutional layer learns the local features of its input. The next step is to put these local features into a bigger context. For this, the details of individual features are less important than the relation between the features. The pooling layer extracts the most dominant aspects of the local features, which can be then analysed in a bigger context. It is a common practice to periodically insert a pooling layer between two convolutional layers, as shown in Fig. 3.14. For illustration, one can imagine that the neurons in the first convolutional layer learn to identify edges in their receptive fields, the pooling layer extracts the dominant parts of these edges, while

the second convolutional layer learns how these edges combine together to outlines of an object.

Fully-connected layer: is usually applied at the end of the CNN as shown in Fig. 3.14. It is a regular ANN where all neurons in one layer are connected to all neurons in the previous layer, as we saw in Fig. 3.13. It can consist of several hidden layers and it performs high-level reasoning by analysing features learned by the previous layers. In the image recognition task, the fully connected network computes a probability with which an input image contains an object from a certain class, e.g. dog or cat.

The CNNs have proved to be very powerful in image classification task, where the output to an image is one or few class labels, e.g. dog, cat, or both. In 2012, a CNN called *AlexNet* [94] won image recognition completion called ImageNet Large Scale Visual Recognition Challenge, significantly surpassing all other traditional methods. However, in the biomedical application the desired output is not just an image label (e.g. whether there is a tumor or not) but also a segmentation, i.e. assigning a class label for each pixel. This demand caused additional modifications in the CNN architectures, leading to so called *fully convolutional neural networks*.

Fully-Convolutional Neural Networks

A fully convolutional neural network (FCNN) is a type of convolutional neural network developed mainly for biomedical image segmentation task. The standard CNN can be seen as a contracting path which reduces the high resolution input image to a small set of features specific to a certain class. The main idea of FCNNs is to supplement this contracting path by an expansive one. The expansive path continuously increases the resolution of the outputs between the layers, until reaching the size of the input image, and it identifies the location of the high resolution features from the contracting path. The expansive path is relatively symmetric to the contracting path, which gives a U-shaped architecture, as shown in Fig. 3.16. This architecture shape led to the name *U-Net* [150]. Each step in the expansive path consists of an up-sampling of the feature maps followed by a convolution ("up-convolution") to increase the resolution. Furthermore, the up-sampled output is concatenated with the high resolution features from the contracting path to enable localization of the features. The combination of contracting and expansive path allows to extract high-level contextual and spatial features.

The U-Net architecture was first proposed in 2015 for segmenting cells from 2D light microscopy images [150]. Since then, it was used for segmenting other biomedical images, including 3D scans. For instance, in [34], we used the U-Net architecture to segment liver and liver lesions from volumetric CT scans, by applying the U-Net in a slice-fashion. However, the slice-based approach does not account for the 3D nature of the scans, which can be crucial for detecting small structures like tumors. Therefore, in 2016 so called *V-Net* architecture [125] was proposed as a 3D extension of the U-Net. In the V-Net, the receptive field of the neurons is a small cube (instead

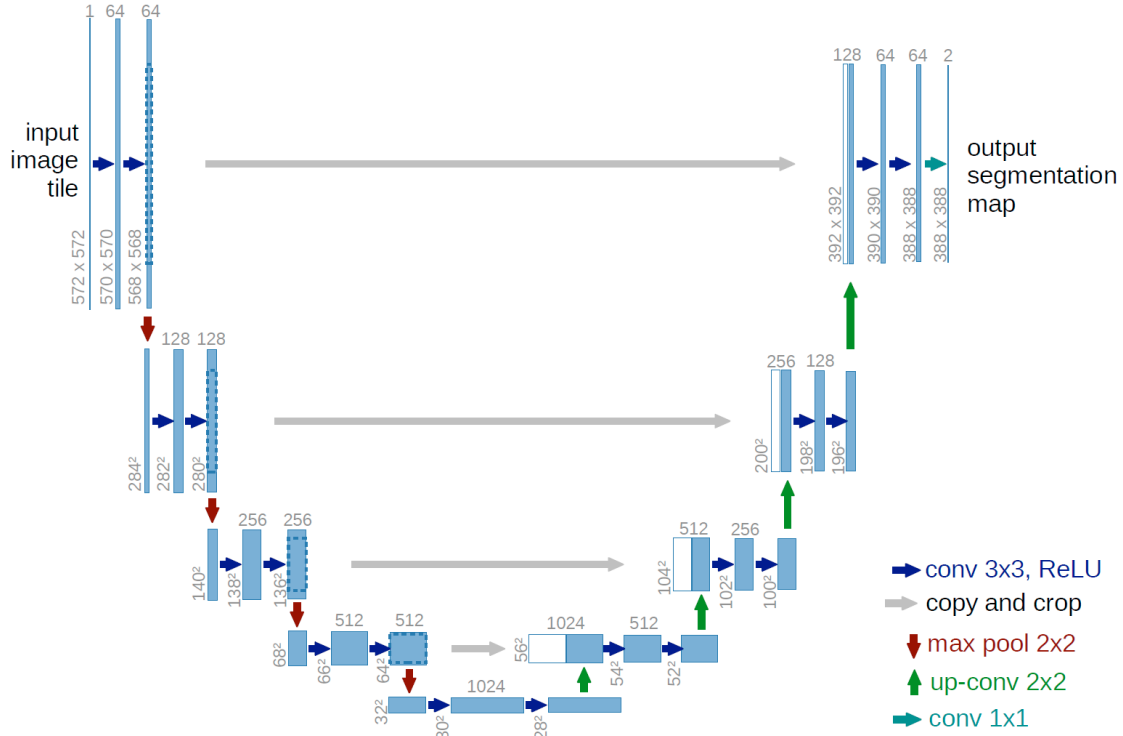


Figure 3.16: The U-Net architecture consists of a contracting path (left side) and an expansive path (right side). The blue boxes correspond to the feature maps, where the number of features is denoted at the top of each box. The arrows denote different operations. Figure taken from [150] (Copyright Springer 2015).

of a 2D slice), which allows to exploit local spatial patterns in the volumetric data. An application of the V-Net architecture is presented in the next section.

3.2.4 Whole-body multiple myeloma bone lesion detection

Herein we present a deep-learning approach for automatic multiple myeloma lesions detection from whole-body hybrid PET/CT scans in a 3D manner.

Motivation

Multiple Myeloma (MM) is a bone marrow malignancy usually manifested by multiple heterogeneous lesions distributed over the whole skeletal system. The proliferation of malignant plasma cells is accompanied by a decrease in the bone mineral density in the affected region. These alterations in the bone density allow MM detection from the CT scans. However, very small lesions that did not yet affect the bone structure might not be visible on the CT scan (see Section 2.2.2). Therefore, the anatomical CT scan is often accompanied by metabolic PET imaging, which is more

sensitive to small lesions. Recently, an over-expression of chemokine CXCR4 has been verified in a variety of cancers, leading to the development of targeted PET tracer ^{68}Ga -Pentixafor [184] (see Section 2.3). This emerging tracer has already demonstrated high sensitivity in the visualization of MM lesions [98, 139].

Even with such advanced imaging techniques, detection of MM bone lesions remains challenging. As shown in Fig. 3.17, the ^{68}Ga -Pentixafor PET imaging exhibit a large variation in uptake values and size, even among the lesions of the same patient. Manual detection of multiple lesions distributed over the whole body is very time consuming and can result in large inter-observer variations [16]. Hitherto, only a few automated methods for MM lesions were developed. A virtual calcium subtraction method has been developed to evaluate MM lesions in the spine [180] and a spatially dependent density model was used for detecting MM lesions in the femur [115]. However, none of these methods account for multimodal PET/CT scans nor can be directly applied to a full-body lesion detection. To the best of our knowledge, no effective automated method has been presented for MM bone lesion detection in the full-body scans.

Here we exploit, for the first time, the FCNNs combing anatomical and molecular information of ^{68}Ga -Pentixafor PET/CT imaging to enable whole-body lesion identification. Besides a V-Net, a cascaded W-Net architecture is investigated. The W-Net consists of two cascaded V-Net, leading to W-shaped architecture. The first network learns a volumetric skeletal representation, while the second network focuses on the lesion detection inside the inferred skeletal structure. Both architectures are tested on 12 clinical PET/CT scans of patients diagnosed with MM.

Methods and Materials

Architecture: In this study, we explore the popular V-Net architecture and its extension to W-Net. The V-Net takes as input both, the CT and the PET scan, and outputs the lesions segmentation. The W-Net consists of two cascaded V-Nets as shown in Fig. 3.18. The first network takes as input only the volumetric CT scan and outputs a binary bone segmentation. The second network takes as input the CT scan, the PET scan, and the bone segmentation estimated by the first network. The PET and CT scans are used for the detection of the lesions while the bone segmentation offers a geometrical boundary. Both V-Net and W-Net use a convolutional filter of size $3 \times 3 \times 3$ and $2 \times 2 \times 2$ patch for max-pooling and up-sampling. In general, the deeper a network goes, the more details vanish, even when using a concatenation with the high resolution features from contracting path. As a result, small lesions, which represent only a fraction of the scan, could be missed by very deep networks. Therefore, a relatively shallow network with only 3 layers is used for the lesion detection in both the V-Net and in the second network of the W-Net. The bone detection in the first part of the W-Net is performed with 5 layers.

Class balancing: Since the lesions represent only a small proportion of the whole image, in comparison to the non-lesions voxels, there is a strong class imbalance in the dataset. This can

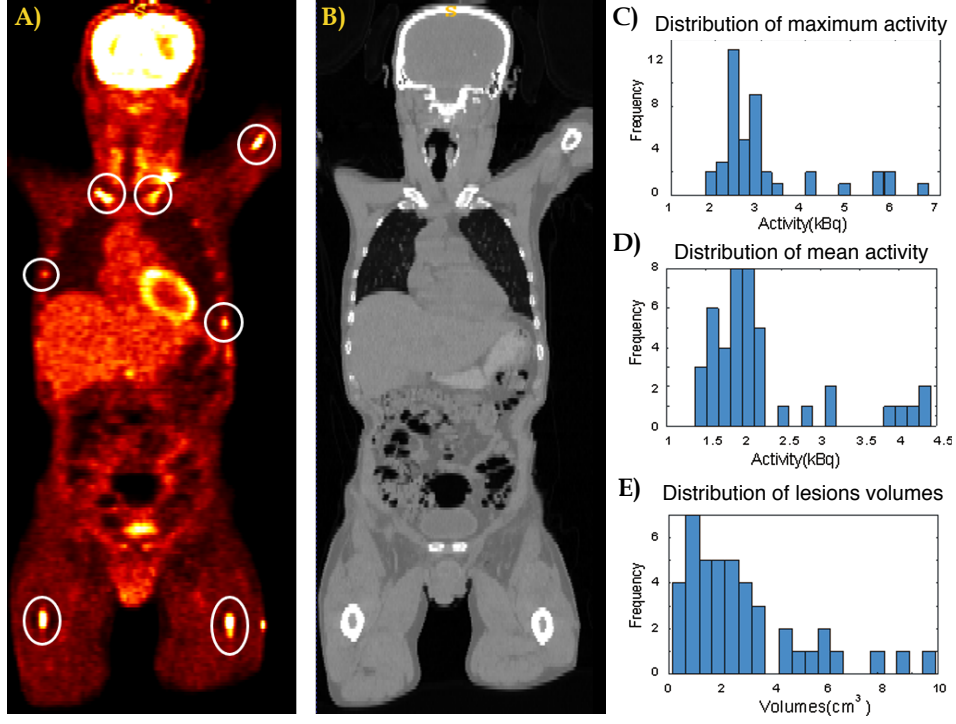


Figure 3.17: A distribution of MM lesions within a patient with ^{68}Ga -Pentixafor PET/CT imaging: A) ^{68}Ga -Pentixafor PET scan. The MM lesions are indicated by the white circles. B) The corresponding CT scan. The distribution of the lesions maximum uptake values C), mean values D) and volumes E).

significantly reduce the network accuracy, especially for small lesions. To overcome this, we adopt a class balancing strategy as used in [34]. The cross entropy loss function L is rescaled with additional weighting factor ω_i^{class} :

$$L = -\frac{1}{N} \sum_{i=1}^N \omega_i^{class} [\hat{P}_i \log(P_i) + (1 - \hat{P}_i) \log(1 - P_i)], \quad (3.7)$$

where P_i is the probability of voxel i belonging to the foreground (e.g. tumor) and \hat{P}_i represents the ground truth. We choose ω_i^{class} as follows:

$$\omega_i^{class} = \begin{cases} \frac{\sum_i (1 - \hat{P}_i)}{\sum_i \hat{P}_i} & \text{if } \hat{P}_i = 1 \\ 1 & \text{if } \hat{P}_i = 0. \end{cases} \quad (3.8)$$

The same class balancing strategy is employed for both lesions and bones.

Training: Both networks are trained on phantom and real patient data using a stochastic gradient descent method. For details about the phantom data see [192]. The convergence curves of both networks are shown in Fig. 3.19. All the experiments are implemented in Theano framework using Python 2.7. The training is performed on NVIDIA TITAN X GPU with 12 GB memory.

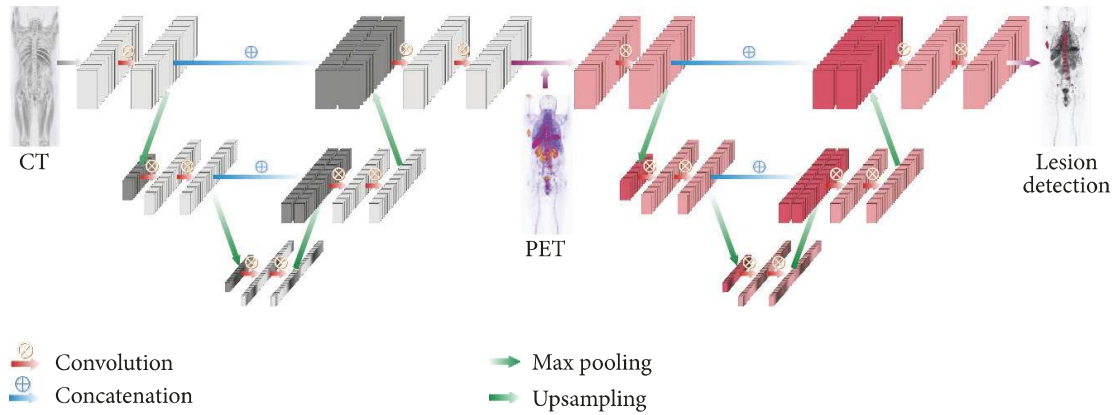


Figure 3.18: A simplified illustration of the W-Net architecture for the whole-body MM lesions detections from the hybrid PET/CT scan. The first network takes as input the CT scan and outputs binary bone segmentation. The second network takes as input the CT scan, the PET scan, and the binary bone segmentation and outputs binary tumor segmentation.

Clinical data. The networks are tested on clinical scans of 12 patients with histologically proven primary MM disease. The patients underwent ^{68}Ga -Pentixafor PET/CT imaging (Siemens Biograph mCT 64; Siemens Medical Solutions, Germany). The study was approved by corresponding ethics committees and patients were given written informed consent prior to the investigation. The lesions were manually annotated under the supervision of an experienced radiologist, then the lesions were segmented by local thresholding at half maximum of the PET uptake.

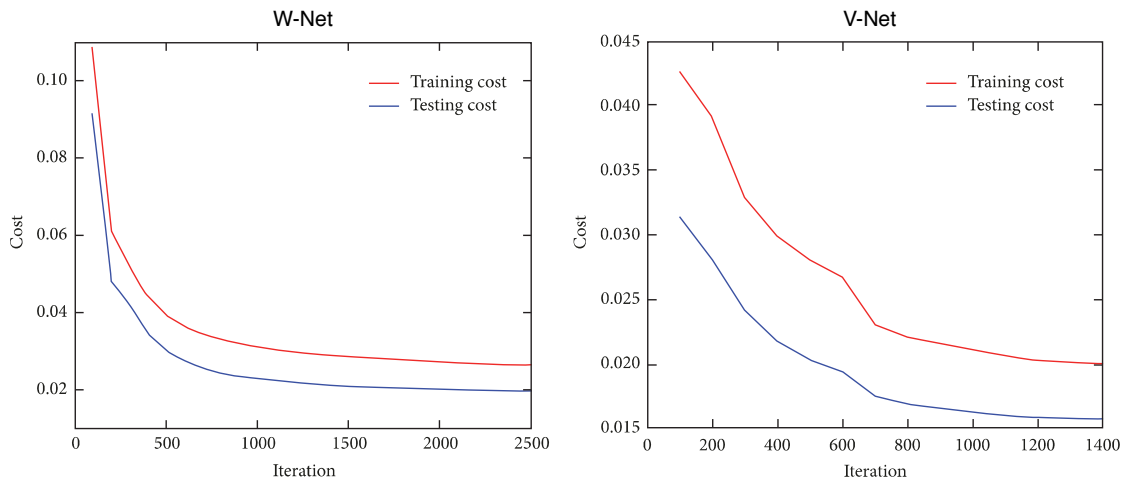


Figure 3.19: Convergence curves of the W-Net (left) and V-Net (right) architectures.

Method	Detection			Segmentation
	<i>Precision</i>	<i>Sensitivity</i>	<i>Specificity</i>	<i>Dice</i>
V-Net + CT	16.08	73.18	94.43	26.37
V-Net + PET	18.53	61.77	96.04	28.51
V-Net + PET/CT	68.00	71.06	99.51	69.49
W-NET + PET/CT	72.46	73.50	99.59	72.98

Table 3.1: Results of the V-Net and W-Net for MM bone lesion detection and segmentation in clinical cases. The best results are shown in yellow.

Results

To evaluate the performance of the proposed methods the following measures are considered. Dice score is used to estimate the segmentation accuracy. The detection accuracy (sensitivity, specificity, and precision) is computed lesion-wise using overlapping criteria. A lesion is considered detected if at least 10% of the predicted lesion voxels overlap with the ground truth segmentation.

The qualitative results are illustrated in Fig. 3.20, while the quantitative results are summarised in Table 3.1. For comparison also the results of the V-Net with only one input modality (i.e. V-Net with PET only and V-Net with CT alone) are reported. Both V-Net and W-Net with hybrid input data reach a significantly better performance than the V-Net with single input modality. This implies that the networks can efficiently utilize the complementary information from structural CT and functional PET scans. The performance of the V-Net with hybrid input data is mainly affected by the false positives findings, as can be seen in Fig. 3.20. This issue is overcome in the W-Net approach, where the bone segmentation extracted from the CT scan provides a geometric boundary for the detection of the lesions. These preliminary results suggest an advantage of the cascaded W-Net architecture over the single V-Net approach.

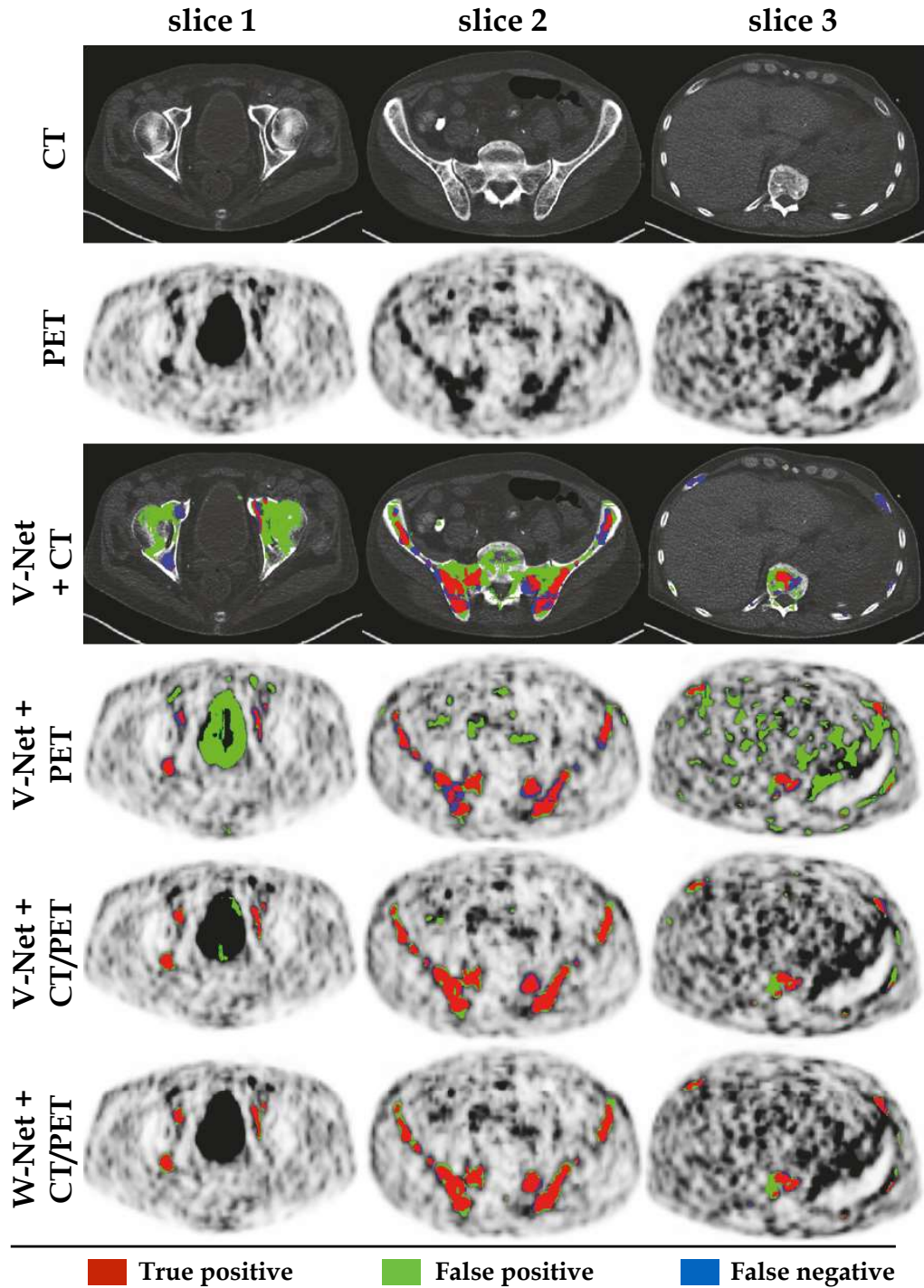


Figure 3.20: Qualitative results of the V-Net and W-Net for the MM lesion detection. The first two rows show three slices across the CT and the PET scans. Results of the V-Net trained with one input modality only are shown in the second and third row, while the results of the V-Net and W-Net with multimodal data are reported in the last two rows. The inferred skeletal structure in the W-Net architecture leads to less false-positive findings in comparison with the V-Net.

3.2.4.1 Conclusion

We have proposed, for the first time, a deep learning method for automatic detection and segmentation of whole-body MM lesions on CXCR4 directed PET/CT imaging. This exploratory study demonstrated the potential of FCNNs in combining multimodal information for lesion detection. The preliminary results indicate that the proposed W-Net architecture leads to better results than standard V-Net. However, the current study suffers from a small number of patient data, which strongly influences the performance of the deep learning methods. Nonetheless, it can be assumed that with increasing incorporation of CXCR4 imaging in clinical practice, more patients will be enrolled for the tests in the future, which will, in turn, improve the performance of the deep learning strategies. We wish to emphasize that the presented study focussed only on the detection of MM lesions inside bones. In advanced stages of the disease, the MM lesions can progress also outside the bone structures. As a consequence, the W-Net architecture would fail to segment any parts of the tumor outside the bone. Therefore, the proposed approach is presented as a detection rather than a segmentation method. This proof-of-concept study encourages further development of FCNNs for the management of MM disease.

Disclaimer: This section is partially reproduced from the article "L. Xu, G. Tetteh, J. Lipková, Yu Zhao, Hongwei Li, Patrick Christ, Marie Piraud, Andreas Buck, Kuangyu Shi, and B. Menze: "Automated Whole-Body Lesion Detection for Multiple Myeloma on ^{68}Ga -Pentixafor PET/CT Imaging Using Deep Learning Methods", Contrast Media & Molecular Imaging Journal, Article ID 2391925, (2018).

3.3 Segmentation challenges

The high clinical relevance of the tumor segmentation task has led to a rich collection of computational algorithms developed over the past two decades. These methods are typically tested on relatively small and private datasets, which hampers a fair comparison of the different segmentation strategies [13, 120]. The major difficulties in the comparison of the methods include, but are not limited to, i) the medical scans employed (including different imaging modalities, acquisition protocols and different scanners); ii) the type of the tumor (low or high grade, primary or secondary, solid or infiltrative tumors); iii) the state of the disease (images might be also acquired post-operatively and therefore showing radiotherapy effects and surgically-imposed cavities); iv) quality of the ground truth segmentations; and v) use of different matrices for performance quantification. As a consequence, it remains difficult to judge what is the real performance of the available algorithms; how they compare against each other or human expert raters; and which segmentation strategies may be worthwhile to pursue in clinical practice. The need for an objective evaluation has led to the organization of so-called segmentation challenges – also referred to as benchmarks.

Main idea

The main characteristic of all segmentation challenges is that different groups optimize their methods on an annotated *training dataset*, provided by the challenge organizers. Afterward, each group applies its optimized method to the *test dataset* and submits the result segmentations to the benchmark platform. The platform automatically computes performance scores for the segmentations submitted by the individual groups and reports the results on the benchmark web-page. This allows the ground truth labels of the test data to remain publicly unavailable and helps to ensure unbiased evaluations. The datasets and the challenge platform remain publicly available, allowing continuous and consistent evaluation of further methods. The established challenges often serve as new standards for an evaluation of the specific task [120].

The further benefit of the challenges is a creation and maintenance of a large, independent, and publicly available set of annotated data specific for the given task. The challenges usually provide very diverse data acquired at multiple centers, with different acquisition protocols and various types of scanners. This variation allows to test the algorithms under diverse, clinically relevant conditions. Moreover, comparison of the submitted methods allows to identify the main features of the winning strategies as well as the weak points, which should be further targeted to enable a translation of the segmentation algorithms into clinical practice.

The popularity of challenges keeps constantly incensing, with more than 30 challenges being started or announced for the year 2018/2019 ². In the following, we present two challenges on

²<https://grand-challenge.org/challenges/>

which organization we participate during the Ph.D. project, mainly the Liver Tumor Segmentation (LiTS) [17] and Brain Tumor Segmentation (BraTS) [13] challenges.

3.3.1 Liver Tumor Segmentation Challenge (LiTS)

The LiTS [17, 33] challenge is a benchmark for segmenting liver and liver lesions from abdominal CT scans, which was organized in conjunction with the IEEE International Symposium on Biomedical Imaging (ISBI) 2017 and Medical Image Computing & Computer Assisted Intervention (MICCAI) 2017. The LiTS dataset consists of 201 abdominal CT scans of patients with various liver lesions. The dataset is created in collaboration with seven hospitals and research institutions and it is manually annotated by three independent radiologists. Up to now, LiTS is the largest publicly available dataset with manually annotated CT scans of liver and liver lesions and it represents the state-of-the-art benchmark for evaluating liver and liver lesion segmentation algorithms.

Motivation

The liver is one of the most common cancer sites, including primary tumors like hepatocellular carcinoma and metastatic tumors that have spread from other sites, usually breast, colon, and prostate. CT is routinely used to detect and evaluate the treatment response of liver lesions. In clinical practice, liver and liver lesions are segmented by manual or semi-manual methods. However, these are time consuming and subjective. Despite the significant effort, the performance of the algorithms for the automatic segmentation of livers and their pathologies remains relatively poor, especially in comparison with segmentation methods for other lesion sites.

The main challenges in segmentation of liver lesions include high levels of noise, low liver-lesion contrast, different types of lesions, and variations in image intensities caused by different acquisition protocols, tissue abnormalities such as surgical resection, metal implants, and changes due to treatment. To illustrate this, Fig. 3.21 shows CT scans of three patients with liver lesions and the corresponding image intensity histograms of lesions and healthy liver tissue. The following segmentation challenges can be observed: i) the mean intensity of healthy liver vary by an order of magnitude among the three case; ii) the significant overlap of the image intensity histograms of lesions and healthy liver indicates the low contrast between these structures; iii) the underlying pathology does not manifest in the same way for all patients. The case A) in Fig. 3.21 shows compact lesions with a well-defined border, while cases (B-C) show infiltrative lesions with mixed liver-lesion interface; iv) the size and shape of lesions, as well as noise levels, vary among all three cases.

These variations significantly complicate the lesion detection and segmentation task. Even the manual lesions segmentations done by expert human raters can vary significantly (in [15] authors reported up to 11% intra-rater variability in volume differences).

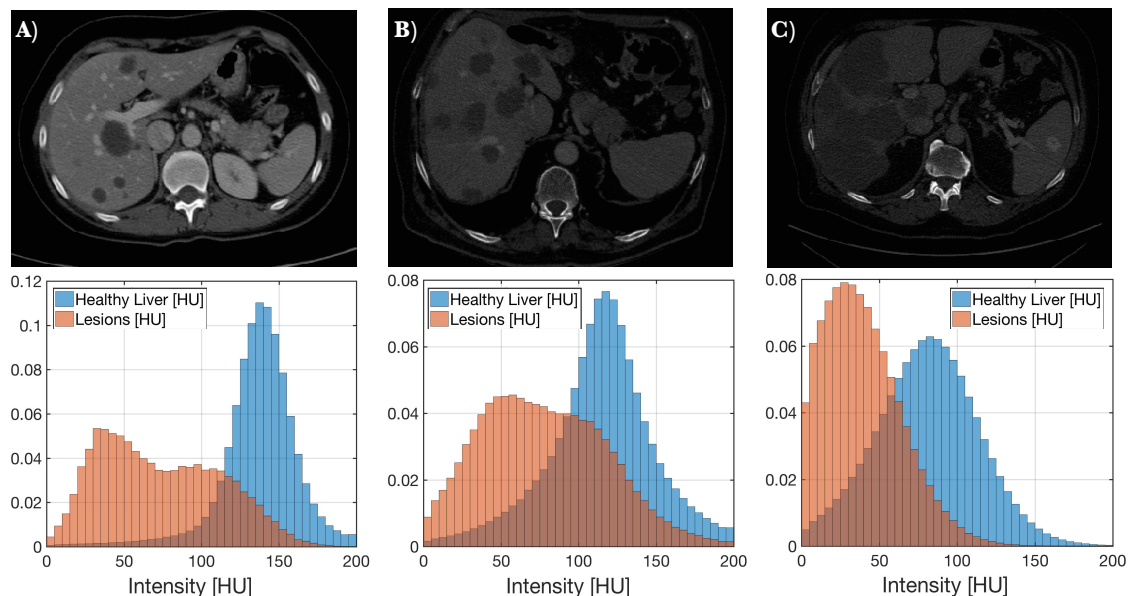


Figure 3.21: Abdominal CT scans of three patients with liver lesions (Top). All scans are clipped to range $[-100,1000]$ HU. Bottom: the corresponding normalised histograms showing the distribution of image intensities in the lesions (orange) and in the healthy part of the liver (blue). Low liver-lesion contrast is evident also from the significant overlap of the histograms. The size, shape, image intensities, and width of the mixed liver-lesion interface vary among the different lesions.

Setup of the LiTS Challenge

The LiTS dataset contains 201 abdominal CT scans collected from seven clinical sites. The scans comprise diverse types of liver tumors, including primary, secondary, and metastatic lesions derived from breast, prostate and lung cancer as well as hyper- and hypointense lesions. The images represent a mix of pre- and post-treatment scans, acquired with different CT scanners and acquisition protocols. The scans have a diverse resolution (varying from 0.45 mm to 6 mm) and image quality (with different levels of noise, image contrast as well as the presence of artifacts such as metal implants). The number of lesions per liver ranges from 0 to 75, while the lesion volumes vary between 0.038cm^3 to 349cm^3 . The average difference in the tumor-liver intensity spread from 0 to 98 HU.

The ground truth segmentations were performed by trained radiologists at every clinical site and consequently reviewed by three independent radiologists. The LiTS dataset was divided into 131 training and 70 test volumes. The same dataset was used for both ISBI and MICCAI challenge. The participants of the ISBI challenge were asked to segment only liver lesions, while the MICCAI challenge required segmentation of both liver and liver lesions. The LiTS challenge is hosted by the Codelab platform³ which also contains a leader board with current results.

³Codelab platform: <https://competitions.codalab.org/competitions/17094>

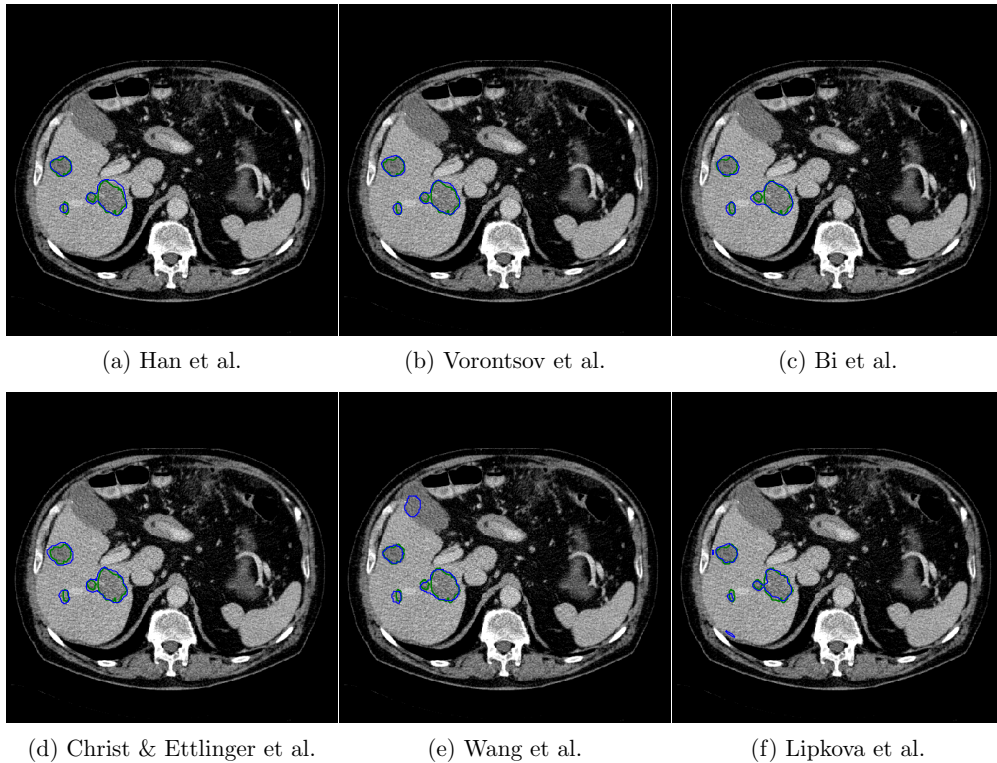


Figure 3.22: Results of the lesions segmentations obtained by the six best methods from the ISBI challenge. The outlines of the ground truth segmentations are shown in green, while results of the individual methods are shown in blue.

Results

The LiTS challenge received 61 valid submissions as a part of the ISBI and MICCAI workshops. Here we present the main results from both workshops, while details of the submitted methods can be found in [17]. The best liver segmentation algorithm reached Dice score 0.96, while Dice score for the best tumor segmentation method was 0.70. All but one participant provided fully automated methods, where majority algorithms rely on supervised learning. The best performing methods employed U-Net derived architectures. Majority strategies used multiple cascaded networks, with one network focussing solely on the liver segmentation, and the second network specializing on the liver lesions. All participants applied some form of data preprocessing with normalization and clipping of the HU being the most frequent one. Several post-processing methods were used, mainly connected component analysis, random forest classifier or morphological filtering.

Figure 3.22 shows a sample of the segmentation results provided by the top six methods from the ISBI challenge⁴. Quantitative results from all submissions, including ISBI and MICCAI

⁴ISBI leader board: https://competitions.codalab.org/competitions/17094#learn_the_details-isbi2017

challenges, are shown in Fig. 3.23 (for the liver segmentations) and Fig. 3.24 (for the lesions segmentations). We found, that no algorithm performed best on all test volumes, suggesting that a fusion of segmentation methods can lead to improved results. We consider the following fused segmentations: i) fusion of all submissions (best_all_vol), ii) fusion of all automated methods (no_human_vol), iii) fusion of the best five methods (best_5_vol), and iv) fusion of the best two methods (best_2_vol). The fusion of the segmentations is obtained by majority voting, except for the last case where averaging of the results is used. As can be seen from Fig. 3.23 and Fig. 3.24, the fusion of multiple methods allows to eliminate outliers and reach a better performance than all individual algorithms. This suggests that rather than a particular method, a combination of multiple strategies, each specialized for a different type of lesions, might lead in the future to an accuracy demanded by clinical practice.

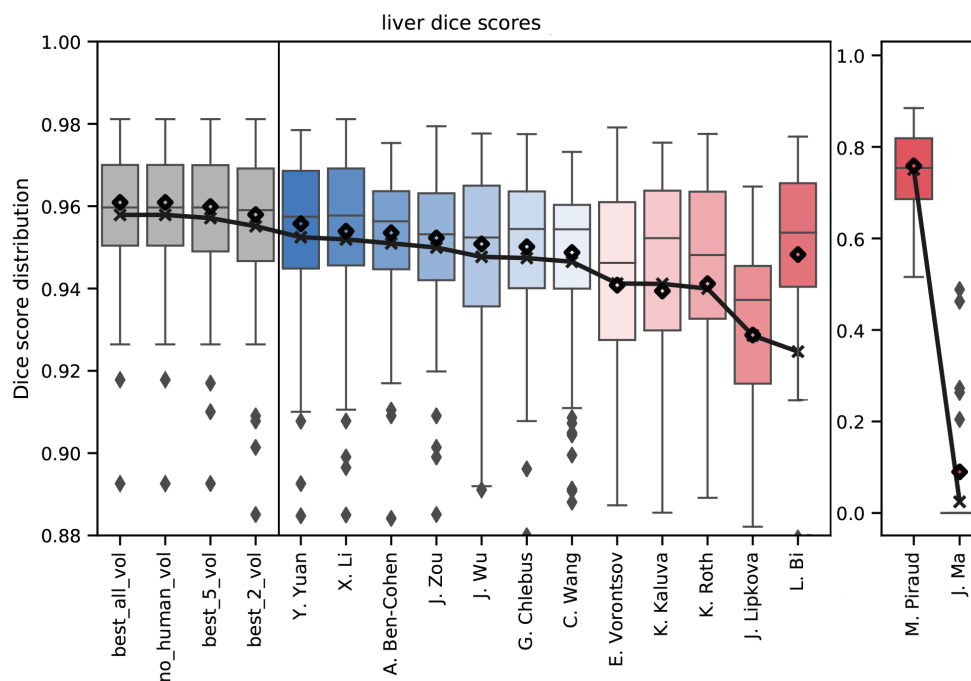


Figure 3.23: Dispersion of Dice scores for liver segmentation task from individual algorithms submitted to LiTS (shown in color) and the fused methods (shown in gray). Boxplots show quartile ranges of the scores on the LiTS test dataset; whiskers indicate the 95% percentile and the diamonds indicate outliers.

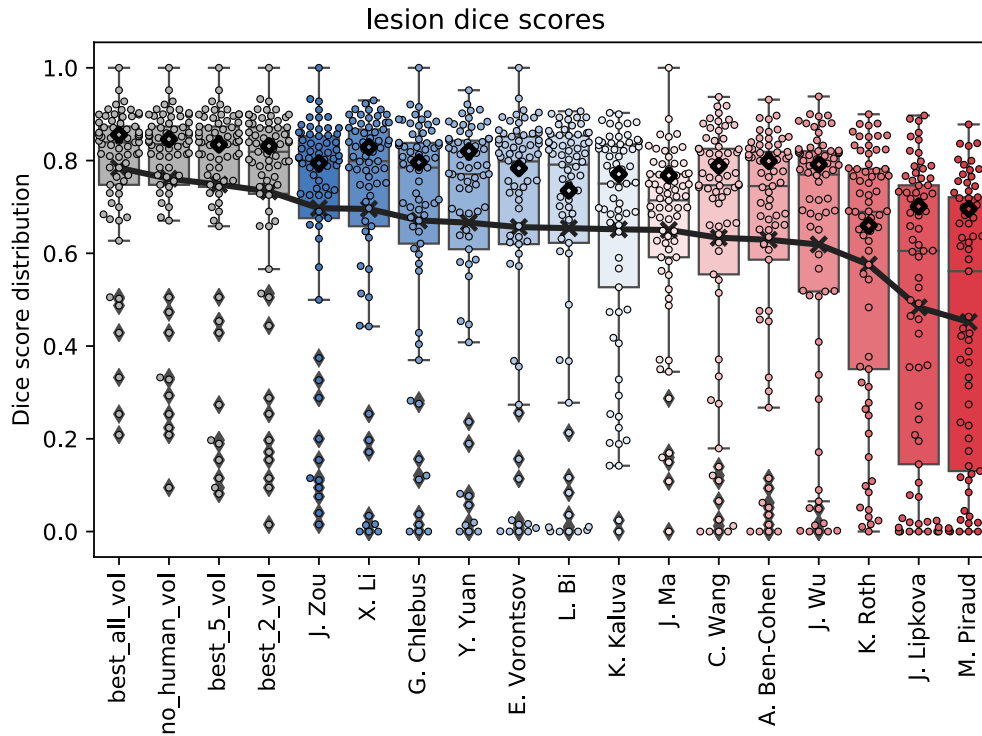


Figure 3.24: Dispersion of Dice scores for liver lesions segmentation task from individual algorithms submitted to LiTS (shown in color) and the fused methods (shown in gray). Boxplots show quartile ranges of the scores on the LiTS test dataset; whiskers indicate the 95% percentile and the diamonds indicate outliers.

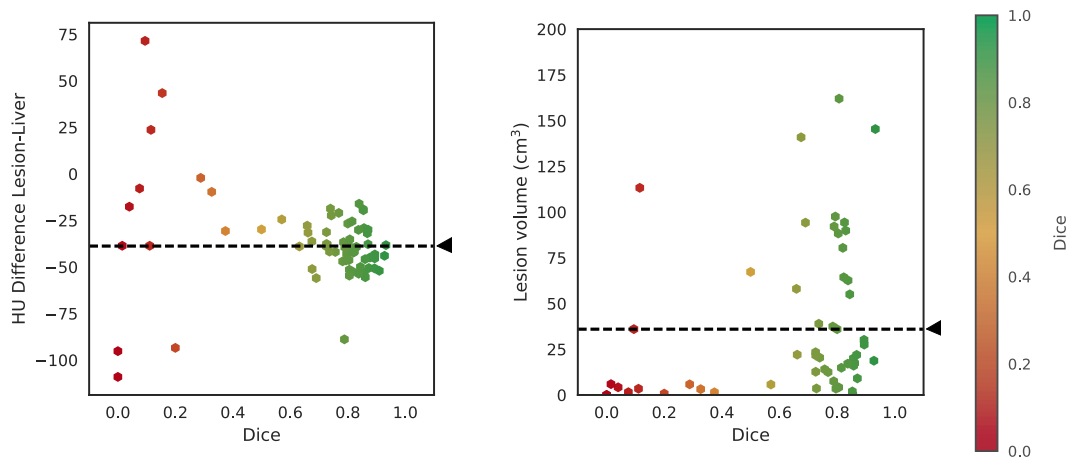


Figure 3.25: A relation between the tumor properties and the performance of the best method from the MICCAI 2017. In general, the methods perform best for large lesions and cases where the difference in the liver and lesion HU values range from -10 to -60 .

Identified pitfalls

While all the methods performed well in liver segmentation task, the scores for the lesion segmentations are still relatively low for the accuracy level required by clinical practice. We identified two main factors that influence the performance of the lesions segmentation methods. The first factor is the volume of the lesions. In general, the methods performed well when segmenting large lesions, but struggled with very small lesions (see Fig. 3.25). This is not completely surprising since many small lesions have a diameter of only a few voxels and appear in scans with relatively low resolution. This is worsened by the considerable noise and artifacts presented in the images, which due to their size and texture similarities are difficult to distinguish from actual lesions. The second factor is the difference in HU of the liver and lesions (see Fig. 3.25). Most methods performed best with this difference being in the range of -10 to -60 . This can be caused by the distribution of HU differences in the dataset. As can be seen from Fig. 3.25, there is a considerably large set of cases with HU differences in the range of -10 to -60 , while other HU differences are represented by only a few cases, making it more difficult for the networks to learn the difference between liver and lesions in such cases.

Conclusion

In the LiTS challenge we generated the largest public dataset for liver and liver lesion segmentation tasks. Current algorithms for liver segmentation reach Dice score over 0.95, however the performance of liver lesion segmentation methods is still relatively low for clinical application, with the best method reaching Dice score of 0.70. A segmentation of small lesions and lesions with very diverse range of HU still remain a challenging task for current automated methods. This suggests that future improvements should focus on identifying local changes in liver structures to better capture small lesions. Since most participating methods rely on deep learning approaches, the current training data set should be extended beyond the 131 volumes, including mainly cases with problematic lesions to further improve the performance of the methods. Moreover, the fusion of multiple segmentation strategies, each specialised for different types of lesions, might hold the key in reaching the level of accuracy required by the clinical practice.

Comment: We participated in the LiTS challenge with a method marked as *Lipkova et al.* in Figs. 3.22 to 3.24. The method uses U-Net for liver segmentation and novel Cahn-Hilliard filtering, presented in Appendix B, for lesions segmentation.

Disclaimer: This section is partially reproduced from the article "P. Bilic, P. F. Christ, E. Vorontsov, G. Chlebus, ..., J. Lipková, ..., B. Menze: The Liver Tumor Segmentation Benchmark (LiTS), (2019)". At the time of writing this thesis – early 2019 – the publication is under a revision, with an arXiv preprint available as arXiv:1901.04056.

3.3.2 Brain Tumor Segmentation Challenge (BraTS)

The BraTS challenge is a benchmark for segmenting brain lesions and their substructures from multimodal MRI scans. It is organized annually in conjunction with MICCAI workshop. Since its initiation in 2012, the BraTS challenge has grown in the number of datasets as well as benchmark tasks. In addition to multi-institutional preoperative MRI scans, the BraTS dataset contains longitudinal scans of tumor progression over time (BraTS 2014-2016) and patients overall survival (BraTS 2017-2018). The challenge tasks have expanded beyond the lesion segmentation, featuring assessments of disease progression and predictions of patient survival. The results from the first two BraTS editions are summarised in [120], while the results from all the seven challenges are described in [13]. Here, we present results from the last challenge (i.e. BraTS 2018) on which organization we have participated.

Motivation

The brain lesions are characterized by a complex structure consisting of various histologically heterogeneous sub-regions, i.e., peritumoral edematous/invaded tissue, necrotic core, active and non-enhancing core. This intrinsic heterogeneity of gliomas is also portrayed in their imaging appearance, as their sub-regions are described by varying intensity profiles disseminated across multimodal MRI scans (see Section 2.3). Each MRI modality provides different type of biological information, and therefore presents different information processing task [120]. Due to highly heterogeneous appearance and shape, segmentation of brain tumors in multimodal MRI scan is one of the most challenging tasks in medical image analysis [13, 120]. Moreover, there is mounting evidence that accurate segmentation of tumor subregions in combination with imaging and radiomics features can offer the basis for quantitative image analysis towards the prediction of patient overall survival. The state-of-the-art tumor segmentation methods as well as potential of Machine Learning (ML) methods to assess patient overall survival are tested in the BraTS 2017 and 2018 challenges.

Setup of the BraTS 2017 and 2018 Challenge

The BraTS 2017 and 2018 challenges focussed on two tasks; *segmentation of tumor substructures* and *prediction of overall survival* of patients diagnosed with primary de novo glioblastoma [13].

Segmentation task. The BraTS dataset consists of preoperative T1w, T1Gd, T2w, and FLAIR scans acquired with different clinical protocols and various scanners from multiple institutions. The participants were asked to segment three tumor subregions: 1) the active tumor (AT), 2) the tumor core (TC), and 3) the whole tumor (WT), as illustrated in Fig. 3.26. The AT is defined by areas that are hyper-intense in T1Gd when compared to T1w. The TC, which is usually resected, comprise of AT, the necrotic and non-enhancing tumor core. The necrotic core appears black,

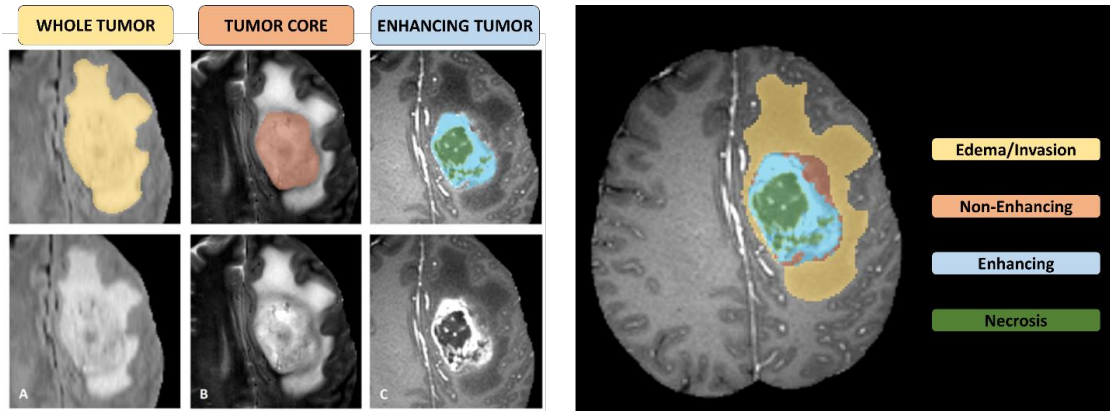


Figure 3.26: Glioma sub-regions considered for the segmentation task. The image patches show from left to right: (A) the whole tumor (yellow) visible in FLAIR, (B) the tumor core (red) visible in T2w, (C) the active tumor (light blue) visible in T1Gd and the components of the necrotic/cystic tumor core (green). The final tumor segmentation contains three labels: active tumor (blue), tumor core (green, blue, red) and whole tumor (green, blue, red, yellow). Figure taken from [13, 120].

while the non-enhancing tumor dark gray in T1Gd when compared to T1w. The WT is defined as the whole visible extent of the disease, consisting of TC and the peritumoral edematous/invaded tissue. All scans were subject to the same pre-processing routine including co-registration to the same anatomical template [149], interpolation to a uniform isotropic resolution (1mm^3) and skull-stripping. The ground truth annotations were created by multiple experts following a specific annotation protocol and were further reviewed for consistency by a single board-certified neuroradiologist.

Survival prediction task. The participants were asked to predict the survival of *de novo* diagnosed glioblastomas patients that did undergo surgery with gross total resection (GTR). The patients were divided into three groups based on their survival, comprising of long-survivors (survival more than 15 months), mid-survivors (survival between 10 and 15 months), and short-survivors (survival less than 10 months). These thresholds were based on the survival distribution across the complete dataset, to avoid potential bias towards one of the survival groups. The participants were expected to combine their tumor segmentations with whatever imaging features extracted from the MRI scans (e.g. texture or image intensities), and the provided patients information about age and gender, to predict the overall survival (OS) after the GTR (Fig. 3.27). The survival predictions were expected in the days and were automatically classified by the evaluation system into the short-, intermediate- and long-survivors.

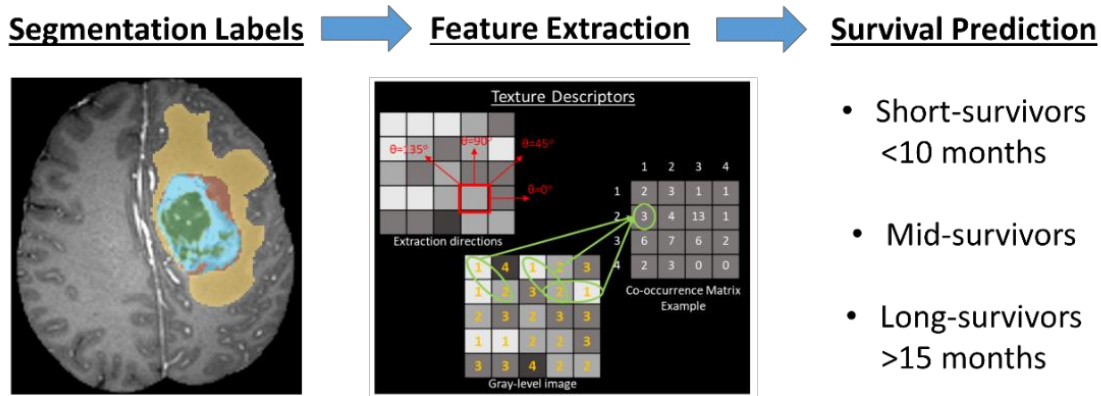


Figure 3.27: The overall survival task combines segmentation of tumor subregions with imaging features extracted from the multimodal MRI scans to predict patient survival in the terms of the three survival groups: short, medium and long survival. Figure taken from [13].

Dataset. The BraTS 2018 dataset contains 542 cases, which were randomly and proportionally divided into three groups, a) *training set* (163 cases, including 59 cases with GTR), b) *validation set* (53 cases, including 28 cases with GTR), and c) *testing set* (130 cases, including 77 cases with GTR). The ground truths labels of the validation and test data are never provided to participants. The validation set allows participants to fine-tune their methods on unseen data, in addition to the training set. The BraTS 2018 challenge is hosted by the UPenn Center for Biomedical Image Computing and Analytics (CBICA) platform⁵, which features downloading of datasets and automatic evaluation of the submitted results.

Results

The ranking scheme for the segmentation task comprised ranking for each tumor region (i.e., AT, TC, WT) of each testing subject and each evaluation measure (Dice score and 95% Hausdorff distance metric). The final ranking score was then calculated by averaging across all these individual rankings and then normalized by dividing by the number of teams. The distribution of patient-wise ranking of all participating methods is shown in Fig. 3.29. A distribution of rankings for each tumor region and each measure is reported in [13]. Similarly, as in the LiTS challenge, we found that no algorithms reached superiority in all segmentation tasks, reflecting the added value of fusing segmentation labels from different methods. Most successful methods employed Deep Learning (DL) strategies, confirming their superiority over traditional ML methods in the segmentation task.

The survival predictions were ranked based on classification accuracy (i.e. the number of correctly classified patients) with respect to the three survival groups. Figure 3.28 shown results of the

⁵ <https://www.med.upenn.edu/sbia/brats2018.html>

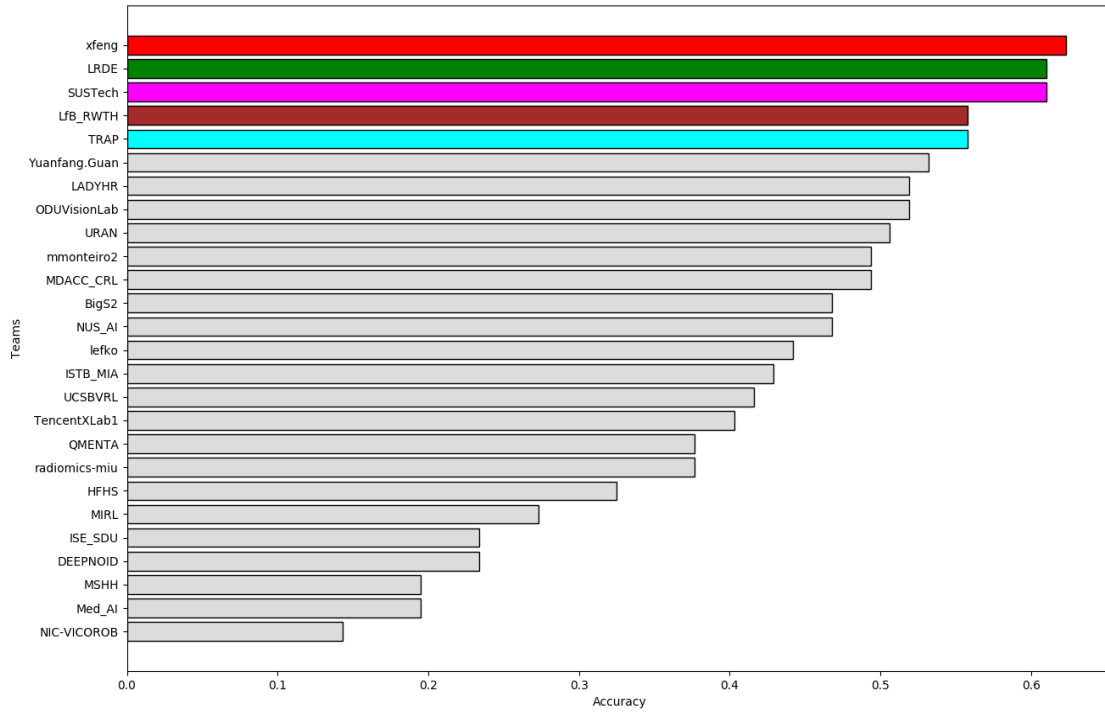


Figure 3.28: Ranking of overall survival prediction task of all teams participating in BraTS 2018. The large values are the better. Figure taken from [13].

survival task, with the top-3 methods reaching an accuracy around 0.6. The participants were also provided with a pairwise error analysis between the predicted and actual survival days, to allow the evaluation of their methods for outliers. Interestingly, the results show the difficulties of DL methods when dealing with relatively small training sets, and highlight the superiority of traditional ML methods in assessing more clinically relevant problems.

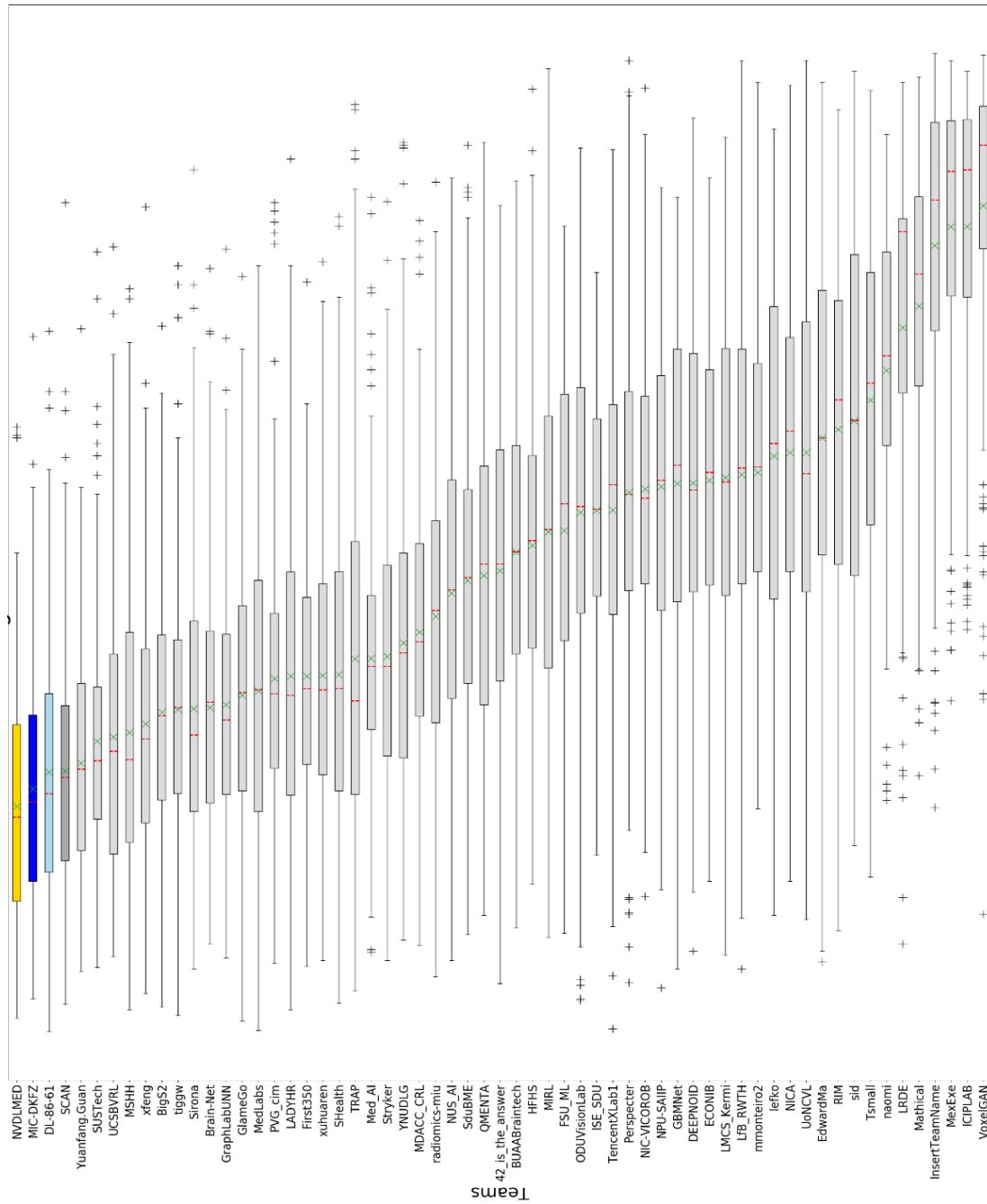


Figure 3.29: The patient-wise distribution of ranking for the segmentation task for all teams participating in BraTS 2018. The higher ranks are represented by smaller values in the plot. Figure taken from [13].

Conclusion

The accuracy of the tumor segmentation algorithms has improved over the last years, however, the robustness of the automated methods is still inferior to expert performance. This robustness is expected to continuously improve as the training set increase in size, together with advances in DL architectures and training strategies. Beyond these expectations, the fusion of segmentation labels from various methods can further improve overall accuracy. The results also highlighted differences in the superiority of DL and traditional ML methods for different tasks. These findings identify the need for potential synergy between DL and traditional ML method, as we transition to larger training sets in the future, which can include more diverse, non-uniformly distributed clinical and/or molecular information.

Translating state-of-the-art algorithms to practice

To leverage translation of the segmentation methods to clinical and scientific practice, BraTS Algorithmic Repository⁶ is being developed. The repository offers successful segmentation methods in the form of Docker containers. The list of currently available methods can be found here⁷. To further facilitate the usage of these methods, we developed software for processing and segmenting head MRI scans. The software allows preprocessing of input MRI scans, using the S3 algorithm for skull-stripping and tissue segmentations, and converts the preprocessed data into a format compatible with the BraTS docker containers. Consequently, the preprocessed data can be segmented with any algorithm available in the BraTS library. The user just needs to provide ID of the docker container with the method that should be used. More information about the software is presented in Chapter 8.

Disclaimer: This section is partly reproduced from the article "S. Bakas, M. Reyes, A. Jakab, ..., J. Lipková, ..., B. Menze: Identifying the Best Machine Learning Algorithms for Brain Tumor Segmentation, Progression Assessment, and Overall Survival Prediction in the BRATS Challenge". At the time of writing this thesis – early 2019 – the publication was still in the preparation, with an arXiv preprint available as arXiv:1811.02629.

⁶<https://github.com/BraTS/Instructions>

⁷https://github.com/BraTS/Instructions/blob/master/Repository_Links.md

3.4 Summary

This chapter has presented the fundamentals of medical image segmentation, followed by two specific approaches; namely atlas-guided and convolutional neural network methods. The first method was exploited to extract brain tissue and segment brain anatomies from head MRI scans, while the second method was applied to detect multiple myeloma bone lesions from full-body hybrid PET/CT scans. The results of the segmentation methods serve as input for the computational tumor models presented in Chapters 4 and 5. This chapter concluded with benchmarks used for an unbiased evaluation of the segmentation methods. The best algorithms from the BraTS challenge and the S3 algorithm are combined into a multimodal head MRI processing software presented in Chapter 8.

IMAGE-BASED TUMOR MODELLING

Mathematical modelling is a compelling tool for simulating the dynamics of complex systems, testing hypotheses and enhancing understanding of governing mechanisms. In oncology, computational models can assist clinical interventions by forecasting tumor progression, survival time or response to treatment. Moreover, *in-silico* experiments can be performed to test and optimize treatment procedures in a non-invasive, patient-specific way.

The tumor mechanisms – and so the corresponding models – operate at different spatio-temporal scales, including molecular, cellular, microscopic and macroscopic scales, as illustrated in Fig. 4.1. The finest scale mechanisms are described by molecular dynamics models, which simulate interactions between molecules (more in Chapter 7). Models at the cellular scale describe intracellular processes, such as proliferation, gene mutations, and malignant transformations [124]. Models at the microscopic scale focus on intercellular interactions within a tissue, such as cell-cell signalling, cell migration (e.g. during wound healing), or formation of new vasculature during angiogenesis [157]. Macroscopic-scale models account for the dynamics of a whole tumor and its interaction with the surrounding tissue. Since these models operate at the scale of medical images, they can be calibrated from patient scans.

This chapter focusses on macroscopic-scale models describing tumor dynamics in a patient-specific anatomy reconstructed from medical scans. In a macroscopic formulation, a tumor is characterized by a tumor cell density and its dynamics is described by a set of partial differential equations (PDEs). First, we present the simplest and most widely used model describing tumor proliferation and infiltration into the surrounding tissue. This model is used to explain the underlying formalisms and concepts, and it serves as a base for more advanced models. Afterward, we extend the basic model to account for the most critical symptoms in glioma patients – particularly, the tumor-induced brain deformations and increased intracranial pressure. The

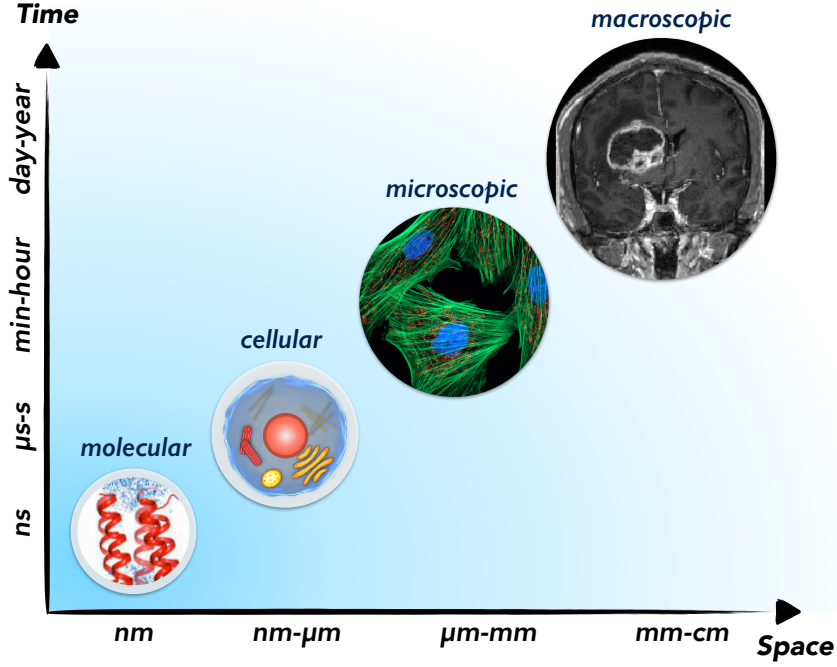


Figure 4.1: An illustration of different spatio-temporal scales of the tumor mechanisms.

model is formulated in a way that allows its calibration from the patient medical scans while model calibration strategies are presented in Chapter 5. To enable simulations of real tumors in patients, the model implementation couples state-of-the-art numerical methods with high performance parallelization strategies across multiple cores and processors.

4.1 Tumor growth modelling

Many tumor growth models are based on the Fisher-Kolmogorov (FK) reaction-diffusion equation [175], which captures the main tumor behavior: *proliferation* and *infiltration* into the surrounding tissue. In the image-based formulation, the FK equation is solved in patient-specific brain anatomy reconstructed from MRI scans, where each voxel corresponds to one simulation grid point. Since the brain tumors infiltrate only white and gray matter, we will denote by $\Omega_1 \in \mathbb{R}^3$ the domain consisting of these two tissues, while other anatomical components, such as skull, ventricles, and CSF act as domain boundaries. Furthermore, we denote by $u_i(t) \in [0, 1]$ the normalized tumor cell density at time t and voxel i at the location $(i_x, i_y, i_z) \in \Omega_1$, where $i = \{1, \dots, N\}$ is the index across all N voxels of the scan. The dynamics of the tumor $\mathbf{u} := \{u_i(t)\}_{i=1}^N$ is modelled as:

$$\frac{\partial \mathbf{u}}{\partial t} = \nabla \cdot (\mathbb{D} \nabla \mathbf{u}) + \rho \mathbf{u} (1 - \mathbf{u}) \quad \text{in } \Omega_1, \quad (4.1)$$

$$\nabla \mathbf{u} \cdot \vec{n} = 0 \quad \text{on } \partial\Omega_1. \quad (4.2)$$

The second term in Eq. (4.1) describes tumor proliferation, where $\rho[1/day]$ is the proliferation rate. The tumor infiltration into the surrounding tissues is modelled as diffusion given by the first term in Eq. (4.1). The invasion is controlled by the tensor $\mathbb{D} = \{D_i \mathbb{I}\}_{i=1}^N$ where \mathbb{I} is a 3×3 identity matrix and

$$D_i = \begin{cases} p_{w_i} D_w + p_{g_i} D_g & \text{if } i \in \Omega_1 \\ 0 & \text{if } i \notin \Omega_1. \end{cases} \quad (4.3)$$

The terms p_{w_i} and p_{g_i} denote the percentage of white and grey matter at voxel i , while D_w and D_g stand for tumor infiltration rates in the corresponding tissues. The tumors infiltrate the white matter faster than the grey matter and it is assumed that $D_w = 10D_g[cm^2/day]$ [119]. The skull and ventricles are not infiltrated by the tumor cells and act as a domain boundary with an imposed no-flux boundary condition given by Eq. (4.2), where \vec{n} is the outward unit normal to $\partial\Omega_1$. The tumor is initialized at voxel ic at location $(ic_x, ic_y, ic_z) \in \Omega_1$ and its growth is modelled from the initial time $t = 0$ until the final time $t = T[day]$. The tumor dynamics is controlled by six model parameters: $\theta_u = \{D_w, \rho, T, ic_x, ic_y, ic_z\}$. The FK model is implemented in *GliomaSolver*, an open-source software presented in Chapter 8.

Simulation

To perform a tumor growth simulation, the model parameters θ_u and the brain anatomy must be selected. Here we use the brain anatomy, shown in Fig. 4.2, which is reconstructed from T1w MRI scan of a healthy subject using the S3 method (see Section 3.2.2). A possible range of the proliferation and infiltration values of the FK model for gliomas, as reported in [68], is shown in Figure 4.4. Here, we take $D_w = 0.0013[cm^2/day]$ and $\rho = 0.025[1/day]$, which corresponds to a HGG tumor. Figure 4.3 shows a simulation of tumor growth over a period of 600 days. It can be seen that the tumor growth pattern is non-trivial, with a complex morphology constrained mainly by the brain anatomy. In the 600th day, the model predicts tumor infiltration through corpus callosum into the right hemisphere. Such predictions are particularly valuable for radiotherapy planning, where the whole tumor extent – including tumor infiltration not visible on the medical scans – should be irradiated (more in Chapter 5).

The FK model describes essential mechanisms governing tumor morphology. Due to its simplicity, the model often serves as a basic building block for more advanced models, such as [194]. Nonetheless, the FK model does not account for the tumor interactions with the surrounding tissue, and therefore it can describe only tumor dynamics on a limited time scale – before the tumor mass effect becomes significant. To overcome this issue, in the next section we propose a model for tumor growth, mechanical interaction with the surrounding brain parenchyma, and corresponding changes in the intracranial pressure.

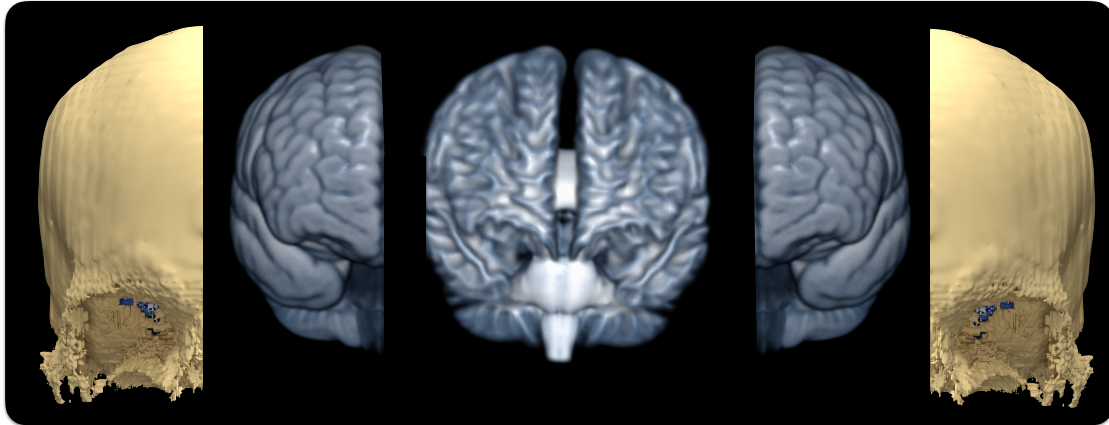


Figure 4.2: The brain anatomy used for the tumor growth simulation presented in Fig. 4.3. Shown are white matter, grey matter, and skull reconstructed from patient MRI scans.

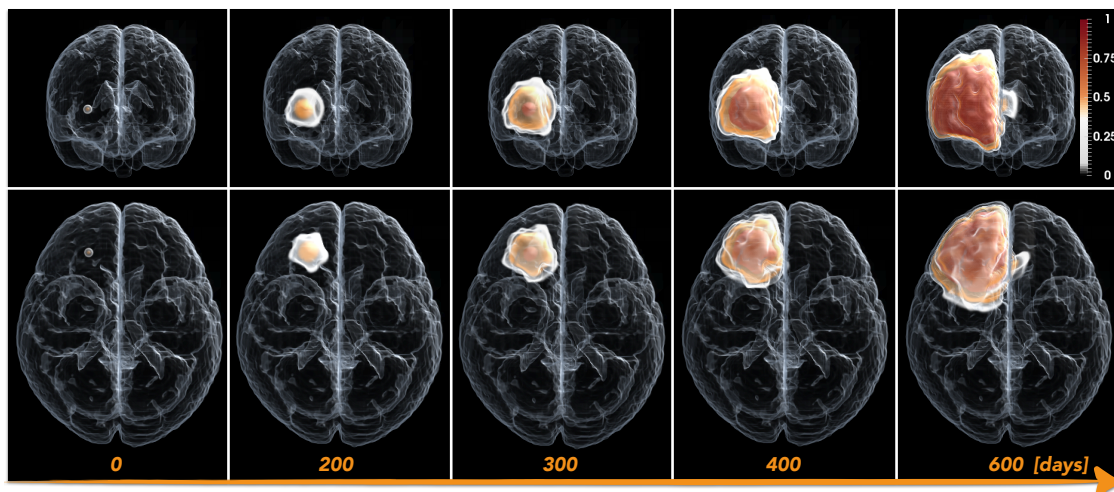


Figure 4.3: Simulation of tumor growth over a period of 600 days. Shown are the front and top view. The outlines of the brain are shown in light grey, while the red/orange/white colors indicate regions with high/medium/low tumor cell density.

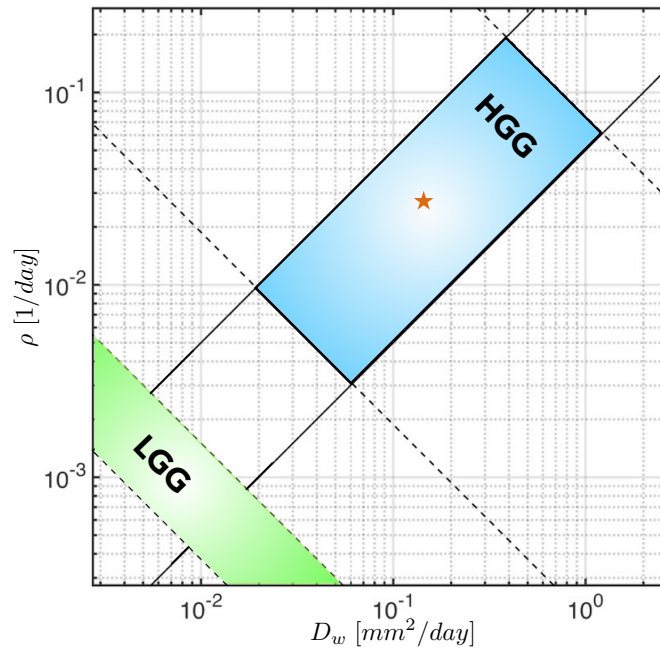


Figure 4.4: A distribution of proliferation (ρ) and infiltration (D_w) parameters for LGG and HGG, as reported in [68]. The orange star marks the parameters values used in the tumor growth simulation shown in Fig. 4.3.

4.2 Tumor-induced brain deformations

Histologically, gliomas are divided into low and high-grade tumors (see Section 2.1.3). The LGGs are related to slower progression and better prognosis. However, if left untreated, almost all low-grade gliomas evolve to high-grade tumors. The HGGs are characterized by fast progression, often accompanied by severe deformations of the brain tissue and increased intracranial pressure (ICP). Tissue compression and ICP elevation are the most critical symptoms – and the main cause of death – in glioma patients. Treatment of HGGs usually involves resection followed by a combined radio- and chemotherapy. LGG patients are often treated with corticosteroids, reducing the tumor edema, in conjunction with regular monitoring for potential tumor progression. In some cases, only palliative treatment targeting increased ICP and related symptoms are provided.

The standard-of-care treatment procedures can be improved by incorporating information from computational models. Most tumor growth models are based on the FK equation; described in the previous section. These models, calibrated for patient-specific conditions, can estimate tumor infiltration even beyond the lesion extend visible on medical scans. This, in turn, allows design of improved, personalized treatment plans (see Chapter 5). Nonetheless, since these models do not account for the tumor mechanical interactions with the surrounding brain tissues (i.e. tumor mass effect), they can only capture tumor dynamics on a limited time scale. The computational models accounting for the tumor mass effect would allow prediction of critical conditions, such as brain midline shift [31], compression of vital nerves or decreased brain perfusion; enabling the application of preventive measures. Moreover, the model estimates about the ICP – a crucial pathological indicator – provide a non-invasive tool to assess the extent of the patient disease, in contrast to contemporary surgery-involving ICP measurements [143].

Hitherto, several computational models describing tumor mass effect on the brain parenchyma were proposed. In [79, 126], authors employed pure mechanical models, where the brain tissue is treated as an elastic material, while the tumor mechanical force is approximated by a constant pressure acting on the tumor boundary. These models were used to design brain atlases with tumor deformations, however, they do not account for the tumor proliferation and infiltration into the surrounding tissue. In [35] the authors used a similar mechanical model in a combination with the FK reaction-diffusion equation describing the tumor dynamics. Nonetheless, in this approach, the tumor reaction-diffusion equation is decoupled from the elasticity equation, and the tumor infiltration coefficient is not updated according to the tumor mass effect, which leads to discrepancies; especially in the case of large deformations. In [40, 80] the tumor dynamics is modelled by a nonlinear reaction-advection-diffusion equation which couples the tumor growth with the subsequent brain tissue deformation. This allows the simulation of large deformations, however, the resulting tumors exhibit relatively simple and homogeneous morphologies.

Despite considerable theoretical contributions, these models have not yet found an application in clinical practice. This can be attributed to the following factors: 1) The existing methods do not model the pressure distribution in the brain, instead, a prescribed constant pressure

increment in the whole parenchyma is assumed. As a consequence, these models can not predict pressure-related critical conditions. 2) The models are relatively complex and computationally expensive which hinders the calibration of the model parameters to the patient-specific conditions. 3) The model parameters affecting the deformation field, such as Young modulus or Poisson's ratio, might be difficult to infer from the tissue deformations observed in the patient's scans since the calibration strategies struggle to distinguish between the compensating effects of these parameters. As a consequence, most approaches use parameters obtained from *in-vivo* animal experiments or *postmortem* studies. However, a translation of these measurements into patient models is hindered by the intra-species variations and significant changes in mechanical properties of the brain tissue even a few minutes after death [188]. This results in considerable deviations in the values of the model parameters used among the authors. For instance, the Young modulus varies by two orders of magnitude between [40] and [35].

Herein we propose a novel model coupling tumor dynamics, brain tissue deformation, and corresponding ICP changes. The model assumes that the growing tumor exerts pressure on the surrounding tissue. The brain tissue partially relaxes this pressure, depending on the tissue-specific mechanical properties, while the remaining pressure contributes into a deformation force. The proposed model provides several advantages over current models. 1) The coupling between tumor dynamics and ICP allows the prediction of pressure-related critical conditions constrained by the patient-specific anatomy. 2) The resulting tumor has a more realistic morphology, than relatively uniform-appearing tumors observed in the previous works. 3) The model has a simpler formulation, with fewer model parameters than the existing methods, which aids in calibration from patient medical scans.

In terms of implementation, the presented numerical approach for solving the model efficiently employs finite differences discretization, which is a natural choice since the medical scans are defined on a regular grid. In contrast, all the aforementioned models rely on finite element methods. These, however, bear several disadvantages, such as the need for robust algorithms for 3D grid generation [40, 158] and deterioration of unstructured grids in the presence of large deformities, which need to be frequently corrected by mapping to the regular grids (i.e. remeshing) [126]. On the other hand, a challenge for using finite difference methods in the previous models is the increased numerical complexity arising from the need to solve a large system of linear equations with a non-symmetric matrix, as pointed out in [40]. The symmetry of the system is broken by the boundary conditions applied on the complex brain anatomy. We overcome this issue by using a diffuse domain method (DDM) [103], which allows solving the model in a regular domain and thus preserving the symmetry of the system. This reduces the computational cost and allows solving the tumor dynamics directly in the domains defined by the patient's medical scans, avoiding the aforementioned disadvantages and registration errors caused by mapping the simulation results from the unstructured grids to the regular grid of the patient medical scans. To illustrate the capability of the proposed model to produce realistic brain deformations and

ICP [mmHg]	ICP [Pa]	Conditions
7 – 15	933 – 1999	Normal
20 – 25	2666 – 3333	Onset of hypertension
25 – 40	3333 – 5332	Hypertension
40 – 50	5332 – 6666	Loss of consciousness
> 50	> 6666	Brain infraction and brain death

Table 4.1: A relation between the intracranial pressure values and the corresponding pathological conditions.


corresponding pathological conditions, the model is tested on synthetic and real cases. Moreover, a highly parallel implementation of the model is publicly released, as a part of the *GliomaSolver*¹ presented in Chapter 8.

The rest of this chapter is organised as follows. Section 4.2.1 introduces the proposed tumor-induced brain deformation model while the diffuse domain formulation is presented in Section 4.2.2. The results – including synthetic and real cases – are presented in Section 4.2.3. Conclusions are presented in Section 4.3.

4.2.1 Method

Herein, we propose a model describing tumor dynamics, the mass effect and the distribution of ICP in the patient brain anatomy. The model assumes that the tumor cells proliferate and infiltrate the neighboring brain tissue. The growing tumor exerts pressure on the surrounding brain tissue, which is modelled as a viscoelastic material. The tissue partially relaxes the pressure, depending on its mechanical properties, while the remaining pressure contributes to the deformation field – causing tissue displacement and compression. The model is solved in the patient brain anatomy reconstructed from the MRI scans, where each voxel corresponds to one simulation grid point. The tumor cells infiltrate only the white and gray matter, whereas the tumor mass affects the whole brain anatomy. Therefore, the following distinct simulation domains are assumed: $\Omega_1(t) \in \mathbf{R}^3$ a domain consisting of white and gray matter only; $\Omega_2 \in \mathbf{R}^3$ a domain including white, grey matter and CSF (i.e. the regions of brain parenchyma); $\Omega_3 \in \mathbf{R}^3$ a rectangular domain including whole brain (e.g. the whole brain scan region); i.e. $\Omega_1(t) \subset \Omega_2 \subset \Omega_3$. The distinct simulation domains are shown in Fig. 4.5. To account for the tumor-induced changes in the brain anatomy, such as compression of ventricles, the domain $\Omega_1(t)$ changes over time. On the other hand, the domains Ω_2 and Ω_3 are time independent since the brain parenchyma is constrained by skull, which does not move.

For the rest of this chapter, the following notation is used: the field variables defined at every voxel, such as tumor cell density, are marked by bold letters e.g. \mathbf{x} ; the vector of field variables, such as velocity, are denoted by bold letters with an arrow, e.g. $\vec{\mathbf{x}}$; scalar variables, like the proliferation rate, are marked by non-bold letters, e.g. x . Finally, the letter $i = \{1, \dots, N\}$ denotes

¹ <https://github.com/JanaLipkova/GliomaSolver>

an index across all N voxels of the input scan. The rest of this section describes the individual components of the proposed model, while Table 4.2 lists all the model parameters.

Tumor dynamics

Let $u_i(t) \in [0, 1]$ be a normalized tumor cell density at time t and voxel i at the location $(i_x, i_y, i_z) \in \Omega_1(t)$. The dynamics of the tumor cell density $\mathbf{u} := \{u_i(t)\}_{i=1}^N$ in the brain tissue $\Omega_1(t)$ is modelled as:

$$\frac{\partial \mathbf{u}}{\partial t} = \nabla \cdot (\mathbb{D} \nabla \mathbf{u}) + \rho \mathbf{u}(1 - \mathbf{u}) - \vec{\mathbf{v}} \cdot \nabla \mathbf{u} \quad \text{in } \Omega_1(t), \quad (4.4)$$

$$\nabla \mathbf{u} \cdot \vec{\mathbf{n}} = 0 \quad \text{in } \partial\Omega_1(t), \quad (4.5)$$

$$\mathbf{u}(t=0) = \mathbf{u}_0 \quad \text{in } \Omega_1(t=0). \quad (4.6)$$

The first term on the right side of the Eq. (4.4) describes tumor infiltration into the surrounding tissue, where $\mathbb{D} = \{D_i(t)\}_{i=1}^N$ is tissue dependent tensor, \mathbb{I} is a 3×3 identity matrix and

$$D_i(t) = \begin{cases} p_{w_i}(t)D_w + p_{g_i}(t)D_g & \text{for } i \in \Omega_1, \\ 0 & \text{for } i \notin \Omega_1, \end{cases} \quad (4.7)$$

where $p_{w_i}(t)$ and $p_{g_i}(t)$ denote the percentage of the white and gray matter at the voxel i at the time t . The constants D_w and D_g describe tumor infiltration rate in white and gray matter, respectively and it is assumed that $D_w = 10D_g$ [cm²/day] [119]. In contrast to the FK model presented in Section 4.1, the infiltration rate $D_i(t)$, the tissue percentage $p_{w_i}(t)$ and $p_{g_i}(t)$, and the domain $\Omega_1(t)$ change over time due to the tumor-induced tissue displacement. The second term on the right side of Eq. (4.4) describes self-limiting tumor proliferation, where ρ [1/day] is the proliferation rate. The growing tumor exerts a pressure onto the surrounding tissue, which is deformed and displaced in response. The displacement of the tissue also displaces the tumor cells infiltrated inside that tissue. This is modelled by the last term on the right side of the Eq. (4.4), where $\vec{\mathbf{v}} = \left\{ (v_{x_i}(t), v_{y_i}(t), v_{z_i}(t)) \right\}_{i=1}^N$ is the velocity of the displacement. The skull, CSF, and ventricles are not infiltrated by the tumor and act as domain boundaries with imposed no-flux boundary condition given by Eq. (4.5), where $\vec{\mathbf{n}}$ is the unit outward normal to $\partial\Omega_1(t)$. The tumor is initialized as a small smooth sphere with a radius 1-2 voxels, centered at voxel ic at the location $(ic_x, ic_y, ic_z) \in \Omega_1(t)$ and its growth is modelled from the initial time $t=0$ until the final time $t=T$ [day].

Pressure and displacement

Let $p_i(t)$ denote the pressure at voxel $i \in \Omega_2$ at the time t . We assume that the source of the pressure $\mathbf{p} := \{p_i(t)\}_{i=1}^N$ in the brain is the growing tumor. Furthermore, the pressure is relaxed by the brain tissue, which is modelled as a viscoelastic material. The remaining pressure generates a deformation force. Using Darcy law, the velocity of the deformation can be derived from the

pressure gradient. The pressure and the velocity field \vec{v} in Ω_2 are modelled as follows:

$$\vec{v} = -\mathcal{M} \cdot \nabla \mathbf{p} \quad \text{in } \Omega_2, \quad (4.8)$$

$$\nabla \cdot \vec{v} = \rho \mathbf{u}(1 - \mathbf{u}) - \kappa \mathbf{p} \quad \text{in } \Omega_2, \quad (4.9)$$

$$\vec{v} = 0 \quad \text{on } \partial\Omega_2. \quad (4.10)$$

The parameter \mathcal{M} denotes the hydraulic conductivity, which describes the ease with which the pressure passes through the tissue. The pressure relaxation is described by the parameter $\kappa := \{\kappa_i(t)\}_{i=1}^N$, where

$$\kappa_i(t) = \begin{cases} p_{w_i}(t)\kappa_w + p_{g_i}(t)\kappa_g + p_{c_i}(t)\kappa_c & \text{for } i \in \Omega_2, \\ 0 & \text{for } i \notin \Omega_2. \end{cases} \quad (4.11)$$

The terms $p_{w_i}(t), p_{g_i}(t), p_{c_i}(t)$ denote the percentage of white matter, gray matter and CSF at voxel i at the time t , while κ_w, κ_g , and κ_c denote the relaxation rate of the corresponding tissues. The softer the material is, the more pressure it relaxes, thus it is assumed that $\kappa_c > \kappa_w > \kappa_g$. For simplicity, we assume a constant hydraulic conductivity $\mathcal{M} = 8.53e-09 [cm^2 \cdot mmHg^{-1} \cdot s^{-1}]$ as reported in [173]. This means, that the tumor exerts the same pressure to all the surrounding tissues, but distinct tissues respond differently, based on their mechanical properties.

Substituting Eq. (4.8) into both Eq. (4.9) and Eq. (4.10) leads to the Helmholtz-like equation, which describes the pressure field as follows:

$$-\nabla \cdot (\mathcal{M} \cdot \nabla \mathbf{p}) = \rho \mathbf{u}(1 - \mathbf{u}) - \kappa \mathbf{p} \quad \text{in } \Omega_2, \quad (4.12)$$

$$\nabla \mathbf{p} \cdot \vec{n} = 0 \quad \text{on } \partial\Omega_2 \quad (4.13)$$

$$\mathbf{p}(t=0) = \mathbf{p}_0 \quad \text{in } \Omega_2. \quad (4.14)$$

The initial pressure \mathbf{p}_0 corresponds to the patient ICP before the tumor onset. Since it might not be known, we assume $\mathbf{p}_0 = 0 [mmHg]$. Then the pressure $p(t)$ corresponds to the tumor-induced pressure increase over the patient's normal ICP. The pressure \mathbf{p} obtained from Eqs. (4.12) to (4.14) is used to compute the velocity field \vec{v} from Eq. (4.8), which is consequently used to model the tissue deformation.

Tissue dynamics

Let $\omega_{w_i}(t), \omega_{g_i}(t)$, and $\omega_{c_i}(t)$ denote the density of white matter, grey matter and CSF, respectively, at voxel $i \in \Omega_2$ at time t . The tumor-induced brain deformation displaces and compresses the brain tissue. Thus the dynamics of each tissue $\omega_s := \{\omega_{s_i}(t)\}_{i=1}^N$, $s \in \{w, g, c\}$ is modelled by the advection-convection equation as follows:

$$\frac{\partial \omega_s}{\partial t} = -\vec{v} \cdot \nabla \omega_s - \omega_s \nabla \cdot \vec{v} \quad \text{in } \Omega_2, \quad (4.15)$$

$$\nabla \omega_s \cdot \vec{n} = 0 \quad \text{on } \partial\Omega_2, \quad (4.16)$$

$$\omega_s(t=0) = \omega_{s_0} \quad \text{in } \Omega_2. \quad (4.17)$$

The advection term describes tissue displacement, while the convection term models tissue compression. Let us note that the tumor in Eq. (4.4) is only subject to displacement since the tumor itself is not compressed. The cell density of each tissue component in Eq. (4.17) is initialized by the tissue segmentation, which can be computed by the S3 method ² (see Section 3.2.2). After the tissue density is updated, the percentage of each tissue component must be recomputed accordingly, i.e. for $\forall i \in \Omega_2$ and $s \in \{w, g, c\}$:

$$p_{s_i}(t) = \frac{\omega_{s_i}(t)}{\omega_{w_i}(t) + \omega_{g_i}(t) + \omega_{c_i}(t)}. \quad (4.18)$$

This ensures that the tissue percentage at each voxel is compatible with the tissue density maps and that $p_{w_i}(t) + p_{g_i}(t) + p_{c_i}(t) = 1$ for $\forall i \in \Omega_2$.

Variable	Units	Description
\mathbf{u}	$[M/L^3]$	tumor cell density
ω	$[M/L^3]$	brain tissue cell density
\mathbb{D}	$[L^2/T]$	tumor infiltration rate
ρ	$[1/T]$	tumor proliferation rate
\mathbf{p}	$[M/LT^2]$	tumor-induced pressure
κ	$[T/L^2]$	pressure relaxation
\vec{v}	$[L/T]$	deformation field
\mathcal{M}	$[L^3/TM]$	hydraulic conductivity

Table 4.2: An overview of the model parameters and their units. The parameters $T[day]$, $L[cm]$ and $M[g]$ denote the characteristic time, length and mass, respectively.

4.2.2 Numerical implementation

This section describes the DDM which is used to reduce the numerical complexity of the proposed model. Details of the numerical implementation are discussed afterwards.

Diffuse domain formulation

The computational bottleneck of the proposed model is the Helmholtz equation given by Eqs. (4.12) to (4.14). Its numerical discretization with the finite difference methods leads to a system of linear equations with a non-symmetric matrix. The non-symmetric nature of the system arises from the complex brain anatomy and the no-flux boundary condition Eq. (4.13). However, the most efficient numerical methods for solving a set of linear equations, such as the Jacoby, Gaus-Siedel or Conjugate gradient methods, require symmetric matrices. This issue can be overcome by DDM [103], which reformulates the original system of PDE equations into a new system defined in a regular domain with arbitrary boundary conditions. Here we consider regular rectangular domain Ω_3 , such that $\Omega_2 \subset \Omega_3$ (see Fig. 4.5), with zero Dirichlet boundary condition on $\partial\Omega_3$. The

²: <https://github.com/JanaLipkova/s3>

DDM relates the complex domain Ω_2 with the regular domain Ω_3 through so called phase-field function $\boldsymbol{\psi} := \{\psi_i\}_{i=1}^N \in \mathbb{R}$. The phase-field function is a smoothed version of the characteristic function of the domain Ω_2 , i.e. $\psi_i = 1$ for $i \in \Omega_2$, $\psi_i = 0$ for $i \in \Omega_3 \setminus \Omega_2$, and ψ varies smoothly at the interface between the domains Ω_2 and Ω_3 , such that $\psi(i) = 0.5$ for $i \in \partial\Omega_2$ (see Fig. 4.5). In the DDM, the Helmholtz equation Eqs. (4.12) to (4.14) is reformulated as:

$$-\nabla \cdot (\mathcal{M} \cdot \boldsymbol{\psi} \nabla \mathbf{p}) = \boldsymbol{\psi} \rho \mathbf{u}(1 - \mathbf{u}) - \boldsymbol{\psi} \boldsymbol{\kappa} \mathbf{p} \quad \text{in } \Omega_3, \quad (4.19)$$

$$\boldsymbol{\psi} \cdot \mathbf{p} = 0 \quad \text{on } \partial\Omega_3, \quad (4.20)$$

$$\boldsymbol{\psi} \cdot \mathbf{p}(t=0) = \mathbf{p}_0 \quad \text{in } \Omega_3. \quad (4.21)$$

The discretization of these equations with the finite-difference method leads to a system of linear equations with a symmetric matrix, which significantly reduces the numerical complexity of the system.


The phase-field function of the domain Ω_2 can be obtained by solving the Cahn-Hilliard equation [22, 178]:


$$\frac{\partial \boldsymbol{\psi}}{\partial t} = \nabla \cdot (\mathcal{A}(\boldsymbol{\psi}) \cdot \nabla (g'(\boldsymbol{\psi}) - \varepsilon^2 \Delta \boldsymbol{\psi})) \quad \in \Omega_3, \quad (4.22)$$

$$\boldsymbol{\psi}(t=0) = \begin{cases} 1 & \text{on } \Omega_2, \\ 0 & \text{on } \Omega_3 \setminus \Omega_2, \end{cases} \quad (4.23)$$

where $g(\boldsymbol{\psi}) = \frac{1}{4} \boldsymbol{\psi}^2 (1 - \boldsymbol{\psi})^2$ is a double-well potential and the term $\mathcal{A}(\boldsymbol{\psi})$ controls the behavior of the phase-field function at the interface while ε is the prescribed interface thickness. Taking $\mathcal{A}(\boldsymbol{\psi}) = \sqrt{4g(\boldsymbol{\psi})}$ prevents interface displacement. The Cahn-Hilliard equation is solved in time until the phase-field function reaches a smooth interface with the desired thickness. To avoid computation of the phase-field function for each new patient, we provided a pre-computed phase-field function together with the brain atlas³. The patient-specific phase-field function can then be obtained by computing a rigid registration \mathcal{F} , that maps the brain mask of the atlas to the patient brain mask. The resulting registration \mathcal{F} is then used to map the pre-computed atlas phase-field function to the patient brain. The pre-computed atlas' phase-field function is shown in Fig. 4.5. The registration software is also provided in our repository⁴. Let us note, that the phase-field function and the domain Ω_2 , do not change over time with the modelled brain deformations. The reason is that the tumor-induced deformations take place only inside the brain parenchyma since the skull is rigid.

The DDM is used only for the Helmholtz equation. In principle, all PDEs presented in the Section 4.2.1 could be expressed using the DDM formalism. However, if the ε is not sufficiently small, the smooth phase-field function could smooth out the interface between very fine anatomical structures, which would reduce accuracy. For example, the CSF region separating the brain

³  <https://github.com/JanaLipkova/GliomaSolver> (atlas phase-field function)

⁴  <https://github.com/JanaLipkova/Registration>

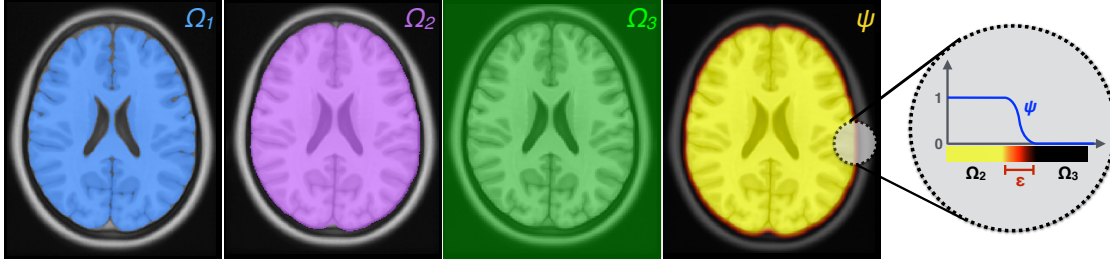


Figure 4.5: An overview of the simulation domains and the phase-field function. The domain infiltrated by the tumor, Ω_1 , is shown in blue while the domain affected by tumor-mass effect, Ω_2 , is displayed in purple. The regular domain used for DDM formulation, Ω_3 , is portrayed in green. The last subplot shows the phase-field-function ψ computed by the Cahn-Hilliard Eq. (4.22).

hemispheres in the frontal lobe has a thickness of only 1-3 voxels, which would require ε to be less than a voxel.

Implementation

To solve the system of equations presented in Section 4.2.1 we use the following algorithm:

Algorithm 2 Implementation of the tumor-induced brain deformation model.

- 1: *Initialise:* $t = 0$, $\mathbf{u}(t = 0) = \mathbf{u}_0$, $\omega_s(t = 0) = \omega_{s_0}$ for $s \in \{w, g, c\}$
 - 2: Compute tissue percentage by Eq. (4.18)
 - 3: **while** ($t \leq T$) **do**
 - 4: Compute time step $\tau = \min(\tau_1, \tau_2)$, where τ_1 and τ_2 are time steps constrained by the numerical stability of Eq. (4.4) and Eq. (4.15)
 - 5: Compute the **pressure** $p(t)$ by solving Eqs. (4.19) to (4.21)
 - 6: Compute the **deformation field** $\vec{v}(t)$ by solving Eqs. (4.8) and (4.10)
 - 7: Update the **tumor** state by solving Eqs. (4.4) and (4.5)
 - 8: Update the **brain tissue** by solving Eqs. (4.15) and (4.16)
 - 9: Recompute the **tissue percentage** by Eq. (4.18)
 - 10: $t = t + \tau$
 - 11: **end while**
-

The model is discretized by finite differences in space and explicit Euler in time. The Helmholtz equation, given by Eqs. (4.19) to (4.21), is solved with multigrid preconditioned conjugate gradient method [53] using the *hypr* library [49]. The advection-convection system in Eqs. (4.15) and (4.16), is solved with the 5th order weighted essentially non-oscillatory (WENO5) scheme [73]. The advantage of the WENO5 scheme is its capability to achieve high accuracy solution in smooth regions while maintaining stable, non-oscillatory and sharp discontinuity transitions, which appear at interfaces between the CSF and white and gray matter. The model is implemented in the *GliomaSolver*, presented in Chapter 8. High performance of the implementation is achieved through a hybrid OpenMP and MPI parallelization.

4.2.3 Results

The proposed deformation model is tested on synthetic and clinical cases. In the first case, the model is used to deform the anatomy from a healthy subject. This example is used to illustrate the model's potential to simulate tumor progression, brain deformation and ICP elevation over time; along with the accompanying critical conditions. Then the model is applied to clinical cases of patients with HGG and LGG lesions. Due to the aggressive nature of the HGGs, usually only scans from a single time point before the surgery are available. Nonetheless, since these scans show significant brain deformations, they are used to show the model's potential to produce realistic brain deformations. Afterward, data showing tumor progression from low to high-grade glioma are used to assess the model potential on the disease progression over time.

Synthetic case

To illustrate the potential of the model to simulate tumor progression, brain deformations, and ICP, the model is used to grow a tumor in a healthy subject and track the resulting changes in the brain anatomy. The simulation is performed with the following parameters: $D_w = 1.3e - 03 [cm^2/day]$, $\rho = 1.2e - 02 [1/day]$, $\kappa_g = 2.0e - 03 [day/cm^2]$, $\kappa_w = 2.0e - 02 [day/cm^2]$, $\kappa_c = 2.0e - 01 [day/cm^2]$ and $\mathcal{M} = 8.53e - 09 [cm^2 \cdot mmHg^1 \cdot s^{-1}]$. Figures 4.6 and 4.7 show the tumor progression over a period of 600 days. The tumor mass effect results in brain tissue deformation, including compression of the right ventricle and midline shift. The later is more visible in the 3D visualization shown in Fig. 4.7. The simulated pressure elevation, shown in Fig. 4.6 (middle), correlates with the critical pressure values reported in Table 4.1. Let us note, the standard procedures measure the ICP only at a single location, whereas the model predicts the distribution of the pressure in the whole parenchyma. The simulation identified the highest pressure accumulation in the frontal lobe, where the growing tumor compresses the brain tissue towards the skull. In contrast, the pressure in the ventricles is much lower, which is consistent with the ability of the CSF to relax the pressure. The deformation field, shown in Fig. 4.6 (bottom), is most pronounced at the interface between the tumor and the tissue, while the deformation effect decreases with the increasing distance from the tumor. The response of the tissue to the tumor-mass effect also results in a more complex and realistic tumor morphology, in comparison to relatively uniform tumors observed in previous works [40, 79, 126].

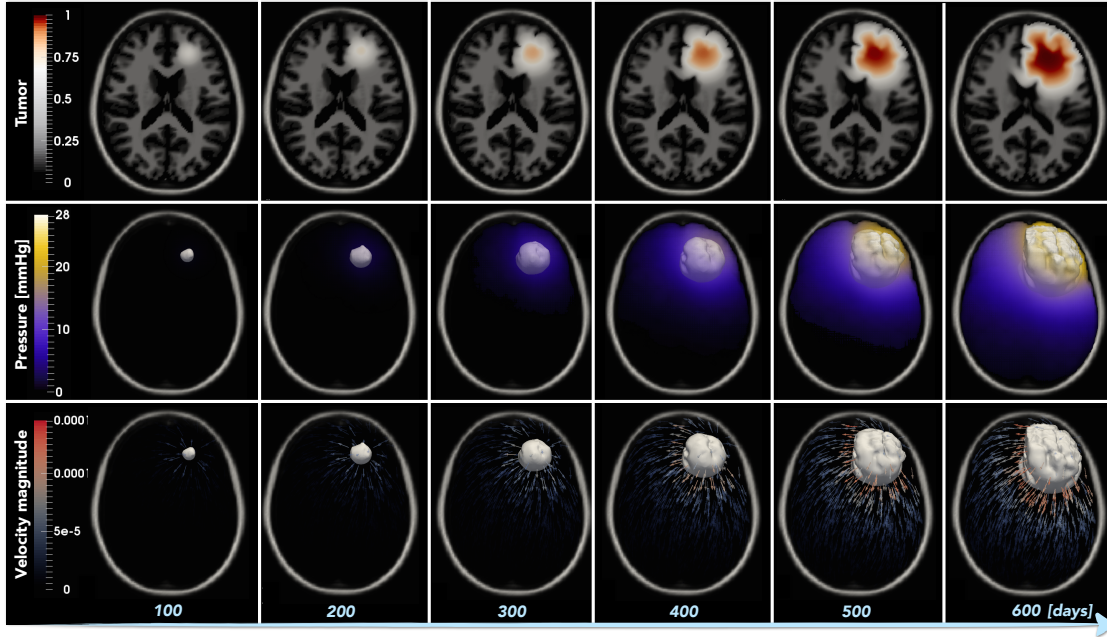


Figure 4.6: Simulation of the tumor-induced brain deformation over a period of 600 days. The upper row shows a 2D slice with the tumour and its effect on the brain anatomy. The pressure distribution and deformation field, together with tumor outline (shown as the white iso-contour given by $u = 0.3$) are shown as 3D views in the middle and bottom rows, respectively.

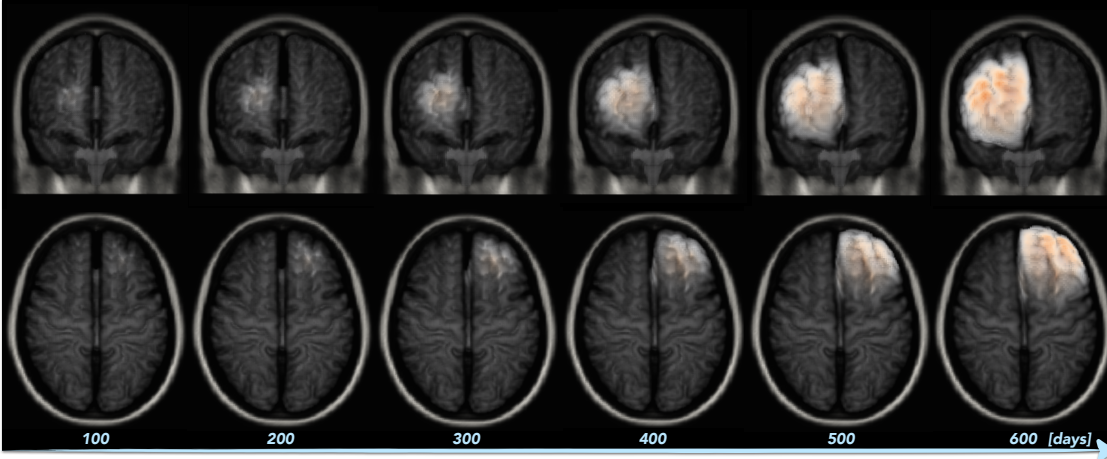


Figure 4.7: Simulation of the tumor-induced brain deformation over a period of 600 days. The 3D representation clearly shows the displacement of the brain midline over time. For visualisation purposes, the signal from the CSF is suppressed.

This example shows that the proposed model is capable to simulate tumor-induced brain deformations and critical conditions such as midline shift and ICP elevation. Moreover, the

predicted pressure distribution allows to assess the impairment of vital nerves in the regions with the high pressure accumulation. For instance, the compression of nerves in the frontal lobe, as in the presented case, would suggest deterioration of motoric functions and speech.

Clinical single-time point data

To assess the capability of the model to produce realistic brain deformations, the model is used to reproduce the deformations observed in MRI scans of patients diagnosed with HGG, shown in Fig. 4.8 (A-B). To perform the simulation, we would like to initialize the tumor in the patient anatomy before the tumor onset, and model its progression and mass-effect until it reaches the state visible on the scans. Since a scan with the patient non-deformed brain anatomy is not available, we approximate it using image registration. Specifically, a rigid registration is used to map the atlas T1w MRI scan to the patient T1w MRI. The T1w MRI scan is preferred over other modalities because of its superior contrast between the brain anatomies and the low enhancement in the tumor region. This approach provides a reasonable approximation of the deformation-free brain anatomy in most cases. However, the rigid registration might not be sufficient to capture atypical anatomical morphologies, such as enlarged ventricles. Figure 4.8 C) shows the approximated deformation-free brain anatomies of the considered patients. The tumor is initialized as a smooth sphere with radius 2 voxels, centered at the center of the mass of the visible tumor. Since the time between the tumor onset and its detection is not known, and since different combinations of time dependent parameters, such as (D_w, ρ, T) , lead to the tumors with the same morphology (see Chapter 5 and [104]), the same parameters as are reported in the synthetic case are used, except the final time T , which is chosen manually.

The results of the model simulations for both cases are shown in Fig. 4.8 (D-F). The predicted tumor-induced deformations mimic the tumor deformations observed in the patients scans. In the case of Patient 1, the model correctly predicts the midline displacement, while for the Patient 2 it accurately reproduces the compression of the ventricles. Small deviations can be attributed to the discrepancies in the approximation of the initial, tumor-free anatomy. For instance, the ventricles in the frontal lobe of the Patient 2, appear smaller in the approximated initial anatomy, then in the patient's FLAIR and T1w MRI scans. Figure 4.8 (E-F) shows the estimated pressure distribution and the deformation field at the top of the patient's T1w MRI scan. The deformation field is most pronounced along the visible tumor outline, which confirms the correctness of the model prediction. The estimated pressure distribution closely follows the morphology of the visible tumor, with the highest pressure accumulation mainly in the tumor core close to the skull. Such predictions can be used to assess the extent of the disease in the patient current scan. The estimated regions with high pressure accumulation can be used to evaluate compression of critical nerves in such regions and to identify regions for pressure revealing surgery.

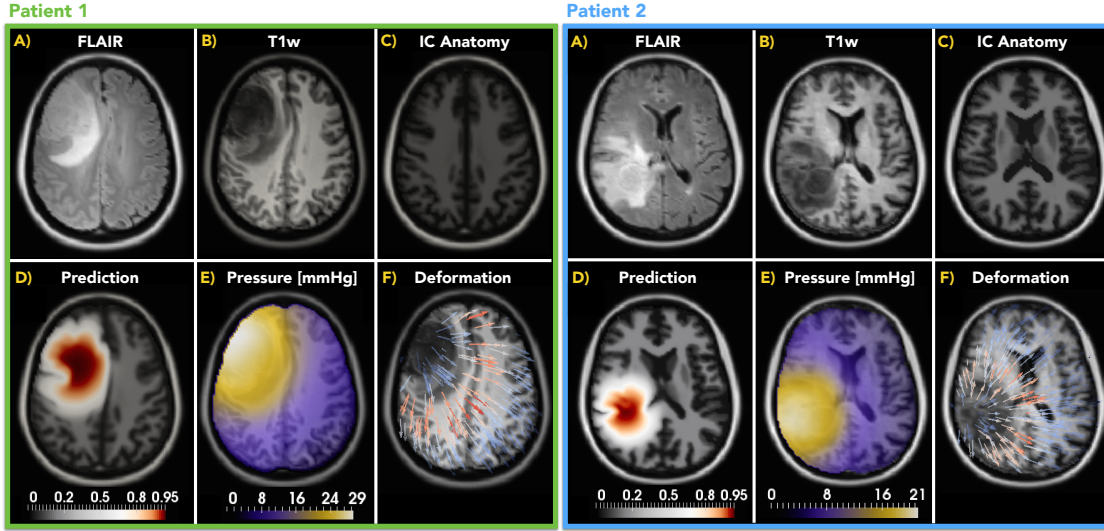


Figure 4.8: Tumor induced-brain deformations in two patients with HGG lesions. The actual patient scans are shown in (A-B) while the approximated tumor free-anatomy is displayed in (C). The predicted tumor and its mass-effect are depicted in (D). The subplots (E-F) show the simulated pressure distribution and the deformation field shown on the top of the patient's T1w MRI scan. The predicted brain deformations mimic the state of the disease visible in the patient's MRI scans. The pressure distribution and the deformation field is compatible with the visible tumor. For both patients, shown is slice across the tumor center of mass.

Clinical temporal data

To evaluate the capability of the model to predict the disease progression over time, we use patient scans acquired at two different time points, as shown in Fig. 4.9. The first time point shows the LGG lesion from the time of the tumor detection, whereas the second time point shows the tumor transition to HGG lesion. In the simulation, the scan from the first time point could be used to initialize the brain anatomy and the tumor. However, this poses two challenges: 1) It is not trivial to estimate the brain anatomy below the visible tumor; 2) The MRI scans show only tumor morphology, whereas the tumor cell density and the invisible tumor infiltration in the surrounding tissue are not known. These challenges complicate the initialization of the brain anatomy and the tumor. In Chapter 5 we present an approach for estimating tumor cell density from the multi-modal MRI and PET scans. However, since PET scan is not available for this patient, the model is initialized same as in the previous cases; the tumor is initialized as a sphere with radius 2 voxels centered at the center of mass of the visible tumor and the registration approach is used to approximate the deformation-free brain anatomy. This initialization also allows to evaluate the model predictions at two different time points. Since the aim of this example is to assess the model potential to predict disease progression, rather than providing exact time estimates, the simulation is performed with the same parameters as in the previous cases.

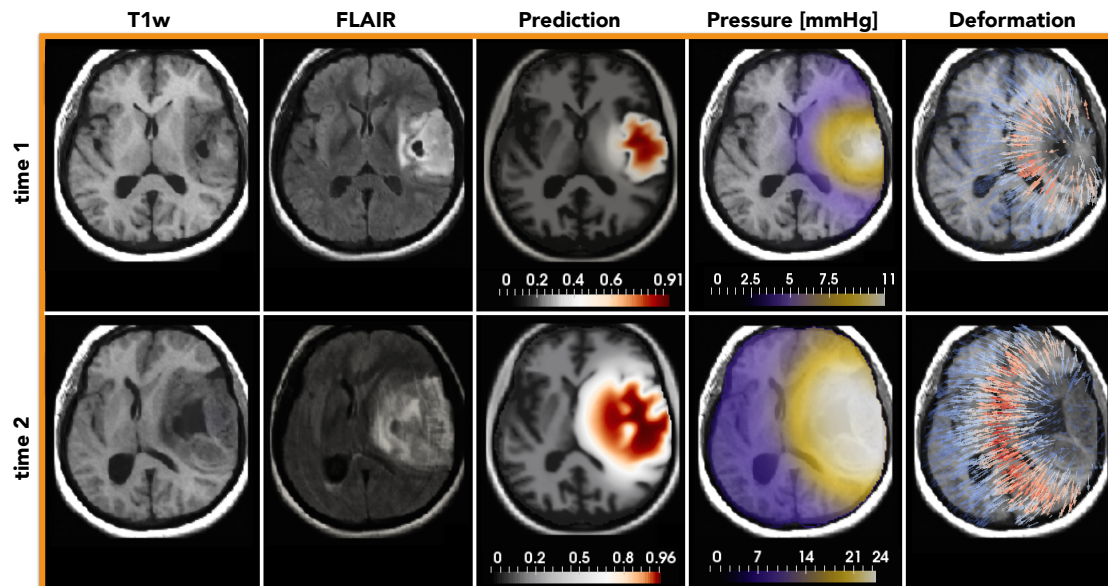


Figure 4.9: Tumor progression from LGG (the first row) to HGG (the second row). The first and the second column show the actual patient's scans, the third column presents the model predictions of the disease progression, while the pressure distribution and the deformation field, shown at the top of the patient's T1w scan, are displayed in the last two columns. The model accurately predicts low mass-effect in the first time point as well as compression of ventricles and midline shift visible in the second time point.

Figure 4.9 shows the results of the simulations, where the first time point corresponds to the simulation time $T = 200 [days]$ and the second time point to $T = 700 [days]$. The model accurately predicts a small tumor-mass effect at the first time point, which is consistent with the low-grade glioma visible on the patient's first scan. At the second time point, the model correctly estimates compression of the right ventricle and the midline displacement in the frontal lobe. The pressure distribution is compatible with the visible tumor, with high pressure accumulation in the tumor core along the skull.

The model, however, did not predict the swelling of the left ventricle visible at the second time point. Such enlargement of ventricles usually appears due to reduced brain perfusion, which can arise for various reasons. Since the model does not simulate brain perfusion, such deformations are not captured. Nonetheless, this example shows the model can provide long term predictions about disease progression, pressure distribution and the tumor transition from a low to a high grade state. Such model predictions can serve as an estimate of the worst case scenario of disease progression in the absence of treatment.

4.3 Summary

In this chapter, we have presented a computational model for tumor growth including the tumor-mass effect and the ICP distribution. The results serve as a proof-of-concept that the proposed deformation model can produce realistic tumor-induced brain deformations and ICP estimation. The model has the potential to assist clinical interventions by estimating the distribution of ICP in the patient scans without invasive interventions. The estimated pressure distribution enables the identification of regions with the highest pressure accumulation, which should be targeted by the surgery. Furthermore, the model can be used to estimate the worst case scenario of disease progression in the absence of treatment as well as critical symptoms arising from the compression of the vital nerves in regions with the high pressure accumulation. All tumor models presented in this chapter are available in the open-source software, called *GliomaSolver*, presented in Chapter 8.

PERSONALIZED MEDICINE

Most of the current medical treatment is based on standards-of-care which are derived from large population studies. Personalized medicine is a move away from this "one-size-fits-all" approach to a treatment tailored for the patient-specific conditions. Although the concept of personalized medicine is not new, and could be dated back to the time of Hippocrates, recent scientific progress has added another dimension to it. An interconnection of advances in high-performance computing, medical imaging, and mathematical modeling offers new possibilities for the personalized treatment.

Herein, we present how these approaches can be exploited in personalized radiotherapy planning. We start with an overview of the standard radiotherapy protocols and identify shortcomings that can be targeted by computational modeling. Afterward, we present a Bayesian machine learning framework for the calibration of the computational models from the patient's multimodal scans. The calibrated models are then used to estimate the tumor infiltration pathways, beyond the lesion outlines visible on the medical scans, to assist a personalized radiotherapy design. An initial clinical population study is used to demonstrate the benefits of the personalized radiotherapy plans over the standard protocols. Additional technical details are given in Appendix A.

5.1 Standard radiotherapy

The RT uses ionizing radiation – primarily x-rays or protons – to kill the cancer cells. High radiation damages the DNA of cells and thus impairs their ability to grow and reproduce. To prevent DNA repairs, the radiation dose is usually delivered in small daily fractions. The conventional schedule for brain lesions contains a total radiation dose of 60 Gy, distributed over 30 sessions with 2 Gy per session. To maximize the RT efficiency the whole tumor, including the

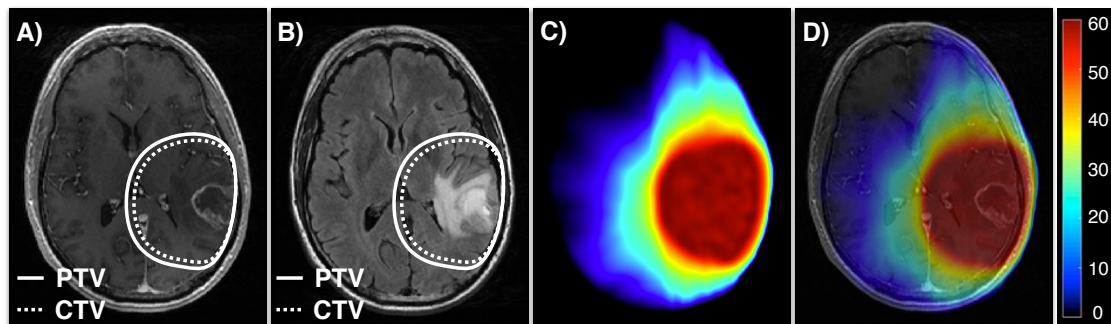


Figure 5.1: An illustration of a standard RT plan for a glioblastoma patient. The outlines of the PTV and CTV margin are shown on the preoperative A) T1Gd and B) FLAIR scans. The radiation dose distribution and its overlay with the T1Gd scan are displayed on C) and D), respectively.

invisible microscopic infiltration, should be irradiated. At the same time, as much as possible of the healthy tissue should be spare to reduce radiation toxicity. The target volume, i.e. the volume irradiated by the highest dose, consists of three co-centered volumes:

- *gross tumor volume (GTV)*: the visible tumor (including the resection cavity)
- *clinical target volume (CTV)*: GTV + margin,
- *planning target volume (PTV)*: CTV + margin.

The CTV margin accounts for the invisible microscopic tumor infiltration, while the PTV margin covers physiological movements such as breathing, uncertainties in the patient positioning and alignment of the therapeutic beams. The size of the margin strongly depends on the type of lesion. The compact tumors in the upper body are usually equipped with small CTV and large PTV – accounting for the breathing – while in the case of the infiltrative brain lesion it is the other way around. Here we focus on brain lesions while more general RT guidelines can be found in [191]. An illustration of RT plan for a glioma patient, including the target volumes and the dose distribution, is shown in Fig. 5.1. Since the brain tissue does not move much, the PTV margin is relatively small, usually between 0.3 to 0.5 cm [191]. Due to the infiltrative nature of the gliomas, the CTV margin is the most crucial but also the most controversial one. The size of the CTV margin varies by a few centimeters even across the official RT guidelines [133]: the European Organization for Research and Treatment of Cancer (EORTC) suggests 2 – 3 cm margin [67]; the Radiation Therapy Oncology Group (RTOG) recommends 2 cm [170]; while several trials from the New Approaches to Brain Tumor Therapy (NABTT) consortium used as small margin as 0.5 cm [117]. Moreover, a recent survey [52] showed that approximately half of the centers use hospital-specific RT guidelines. In principle, the same patient might receive very different treatment; depending on the country or hospital of the treatment.

Besides the large variation in the size of the CTV margin, standard RT protocols bear other

shortcomings. Since the glioma growth is highly anisotropic, constrained by the patient anatomy, a uniform margin very likely does not provide an optimal dose distribution. Moreover, glioma invasiveness is highly patient-specific, and thus not all patients benefit equally from the same margin, which impairs comparison and advancement of RT protocols.

Despite treatment, almost all HGGs recur [141]. Biopsies [163] and post-mortem studies [67] showed that tumor cells can invade even beyond the CTV margin, which reduces RT efficiency and is a possible cause of recurrence. At the same time, radioresistance of tumor cells inside the CTV can further reduce the RT efficiency. Radioresistance tends to occur in regions with complex microenvironment and hypoxia [148], both of which are commonly encountered in areas of high tumor cellularity. To address tumor radioresistance, several studies have suggested local dose-escalations [39, 148, 182]. In these approaches, a boosted dose is delivered into a single or multiple co-centered regions defined by adding uniform margins to the tumor outlines visible in MRI scans [77]. Although a uniform margin might not be an optimal choice, the RTOG phase-I-trial [182] showed an increase in median survival of 8 months with dose-escalation. However, no benefit in progression-free survival was observed, indicating a complex relationship between the true progression of the underlying disease and the tumor extent visible in MRI scans.

Alternatively, PET scans can be used to identify radioresistant regions. As shown in Section 2.3, the FET tracer is a promising HGG marker [146], whose uptake values have been shown to be proportional to tumor cell density, although the constant of proportionality is unknown and patient-specific [83, 167]. A prospective phase-II-study [141] demonstrated that dose-escalation based on FET-PET enhancement delineates the tumor structure better than uniform margins, thus leading to lower radiation toxicity. Still, the FET-PET based dose-escalation did not increase progression-free survival. One possible explanation is that PET enhances mainly the tumor core, which is usually resected, while the PET uptake values in the remaining tumor periphery coincide with the baseline signal from the healthy tissue. This, together with a rather low resolution of PET scans, limits their ability to fully detect the radioresistant tumor residuals. This is also consistent with our findings presented in Section 5.3.

Standard RT plans can be improved by incorporating information from computational tumor models. These models, calibrated against patient medical scans, provide estimates of tumor infiltration that extend the information available in medical images. Such estimates offer an advantage in determining the CTV margins as well as regions for dose escalation and thus provide a non-invasive tool for the rational design of improved, personalized RT plans.

5.2 Bayesian model calibration

Hitherto, several calibration strategies for tumor growth models were developed [68, 71, 86, 92, 99, 119, 147, 183]. Despite the extensive effort, a translation of the computational models into clinical practice remains very limited. We postulate that there are (at least) three translational weakness:

1) Most model calibrations rely on data not commonly available in clinical practice. For example, in [68, 71, 86, 92, 99, 119, 147] medical scans with visible tumor progression from at least two time points are used for the model calibration. However, for HGG patients only scans acquired at single preoperative time point are available. 2) Models are based on simplified assumptions motivated by *in-vitro* studies. For instance, it is frequently assumed that the tumor cell density is constant along the tumor borders visible on MRI scans (e.g., [68, 71, 86, 92, 99, 147, 183]). However, the tumor cell density varies significantly along the visible lesion borders due to anatomical restrictions and anisotropic tumor growth. 3) Even if advanced calibration techniques as in [119] are used, it is not clear how robust the model predictions are and what benefits they offer over the standard treatment protocols.

Here, we address these translational issues and provide clinically relevant calibration of tumor growth models for a personalized RT design. We present a Bayesian machine learning framework to calibrate tumor growth models from multimodal medical scans. We show that integration of information from complementary structural MRI and functional FET-PET metabolic maps enables the robust inference of the tumor cell densities from scans acquired at a single time point. To the best of our knowledge, this is the first study making joint use of FET-PET and MRI scans for the patient-specific calibration of a tumor growth model. Our Bayesian approach infers modeling and imaging parameters under uncertainties arising from measurement and modeling errors. We propagate these uncertainties through the computational tumor model to obtain robust estimates of the tumor cell density together with credible intervals that can be used for personalized RT design, as shown in Section 5.3.

5.2.1 Image-based model calibration

The proposed Bayesian framework combines a *deterministic model* M_u describing tumor growth with a *stochastic imaging model* $M_{\mathcal{I}}$ which relates the model predictions with tumor observations available from the patient medical scans. Bayes theorem is used to estimate the probability distribution of the unknown parameters of both models, accounting for modeling and measurement uncertainties. Identified parametric uncertainties are propagated to obtain robust patient-specific tumor predictions. An overview of the framework is given in Fig. 5.2.

Tumor growth model

Although, computational tumor growth models of various complexity can be calibrated by the proposed Bayesian framework, here we follow the Occam's razor principle and pick the simplest model that is sufficient to describe the tumor proliferation and infiltration in the patient anatomy. Thus, the FK equation is used to describe the model M_u . For the details about the FK model see Section 4.1. The model M_u has six parameters $\theta_u = \{D_w, \rho, T, ic_x, ic_y, ic_z\}$, which are assumed unknown and patient-specific. An overview of the model M_u and its parameters is shown in Fig. 5.2 (II. A-C).

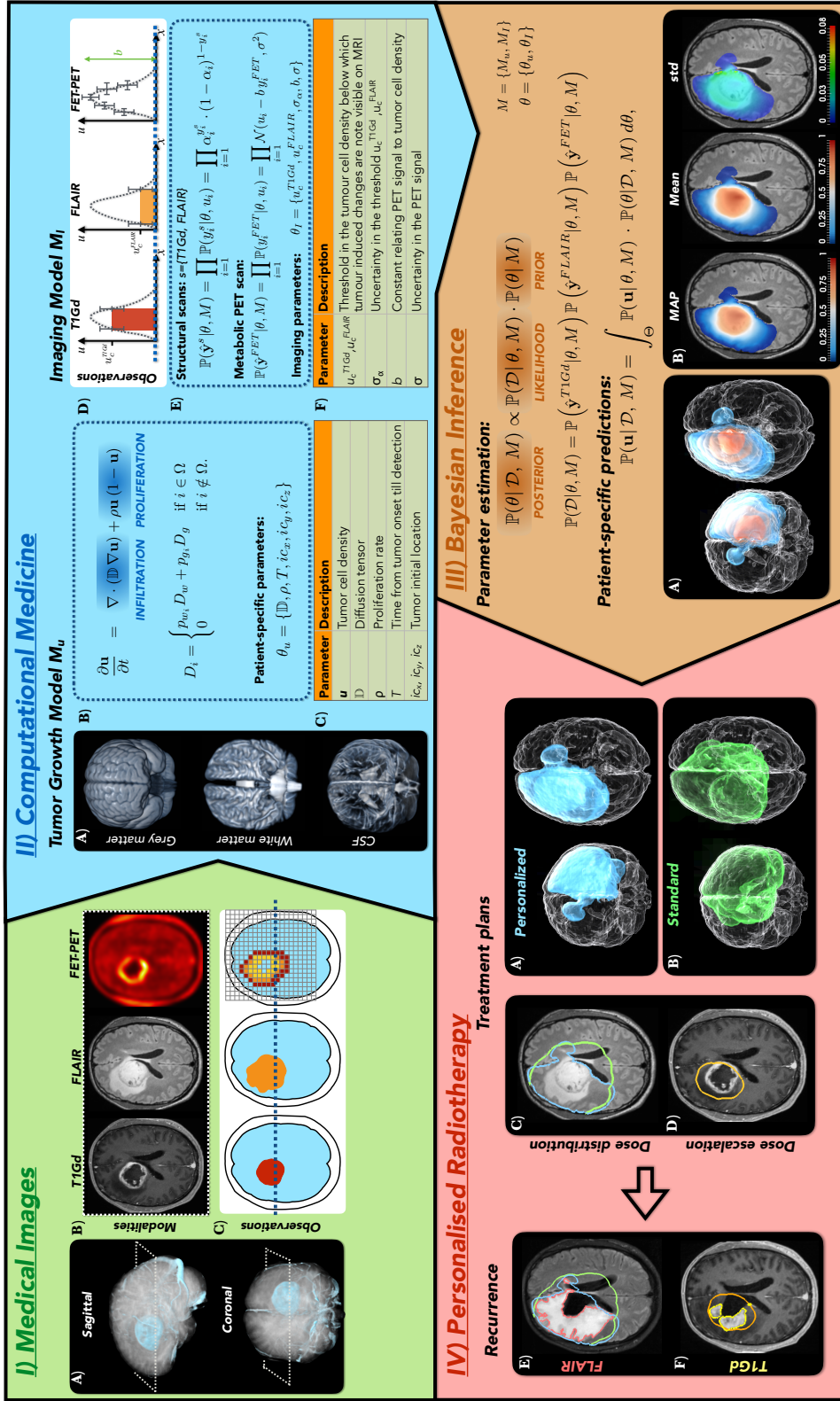


Figure 5.2: Overview of the inference framework. **D Medical images** show preoperative patient scans: (I.A) 3D reconstruction of T1Gd images and (I.B) slices across all modalities. Tumor observations (e.g., segmentations) extracted from each modality are illustrated in (I.C). **II Computational medicine** includes a tumor growth model M_u (II.A), which simulates tumor evolution in the patient anatomy (II.A), and imaging model M_I (II.B) which relates the image observations with the modeled tumor cell density u . Subplot (II.D) shows a schematic representation of the actual tumor cell density along the dashed line shown in (I.C) and its relation to each tumor observation available from the medical scans. The unknown, patient-specific parameters for each model are listed in Tables (II.C,F). **III Bayesian inference** is used to identify the probability distributions of the unknown parameters, accounting for the modeling and measurement uncertainties. Parametric uncertainties are then propagated to obtain robust predictions about patient-specific tumor cell densities. The most probable tumor cell density, given by the maximum a posteriori (MAP) estimate, is shown in (III.A,B), while the mean and standard deviation (std) are shown in (III.B). **IV Personalized Radiotherapy** uses the patient-specific predictions to improve dose-distribution and escalation design. A comparison of a standard and personalized dose distributions is shown in (IV.A-C). The regions of estimated high tumor cell densities are marked by the orange isocount in (IV.D,F). Observed tumor recurrences in T1Gd and FLAIR, marked by the pink and yellow curves in (IV.E,F), are used to compare the treatment plans. The personalized plan spares more healthy tissue, while achieving tumor coverages comparable to the standard protocol and guides the design of personalized dose escalation plans.

Multimodal imaging model

For the model calibration, we consider routinely acquired T1Gd and FLAIR MRI scans in combination with FET-PET maps. A stochastic imaging model $M_{\mathcal{G}}$ is designed to relate model predictions of the tumor cell density \mathbf{u} and the tumor observations $\mathcal{D} = \{\hat{\mathbf{y}}^{T1Gd}, \hat{\mathbf{y}}^{FLAIR}, \hat{\mathbf{y}}^{FET}\}$ available from the medical scans. Here, $\hat{\mathbf{y}}$ denotes a vector of tumor observations obtained from a certain image modality, y_i is an entry in $\hat{\mathbf{y}}$ and i enumerates all N voxels in the given image. A voxel i corresponds to the same location (i_x, i_y, i_z) in each scan and the simulation domain Ω_1 . See Fig. 5.2 for an overview of all the imaging modalities (I.B), corresponding tumor observations (I.C) and their relation to tumor cell density \mathbf{u} (II.D).

The MRI scans provide morphological information about the visible tumor in the form of binary segmentations. The segmentation $\hat{\mathbf{y}}^s, s \in \{T1Gd, FLAIR\}$ assigns a label $y_i^s = 1$ to each voxel with visible tumor and $y_i^s = 0$ otherwise. The probability of observing a segmentation $\hat{\mathbf{y}}^s$ with a simulated tumor cell density \mathbf{u} is modeled by a Bernoulli distribution [119]:

$$\mathbb{P}(\hat{\mathbf{y}}^s | \theta, \mathbf{M}) = \prod_{i=1}^N \mathbb{P}(y_i^s | \theta, u_i) = \prod_{i=1}^N \alpha_i^{y_i^s} \cdot (1 - \alpha_i)^{1-y_i^s}. \quad (5.1)$$

Here α_i is the probability of observing the tumor in the MRI scan and it is assumed to be a double logistic sigmoid:

$$\alpha_i(u_i, u_c^s) = 0.5 + 0.5 \cdot \text{sign}(u_i - u_c^s) \left(1 - e^{-\frac{(u_i - u_c^s)^2}{\sigma_\alpha^2}} \right), \quad (5.2)$$

where u_c^s denotes an unknown cell density threshold below which tumor cells are not visible in the MRI scan, while the term σ_α^2 represents uncertainty in u_c^s . The parameters $\{\theta_{\mathcal{G}^{T1Gd}}, \theta_{\mathcal{G}^{FLAIR}}\} = \{u_c^{T1Gd}, u_c^{FLAIR}, \sigma_\alpha^2\}$ are assumed unknown and patient-specific.

The FET-PET signal is proportional to tumor cell density with an unknown constant of proportionality [83, 167]. Let $\hat{\mathbf{y}}^{FET}$ be the normalized FET-PET signal after subtracting the patient-specific baseline signal from healthy tissue i.e., $y_i^{FET} \in [0, 1]$ and b is the corresponding constant of proportionality. We assume that y_i^{FET} can be related with the modeled tumor cell density u_i as

$$y_i^{FET} = \frac{1}{b} u_i + \varepsilon, \quad (5.3)$$

where ε is prediction error accounting for modeling and measurement uncertainties. Because of the noisy nature of the PET scan, the error term is assumed to follow a normal distribution $\varepsilon \sim \mathcal{N}(0, \sigma^2)$. The probability of observing the PET signal $\hat{\mathbf{y}}^{FET}$ with the simulated tumor cell density \mathbf{u} is then modeled as

$$\mathbb{P}(\hat{\mathbf{y}}^{FET} | \theta, \mathbf{M}) = \prod_{i=1}^N \mathbb{P}(y_i^{FET} | \theta, u_i) = \prod_{i=1}^N \mathcal{N}\left(y_i^{FET} - \frac{1}{b} u_i, \sigma^2\right). \quad (5.4)$$

The PET scan, acquired at 4 mm resolution, is registered to the MRI scans with 1 mm resolution. To justify the product in Eq. (5.4), only voxels separated by distance 4 mm are used. The parameters $\theta_{\mathcal{G}^{FET}} = \{b, \sigma\}$ are unknown and patient-specific. An overview of the imaging model $M_{\mathcal{G}}$ and its parameters is shown in Fig. 5.2 (II. D-F).

5.2.2 Parameters estimation and uncertainty propagation

The parameters $\theta = \{\theta_u, \theta_{\mathcal{J}}\}$ of the model $M = \{M_u, M_{\mathcal{J}}\}$ where $\mathcal{J} = \{\mathcal{J}^{TIGd}, \mathcal{J}^{FLAIR}, \mathcal{J}^{PET}\}$, are assumed unknown and a probability distribution function (PDF) is used to quantify their plausible values. A *prior* PDF $\mathbb{P}(\theta|M)$ is used to incorporate any prior information about θ . Bayesian model calibration updates this prior information based on the available data \mathcal{D} . The updated *posterior* PDF is computed by the Bayes theorem:

$$\mathbb{P}(\theta|\mathcal{D}, M) \propto \mathbb{P}(\mathcal{D}|\theta, M) \cdot \mathbb{P}(\theta|M), \quad (5.5)$$

where $\mathbb{P}(\mathcal{D}|\theta, M)$ is the *likelihood* of observing data \mathcal{D} from the model M for a given value of θ . Since each of the medical scans captures a different physiological process, the tumor observations are assumed independent and the likelihood function can be expressed as:

$$\mathbb{P}(\mathcal{D}|\theta, M) = \mathbb{P}(\hat{\mathbf{y}}^{TIGd}|\theta, M) \cdot \mathbb{P}(\hat{\mathbf{y}}^{FLAIR}|\theta, M) \cdot \mathbb{P}(\hat{\mathbf{y}}^{PET}|\theta, M).$$

The prior PDF is assumed uniform with details specified in Appendix A. Since an analytical expression for Eq. (5.5) is not available, sampling algorithms are used to obtain samples $\theta^{(l)}$, $l \in \{1, \dots, S\}$ from the posterior $\mathbb{P}(\theta|\mathcal{D}, M)$. We use Transitional Markov Chain Monte Carlo (TMCMC) algorithm [32] which iteratively constructs series of intermediate PDFs:

$$\mathbb{P}_j(\theta|\mathcal{D}, M) \sim \mathbb{P}(\mathcal{D}|\theta, M)^{p_j} \cdot \mathbb{P}(\theta|M), \quad (5.6)$$

where $0 = p_0 < p_1 < \dots < p_m = 1$ and $j = \{1, \dots, m\}$ is a generation index. The term p_j controls the convergence of the sampling procedure and is computed automatically by the TMCMC algorithm. TMCMC method constructs a large number of independent chains that explore parameter space more efficiently than traditional sampling methods [32] and allow parallel execution. We use a highly parallel implementation of the TMCMC algorithm provided by the $\Pi 4U$ framework [64]. The inferred parametric uncertainties are propagated through the model M to obtain robust predictions about \mathbf{u} given by:

$$\mathbb{P}(\mathbf{u}|\mathcal{D}, M) = \int_{\Theta} \mathbb{P}(\mathbf{u}|\theta, M) \cdot \mathbb{P}(\theta|\mathcal{D}, M) d\theta, \quad (5.7)$$

or by simplified measures such as the mean $\mu_{\mathbf{u}} = E[\mathbf{u}(\theta)] \equiv m_1$ and variance $\sigma_{\mathbf{u}}^2 = E[\mathbf{u}^2(\theta)] - m_1^2 \equiv m_2 - m_1^2$ derived from the first two moments m_k , $k = 1, 2$:

$$m_k = \int_{\Theta} (\mathbf{u}(\theta|M))^k \cdot \mathbb{P}(\theta|\mathcal{D}, M) d\theta \approx \frac{1}{S} \sum_{l=1}^S \left(\mathbf{u}(\theta^{(l)}|M) \right)^k,$$

where Θ is the space of all unknown parameters. The most probable tumor cell density estimate is given by the maximum a posteriori (MAP) defined as $\mathbf{u}^{MAP} = \operatorname{argmax}_{\theta} \mathbb{P}(\mathbf{u}|\mathcal{D}, M)$.

5.2.3 Sensitivity study

To test the sensitivity of the inference and to illustrate the role of multimodal image information, the proposed Bayesian framework is first applied to synthetic data. The model M_u is used to generate a 3D synthetic tumor in brain anatomy obtained from [37] using the parameters reported in Table 5.1. A 2D slice of the simulated ground-truth (GT) tumor cell density is shown in Fig. 5.3 (A). The synthetic T1Gd and FLAIR tumor segmentations are constructed by thresholding the GT tumor cell density at $u_c^{T1Gd} = 0.7$ and $u_c^{FLAIR} = 0.25$. The FET-PET signal is designed by taking the GT tumor cell density within the T1Gd and FLAIR segmentations, adding Gaussian noise with zero mean and standard deviation (std) σ , and normalizing the result. The value of σ is chosen as the average std of the FET signal from the healthy brain tissue. The generated synthetic image observations are shown in Fig. 5.3 (B).

A sensitivity study for the number of samples is performed, indicating that 6000 samples is adequate for the model. The manifold of the inferred probability distribution is presented in Fig. 5.4 and the calibrated parameters are given in Table 5.1. As seen from the probability distribution manifold, the tumor observations from a single time point do not contain enough information to infer time dependent parameters (D_w, ρ, T) exactly, since different combinations of these parameters can generate the same tumor cell density as shown in Fig. 5.5. The lack of identifiability of (D_w, ρ, T) poses a challenge for calibration approaches searching only for a single value of θ . Instead, Bayesian calibration provides a fairer estimate; the inferred probability distribution identifies a strong correlation between the parameters (D_w, ρ, T) , while the high std values imply low confidence in these parameters. On the other hand, parameters that affect the tumor spatial pattern, e.g. (ic_x, ic_y, ic_z) , are identified with high accuracy, which is reflected by their low std. The image related parameters $(u_c^{T1Gd}, u_c^{FLAIR}, b, \sigma)$ are slightly overestimated due to the assumed correlation length and the effect of the complex brain anatomy. The role of the anatomy is discussed further in Appendix A.

The inferred parametric uncertainties are propagated to obtain robust posterior predictions about the tumor cell density shown in Fig. 5.3 (C-E). Despite the large parametric uncertainties, the MAP and mean tumor cell density estimates are almost indistinguishable from the GT tumor. The low std values imply that using our Bayesian formulation, the information contained in

	D_w	ρ	T	ic_x	ic_y	ic_z	σ	b	u_c^{T1Gd}	u_c^{FLAIR}	σ_α^2
GT	0.1300	0.0250	302.00	80.64	171.52	128.00	0.0230	0.8800	0.7000	0.2500	-
MAP	0.1226	0.0296	271.13	80.61	171.55	127.92	0.0280	0.9884	0.8440	0.4874	0.0502
mean	0.1543	0.0361	253.85	80.64	171.47	127.80	0.0294	0.9775	0.8325	0.4841	0.0505
std	0.0530	0.0125	107.59	0.1280	0.1024	0.2048	0.0022	0.0139	0.0132	0.0076	0.0004

Table 5.1: Results of the Bayesian calibration for the synthetic case generated with the ground truth (GT) values. Reported is maximum a posteriori (MAP), mean and standard deviation (std). The units are $D_w \sim mm^2/day$; $\rho \sim 1/day$; $T \sim day$; and $ic_x, ic_y, ic_z \sim mm$.

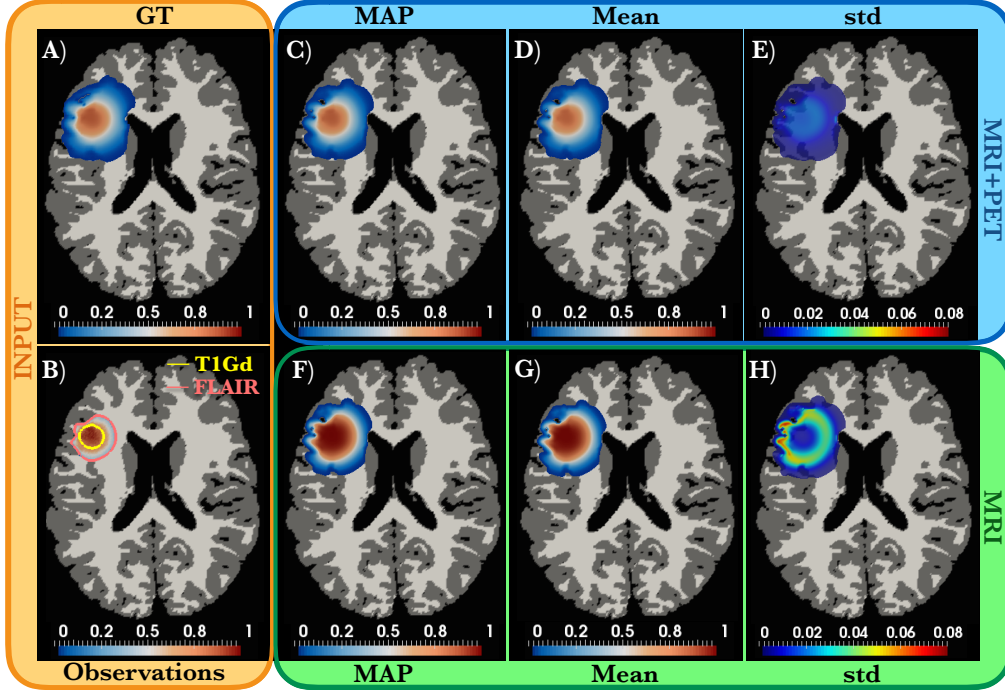


Figure 5.3: Synthetic test case. **Orange box:** A 2D slice of the synthetic ground truth (GT) tumor cell density (A) and corresponding image observations (B): the normalized FET-PET signal with additive noise (red-blue color scale) and the outlines of the T1Gd (yellow) and FLAIR (pink) binary tumor segmentations. **Blue box:** Results of the Bayesian calibration with multimodal data. The results are in close agreement with GT data. **Green box:** Calibration results using only the MRI data, which do not provide enough information to recover the tumor cell density profile correctly.

multimodal data is sufficient to infer tumor cell density from single time point scans.

For comparison, if the model calibration is performed only with the MRI data, i.e. $\mathcal{D} = \{\hat{\mathbf{y}}^{T1Gd}, \hat{\mathbf{y}}^{FLAIR}\}$, the estimated tumor cell densities – shown in Fig. 5.3 (F-G) – deviate from the GT tumor mainly in the central part of the lesion, which is also consistent with the regions of high std shown in Fig. 5.3 (H). Nonetheless, the outlines of the predicted tumor are similar to those of the GT tumor. This is because the tumor morphology is mainly constrained by the MRI data since the FET-PET signal coincides with the baseline signal of the healthy tissue in the regions of lower tumor infiltration. On the other hand, the FET-PET signal constrains the tumor cell density profile in the regions of high tumor infiltration. This highlights the importance of integrating structural and functional image information for the model calibration when dealing with single time point data.

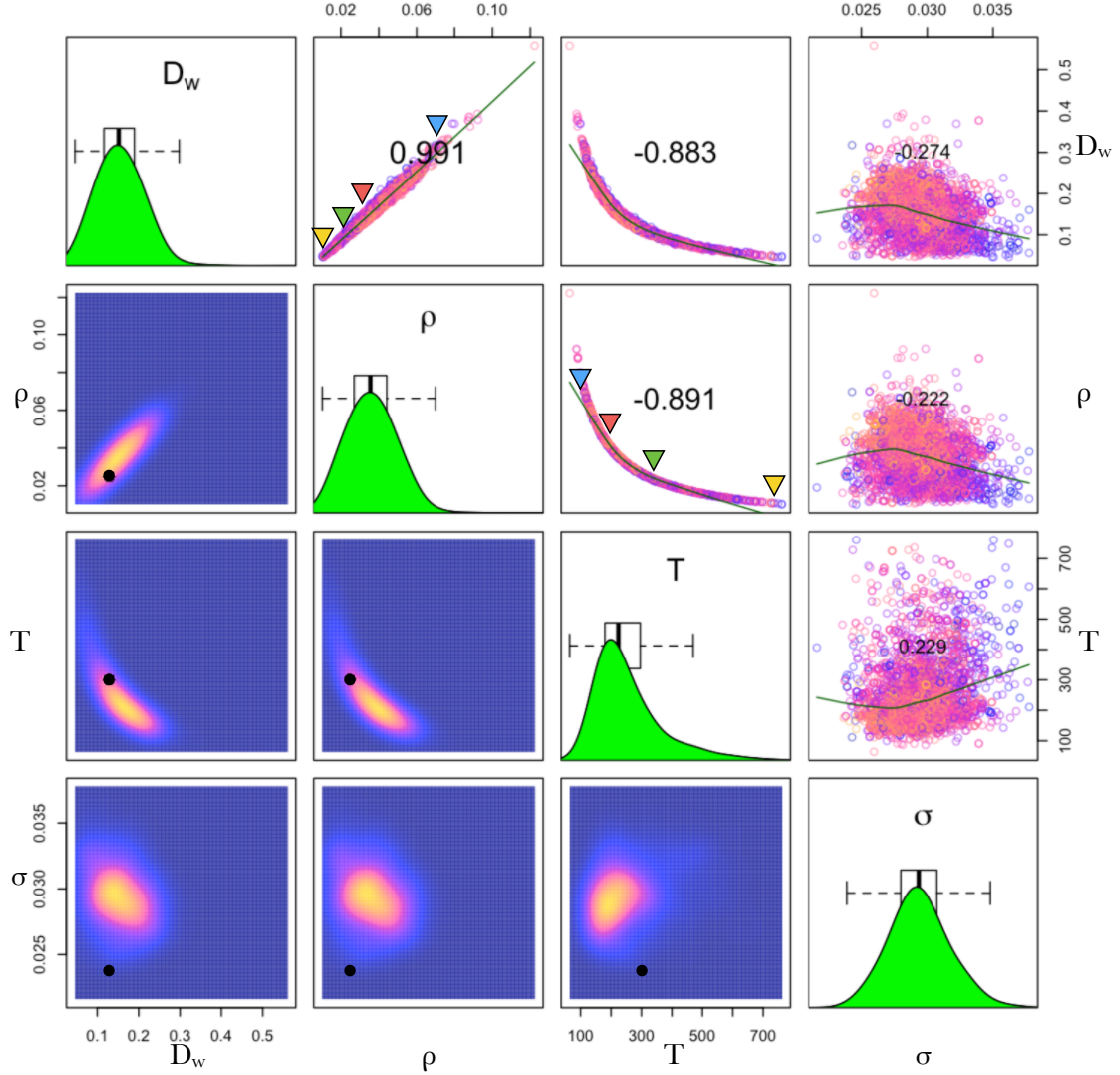


Figure 5.4: The results of the Bayesian calibration for the synthetic case. **Above the diagonal:** Projection of the TMCMC samples of the posterior distribution $\mathbb{P}(\theta|\mathcal{D}, M)$ in 2D space of the indicated parameters. The colors indicate likelihood values of the samples. The number in each plot shows the Pearson correlation coefficient between the parameter pairs. The colored triangles mark the four selected parameters used in Fig. 5.5. **Diagonal:** Marginal distributions obtained with Gaussian kernel estimates. Boxplot whiskers demarcate the 95% percentiles. **Below the diagonal:** Projected densities in 2D parameter space constructed by 2D Gaussian kernel estimates. The black dots mark the values used to generate the synthetic data.

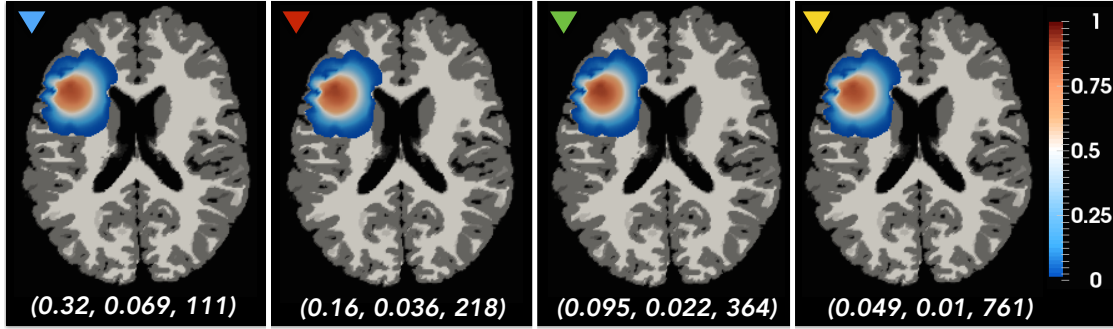


Figure 5.5: Insensitivity of the tumor cell density to the speed of the growth. Shown are slices of the tumor cell densities computed with different combinations of parameters (D_w, ρ, T) as listed at the bottom of each plot. These correspond to the colored triangles in Fig. 5.4. Despite significant variation in the parameter values, all combinations lead to very similarly-appearing tumors. In the absence of temporal information, the time dependent parameters are not identifiable, since the model calibration cannot distinguish between compensating effects among the parameters affecting the dynamics. As shown here, tumors with similar D_w/ρ and $T \cdot \rho$ values appear very similar to one another (here $D_w/\rho \approx 4.5$, $T \cdot \rho \approx 7.7$). Hence, the Bayesian calibration identifies the probability distribution of all the plausible values.

5.3 Personalized radiotherapy

The proposed Bayesian calibration framework is applied to clinical data to infer patient-specific tumor cell densities, which are in turn used for personalized RT design. Tumor recurrence patterns are used to compare the proposed and standard RT plans. The software and data used in this paper are publicly available¹, while the details about the software are presented in Chapter 8.

5.3.1 Patient-specific predictions

A retrospective clinical study is conducted on 8 patients diagnosed with glioblastoma (GBM). Scans of the patients *P1-P8* are shown in Fig. 5.6 while the details about acquisition protocols and image processing are reported in Appendix A. All patients received the standard treatment; surgery followed by combined radio- and chemotherapy [170]. There was no visible tumor after the treatment and patients were regularly monitored for recurrence. The preoperative scans, shown in Fig. 5.6 (A-D), are used for the Bayesian inference. The calibrated parameters are reported in Table A.1 in Appendix A and the robust posterior predictions about the tumor cells densities of each patient are shown in Fig. 5.6 (E-G). These patient-specific predictions provide estimates about the possible tumor cell migration pathways in the surrounding of the visible tumor, constrained by the patient anatomy and the available tumor observations.

¹ <https://github.com/JanaLipkova/GliomaSolver>

The predicted tumor infiltration pathways can be validated by the patterns of the first detected tumor recurrence shown in Fig. 5.6 (H), where the outlines of the predicted infiltrations (blue) and recurrence tumors (pink) are depicted. For patients $P5, P7, P8$ the model accurately predicts tumor infiltration also inside the healthy-appearing collateral hemisphere, whereas for cases $P1-P4$ the tumor predictions are correctly restricted only to one hemisphere. Moreover, despite a similar appearance of the preoperative tumors in patients $P1$ and $P2$, the model correctly predicts more infiltrative behavior for the patient $P1$, which is consistent with the recurrence pattern. The high confidence in the predictions is reflected by low std shown in Fig. 5.6 (F).

5.3.2 Clinical study

The patient-specific tumor cell density predictions can be used to design margins of the CTV and to identify high cellularity regions that could mark areas of increased radioresistance. The personalized RT plan can be based either on *the most probable scenario* given by MAP estimate or *the worst case scenario* given as a sum of the mean and std of the tumor cell density. Since in the presented study, the mean and MAP estimates are very similar, and the std values are small, the MAP estimates are used. An overview of the proposed personalized RT design is shown in Fig. 5.2 (IV), while the details are described in the following subsections. The tumors recurrence patterns are used to assess the benefits of the proposed RT plan over the standard treatment protocol. For evaluation purposes, all recurrence scans are registered to the preoperative anatomy. To prevent registration errors arising from mapping the anatomy with the resection cavity to the preoperative brain, rigid registration is used. This provides a sufficient mapping for most cases, however, it cannot capture the post-treatment tissue displacement around the ventricles as seen in patients $P7-P8$; making the mapping less accurate in these regions. The design of methods that provide robust registration between pre- and post-operative brain anatomies is still an open problem.

Dose distribution

An ideal CTV covers all the residual tumor, including infiltrating tumor cells that are invisible on the pretreatment imaging scans, while sparing healthy tissue. We use the tumor recurrence pattern to evaluate the efficiency (η^{CTV}) of the CTV, defined here as the relative volume of the recurrence tumor (V^{REC}) contained within the CTV:

$$\eta^{CTV} = \frac{|V^{REC} \cap CTV|}{V^{REC}} \times 100\%. \quad (5.8)$$

Figure 5.6 (H) shows the FLAIR scans with the first detected tumor recurrence outlined by the pink lines. The margin of the administered CTV^{RTOG} , designed by the standard RTOG protocol with a 2 cm margin around the visible tumor, is marked by the green lines in (E,F,H). The personalized CTV, referred to as CTV^{MAP} , is constructed by thresholding the MAP tumor cell density at $u = 0.1\%$ for all patients. This value was chosen so that the efficiency of the

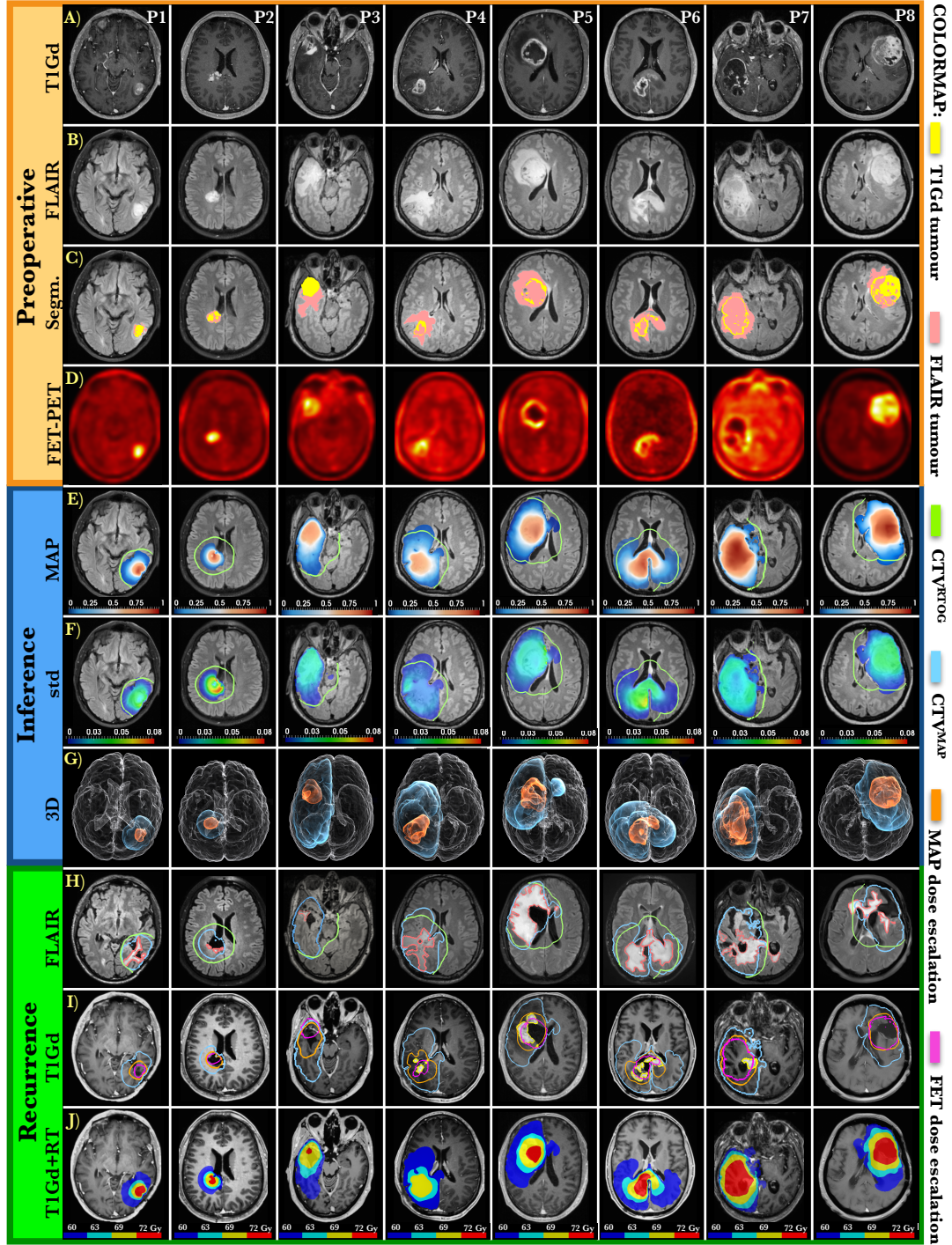


Figure 5.6: Results of the Bayesian calibration for patients $P1$ - $P8$. **Orange box:** Preoperative scans showing (A) T1Gd; (B) FLAIR; (C) Tumor segmentations: T1Gd (yellow) and FLAIR (pink); (D) FET-PET. **Blue box:** (E) MAP and (F) std of the inferred tumor cell densities shown in the preoperative FLAIR scans. The CTV^{RTOG} margin is shown as the green curves. (G) The 3D reconstructions show outlines of the MAP tumor (blue) together with tumor extent visible on the FET-PET scans (orange) in the preoperative anatomy (white). **Green box:** Scans of the first detected tumor recurrence. (H) FLAIR tumor recurrence (pink), CTV^{RTOG} (green), and CTV^{MAP} (blue) margins. (I) T1Gd tumor recurrence (yellow) and the dose-escalation outlines proposed by FET enhancement (magenta) and MAP estimates (orange). (J) Multilevel dose-escalation designed by MAP estimates.

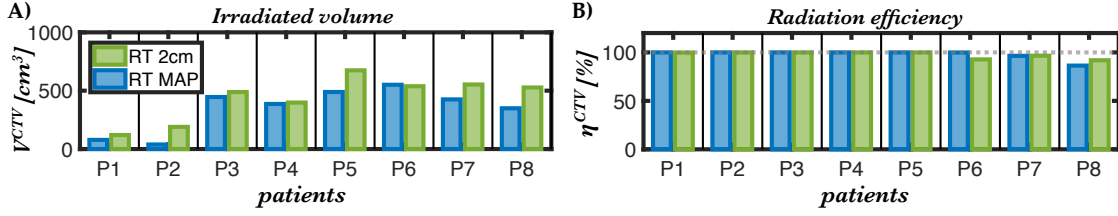


Figure 5.7: A comparison of the RT plan based on the RTOG protocol (green) and MAP estimates (blue). (A) The overall irradiated volume V_{CTV} and (B) the corresponding efficiency η_{CTV} . The CTV^{MAP} uses a smaller irradiation volume while having a comparable efficiency as the CTV^{RTOG} .

CTV^{MAP} is comparable to that of the CTV^{RTOG} . The outlines of the proposed CTV^{MAP} are shown as the blue isocontours in Fig. 5.6 (H-I). A visual comparison of the CTVs shown in Fig. 5.6 (H) and Fig. 5.2 (IV), and a quantitative comparison presented in Fig. 5.7, show that the proposed personalized plans spare more healthy tissue, hence reducing radiation toxicity while maintaining the efficiency of the standard RTOG protocol. Both plans show reduced efficiency for patients P7-P8, mainly around the ventricles, which may be caused by a misalignment between the preoperative and recurrence anatomies.

These preliminary results imply that the regions predicted as a tumor-free by the model, remain tumor-free and thus the model predictions have the potential to guide personalized CTV design. The standard or hospital-specific protocols can be updated by the model predictions to spare brain tissue not infiltrated by the tumor. This can lead to significant savings in the healthy tissue, especially in the cases of large lesions or lesions close to hemispheres separation and other anatomical constraints.


Dose escalation

No dose-escalation plan for HGG patients has been yet approved by phase-III-clinical trials. Here, we present a theoretical comparison of two escalation plans targeting high tumor cellularity regions identified by: 1) FET-PET enhancement as proposed in [141] and 2) MAP estimates. We evaluate the efficiency of an escalation plan by its capability of targeting T1Gd-enhanced tumor recurrence regions. In these regions, the recurrent tumor has high cellularity, despite having received the full radiation dose, suggesting tumor radioresistance. Figure 5.6 (I) shows the T1Gd scans with the first detected tumor recurrence. The margins of the T1Gd-enhanced tumor recurrence are marked by the yellow lines, while the outlines of the dose-escalation plans designed by the FET-PET enhancements are shown in magenta. The FET enhancements do not fully cover the T1Gd recurrent tumor in patients P4-P7, providing a possible explanation for why improvements in progression-free survival have not been observed in [141]. In comparison, the MAP estimates, calibrated by the FET-PET signal, extend the information about the tumor cell density in the periphery of the visible lesion. Figure 5.6 shows two possible dose-escalation

plans based on the inferred MAP tumor cell density: (*I*) a single-level dose-escalation based on the thresholded MAP solution with threshold $u = 30\%$ marked by the orange lines and (*J*) a cascaded four-level escalation plan constructed by thresholding the MAP tumor cell density at $u = [0.1, 25, 50, 75]\%$. The optimal design of a personalized dose-escalation plan would require more extensive studies. However, these preliminary results show that the inferred high cellularity regions coincide with the areas of tumor recurrence better than those suggested by the FET-PET enhancement alone. The Bayesian inference framework developed here thus provide a promising tool for rational dose-escalation design.

5.4 Summary

In this chapter, we have demonstrated how the synergy of computational modeling, high-performance computing, and medical imaging can lead to improved, personalized RT design for infiltrative brain lesions. We combined patient structural and metabolic scans from a single time point with a computational tumor growth model through a Bayesian inference framework and predicted the tumor distribution beyond the outlines visible in medical scans. The patient-specific tumor estimates can be used to design personalized RT plans, targeting shortcomings of standard RT protocols. The software and data used in this work are publicly released² to facilitate translation to clinical practice and to encourage future improvements. More details about the software are presented in Chapter 8. In the future, the Bayesian framework developed here could also be extended to predict individual patient responses to RT by incorporating data obtained during the course of treatment as done in [177], in which non-spatial tumor models were used. In this way, the treatment can be further improved by adaptively refining the RT plans based on the predicted patient responses. Moreover, the basic FK tumor growth model could be replaced by a Fokker-Planck diffusion model [174], which would not increase the number of unknown parameters or affect the computational complexity significantly, but might provide a better description of biological diffusion. Future work could also incorporate more advanced models, such as [195], that account for cancer stem cells, their progeny and nonlinear coupling between the tumor and the neovascular network. However, it remains to be seen whether scans acquired at a single time point would provide enough information to calibrate the advanced models sufficiently. If not, then simpler, well-calibrated models may prove to be more informative. Finally, in future studies, the computational framework developed here will be tested on a larger patient cohort and prospective clinical trials will be performed. In summary, the results presented here provide a proof-of-concept that multimodal Bayesian model calibration holds a great promise to assist the development of personalized RT protocols.

²  <https://github.com/JanaLipkova/GliomaSolver>

Disclaimer: This chapter is partially reproduced from the article J. Lipková, P. Angelikopoulos, S. Wu, E. Alberts, B. Wiestler, C. Diehl, C. Preibisch, T. Pyka, S. Combs, P. Hadjidoukas, K. Van Leemput, P. Koumoutsakos, J. Lowengrub, B. Menze: "Personalized Radiotherapy Design for Glioblastoma: Integrating Mathematical Tumor Models, Multimodal Scans and Bayesian Inference.", published in IEEE transactions on medical imaging, (2019).

CLINICAL STUDY OF CXCR4-DIRECTED PET

Central nervous system lymphoma (CNSL) is a rare and aggressive neoplasm of the CNS. In contrast to other brain lesions, CNSL originates from lymphocytes (white blood cells), instead of brain cells. Due to its specific origin, CNS lymphoma requires different treatment than glioma. However, diagnostics of this uncommon tumor is a challenging task and the missed or delayed diagnosis contributes to mismanagement and worsen prognosis. Unfortunately, current imaging modalities – such as MRI and FDG-PET – do not provide enough specificity to distinguish CNSLs from other brain lesions. Therefore, identification and incorporation of novel targeted imaging strategies are of crucial importance for the improvement of the diagnostic work-up in CNSLs.

In this chapter, we present a pilot clinical study that investigates the diagnostic and prognostic potential of CXCR4-directed PET imaging for patients with CNSL. This work also illustrates how an interplay between medical imaging and image analysis can contribute to clinical advancements.

6.1 Motivation

CNSL includes both primary and secondary lymphomas (for details see Section 2.1.4). The standard imaging modality for patients suspected with CNSL is the contrast-enhanced MRI imaging. MRI provides high sensitivity but only moderate specificity, making the discrimination of the CNSL from other brain lesions a challenging task. Neither the FDG-PET tracer has been proven as a sufficient marker in this disease and bears limitations due to high uptake values in the healthy brain parenchyma [74]. Therefore, the diagnosis has to be histopathological confirmed – preferably by a stereotactic biopsy from a CNS lesion – which is often complicated by the localization of CNSL in vulnerable brain regions [14].

Even though the prognosis of PCNSL has significantly improved over the last decades (median survival improved from 2.5 to 26 months [118]), there is no evidence-based therapy established for CNSLs. Incorporation of novel invasive treatments, including autologous stem cell transplantation, has shown long-term remission in some patients [93]. However, due to severe side effects, it is usually restricted to younger patients. Moreover, it is not well understood which patients profit from such invasive treatment. For patients that relapse on the first-line treatment, there is currently no established salvage therapy and whole-brain radiotherapy – that comes along with severe neurotoxicity – often remains the only possible treatment option [81, 129]. Identification of prognostic and targeted imaging modalities is therefore highly desirable to facilitate a diagnostic work-up in CNSL.

The chemokine receptor CXCR4 – with its sole known ligand CXCL12 – plays an important role during embryonic organogenesis and orchestrates important immunological functions as master regulator of leukocyte migration, homing and hematopoietic stem and progenitor cell retention in bone marrow niches [38, 128, 199]. High CXCR4 expression has been shown also in various hematologic malignancies [97, 140], including multiple myeloma presented in Section 3.2.4. Furthermore, the feasibility of CXCR4-directed endoradiotherapy with Pentixafer – the therapeutic twin of the imaging peptide Pentixafor – has been already demonstrated in small patient cohorts with multiple myeloma and acute myeloid leukemia [63, 76]. Elevated CXCR4 expression has been recently observed also in PCNSL and SCNSL [20, 165, 198]. However, the potential of this marker is not yet well understood for CNSL.

Herein, we investigate the diagnostic and prognostic capabilities of CXCR4-directed PET imaging with ^{68}Ga -Pentixafor and its suitability for a targeted endoradiotherapy approach in CNSLs. We present an observational pilot study which is used to conduct explorative analysis. The sample size of the clinical cohort was chosen to serve this purpose.

6.2 Patient cohort

The study was conducted on 8 patients with either PCNSL or SCNSL. For all patients, T1-contrast enhanced (T1c) MRI, FLAIR MRI, and CXCR4-directed PET imaging with ^{68}Ga -Pentixafor marker were acquired prior to the treatment; between June 2014 and December 2017. All patients had histologically confirmed CNS lymphoma. Detailed characteristics for the patient cohort are given in Table 6.1. The two patients with the SCNSL had a CNS relapse of diffuse large B-Cell lymphoma. Of note is that the patients received corticosteroids before CXCR4-directed PET imaging to relief lymphoma derived symptoms. After treatment, 7 out of 8 patients were monitored with T1c and FLAIR MRI follow-up scans. All scans were registered to pre-treatment T1c MRI scan using rigid ANTs registration [11]. The tumors were segmented with the brain-tumor processing pipeline presented in Section 8.2. The tumor segmentations were inspected and corrected by a board-certified radiologist. The PET scan of each patient was normalized by

subtracting the mean PET uptake value from a healthy appearing region in the brain parenchyma.

patient	sex	age (y)	diagnosis	disease stage	no. of relapse
#1	f	63	SCNSL	CNS relapse	3
#2	f	65	PCNSL	first diagnosis	0
#3	m	80	PCNSL	first diagnosis	0
#4	m	59	PCNSL	first diagnosis	0
#5	m	66	PCNSL	first diagnosis	0
#6	m	58	PCNSL	first diagnosis	0
#7	m	64	PCNSL	first diagnosis	0
#8	m	79	SCNSL	CNS relapse	1

Table 6.1: Patients characteristics. Abbreviations: y: year; no.: number; CNS: central nervous system; PCNSL: primary CNS lymphoma; SCNSL: secondary CNS lymphoma.

6.3 Specificity of CXCR4-PET

Figure 6.2 shows the pre-treatment MRI scans of all patients together with the CXCR4-directed PET imaging with ^{68}Ga -Pentixafor. The CXCR4-PET is visually positive in all 8 patients, with very good contrast to the surrounding brain parenchyma. The PET enhancement correlates well with the lymphoma lesions determined by T1c MRI. On the other hand, the surrounding brain edema seen in FLAIR does not show correlation with CXCR4-directed PET enhancement. In 4 patients where lymphoma biopsies in close time-proximity to PET imaging were available, CXCR4 expression levels were generally high within the tumor (Fig. 6.1). The high CXCR4 expression in all these patients suggests the diagnostic potential of CXCR4-directed PET imaging in lymphomas of CNS. Moreover, it renders CXCR4 as a potential theranostic target for endoradiotherapy with Penitixather in CNSL.

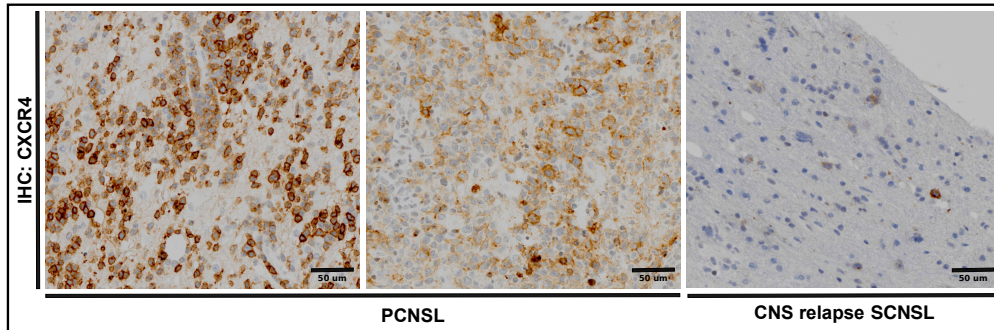


Figure 6.1: Ex-vivo CXCR4 expression within lymphoma lesions.

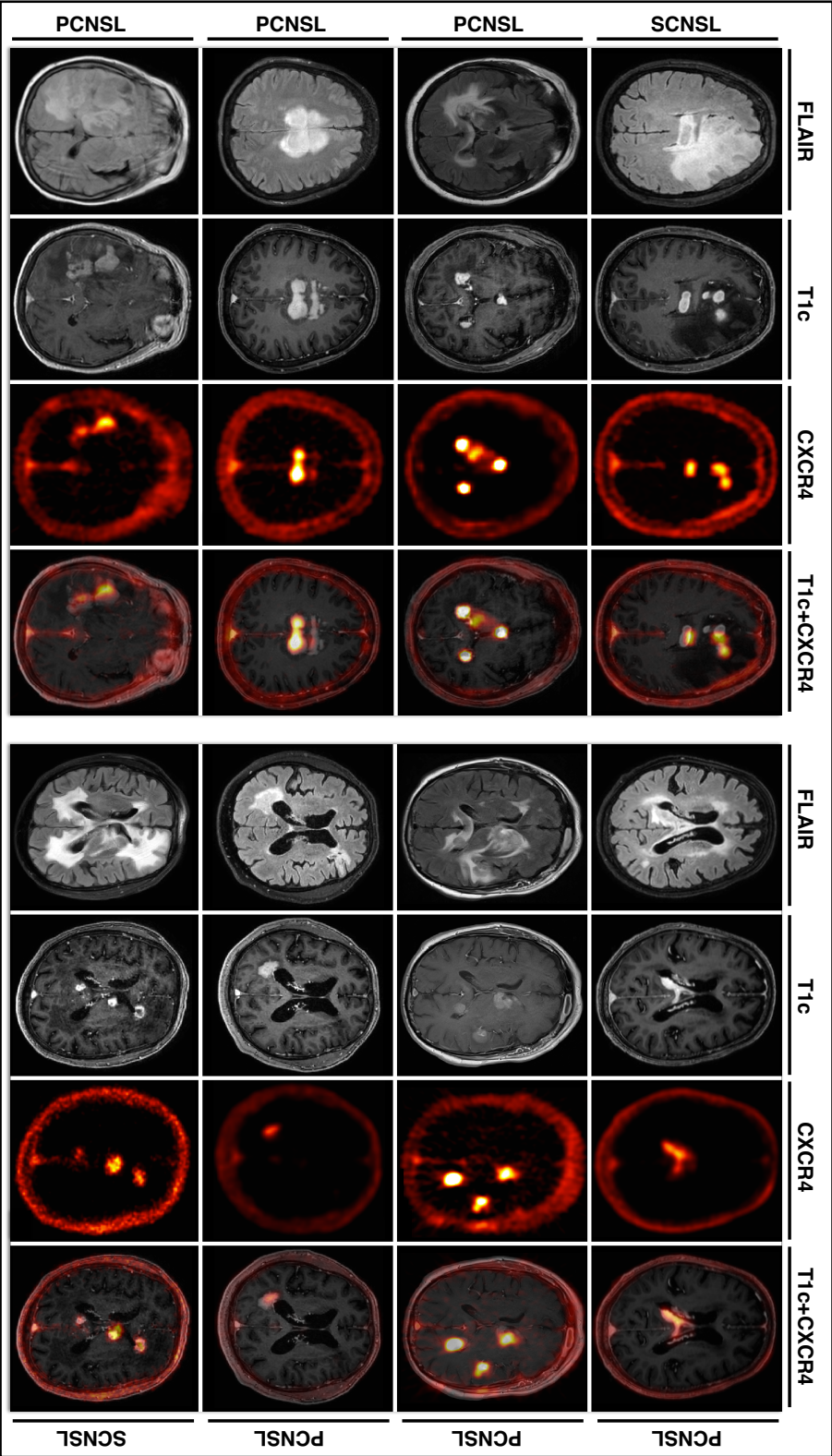


Figure 6.2: Specificity of the CXCR4-directed PET imaging for CNSLs. Shown are pre-treatment scans of 8 patients diagnosed with either PCNSL or SCNSL. The CXCR4-PET is visually positive in all 8 patients and correlates well with the lymphoma lesions determined by the T1c MRI.

6.4 Prognostic value of CXCR4-PET

To evaluate the prognostic value of the CXCR4-directed PET imaging, the relation between the treatment efficiency and various tumor properties extracted from the pre-treatment T1c MRI and PET scans were computed. Only patients with available follow-up scans were considered, resulting in 7 patients. Despite the diagnostic importance of the FLAIR scan, it was not included in the prognostic performance study. The reason was that the FLAIR-enhancing lesion might be difficult to distinguish from a tissue response to the treatment. Figure 6.3 shows the treatment response of the patients over time. To account for the treatment response of each lesion, the analysis was performed across all lymphoma lesions, leading to a total of 14 individual lesions with available follow-up scans.

The efficiency of the treatment η , was defined as a relative change of the tumor volume detected by T1c MRI at the first and the last available scan, i.e.:

$$\eta = \frac{\mathcal{V}^{first}(T1c) - \mathcal{V}^{last}(T1c)}{\mathcal{V}^{first}(T1c)} \times 100\%. \quad (6.1)$$

For each lesion, the following four properties were extracted from the pretreatment scans: 1) volume of the T1c-enhanced lesion $\mathcal{V}(T1c)$, 2) volume of the PET enhanced lesion $\mathcal{V}(PET)$, 3) maximum PET uptake value inside each lesion $\max(PET)$, and 4) the PET uptake values integrated across the PET-enhancing lesion:

$$\mathcal{J}(PET) = \int_{i \in \Omega} \phi(i) dv, \quad (6.2)$$

where $\phi(i)$ denotes the PET uptake value at the voxel i inside the region of the PET-enhancing lesion Ω and dv is the volume of the voxel i . The integrated PET uptake value $\mathcal{J}(PET)$ accounts for the tracer distribution inside the tumor as well as the lesion size.

For each of the extracted tumor properties, the Pearson correlation with the treatment efficiency was computed together with the p -value describing the significance of the correlation, as shown in Fig. 6.4. The volume of the tumor lesions at diagnosis – neither determined by MRI nor PET – is not a significant indicator for treatment response in the 7 studied patients. On the other hand, the PET uptake values given by $\max(PET)$ and $\mathcal{J}(PET)$ have significant prognostic value, with Pearson correlation coefficient $c^{\max(PET)} = -0.59$ ($p = 0.028$) and $c^{\mathcal{J}(PET)} = -0.71$, ($p = 0.005$). The results imply that the lesions with smaller PET uptake values are related with a better response to the treatment. The $\mathcal{J}(PET)$ is the most significant prognostic factor in the presented study.

This preliminary results suggest that the CXCR4-directed PET imaging bears the potential to predict the treatment response and therefore might serve as a biomarker for the selection of patients that profit from intense treatment protocols.

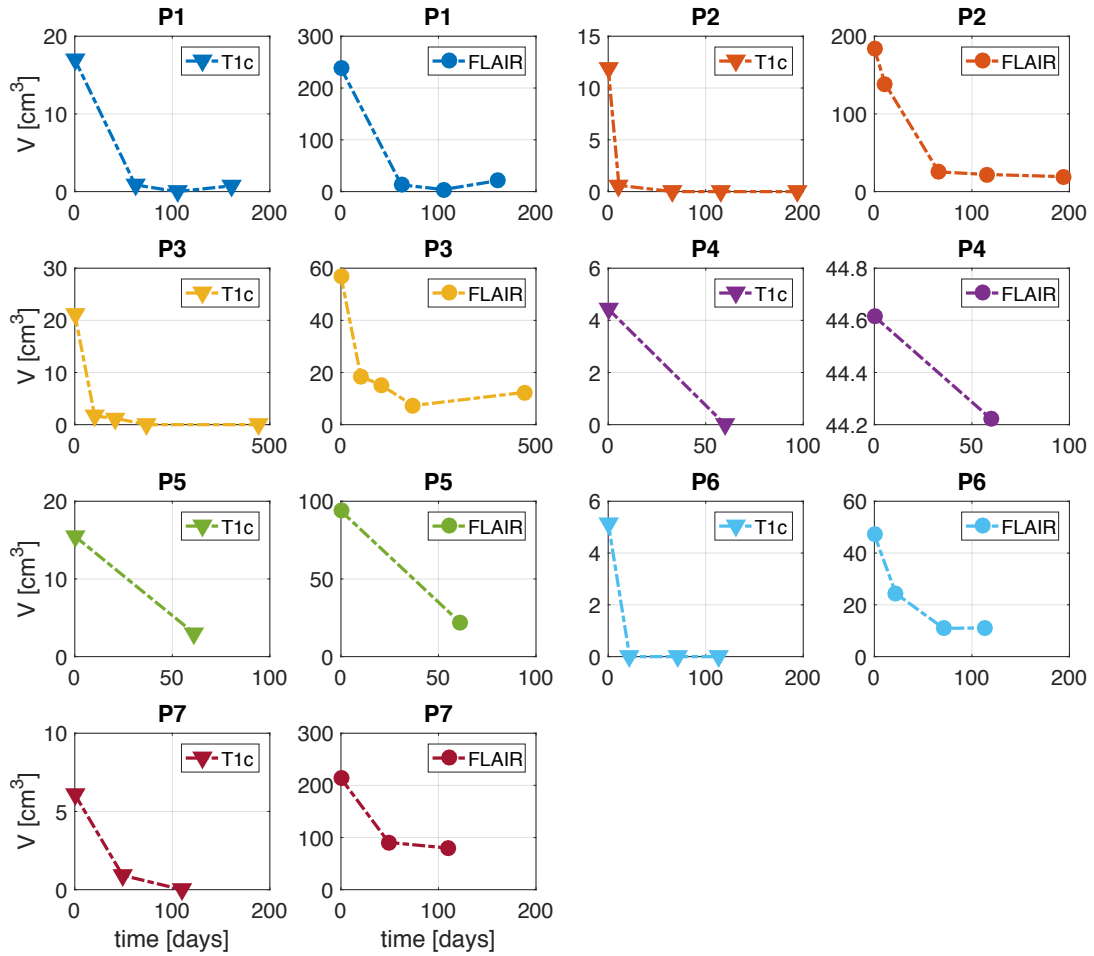


Figure 6.3: Tumor dynamics upon treatment determined by MRI (T1c and FLAIR) in 7 patients with available follow-up scans.

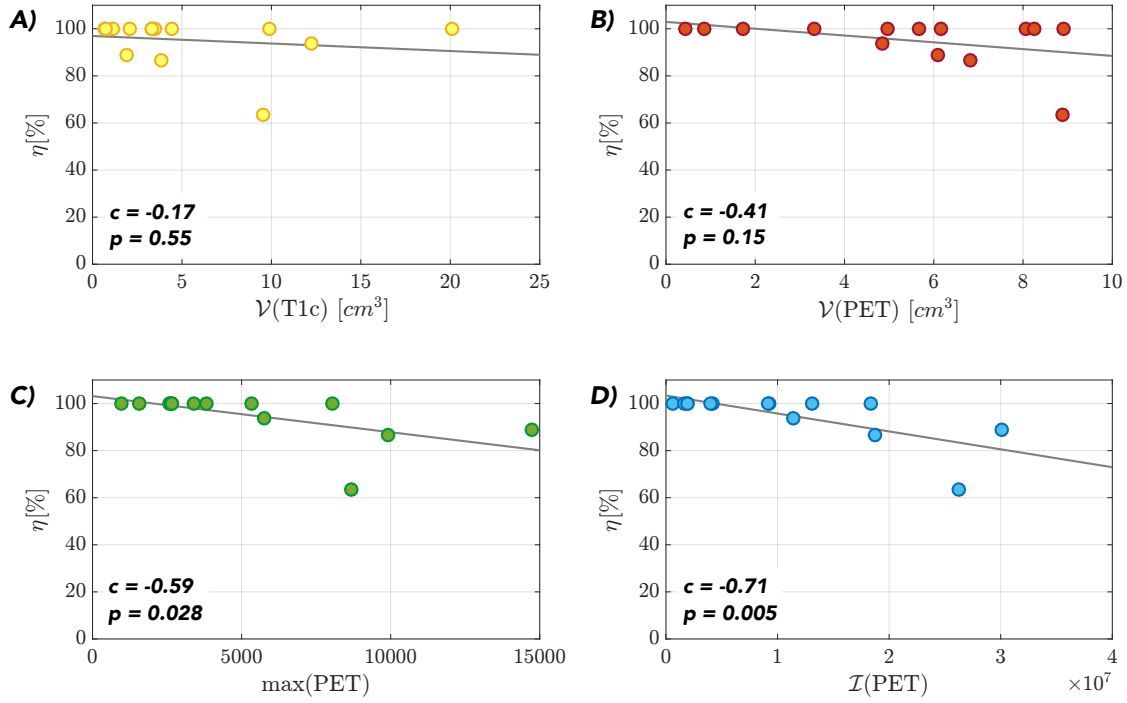


Figure 6.4: Correlation between the treatment efficiency η and the tumor properties extracted from the pretreatment scans: A) volume of the T1c enhancing lesion $\mathcal{V}(T1c)$, B) volume of the PET enhancing lesion $\mathcal{V}(PET)$, C) maximum PET uptake value $\max(PET)$, and D) integrated PET uptake values. Each dot represents one of the 14 diagnosed lymphoma lesions. The Pearson correlation coefficient c and the p -value are reported inside each plot. The least-squares regression line is shown in gray.

6.5 Summary

This proof-of-concept study has revealed that the CXCR4-directed PET imaging with ^{68}Ga -Pentixafor is feasible in the lymphoma of the CNS. This new PET imaging modality provides excellent contrast properties to the surrounding brain parenchyma and might have the potential to predict treatment response.

The presented study suggests three potential benefits of CXCR4-PET imaging. First, since the CXCR4-PET has been shown positive in all patients with active disease, it might provide useful information during diagnostic workup to distinguish between lymphoma of the CNS and brain-derived tumor. Secondly, as CXCR4-directed PET has been proven to have a predictive value for treatment response in this proof-of-concept study, it might serve as a biomarker for selecting older patients that could profit from a more intense consolidation therapy followed by autologous transplantation. Third, high expression of CXCR4 in the lymphoma lesions opens the possibilities for CXCR4-directed endoradiotherapy with Pentixafor. Thanks to its localized effect, the endoradiotherapy would result in lower toxicity and less side effects than the standard whole-brain radiotherapy used for patients with CNSL relapse. Moreover, thanks to the lower toxicity, the CXCR4-directed endoradiotherapy could be incorporated into the first-line treatment to potentially increase the treatment response rate. Furthermore, less toxic high dose chemotherapy protocols in combination with the CXCR4-directed endoradiotherapy and autologous stem cell transplantation could be applied in older patients with adverse prognosis.

This proof-of-concept study has clearly demonstrated the utility of CXCR4-directed PET imaging with ^{68}Ga -Pentixafor. Albeit the small sample size and the very heterogeneous patient population within this study, the diagnostic potential of CXCR4-directed PET imaging with ^{68}Ga -Pentixafor should be studied in prospective clinical trials.

Disclaimer: This chapter is partially reproduced from the article: P. Herhaus, J. Lipková, T. Vag, F. Lammer, J. S. Huspennina, C. Lapa, B. Wiestler, I. Ezhov, B. Menze, T. Pukrop, I. Iakuchev, D. Hellwig, A. K. Buck, M. Deckert, H. J. Wester, M. Schweiger and U. Keller, "CXCR4-targeted positron emission tomography imaging of central nervous system B-cell lymphoma", submitted to American Society of Hematology, (2019).

STOCHASTIC SIMULATION METHODS

Many processes of tumor metabolism and treatment procedures occur at the molecular scale level (see Fig. 4.1). These processes, for instance, include phenomena such as binding of the molecules of the imaging tracer with particular tumor cells receptors, the effect of chemotherapeutic drugs on the tumor signaling pathways or the impact of ionized radiation on the tumor cells DNA. Computational modeling offers means for analyzing and studying such phenomena. The dynamic of these processes is often driven by specific molecules, which appear at a very small amount. For instance, often there are only one or two molecules of a particular gene or chemical presented in the cell [46]. In such a case, the system cannot be described by the density of the involved chemicals and partially/ordinary differential equations cannot be used to model such systems. Instead, discrete stochastic methods characterizing dynamics of individual molecules have to be used.

This chapter presents stochastic methods for simulating chemical reactions in biological systems. First, the basic theory of stochastic algorithms is presented, followed by an overview of the state-of-the-art methods; in particular the Gillespie's algorithm [54] and its accelerated versions τ -leaping [56] and R -leaping [10]. Each of these accelerated methods is more efficient under different conditions. However, even a small change in a system's set-up or its evolution in time can significantly alter the nature of the system and thus reduce the efficiency of the selected method. To overcome this issue, we propose a new accelerated algorithm, called S -leaping, which provides an optimal coupling between τ - and R -leaping methods. Thanks to the efficient coupling, the proposed algorithm maintains its efficiency under different conditions. Moreover, in the case of large and stiff systems or systems with fast dynamics, the S -leaping outperforms both methods. We demonstrate the performance and the accuracy of the S -leaping in comparison with the τ - and R -leaping on a number of benchmark systems involving biological reaction networks.

7.1 Introduction

Herein, we present stochastic simulation algorithms describing continuous-time Markov chains systems. An example of such system is a well-stirred chemically reacting system with a small population of reactants [8].

First, let us present the main concepts and terminology used in the stochastic simulations. We consider a well-stirred system of N molecular species $\{S_1, \dots, S_N\}$ which can react through M chemical reaction channels $\{R_1, \dots, R_M\}$. In what follows, the index $i \in \{1, \dots, N\}$ will be used for chemical species, e.g., S_i and the index $j \in \{1, \dots, M\}$ for chemical reactions, e.g., R_j . The state of the system is characterized by a *state vector* $\mathbf{x} := \mathbf{X}(t) = (X_1(t), \dots, X_N(t))$, where $X_i(t)$ denotes the number of molecules S_i at time t . The dynamics of each reaction channel R_j is characterized by a *propensity function* a_j and a *state change vector* $\mathbf{v}_j = (v_{1j}, \dots, v_{Nj})$. Given the state vector \mathbf{x} , the quantity $a_j(\mathbf{x})dt$ gives the probability that the reaction R_j will occur in the next infinitesimal time interval $[t, t+dt)$. The state change vector \mathbf{v}_j gives the change in the molecular population caused by one reaction R_j . Finally, we define a_0 as the sum of all propensity functions $a_0(\mathbf{x}) = \sum_{j=1}^M a_j(\mathbf{x})$. Figure 7.1 shows an example of a reaction system, illustrating the aforementioned terms, while more technical details can be found in [8, 45].

For the rest of this chapter, we will use the notation $\mathcal{B}, \Gamma, \mathcal{E}, \mathcal{M}$, and \mathcal{P} to denote the probability distribution function of the binomial, the gamma, the exponential, the multinomial and the Poisson distribution, respectively. The same notation will be used to denote the function that produces pseudo-random numbers from the respective distribution. With $\lfloor x \rfloor$ we will denote the closest integer to x .

7.1.1 The Gillespie algorithm

The Gillespie stochastic simulation algorithm (SSA) [55] is an exact algorithm for simulating the time evolution of well-stirred chemically reacting systems. It is an exact algorithm in the sense that the generated sample paths are distributed according to the solution of the corresponding chemical master equation [55]. The SSA algorithm is summarised in Algorithm 3. Since SSA simulates only one reaction event per time step, it becomes inefficient for large systems and long time scales.

Algorithm 3 Gillespie Stochastic Simulation Algorithm (SSA)

- 1: Initialise: $T_{\text{end}}, t \leftarrow 0, \mathbf{x} \leftarrow \mathbf{X}(0)$
 - 2: **while** $t < T_{\text{end}}$ **do**
 - 3: Compute $a_j(\mathbf{x})$ for $j = 1, \dots, M$ and $a_0(\mathbf{x})$
 - 4: $\tau \leftarrow \mathcal{E}(1/a_0(\mathbf{x}))$
 - 5: Choose the j -th reaction with probability $a_j(\mathbf{x})/a_0(\mathbf{x})$
 - 6: $\mathbf{x} \leftarrow \mathbf{x} + \mathbf{v}_j$
 - 7: $t \leftarrow t + \tau$
 - 8: **end while**
-

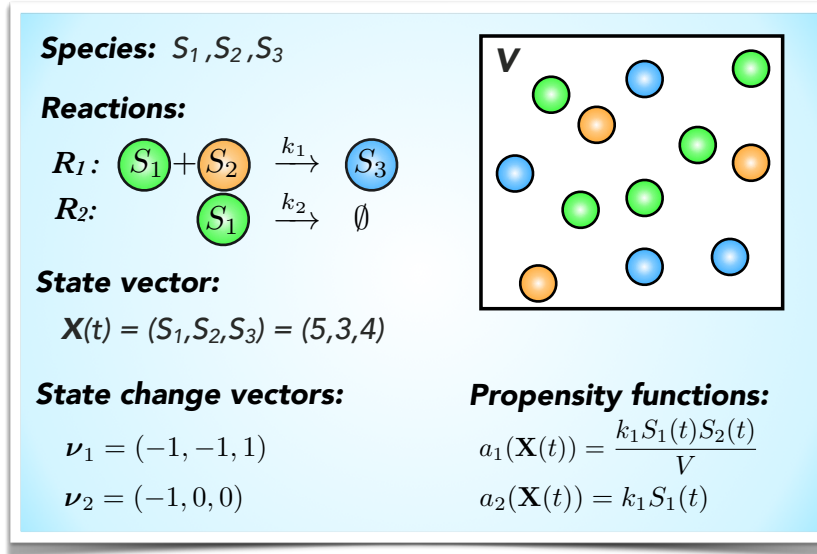


Figure 7.1: An illustration of a well-stirred system with volume V containing three species S_1, S_2 , and S_3 , which are subjects to two chemical reactions R_1 and R_2 with reaction rates k_1 and k_2 , respectively.

Approximate accelerated stochastic simulation algorithms

Several approximate stochastic simulation algorithms [10, 24, 25, 56] have been introduced to accelerate the SSA at the expense of slightly reduced accuracy. These methods advance the simulated system with larger time steps, which allows to fire multiple reactions per time step. The accurate advancement of the system is limited by the so-called *leap condition*, which states that propensities $a_j(\mathbf{x})$ should remain approximately constant over the time interval $[t, t + \tau]$, i.e.:

$$|a_j(\mathbf{X}(t + \tau)) - a_j(\mathbf{X}(t))| \leq \varepsilon a_0(\mathbf{x}), \quad j = 1, \dots, M, \quad (7.1)$$

where $0 < \varepsilon \ll 1$ is a user defined parameter that controls the models accuracy.

7.1.2 The τ -leaping algorithm

The τ -leaping algorithm [56] accelerates the SSA by advancing the system with pre-selected deterministic time step τ , which is much bigger than the mean stochastic time step of SSA. Then, the number of times $k_j^{\mathcal{P}}$ the reaction R_j will be fired during the time interval $[t, t + \tau]$ is sampled from a Poisson distribution with parameter $a_j(\mathbf{x})\tau$. Since the Poisson random variables $k_j^{\mathcal{P}}$ are unbounded, the algorithm might result in negative populations. To overcome this problem a non-negative version of the τ -leaping algorithm was proposed in [25].

7.1.2.1 Non-negative τ -leaping

The algorithm reduce appearance of negative population by identifying so called critical reactions, i.e. the reactions which are N_c firings from exhausting one of its reactants. No more than one critical reaction can occur within the time leap τ , while multiple non-critical reactions are allowed. The critical reaction is handled by the SSA, while the non-critical reactions are modelled by the τ -leaping method. Several methods [24, 56, 57] were introduced for the computation of the leap length τ . The most efficient one [24] selects τ as

$$\tau = \min_{i \in I_{rs}} \left\{ \frac{\max \left\{ \frac{\varepsilon x_i}{g_i(\mathbf{x})}, 1 \right\}}{|\mu_i(\mathbf{x})|}, \frac{\max \left\{ \frac{\varepsilon x_i}{g_i(\mathbf{x})}, 1 \right\}^2}{|\sigma_i^2(\mathbf{x})|} \right\}, \quad (7.2)$$

where $\mathbf{x} = \mathbf{X}(t)$ and I_{rs} denote the set of indices of all reactant species. The factor g_i takes into account the highest order of reaction, denoted as h_i , in which species S_i appears as a reactant,

$$g_i(\mathbf{x}) = h_i + \frac{h_i}{n_i} \sum_{j=1}^{n_i-1} \frac{j}{x_i - j}, \quad (7.3)$$

where n_i denotes the maximum number of S_i molecules required by any of the highest order reactions [155]. Finally, the terms μ_i and σ_i^2 are given by

$$\mu_i(\mathbf{x}) = \sum_{j \in J_{ncr}} \nu_{ij} a_j(\mathbf{x}), \quad \forall i \in I_{rs}, \quad (7.4)$$

$$\sigma_i^2(\mathbf{x}) = \sum_{j \in J_{ncr}} \nu_{ij}^2 a_j(\mathbf{x}), \quad \forall i \in I_{rs}, \quad (7.5)$$

where J_{ncr} is the set of all non-critical reactions. The non-negative τ -leaping algorithm is outlined in Algorithm 4.

7.1.2.2 Adaptive τ -leaping

An adaptive version of the τ -leaping algorithm was introduced in [26]. It automatically alternates between the explicit (Algorithm 4) and implicit τ -leaping [145]. The implicit τ -leaping is inspired by the implicit Euler method for differential equations, which provides considerable speed-up over explicit methods mainly in stiff systems. In the implicit formulation, we would like to compute the state $\mathbf{X}(t + \tau)$ as

$$\mathbf{X}(t + \tau) = \mathbf{X}(t) + \sum_{j=1}^M \mathbf{v}_j k_j^{\mathcal{P}}(\mathbf{X}(t + \tau)). \quad (7.6)$$

However, this would require to generate random samples from a Poisson distribution with unknown parameter, i.e.:

$$k_j^{\mathcal{P}}(\mathbf{X}(t + \tau)) \sim \mathcal{P}(a_j(\mathbf{X}(t + \tau))\tau).$$

Algorithm 4 Non-negative τ -leaping

```

1: Initialise:  $T_{\text{end}}, t \leftarrow 0, \mathbf{x} \leftarrow \mathbf{X}(0), N_c \leftarrow 10$ .
2: while  $t < T_{\text{end}}$  do
3:   Compute  $a_j(\mathbf{x})$  for  $j = 1, \dots, M$  and  $a_0(\mathbf{x})$ 
4:   Compute the list of critical reactions  $J_{\text{crit}}$ . The reaction  $R_j$  is critical if:


$$a_j(\mathbf{x}) > 0 \quad \text{and} \quad \min_i \left\lfloor \frac{x_i}{|v_{ij}|} \right\rfloor \leq N_c$$


5:   Compute time the step  $\tau_1$  by Eq. (7.2)
6:   if  $\tau_1 < 10 \frac{1}{a_0(\mathbf{x})}$  then
7:     Execute 100 steps of the SSA
8:   else
9:      $a_0^c(\mathbf{x}) = \sum_{j \in J_{\text{crit}}} a_j(\mathbf{x})$  and  $\tau_2 \leftarrow \mathcal{E}(1/a_0^c(\mathbf{x}))$  {time of critical reaction}
10:    if  $\tau_1 \leq \tau_2$  then
11:       $\tau \leftarrow \tau_1$ 
12:       $k_j \leftarrow \mathcal{P}(a_j(\mathbf{x})\tau), \quad j \notin J_{\text{crit}}$ 
13:       $k_j = 0, \quad j \in J_{\text{crit}}$ 
14:    else
15:       $\tau \leftarrow \tau_2$ 
16:      Choose  $j_c$  with probability  $a_{j_c}(\mathbf{x})/a_0^c(\mathbf{x})$  and  $j_c \in J_{\text{crit}}$ 
17:       $k_{j_c} \leftarrow 1$ 
18:       $k_j \leftarrow 0$  for  $j \in J_{\text{crit}}$  and  $j \neq j_c$ 
19:       $k_j \leftarrow \mathcal{P}(a_j(\mathbf{x})\tau)$  for  $j \notin J_{\text{crit}}$ 
20:    end if
21:  end if
22:  if there is a negative component in  $\mathbf{x} + \sum_{j=1}^M k_j \mathbf{v}_j$  then
23:     $\tau_1 \leftarrow \tau/2$  and go to 6.
24:  else
25:     $\mathbf{x} \leftarrow \mathbf{x} + \sum_{j=1}^M k_j \mathbf{v}_j$ 
26:     $t \leftarrow t + \tau$ .
27:  end if
28: end while

```

To avoid this difficulty, a partial implicit approach was introduced in [145]. It states that if $k_j^{\mathcal{P}}$ is a random variable that follows a Poisson distribution with mean $a_j\tau$, then $k_j^{\mathcal{P}}$ can be expressed as a sum of a random variable with mean $a_j\tau$ and zero mean random variable $k_j^{\mathcal{P}} - a_j\tau$,

$$k_j^{\mathcal{P}} = a_j\tau + k_j^{\mathcal{P}} - a_j\tau. \quad (7.7)$$

The partial implicit approach evaluates the variable $a_j\tau$ at the state $\mathbf{X}(t+\tau)$ and the zero mean variable $k_j^{\mathcal{P}} - a_j\tau$ at the state $\mathbf{X}(t)$. Applying this approach to the firings $k_j^{\mathcal{P}}$ in Eq. (7.6) leads to the following implicit system of equations:

$$\mathbf{x}' = \mathbf{x} + \sum_{j=1}^M \mathbf{v}_j a_j(\mathbf{x}')\tau + \sum_{j=1}^M \mathbf{v}_j (k_j^{\mathcal{P}}(\mathbf{x}) - a_j(\mathbf{x})\tau), \quad (7.8)$$

for $\mathbf{x} = \mathbf{X}(t)$ and $\mathbf{x}' = \mathbf{X}(t+\tau)$. If we denote by \mathbf{X}^* the solution of the above implicit system, which can be obtained with the Newton-Raphson method, the implicit state update in Eq. (7.6) is given by,

$$\mathbf{X}(t+\tau) = \mathbf{X}(t) + \sum_{j=1}^M \mathbf{v}_j k_j^{\mathcal{P}*}, \quad (7.9)$$

where

$$k_j^{\mathcal{P}*} = \left\lfloor a_j(\mathbf{X}^*)\tau + k_j^{\mathcal{P}}(\mathbf{X}(t)) - a_j(\mathbf{X}(t))\tau \right\rfloor. \quad (7.10)$$

The rounding in Eq. (7.10) ensures that the updated population will remain integer.

Implicit numerical methods provide an efficient way for solving stiff systems since they advance the system with bigger time step than explicit methods. While the implicit methods for differential equations are unconditionally stable, the time step in the implicit τ -leaping is bounded by the leap condition of Eq. (7.1). In [26] authors propose the computation of the implicit time step τ , under the condition of partial equilibrium. The assumption is that if some reaction channels are in equilibrium or close to a partial equilibrium, then the net change of their propensities would be small. Thus the dynamics of the system would be driven by the reactions outside the equilibrium and the implicit time step can be computed as

$$\tau^{(\text{im})} = \min_{i \in I_{\text{rs}}} \left\{ \frac{\max\left\{\frac{\varepsilon x_i}{g_i(\mathbf{x})}, 1\right\}}{|\mu_i^{(\text{im})}(\mathbf{x})|}, \frac{\max\left\{\frac{\varepsilon x_i}{g_i(\mathbf{x})}, 1\right\}^2}{\sigma_i^{(\text{im})}(\mathbf{x})^2} \right\}, \quad (7.11)$$

where g_i is given by Eq. (7.3) and $\mu_i^{(\text{im})}$, $\sigma_i^{(\text{im})}$ are given by

$$\mu_i^{(\text{im})}(\mathbf{x}) = \sum_{j \in J_{\text{necr}}} \nu_{ij} a_j(\mathbf{x}), \quad \forall i \in I_{\text{rs}}, \quad (7.12)$$

$$\sigma_i^{(\text{im})}(\mathbf{x})^2 = \sum_{j \in J_{\text{necr}}} \nu_{ij}^2 a_j(\mathbf{x}), \quad \forall i \in I_{\text{rs}}, \quad (7.13)$$

where $\mathbf{x} = \mathbf{X}(t)$ and J_{necr} denotes the set of indices of the reaction channels that are neither critical nor in partial equilibrium.

Algorithm 5 Adaptive τ -leaping

```

1: Initialise:  $T_{\text{end}}, t \leftarrow 0, \mathbf{x} \leftarrow \mathbf{X}(0), N_c \leftarrow 10$ .
2: while  $t < T_{\text{end}}$  do
3:   Compute  $a_j(\mathbf{x})$  for  $j = 1, \dots, M$  and  $a_0(\mathbf{x})$ 
4:   Compute the list of critical reactions  $J_{\text{crit}}$ . The reaction  $R_j$  is critical if:


$$a_j(\mathbf{x}) > 0 \quad \text{and} \quad \min_i \left\lfloor \frac{x_i}{|v_{ij}|} \right\rfloor \leq N_c$$


5:   Compute  $\tau^{(\text{ex})}$  using Eq. (7.2) and  $\tau^{(\text{im})}$  using Eq. (7.11)
6:   if  $\tau^{(\text{im})} > 100 \tau^{(\text{ex})}$  then
7:     The system is stiff and  $\tau_1 \leftarrow \tau^{(\text{im})}$ 
8:   else
9:     The system is non-stiff and  $\tau_1 \leftarrow \tau^{(\text{ex})}$ 
10:  end if
11:  if  $\tau_1 \leq 10 \frac{1}{a_0(\mathbf{x})}$  then
12:    Execute 100 steps of the SSA.
13:  else
14:     $a_0^c(\mathbf{x}) = \sum_{j \in J_{\text{crit}}} a_j(\mathbf{x})$  and  $\tau_2 \leftarrow \mathcal{E}(1/a_0^c(\mathbf{x}))$  {time of critical reaction}
15:    if  $\tau_2 > \tau_1$  then
16:       $\tau \leftarrow \tau_1$ 
17:      if the system is currently stiff then
18:        Compute  $k_j$  using Eq. (7.10) for  $j \notin J_{\text{crit}}$ 
19:      else
20:         $k_j \leftarrow \mathcal{P}(a_j(\mathbf{x})\tau)$  for  $j \notin J_{\text{crit}}$ 
21:      end if
22:    else
23:       $\tau \leftarrow \tau_2$ 
24:      Choose  $j_c$  with probability  $a_{j_c}(\mathbf{x})/a_0^c(\mathbf{x})$  and  $j_c \in J_{\text{crit}}$ 
25:       $k_{j_c} \leftarrow 1$ 
26:       $k_j \leftarrow 0$  for  $j \in J_{\text{crit}}$  and  $j \neq j_c$ 
27:      if  $\tau_2 < \tau^{ex}$  or the system is non-stiff then
28:         $k_j \leftarrow \mathcal{P}(a_j(\mathbf{x})\tau)$  for  $j \notin J_{\text{crit}}$ 
29:      else
30:        Compute  $k_j$  using Eq. (7.10) for  $j \notin J_{\text{crit}}$ 
31:      end if
32:    end if
33:    if there is a negative component in  $\mathbf{x} + \sum_{j=1}^M k_j \mathbf{v}_j$  then
34:       $\tau_1 \leftarrow \tau/2$  and go to 11
35:    else
36:       $\mathbf{x} \leftarrow \mathbf{x} + \sum_{j=1}^M k_j \mathbf{v}_j$ 
37:       $t \leftarrow t + \tau$ 
38:    end if
39:  end if
40: end while

```

In general, it is difficult to detect which reaction channels are currently in partial equilibrium, however, it can be easily done for reversible reactions [26]. Let R_+ and R_- denote a pair of reversible reactions, with the corresponding propensity functions a_+ and a_- . If the reaction R_+ and R_- are in partial equilibrium, their propensities must be similar, i.e.:

$$|a_+(\mathbf{x}) - a_-(\mathbf{x})| \leq \delta \min\{a_+(\mathbf{x}), a_-(\mathbf{x})\}, \quad (7.14)$$

where δ is a small positive number, usually chosen around 0.05 [26]. The adaptive τ -leaping algorithm is outlined in Algorithm 5.

7.1.3 The R -leaping algorithm

The R -leaping algorithm [10], instead of prescribing the time-step, imposes the total number of reactions L that can be fired during the next time interval. Under the leap condition of Eq. (7.1), the number of firings is computed as [10],

$$L = a_0(\mathbf{x}) \min_{i \in I_{rs}} \left\{ \frac{\max\left\{\frac{\varepsilon x_i}{g_i(\mathbf{x})}, 1\right\}}{|\mu_i(\mathbf{x})|}, \frac{\max\left\{\frac{\varepsilon x_i}{g_i(\mathbf{x})}, 1\right\}^2}{|\sigma_i^2(\tilde{\mathbf{x}}) - |\mu_i^2(\tilde{\mathbf{x}})/a_0(\mathbf{x})|} \right\}, \quad (7.15)$$

for $\mathbf{x} = \mathbf{X}(t)$, I_{rs} the set of indices of all reactant species and the terms g_i , $\mu_i(\mathbf{x})$ and $\sigma_i^2(\mathbf{x})$ given by Eq. (7.3), (7.4) and (7.5), respectively. The time span τ_L for the L reactions follows the gamma distribution, $\tau_L \sim \Gamma(L, 1/a_0(\mathbf{x}))$. The number of firings $k_j^{\mathcal{B}}$ for the reaction channel R_j , fired within the time span τ_L , is sampled from a sequence of correlated binomial distributions,

$$k_j^{\mathcal{B}} \sim \mathcal{B} \left(L - \sum_{m=1}^{j-1} k_m^{\mathcal{B}}, \frac{a_j(\mathbf{x})}{a_0(\mathbf{x}) - \sum_{m=1}^{j-1} a_m(\mathbf{x})} \right). \quad (7.16)$$

This approach requires at most $M - 1$ drawings of random numbers since $k_M^{\mathcal{B}} = L - \sum_{j=1}^{M-1} k_j^{\mathcal{B}}$. Furthermore, it can be shown that the sampling procedure is invariant under the permutation of reaction channels indices [10]. This fact can be exploited to reduce the number of samples drawn per time step by reordering the reactions indices in a way that the most probable reactions channels are sampled first. The R -leaping algorithm is summarised in Algorithm 6.

The sampling of reaction channels from the bounded binomial distribution reduces the appearance of negative species, compared to sampling from the unbounded Poisson distribution. However, in systems involving species with a population close to zero taking place in very fast reactions, the R -leaping algorithm might also introduce negative population. To control the appearance of the negative population, an additional bounding condition for L was proposed [10]. In systems with high rejection rates of the proposed state update, the total number of firings is computed as $L = \min(L', L'')$, where L' is given by Eq. (7.15) and

$$L'' = \min_{j=1, \dots, M} \left(1 - \theta \left(1 - \frac{a_0(\mathbf{x})}{a_j(\mathbf{x})} \right) \right) L_j, \quad (7.17)$$

where

$$L_j = \min_{\substack{i=1,\dots,N \\ v_{ij} < 0}} \left\lfloor \frac{x_i}{|v_{ij}|} \right\rfloor. \quad (7.18)$$

The parameter θ controls the appearance of negative species. Smaller values of θ lead to better control of negative species but also to lower performance.

Algorithm 6 R-Leaping

```

1: Initialise:  $T_{\text{end}}, t \leftarrow 0, \mathbf{x} \leftarrow \mathbf{X}(0), \text{steps} \leftarrow 0, p \leftarrow$  frequency of reordering.
2: while  $t < T_{\text{end}}$  do
3:   Compute  $a_j(\mathbf{x})$  for  $j = 1, \dots, M$  and  $a_0(\mathbf{x})$ 
4:   if  $\text{mod}(\text{steps}, p) = 0$  then
5:     Reorder the reaction channels such that  $a_1(\mathbf{x}) \geq a_2(\mathbf{x}) \geq \dots \geq a_M(\mathbf{x})$ 
6:   end if
7:   Compute  $L$  by Eq. (7.15), then set  $L \leftarrow \max(L, 1)$ 
8:   Sample  $k_j$  by Eq. (7.16)
9:   if there is a negative component in  $\mathbf{x} + \sum_{j=1}^M k_j \mathbf{v}_j$  then
10:     $L \leftarrow L/2$  and go to 8.
11:  else
12:     $\tau \leftarrow \Gamma(L, 1/a_0(\mathbf{x}))$ 
13:     $\mathbf{x} \leftarrow \mathbf{x} + \sum_{j=1}^M k_j \mathbf{v}_j$ 
14:     $t \leftarrow t + \tau$ 
15:     $\text{steps} = \text{steps} + 1$ 
16:  end if
17: end while

```

7.2 The S-leaping algorithm

Here, we propose the *S*-leaping, an algorithm which combines the advantages of the τ - and *R*-leaping methods. The *S*-leaping couples the efficient time step selection of the τ -leaping with the effective binomial sampling of the *R*-leaping. The coupling of the algorithms is achieved in the following way. First, the time-step τ is selected according to Eq. (7.2). Then the total number of firings L that will take place in the time interval $[t, t + \tau)$ is estimated. Since in the τ -leaping each reaction channel is independently sampled as $k_j \sim \mathcal{P}(a_j(\mathbf{x})\tau)$, the total amount of all firings L follows the Poisson distribution with parameter $a_0(\mathbf{x})\tau$, i.e.,

$$L(t) \sim \mathcal{P}(a_0(\mathbf{x})\tau), \quad (7.19)$$

where $\mathbf{x} = \mathbf{X}(t)$. Knowing the number of reactions that will take place in $[t, t + \tau)$, the firings of each channel k_j can be sampled from the binomial distribution given by Eq. (7.16). If the sampled L is zero, it means the system will advance to the time $t = t + \tau$ without any changes since no reaction will be fired. In such case, the system can be further advanced by setting $L = 1$ and $\tau \sim \Gamma(1, 1/a_0(\mathbf{x}))$ and proceeding with the *S*-leaping algorithm. Notice that this is just one step of SSA since the Γ distribution with parameters 1 and $1/a_0(\mathbf{x})$ is equal to the exponential

distribution with parameter $1/a_0(\mathbf{x})$. The S -leaping algorithm is summarised in Algorithm 7.

Algorithm 7 S -Leaping

```

1: Initialise:  $T_{\text{end}}, t \leftarrow 0, \mathbf{x} \leftarrow \mathbf{X}(0), \text{steps} \leftarrow 0, p \leftarrow$  frequency of reordering.
2: while  $t < T_{\text{end}}$  do
3:   Compute  $a_j(\mathbf{x})$  for  $j = 1, \dots, M$  and  $a_0(\mathbf{x})$ 
4:   if  $\text{mod}(\text{steps}, p) = 0$  then
5:     Reorder the reaction channels such that  $a_1(\mathbf{x}) \geq a_2(\mathbf{x}) \geq \dots \geq a_M(\mathbf{x})$ 
6:   end if
7:   Compute  $\tau$  by Eq. (7.2)
8:   Sample  $L$  by Eq. (7.19)
9:   if  $L=0$  then
10:     $t \leftarrow t + \tau$ 
11:     $L \leftarrow 1$  and  $\tau \leftarrow \Gamma(1, 1/a_0(\mathbf{x}))$ 
12:  end if
13:  Sample  $k_j$  by Eq. (7.16)
14:  if there is a negative component in  $\mathbf{x} + \sum_{j=1}^M k_j \mathbf{v}_j$  then
15:     $\tau \leftarrow \tau/2$  and go to 8
16:  else
17:     $\mathbf{x} \leftarrow \mathbf{x} + \sum_{j=1}^M k_j \mathbf{v}_j$ 
18:     $t \leftarrow t + \tau$ 
19:     $\text{steps} = \text{steps} + 1$ .
20:  end if
21: end while
    
```

To control the appearance of the negative species, the S -leaping can inherit the control mechanism from the τ - or R -leaping. Here we bound L similarly as in the R -leaping method. In systems with high rejections rates, the total amount of firings is computed as $L = \min(L', L'')$, where L' is given by Eq. (7.19) and L'' by Eq. (7.17). If L'' was chosen, then the time step τ should be recomputed as $\tau \sim \Gamma(L, 1/a_0(\mathbf{x}))$.

Thanks to the coupling of the two algorithms, the S -leaping performs always as well as the τ - or R -leaping algorithm. In the non-stiff systems, the S -leaping benefits from the efficient time step selection and might outperform the R -leaping. On the other hand, in the case of big and stiff systems, the S -leaping surpasses the τ -leaping due to the effective sampling of the reaction channels. Since the behavior of the system might change over time, the S -leaping can outperform both the R - and τ -leaping, as shown in Section 7.3. Moreover, since the S -leaping uses the same time-step selection as the τ -leaping, the algorithm can be extended to an adaptive explicit-implicit version, as shown in the next section.

Adaptive S-leaping

The adaptive S-leaping switch between explicit (Algorithm 7) and implicit method depending on the stiffness of the system. The implicit S-leaping formulation would update the system state as,

$$\mathbf{X}(t + \tau) = \mathbf{X}(t) + \sum_{j=1}^M \mathbf{v}_j k_j^{\mathcal{B}}(\mathbf{X}(t + \tau)). \quad (7.20)$$

However, this would require sampling random numbers $k_j^{\mathcal{B}}(\mathbf{X}(t + \tau))$ from the binomial distribution $\mathcal{B}(\alpha(\mathbf{x}'), \beta(\mathbf{x}'))$ with mean and variance evaluated at the unknown state $\mathbf{x}' = \mathbf{X}(t + \tau)$ given by

$$\begin{aligned} \alpha(\mathbf{x}') &= L(\mathbf{x}') - \sum_{m=1}^{j-1} k_m^{\mathcal{B}}(\mathbf{x}'), \\ \beta(\mathbf{x}') &= \frac{a_j(\mathbf{x}')}{a_0(\mathbf{x}') - \sum_{m=1}^{j-1} a_m(\mathbf{x}')} . \end{aligned}$$

In the implicit τ -leaping algorithm, each firing $k_j^{\mathcal{P}}$ is independently approximated by the partially implicit formulation given by Eq. (7.7). This cannot be directly applied in the S-leaping since each sample $k_j^{\mathcal{B}}$ depends on all previously drawn samples $k_\ell^{\mathcal{B}}$, $\ell = 1, 2, \dots, j-1$. The partially implicit treatment for the S-leaping can be obtained by rather considering the distribution of the whole vector of all firings (k_1, \dots, k_M) , i.e., the multinomial distribution with parameter $(\frac{a_1(\mathbf{x})}{a_0(\mathbf{x})}, \dots, \frac{a_M(\mathbf{x})}{a_0(\mathbf{x})})$ and L the number of trials. If $k_j^{\mathcal{M}}$ is the j -th entry of a random vector that follows the multinomial distribution with parameters $(\frac{a_1(\mathbf{x})}{a_0(\mathbf{x})}, \dots, \frac{a_M(\mathbf{x})}{a_0(\mathbf{x})})$ and L , then $k_j^{\mathcal{M}}$ can be expressed as the sum of a random variable with mean $\frac{a_j(\mathbf{x})}{a_0(\mathbf{x})}L$ and the zero mean variable $k_j^{\mathcal{M}} - \frac{a_j(\mathbf{x})}{a_0(\mathbf{x})}L$, i.e.,

$$k_j^{\mathcal{M}} = \frac{a_j(\mathbf{x})}{a_0(\mathbf{x})}L + k_j^{\mathcal{M}} - \frac{a_j(\mathbf{x})}{a_0(\mathbf{x})}L. \quad (7.21)$$

The variable $\frac{a_j}{a_0}L$ is evaluated at the unknown state $\mathbf{X}(t + \tau)$, while the variable $k_j^{\mathcal{M}} - \frac{a_j}{a_0}L$ is evaluated at the known state $\mathbf{X}(t)$. The partial implicit approximation of the variables $k_j^{\mathcal{M}}$ leads to the following system of implicit equations,

$$\mathbf{x}' = \mathbf{x} + \sum_{j=1}^M \mathbf{v}_j \frac{a_j(\mathbf{x}')}{a_0(\mathbf{x}')} L(t + \tau) + \sum_{j=1}^M \mathbf{v}_j \left(k_j^{\mathcal{M}}(\mathbf{x}) - \frac{a_j(\mathbf{x})}{a_0(\mathbf{x})} L(t) \right), \quad (7.22)$$

for $\mathbf{x} = \mathbf{X}(t)$ and $\mathbf{x}' = \mathbf{X}(t + \tau)$. Since the multinomial random vectors $k_j^{\mathcal{M}}$ in Eq. (7.22) depend on the known state \mathbf{x} and since the j -th element of the multinomial distribution follows binomial distribution, $k_j^{\mathcal{M}}(\mathbf{x})$ are computed by Eq. (7.16). However, $L(t + \tau)$ is also a random variable from the Poisson distribution with the parameter evaluated at the unknown state $\mathbf{X}(t + \tau)$:

$$L(t + \tau) \sim \mathcal{P}(a_0(\mathbf{X}(t + \tau))\tau). \quad (7.23)$$

The term $L(t + \tau)$ could be expressed in the partial implicit manner following Eq. (7.7). However, a simpler formulation can be obtain by a mean approximation:

$$L(t + \tau) \approx a_0(\mathbf{X}(t + \tau))\tau, \quad (7.24)$$

which corresponds to the computation of the L in the R -leaping method.

Algorithm 8 Adaptive S-Leaping

```

1: Initialise:  $T_{\text{end}}, t \leftarrow 0, \mathbf{x} \leftarrow \mathbf{X}(0), \text{steps} \leftarrow 0, p \leftarrow$  frequency of reordering.
2: while  $t < T_{\text{end}}$  do
3:   Compute  $a_j(\mathbf{x})$  for  $j = 1, \dots, M$  and  $a_0(\mathbf{x})$ 
4:   if  $\text{mod}(\text{steps}, p) = 0$  then
5:     Reorder the reaction channels such that  $a_1(\mathbf{x}) \geq a_2(\mathbf{x}) \geq \dots \geq a_M(\mathbf{x})$ 
6:   end if
7:   Compute  $\tau^{(\text{ex})}$  by Eq. (7.2) and  $\tau^{(\text{im})}$  by Eq. (7.11)
8:   if  $\tau^{(\text{im})} > 100 \tau^{(\text{ex})}$  then
9:     System is stiff and  $\tau \leftarrow \tau^{(\text{im})}$ 
10:  else
11:    System is non-stiff and  $\tau \leftarrow \tau^{(\text{ex})}$ 
12:  end if
13:  if the system is currently non stiff then
14:    Compute  $L$  by Eq. (7.19)
15:    if  $L=0$  then
16:       $t \leftarrow t + \tau$ 
17:       $L \leftarrow 1$  and  $\tau \leftarrow \Gamma(1, 1/a_0(\mathbf{x}))$ 
18:    end if
19:    Sample  $k_j$  by Eq. (7.16)
20:  else
21:    Compute  $k_j$  by Eq. (7.26), where  $L(t)$  is given by Eq. (7.19)
22:  end if
23:  if there is a negative component in  $\mathbf{x} + \sum_{j=1}^M k_j \mathbf{v}_j$  then
24:     $\tau \leftarrow \tau/2$  and go to 13
25:  else
26:     $\mathbf{x} \leftarrow \mathbf{x} + \sum_{j=1}^M k_j \mathbf{v}_j$ 
27:     $t \leftarrow t + \tau$ 
28:     $\text{steps} = \text{steps} + 1$ .
29:  end if
30: end while
    
```

The advantage of the mean approximation in Eq. (7.24) is that it significantly reduces the numerical complexity of the implicit system in Eq. (7.22), while the partial implicit approximation provided by Eq. (7.7) would increase the complexity even more. Since we are dealing with a stiff system, increased complexity could reduce the accuracy of the numerical methods used for solving the implicit system of equations. If \mathbf{X}^* is the solution of the implicit system of Eq. (7.22), then the implicit update is obtained as

$$\mathbf{X}(t + \tau) = \mathbf{X}(t) + \sum_{j=1}^M \mathbf{v}_j k_j^{\mathcal{M}*}, \quad (7.25)$$

where

$$k_j^{\mathcal{M}*} = \left[a_j(\mathbf{X}^*)\tau + k_j^{\mathcal{M}}(\mathbf{X}(t)) - \frac{a_j(\mathbf{X}(t))}{a_0(\mathbf{X}(t))} L(t) \right]. \quad (7.26)$$

This means that both, the implicit τ - and implicit S-leaping algorithm solve the implicit system with the same computational complexity. However, since the implicit S-leaping can exploit the

reordering of the reaction channels, it might result in less random number generations (at most M samples) than the implicit τ -leaping (always M samples). This might allow the implicit S -leaping to outperform the implicit τ -leaping, especially in large stiff systems where only a few reaction channels are fired per time step. The adaptive S -leaping method is summarised in Algorithm 8.

7.3 Numerical results

To demonstrate the efficiency of the S -leaping algorithm, it is studied in comparison with the τ - and R -leaping on four reaction networks. The first one is a non-stiff system simulating decaying dimerization. The second system is a stiff decaying dimerization with reversible reaction channels in partial equilibrium. The third one is a system with very fast dynamics simulating the evolution of *Bacillus subtilis*. The last one is a LacZ/LacY system, which consists of a relatively large amount of reactions and which stiffness change over time. For each reaction network and each algorithm, we measure two quantities: the error and the execution time of the algorithm.

The error measurements. The error is measured as follows. For 25 equally distributed time points and all species, we estimate the distance between the distributions of the tested algorithm and the SSA [24]. Since the methods do not advance the system with a fixed time step, the population at a given time is approximated by the population at the closest time where the algorithm has landed. The distance d between two distributions P and Q is approximated by the estimated histogram as

$$d = \Delta \sum_k |\tilde{P}(k) - \tilde{Q}(k)|, \quad (7.27)$$

where Δ is the bin size and $\tilde{P}(k), \tilde{Q}(k)$ are the values of the histogram for P and Q at the k -th bin. The histogram is computed using $N_s = 10^4$ independent trajectories and $K = 10$ number of bins. Finally, the average error over all time points and all species is reported. This definition of the error can be interpreted as a global error since it accounts for the temporal and interspecies error of the algorithm. Averaging the error over many time points takes into account the error not only at equilibrium but at transient regimes as well.

The histogram self-distance. In [27] the histogram self-distance was introduced as a measure of the accuracy of the histogram distance estimation. Any estimate below the value of self-distance should be considered inaccurate. A bound for the self-distance was derived in [27] and is given by $\sqrt{4K/(\pi N_s)}$. In all the histogram error plots we show the self-distance estimate as a constant blue line. Although the errors close or below this line should not be considered accurate we present them for completeness.

The speed-up measurements. The execution time is averaged over 10 independent runs. The ratio between the execution time of SSA and the execution time of each algorithm is reported

as a speed-up. Note that here the SSA is used only as a reference in order to compare the relative speed-up of the three approximate algorithms; the τ -, the R - and S -leaping. The execution times of the three methods are compared using as a reference the execution time of SSA. Hence changing the base implementation of SSA will not affect these comparisons results. Moreover, since we report the speed-up over the baseline SSA rather than CPU time, the presented results do not depend on the type of the used computer.

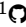
Software. All the tested methods are implemented in the C++ language, using the C++11 random number generator library. The code is publicly available¹ and the software is presented in Chapter 8.

7.3.1 Non-stiff decaying dimerization

Following the same test as in [10, 56, 57] we consider the non-stiff decaying dimerization system summarised in Table 7.1. The initial populations are $\mathbf{X}(0) = (4150, 39565, 3445)$ and the system is evolved until $T_{\text{end}} = 10$ using $\varepsilon = \{0.01, 0.03, 0.05\}$. Figure 7.2 shows the convergence of the histograms of the accelerated methods to the exact solution computed by the SSA for the species S_2 at time $t = 10$. All the approximate methods converge to the SSA solution as the accuracy parameter ε decreases. Fig. 7.3 shows the accuracy (left) and the speed-up over SSA (right) for all leap methods with different accuracy parameter ε . In this system, all the leaping methods have comparable accuracy and performance. No additional speed-up was obtained by reordering of the reaction channels in the R - and S -leaping since in each step of the simulation all reaction channels are fired.

	Reaction	Reaction Rate (non-stiff)	Reaction Rate (stiff)
R_1	$S_1 \longrightarrow \emptyset$	1	1
R_2	$S_1 + S_1 \longrightarrow S_2$	0.002	10
R_3	$S_2 \longrightarrow S_1 + S_1$	0.5	1000
R_4	$S_2 \longrightarrow S_3$	0.04	0.1

Table 7.1: The reaction network for the dimerization system studied in Sections 7.3.1 and 7.3.2.

¹ <https://github.com/JanaLipkova/SSM>

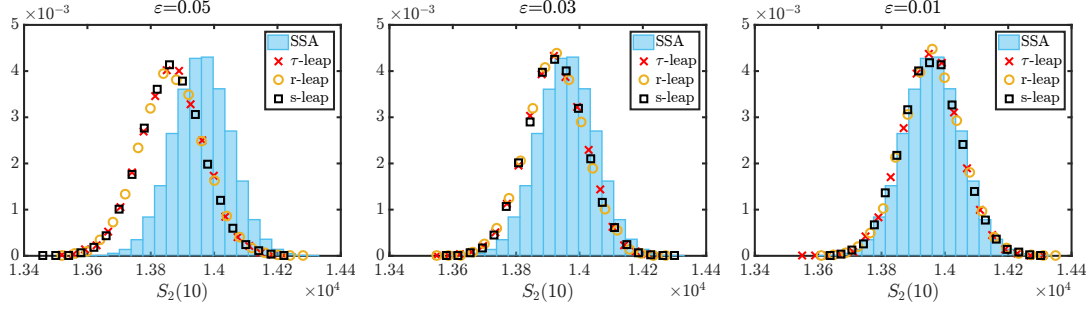


Figure 7.2: Convergence of the approximate leap solutions to the exact SSA solution with decreasing values of the accuracy parameter ε for the non-stiff dimerization system of Section 7.3.1.

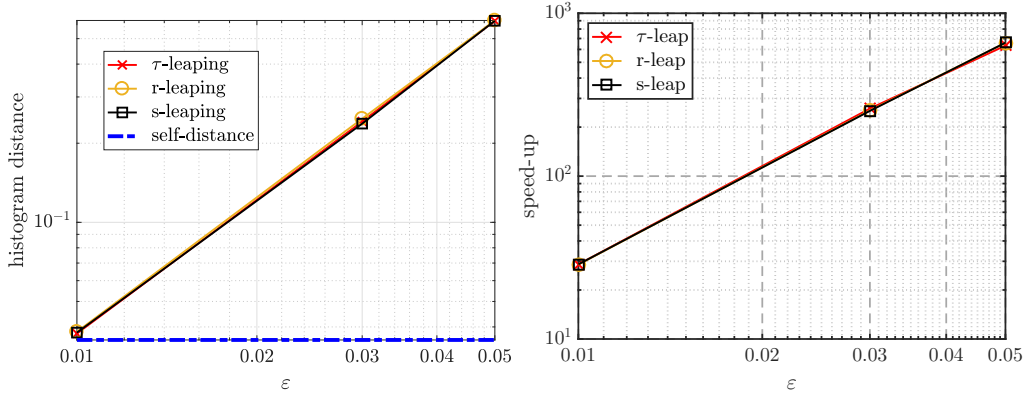


Figure 7.3: Errors and speed-up for non-stiff dimerization system of Section 7.3.1.

7.3.2 Stiff decaying dimerization

To study the efficiency of the adaptive S-leaping method we consider the stiff decaying dimerization system studied in [26, 145]. The system is defined by the same set of reactions and initial conditions as in Section 7.3.1, see Table 7.1. The stiffness arises from the reaction rates that vary by a few orders of magnitude. The behavior of this system changes over time; starting with a non-stiff phase and progressing to stiff phase once the reversible reactions R_2 and R_3 approach the equilibrium. Under this set-up S_1 and S_2 are the fast variables, while S_3 is the slow variable. The system is evolved until the final time $T_{\text{end}} = 10$ for $\varepsilon = \{0.01, 0.03, 0.05\}$.

Figure 7.4 shows the accuracy and the performance of the adaptive τ - and adaptive S-leaping as well as the explicit R-, τ - and S-leaping. All explicit methods reach comparable accuracy and performance. The adaptive methods provide significant speed-up over their explicit counterparts. The reduced accuracy of the adaptive methods arises from the dumping effect of the implicit methods on the fast variables. As reported in [145], the implicit schemes capture the distribution of the slow variable S_3 correctly. However, for the fast variables S_1 and S_2 , the mean is computed correctly but the histogram distribution around the mean is too narrow. In [145] a downshifting

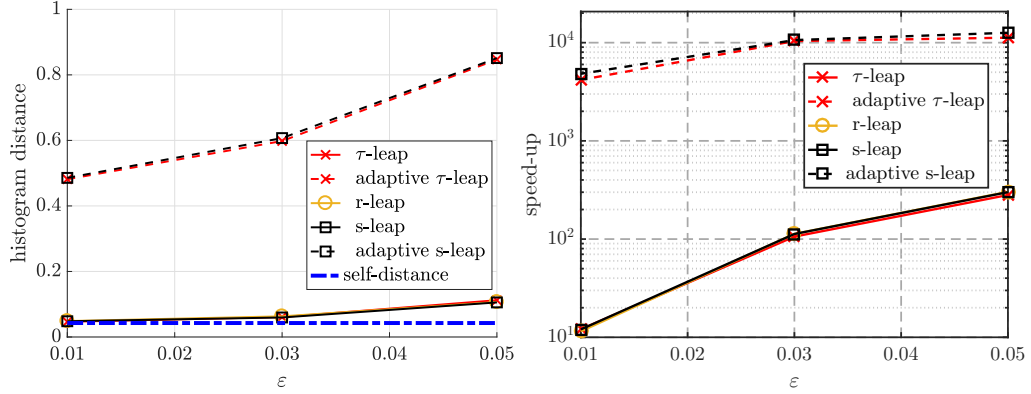


Figure 7.4: Errors and efficiency for stiff dimerization system discussed in Section 7.3.2.

strategy was proposed to restore the natural fluctuations in the fast variables by simulating the final time steps of the adaptive method with the explicit method. As shown in [25, 145], the downshifting leads to correct histogram distributions for all variables at the final time. Since the downshifting procedure corrects the dumping effect only in the final time, the global error of the adaptive method will not be reduced to the level of the explicit methods. Since we report the global error, the downshifting strategy was not applied here. However, the downshifting procedure can be used to increase the accuracy of the adaptive τ - and adaptive S -leaping method at the fixed time point.

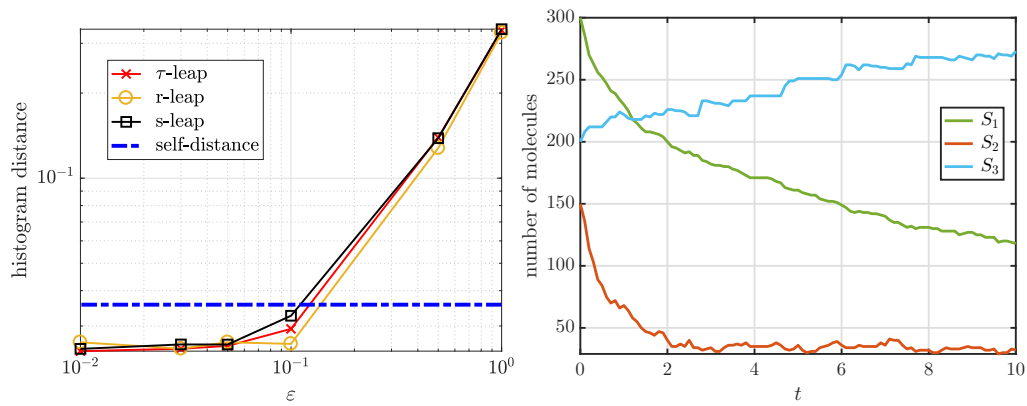
7.3.3 *Bacillus subtilis*

This system describes the cellular differentiation dynamics of the *Bacillus subtilis* which exhibits stochastic behavior at the single-cell level [113, 171]. The differentiation dynamics depends on the expression of the transcriptional genes $S_1 = Spo0A$, $S_2 = ComG$ and $S_3 = sinI$ and the reaction network is presented in Table 7.2 [29]. The system is evolved until the final time $T_{\text{end}} = 10$ with initial population $\mathbf{X}(0) = (300, 150, 200)$. Fig. 7.5 (right) shows a single realization of the *Bacillus subtilis* system computed with SSA. This system exhibits diverse reaction rates and very fast dynamics. As a consequence, the leap methods are strongly restricted by the leap condition and do not provide additional speed-up over SSA. Table 7.3 shows the average number of steps executed by each method and the averaged CPU time for $\epsilon = 0.05$. The R -leaping algorithm advances the system only with one reaction per time step, emulating the SSA. In comparison, the τ -leaping executes two times more steps than SSA. In this system, the S -leaping is the only method which requires less steps than SSA. Since in this case, the leap methods do not provide additional speed up, the SSA alone would be the best choice. This example, however, shows that the S -leaping maintains its performance even in fast dynamical systems and outperforms the other leap methods. All methods reach comparable accuracy as shown in Fig. 7.5 (left).

	Reaction	Reaction Rate
R_1	$\emptyset \longrightarrow S_1 + 3S_3$	1.51×10^{-1}
R_2	$S_1 + S_2 \longrightarrow 4S_3$	3.1×10^{-4}
R_3	$S_2 \longrightarrow 4S_3$	3.4×10^{-3}
R_4	$S_3 \longrightarrow S_1 + S_2$	2.0×10^{-2}
R_5	$S_1 + 2S_2 \longrightarrow \emptyset$	6.2×10^{-5}
R_6	$2S_1 \longrightarrow S_1 + S_2$	4.9×10^{-4}

Table 7.2: The reaction network for the *Bacillus subtilis* system studied in Section 7.3.3.

Method	Average number of steps	Average CPU time [sec]
SSA	266.6	0.028
τ -leap	423.4	0.086
R -leap	263.2	0.053
S -leap	220.8	0.045

Table 7.3: The averaged number of simulation steps and the execution time for the *Bacillus subtilis* system with the $\varepsilon = 0.05$ presented in Section 7.3.3.Figure 7.5: Error of the leap methods (left) and a single trajectory of the *Bacillus subtilis* computed with SSA (right).

7.3.4 LacZ/LacY

In this section, we consider the LacZ/LacY model which describes the expression of the LacZ and LacY genes and the activity of LacZ and LacY proteins in *Escherichia Coli* [88]. The reaction network consists of 22 reactions and 23 species. We present the reaction network, along with the reaction rate of each reaction in Table 7.4. The propensity functions of this system vary by a few orders of magnitude making the system stiff. Moreover, the reaction system is considered inside a growing cell, with generation time $T_{\text{gen}} = 2100$. The growing volume changes the stiffness of the system over time since the propensities of the second and higher order reactions have to be rescaled by the volume. We consider two different initial conditions. In the first case, we assume a small initial population where all species are initially 0 except for $PLac = 1$. In the second case, we consider bigger initial populations with all species initialized at 50 and $PLac=100$. In addition, the number of the species *RNAP* and *ribosome* are sampled every time step from a normal distribution $\mathcal{N}(35(1 + t/T_{\text{gen}}), 3.5^2)$ and $\mathcal{N}(350(1 + t/T_{\text{gen}}), 35^2)$, respectively for each case. The role of the system with a small initial population is to investigate the behavior of all methods in the presence of negative population, while the behavior without the appearance of negative populations is studied in the system with the bigger initial population.

The small initial population. The system with a small initial population is simulated until $T_{\text{end}} = 2100$. Since none of the reversible reactions approached partial equilibrium during this time interval, only explicit methods are reported. To control the appearance of negative species, the τ -leaping algorithm is used with the control parameter $N_c = 10$ [25], while the *S*- and *R*-leaping use $\theta = 0.1$, as suggested in [10]. For comparison purposes, all three methods are also considered without the control mechanism. The frequency of reordering in the *R*- and *S*-leaping is set to $p = 10000$, as proposed in [10]. Fig. 7.6 (right) shows the speed-up for the leap methods over SSA for $T_{\text{end}} = 2100$. A single evaluation of the SSA for time $T_{\text{end}} = 2100$ takes around 45 min, making the evaluation of the models accuracy at this time point computationally expensive. Instead, Fig. 7.6 (left) reports the error for all methods over the time interval $[0, 100]$. For this system, the error is averaged over the species *TrLacZ2*, *TrRbsLacZ*, and *RbsribosomeLacY*.

The τ -leaping algorithm, as presented in Algorithm 4, executes mainly SSA steps and provides almost no speed up over SSA. Therefore, we turned off the SSA execution in the reported τ -leaping. The leap methods without the control mechanism provide better speed-up over SSA, however, their accuracy is reduced due to the high rejection rate. The sampling of reaction channels from the correlated binomial distribution in the *R*- and *S*-leaping leads to a lower rejection rate in comparison with the τ -leaping, which is also reflected by the lower accuracy of the τ -leaping.

The control mechanisms in all leap methods result in high accuracy, at the cost of slightly reduced performance. The error reported in Fig. 7.6 (left) is relatively constant and do not scale with ϵ , since the accuracy of these leap methods is mainly restricted by the mechanism preventing the appearance of the negative species. The *S*-leaping reached comparable accuracy with the

	Reaction	Reaction Rate
R_1	$\text{PLac} + \text{RNAP} \longrightarrow \text{PLacRNAP}$	0.17
R_2	$\text{PLacRNAP} \longrightarrow \text{PLac} + \text{RNAP}$	10
R_3	$\text{PLacRNAP} \longrightarrow \text{TrLacZ1}$	1
R_4	$\text{TrLacZ1} \longrightarrow \text{RbsLacZ} + \text{PLac} + \text{TrLacZ2}$	1
R_5	$\text{TrLacZ2} \longrightarrow \text{TrLacY1}$	0.015
R_6	$\text{TrLacY1} \longrightarrow \text{RbsLacY} + \text{TrLacY2}$	1
R_7	$\text{TrLacY2} \longrightarrow \text{RNAP}$	0.36
R_8	$\text{Ribosome} + \text{RbsLacZ} \longrightarrow \text{RbsribosomeLacZ}$	0.17
R_9	$\text{RbsribosomeLacZ} \longrightarrow \text{Ribosome} + \text{RbsLacZ}$	0.45
R_{10}	$\text{Ribosome} + \text{RbsLacY} \longrightarrow \text{RbsribosomeLacY}$	0.17
R_{11}	$\text{RbsribosomeLacY} \longrightarrow \text{Ribosome} + \text{RbsLacY}$	0.45
R_{12}	$\text{RbsribosomeLacZ} \longrightarrow \text{TrRbsLacZ} + \text{RbsLacZ}$	0.4
R_{13}	$\text{RbsribosomeLacY} \longrightarrow \text{TrRbsLacY} + \text{RbsLacY}$	0.4
R_{14}	$\text{TrRbsLacZ} \longrightarrow \text{LacZ}$	0.015
R_{15}	$\text{TrRbsLacY} \longrightarrow \text{LacY}$	0.036
R_{16}	$\text{LacZ} \longrightarrow \text{dgrLacZ}$	6.42×10^{-5}
R_{17}	$\text{LacY} \longrightarrow \text{dgrLacY}$	6.42×10^{-5}
R_{18}	$\text{RbsLacZ} \longrightarrow \text{dgrRbsLacZ}$	0.3
R_{19}	$\text{RbsLacY} \longrightarrow \text{dgrRbsLacY}$	0.3
R_{20}	$\text{LacZ} + \text{lactose} \longrightarrow \text{LacZlactose}$	9.52×10^{-5}
R_{21}	$\text{LacZlactose} \longrightarrow \text{product} + \text{LacZ}$	431
R_{22}	$\text{LacY} \longrightarrow \text{lactose} + \text{LacY}$	14

Table 7.4: The reaction network for the LacZ/LacY system discussed in Section 7.3.4.

R-leaping since they both use similar control mechanisms. On the other hand, the τ -leaping considers most reactions critical and thus advance them with SSA, which lead to higher accuracy. The *R*- and *S*-leaping benefit from the reordering of reaction channels and outperform the τ -leaping. Moreover, since the stiffness of the system changes over time, the *S*-leaping outperforms both methods.

The large initial population. The system with big initial population is evolved until time $T_{\text{end}} = 100$. As before, the τ -leaping with the SSA-step performs mostly SSA and therefore the SSA-step was disabled. Since all species appear in relatively large populations, the leap methods are considered without the control of the negative population. The performance and accuracy of all methods is shown in Fig. 7.7. The *S*-leaping algorithm again outperforms both the τ - and *R*-leaping due to the combined advantages inherited from both methods.

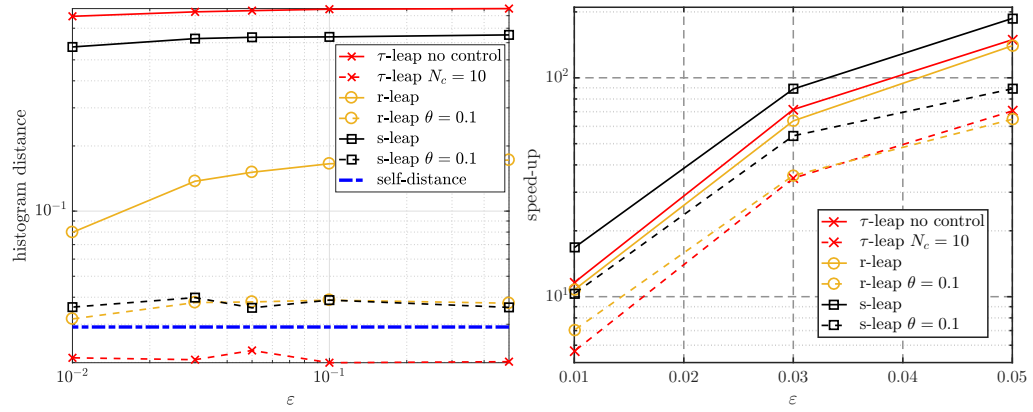


Figure 7.6: Errors and efficiency for the LacZ/LacY system discussed in Section 7.3.4, with small initial population.

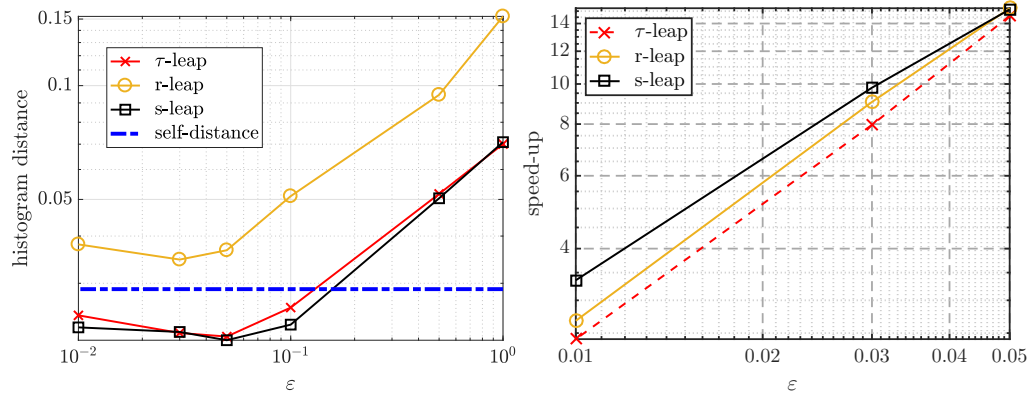


Figure 7.7: Errors and efficiency for the LacZ/LacY system discussed in Section 7.3.4, with large initial population.

7.4 Summary

This chapter has presented stochastic simulation algorithms for chemically reacting systems and introduced the *S*-leaping, an approximate algorithm for accelerating the SSA. The proposed algorithm combines the main advantages from the τ - and *R*-leaping; particularly the efficient time step selection intrinsic to the τ -leaping and the efficient sampling procedures from the *R*-leaping. The first advantage enables the extension of the *S*-leaping to adaptive explicit/implicit version. The second one reduces the sampling cost as well as the appearance of negative species. Thanks to this fusion, the performance of the *S*-leaping is comparable with the fastest method from the τ - and *R*-leaping alternative or it even outperforms both of them. The *S*-leaping can be thus considered as optimal adaptive coupling of the *R*- and τ -leaping method.

The increased performance provided by the *S*-leaping allows to study larger and more complex systems. Moreover, the *S*-leaping can be further combined with the compartment-based approach [46] or Brownian dynamics models [110] to extend the simulation framework to reaction-diffusion processes. This would, for instance, allow the simulation of diffusion of the imaging tracers or chemotherapeutic drugs as well as their interaction with the tumor cells.

Disclaimer: This chapter is partially reproduced from the article J. Lipková, G. Arampatzis, P. Chatelain, B. Menze and P. Koumoutsakos: "S-Leaping: An adaptive, accelerated stochastic simulation algorithm, bridging τ -leaping and R-leaping", published in Bulletin of Mathematical Biology, 80 (459) (2018).

SCIENTIFIC SOFTWARE

Open-source software has become a remarkable solution to deploy scientific research. It contributes to transparency, reproducibility, and scientific progress. To follow the open-source initiative, the software packages developed during this Ph.D. work are publicly released. In this chapter, the following three platforms are presented: 1) *Glioma solver*, 2) *Brain tumor processing pipeline*, and 3) *Stochastic simulation methods software*. The first one is a software for simulating tumor dynamics in the patient-specific anatomy reconstructed from the medical scans, as presented in Chapters 4 and 5. The second platform executes processing of multimodal head MRI scans of patients with brain lesions, including features like skull-stripping, tumor and tissue segmentation, along with an interactive graphical user interface (GUI) for easy inspection and correction of the segmentations. The last software performs simulations of chemical reaction networks, as presented in Chapter 7. Each software is presented together with the main implementation and application details. Modularity and extensibility of each platform are discussed to enable future development. The reader is directed to the repository of respective softwares for installation instructions and user manuals. The software packages developed here are released with the hope to facilitate their deployment in scientific and clinical practice and to encourage further improvements.



8.1 Glioma solver

The *Glioma solver* is a software for simulating tumor dynamics in the patient-specific anatomies reconstructed from medical scans. The platform currently supports the following models:

- Tumor growth model (see Section 4.1)
- Tumor mass effect and intracranial pressure (see Section 4.2)
- Bayesian model calibration for personalized radiotherapy planning (see Chapter 5)
- Cahn-Hilliard solver (see Section 4.2 and Appendix B)

The main advantages of the software include:

1. **Fast execution:** thanks to *highly-parallel implementation* and *adaptive grid refinement*
2. **User-friendly:** the user needs to provide only the input anatomy, name of the selected tumor model and the simulation parameters
3. **Modularity:** all numerical operations (e.g. Laplace, time integration) are implemented as independent operators. This enables easy implementation of new operators and their combination with the existing ones in order to describe new tumor models.
4. **Transferability:** the software can be used to model other types of infiltrative tumors (e.g. multiple myeloma or liver lesions)
5. Compatible with **Linux / Mac OS**

The software is publicly available at : <https://github.com/JanaLipkova/GliomaSolver>, while the software's homepage with installation packages, pre-compiled executables and tutorials can be found at : <http://tdo.sk/~janka/GliomaWebsite//index.html>.

Architecture

The *Glioma solver* is implemented in the C++ language, using Thread Building Blocks (TBB) and Message Passing Interface (MPI) parallelization. The software's architecture is shown in Fig. 8.1. The solver takes as input a file specifying: the path to the patient anatomy, name of the selected model and the simulation parameters. The main function – called `Glioma_main.cpp` – interprets the input file, sets-up the simulation environment and launches the selected tumor model simulation. Each numerical operator is implemented as an independent C++ class, allowing an easy extension for new operators in the future. The individual operators can be arbitrarily combined to describe given system of equations. For instance, the reaction-diffusion tumor growth model (presented in Chapter 4) combines the reaction-diffusion operator, time integration and I/O operators; as illustrated in Fig. 8.1. The solver outputs the state of the system at the regular time intervals prescribed by the user.

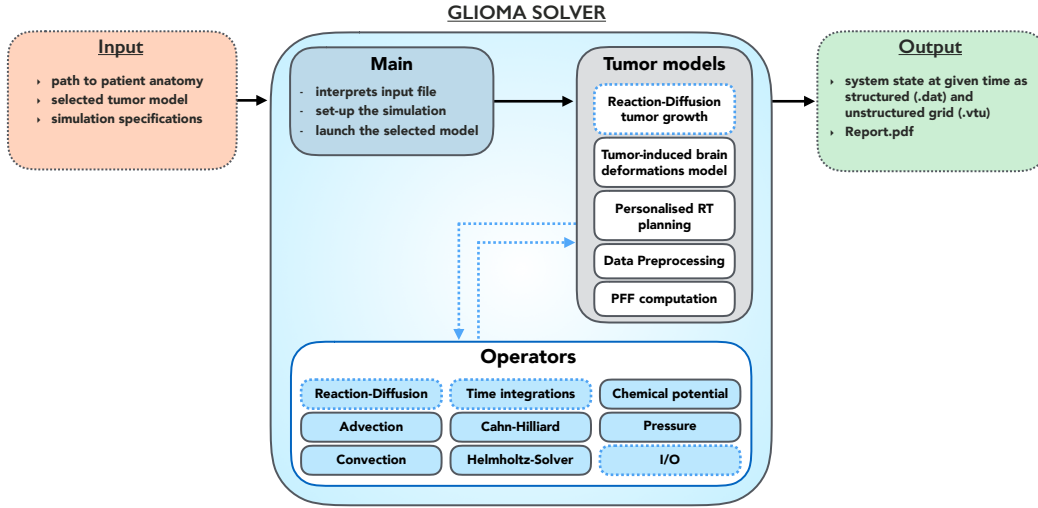


Figure 8.1: The architecture of the *Glioma solver*. The main function interprets the input file, set-ups the environment and launches the selected simulation. The currently supported tumor models are listed in the gray box while the numerical operators are shown in the white box. Each model calls a combination of the numerical operators describing its individual components. For instance, the reaction-diffusion tumor growth model combines the reaction-diffusion operator, time integration and I/O operator (all marked by the dashed blue lines). The simulation outputs the state of the system at the prescribed time intervals.

Parallelization

To ensure fast execution, the solver is implemented in a 3D extension of Multi-Resolution-Adaptive-Grid (MRAG) solver [153] that allows parallel processing and adaptive refinement of the simulation grid. The main idea of the MRAG grid handling is as follows. The simulation domain consists of blocks, which are processed in parallel using TBB library (see Fig. 8.2). The resolution of the individual blocks changes adaptively, such that the finest resolution is kept only in the blocks that contain the quantity of interest – usually the tumor cell density – while the remaining blocks are coarsened to accelerate the computation (see Fig. 8.3). The grid is adaptively refined and coarsened to ensure high accuracy together with high performance. The user can control the grid resolution, parallelization, and level of refinement. For more details see the documentation in the solver homepage.

An additional level of parallelization is provided by MPI communication. The MPI parallelization is used for computationally intensive models – such as the tumor-induced brain deformation model – where the speed-up from the distributed-memory computation surpasses the cost of the MPI communication. The MPI parallelization is also employed in the Bayesian calibration framework, where multiple evaluations of the same tumor model with different parameters are required. The Bayesian calibration further exploits the Π 4U framework [64] and *torc* [65] – a library for platform-independent task parallelization.

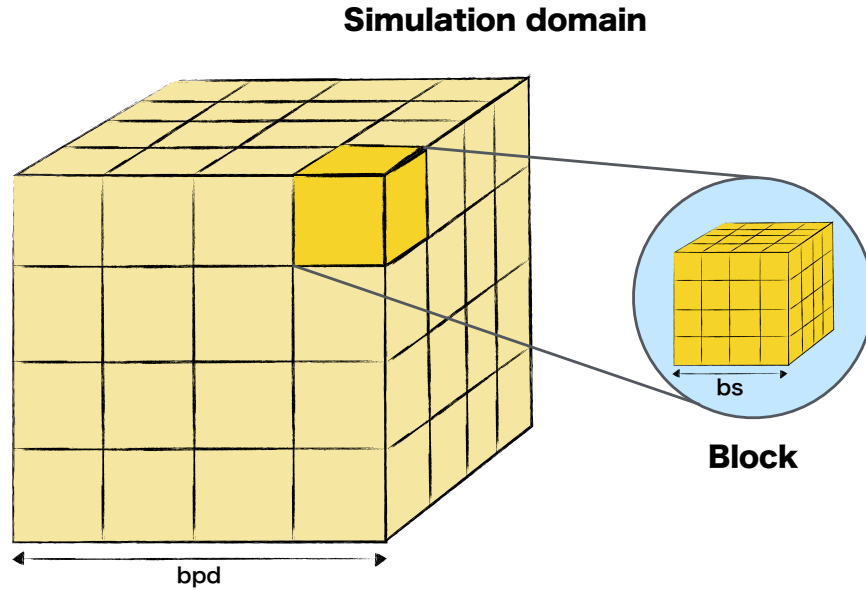


Figure 8.2: The simulation domain in the *Glioma solver* consists of blocks which are processed in parallel. Shown is a 3D domain with 4 blocks per dimension (bpd) and 4 grid points per block, referred to as a block size (bs).

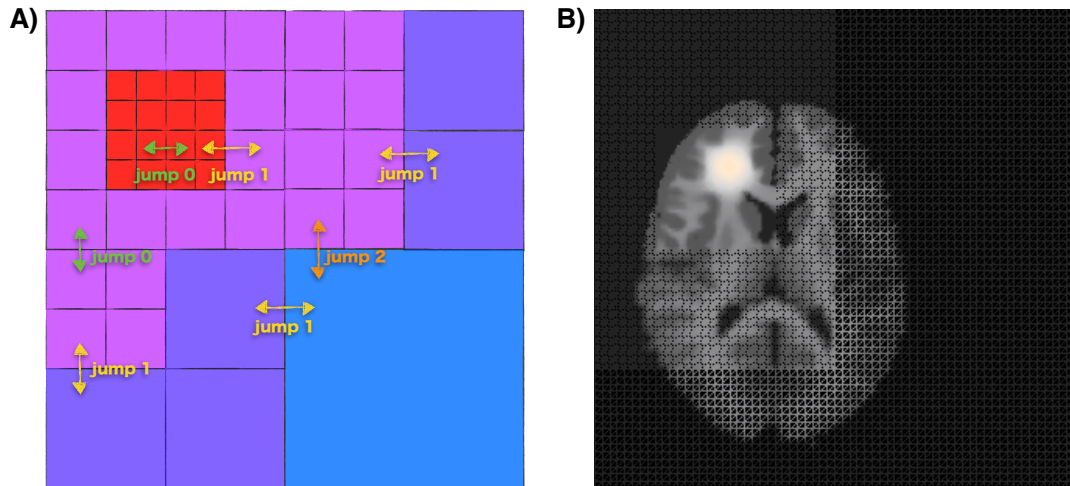


Figure 8.3: The adaptive grid refinement and compression. A) An illustration of the different levels of the jumps in the grid resolution caused by refinement/compression. B) An actual grid refinement/compression in the tumor growth simulation. The highest resolution is kept in the blocks containing the tumor, while the blocks distant from the tumor are compressed to accelerate the computation. The grid is adaptively compressed and refined with the growing tumor to maintain high accuracy and high performance (also see Fig. 8.4).

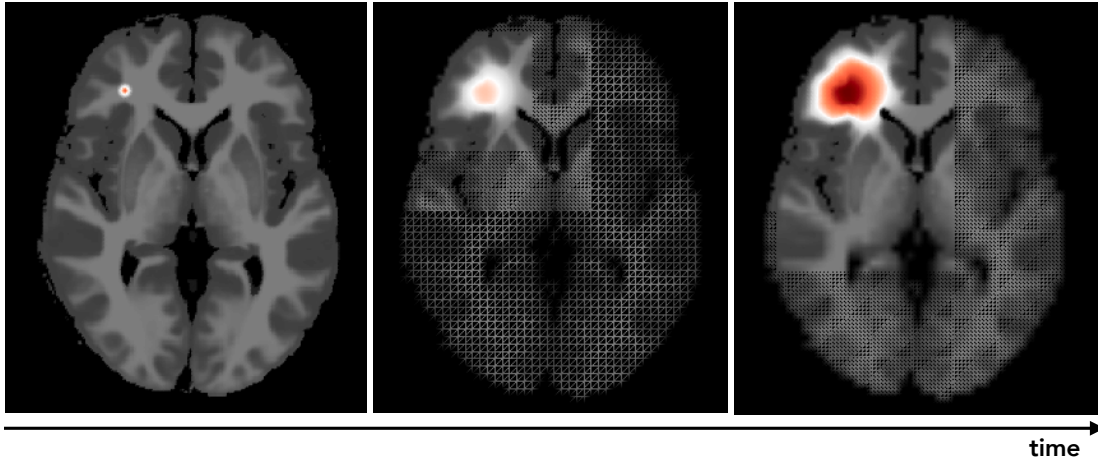


Figure 8.4: The results of the reaction-diffusion tumor growth model visualized with *ParaView*. The shown slice depicts the tumor cell density inside the brain anatomy (i.e. the *channel1*) at the three time points. The wireframe rendering is used to visualize the changes in the grid resolution.

Input

The *Glioma solver* takes as an input a path to the folder with the patient anatomy, name of the selected tumor model, and the simulation parameters. The patient input anatomy (i.e. white matter, gray matter and CSF) should be each provided as an individual file in the form of a 3D matrix in the *.dat* format. The software provides scripts for data conversion between *.nifty* and *.dat* format. The input anatomy is automatically mapped to the selected simulation grid. It means that the same input data can be used to perform lower-resolution simulations (e.g. during the testing phase) and high-resolution simulations (e.g. in the final phase). The Bayesian personalized RT planning framework is fully automated and accepts the input data also in the *.nifty* format. An example of the input file for each tumor model is provided in the tutorial in the software homepage.

Output

The solver outputs data in the prescribed time intervals using two data formats: *.dat* and *.vtu*. The *.dat* output contains the tumor cell density stored as a 3D matrix at the uniform grid, whereas the *.vtu* output contains multiple data (e.g. tumor cell density, brain anatomy) stored as individual channels on a non-uniform grid. The *.dat* output can be directly converted to *nifty* structure with the provided conversion scripts. The resolution of the non-uniform *.vtu* output grid is given by the resolution of the individual blocks of the simulation domain (see Fig. 8.3). Thus the grid refinement not only accelerates computation but it also reduces the memory requirements of the output data as well as the time needed for the writing of the output. The number of

channels stored in the *.vtu* output depends on the selected tumor model. For instance, in the reaction-diffusion tumor growth model the following channels are provided:

- **channel0** = tumor cell density
- **channel1** = tumor cell density inside the brain anatomy
- **channel2** = percentage of the white matter
- **channel3** = percentage of the gray matter
- **channel4** = percentage of the CSF

The channels of the *.vtu* output can be visualized in the parallel visualization tool called *ParaView* [12]. Figure 8.4 shows the *ParaView* visualization of the **channel1** of the reaction-diffusion tumor growth simulation. An overview of all output channels of all models is provided on the software homepage in the *Documentation* section.

Personalized RT planning model: The Bayesian framework for the personalized radiotherapy planning is designed in a fully automated way. For the given input patient data it provides the following output:

- **MAP.nii** - the estimated MAP tumor cell density mapped to the patient space.
- **Report.pdf** - report file with an overview of the performed calibration set-up, calibrated model parameters, visualization of the probability density function, an overview of the used imaging modalities and the MAP tumor cell density (see Fig. 8.5).
- **Details** - folder with more detail information, including a file with the samples from the posterior distribution.

Modularity and extensibility

The software can be easily extended to accommodate **new tumor models**. The existing operators can be combined to solve a given set of partial differential equations, while new operators can be easily added as follows:

- Create C++ structure with the new operator.
- Place the new operator inside the Glioma/Operators folder.
- Link the structure with the solver in Glioma/Glioma_Types.h.

For consistency with the platform, please follow the pattern of the existing operators.

The software can be further deployed to simulate **other types of infiltrative tumors**, such as multiple myeloma or liver lesions. To do so, the input brain anatomy should be replaced by corresponding new anatomy. For instance, to simulate the multiple myeloma dynamics inside

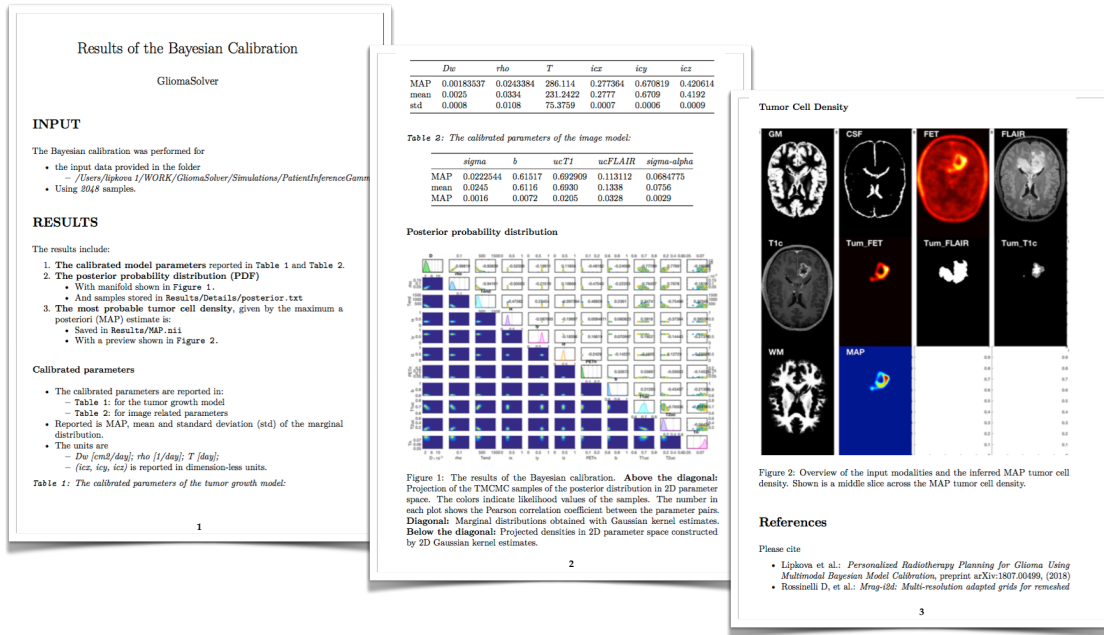


Figure 8.5: The report file created by the Bayesian calibration framework for the personalized RT planning. The file provides an overview of the performed simulation, calibrated parameters, visualization of the probability distribution function, used imaging modalities and the predicted MAP tumor cell density.

a vertebra, the gray and white matter segmentations can be replaced by the segmentation of cortical and cancellous bone¹, respectively. Afterward, the solver can be used to simulate tumor dynamics, accounting for the faster tumor infiltration inside the softer cancellous bone and slower involvement inside the denser cortical bone. The solver was also used to simulate tumor growth in rat brain anatomy in [47].

The provided Bayesian framework can be exploited to **calibrate other tumor models**. To see how to incorporate new models or imaging modalities to the calibration pipeline please see the *Tips & Tricks* section at the software homepage.

Disclaimer:

- The software presented in this section was publicly released in conjunction with the publication: J. Lipkova et al.: "Personalized Radiotherapy Design for Glioblastoma: Integrating Mathematical Tumor Models, Multimodal Scans, and Bayesian Inference", *IEEE Transactions on Medical Imaging*, (2019).

¹The cortical bone is the dense outer part of the bone, while the cancellous bone is the sponge-like tissue inside the bone containing the bone marrow.

- *The software was used to create simulations presented in Chapters 4 and 5 and Appendix B as well as in the publication: I. Ezhov, J. Lipkova, S. Shift, F. Kofler, N. Collomb, B. Lemasson, E. Barbier, and B. Menze: "Neural parameters estimation for brain tumor growth modeling." accepted at MICCAI, (2019).*
- *The software is implemented in the MRAG platform written by Diego Rossinelli. Part of the Glioma solver was written during my stay at CSE-Lab (ETHZ) by Prof. Petros Koumoutsakos.*

8.2 Brain tumor processing pipeline

Herein we present a modular software for processing head MRI scans of patients with brain lesions. The software accepts as input four commonly used MRI modalities (i.e. T1w, T1Gd, T2w, and FLAIR scans) and provides the following features:

- Data anonymization and conversion from *dicom* to *nifty*
- Registration of the multimodal scans
- Skull-stripping
- Tissue segmentation
- Tumor segmentation (edema, active tumor, non-active tumor, and whole tumor)
- Supervoxels computation
- An interactive tool for inspection and correction of the tumor segmentation

The pipeline offers four main advantages over standard image processing tools:

1. The software is designed in a **modular way** which allows the computation of tumor segmentations with any method available in the BraTS docker library (see Section 3.3.2) or with the provided default method. Hence, the pipeline can be always used with up-to-date methods.
2. The **interactive tool** allows the visualization of patient’s multimodal scans together with the tumor segmentation. The segmentation can be easily corrected by changing a label of a supervoxel², instead of manual corrections of multiple voxels across several slices; as it is in other image processing tools. This significantly reduces the correction time and increase the reproducibility of the results.
3. All processing steps are available within a **single platform**, liberating the user from switching between multiple processing softwares with various input/output formats.
4. Data of **multiple patients** can be processed at the same time using **different segmentation methods**.

The software is available at 🐙: gitlab.lrz.de:stevicaB/brain-tumor-segmentation, together with the installation instructions, user manual, and test data. The segmentation methods currently available in the BraTS dockers library can be found at 🏠: https://github.com/BraTS/Instructions/blob/master/Repository_Links.md.

²Supervoxel is a polyhedral part of a three-dimensional digital image, larger than a normal voxel, that is rendered in the same image intensity.

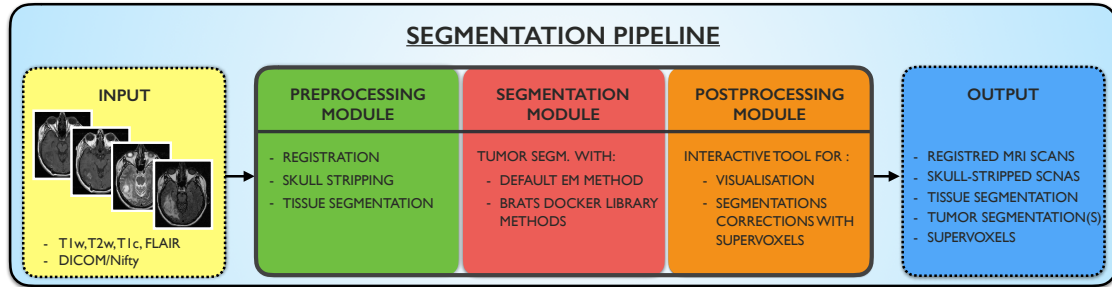


Figure 8.6: The architecture of the brain tumor processing pipeline. The software consists of three main parts: preprocessing, segmentation, and postprocessing module.

Architecture

The software is implemented in Python. The released version is Python 2.7, while Python 3 implementation is being currently tested. Figure 8.6 shows the architecture of the software. The software consists of three main modules: *preprocessing*, *segmentation* and *postprocessing module*. The individual modules can be used independently. The methods inside the modules can be replaced without a loss of compatibility with the rest of the pipeline. This is particularly useful for the segmentation module, where the default tumor segmentation method can be replaced by any method available in the BraTS docker library (see Section 3.3.2). Since new segmentation methods are added to the library with each new BraTS challenge, the pipeline can be always used with the up-to-date algorithms. The software comes with a GUI for easy data manipulation.

Input

The platform provides GUI, shown in Fig. 8.8, which allows to import and handle the patient data. The input data has to be provided in a specific structure, as shown in Fig. 8.7. For each patient, a folder with four MRI modalities named: "T1", "T1c", "T2" and "FLAIR", has to be provided. The platform supports both *nifty* (.nii or .nii.gz) and *dicom* formats. The GUI allows to load data of one or multiple patients at the same time. A detailed description of the data handling is provided in the *user manual* available in the software's repository.

Preprocessing module

This module performs all preprocessing steps needed prior to the tumor segmentation. The data are first converted from *dicom* to *nifty* – if *dicom* is the input format. All scans are then registered to the patient's T1w MRI scan to provide alignment between the modalities. To ensure compatibility with the algorithms in the BraTS dockers library, all scans are further mapped to the BraTS space. This step is not necessary if the default segmentation method is used. Nonetheless, it might be beneficial to map all scans to the same reference space, especially if

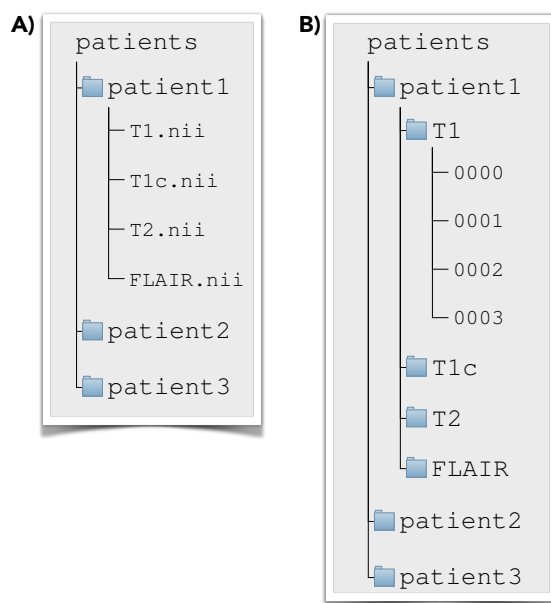


Figure 8.7: An illustration of the required folder structure with the input patient data in *nifty* (A) and *dicom* (B) format. Shown is a root folder, called *patients*, with data of three patients. Each patient folder has to contain four modalities. In the case of the *nifty* input, the modalities should be named "T1", "T1c", "T2" and "FLAIR" – provided in *.nii* or *.nii.gz* format. For the input *dicom* format, each patient folder has to contain four folders named: "T1", "T1c", "T2" and "FLAIR". Each of these folders should contain the corresponding *dicom* data. If the above folder structure is maintained, the software allows to load data of one or multiple patients at the same time.

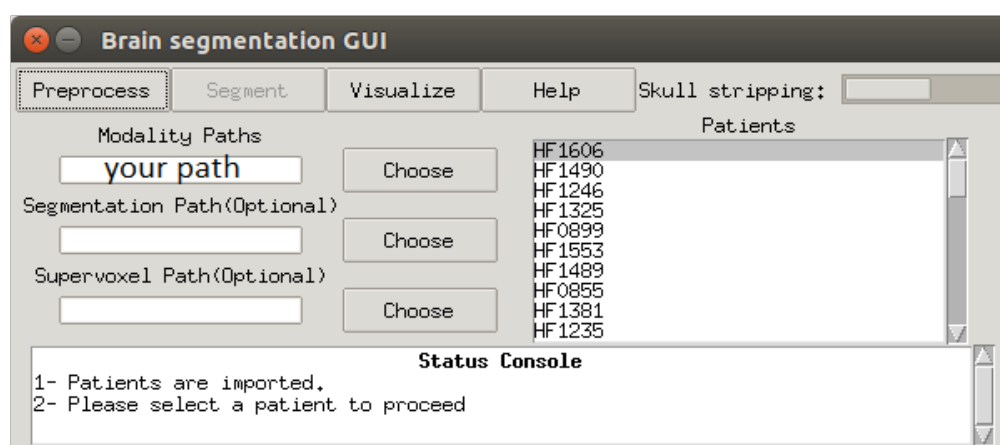


Figure 8.8: The central window of the GUI with imported data from multiple patients. The patient folder named HF1606 is selected for preprocessing, although multiple patients folders can be selected at once.

data from multiple patients or time points are studied. All aforementioned registrations are performed with ANTs library [11], using the rigid registration. Afterward, the S3 method (shown in Section 3.2.2) is used to skull-strip the scans and to obtain the brain tissue segmentations (white matter, gray matter, and CSF). The preprocessed data are used as input for the tumor segmentation module.

Tumor segmentation module

The second module takes as input the preprocessed data from the first module and computes tumor segmentation with the following four labels: edema, active tumor, non-active tumor, and whole tumor. The user can apply the default segmentation method or any method available in the BraTS docker library. The **default method** is the EM algorithm with a supervoxel classifier [4]. The method uses a random forest – trained on the supervoxels grid – to refine the segmentation and to ensure their spatial coherence across the modalities. To use segmentation **method from the BraTS library**, the docker container of the given method needs to be loaded to the pipeline. This is done by the "Manage Dockers" option in the GUI (see Fig. 8.9), where the user provides an image ID of the docker that should be loaded. The image ID can be found in the BraTS library webpage. The GUI allows the loading and usage of multiple segmentation methods at the same time. The segmentations from various methods can be fused, through majority voting or STAPLE [187] algorithm, which can lead to improved results as we have seen in Section 3.3.2. Since no automated method is perfect, the segmentations should be visually inspected and corrected, which is done by the last module.

Postprocessing module

The last module offers an interactive tool for visualization and correction of the segmentations. As shown in Fig. 8.10, the GUI allows the visualization of multimodal patient data together with the tumor segmentation. If the default segmentation method is used, the GUI also loads the supervoxels grid, which is computed during the segmentation phase. If a method from the docker library is used, the supervoxels will be computed in the visualization tool and displayed consequently. In both cases, the supervoxels are computed from the skull-stripped multimodal scans and the tumor segmentation, using the SLIC library [2]. The resulting supervoxels are 3D elements constrained by similar image intensities and consistency of the tumor segmentation across the modalities (see Fig. 8.10). Thanks to this, the supervoxels can be deployed in the correction of the tumor segmentation. To correct a segmentation, it is enough to select one or multiple supervoxels and change the corresponding segmentation label, as shown in Fig. 8.10. This accelerates the segmentation correction task and increases the reproducibility of the results, in comparison to standard approaches where multiple voxels across several slices have to be corrected manually.

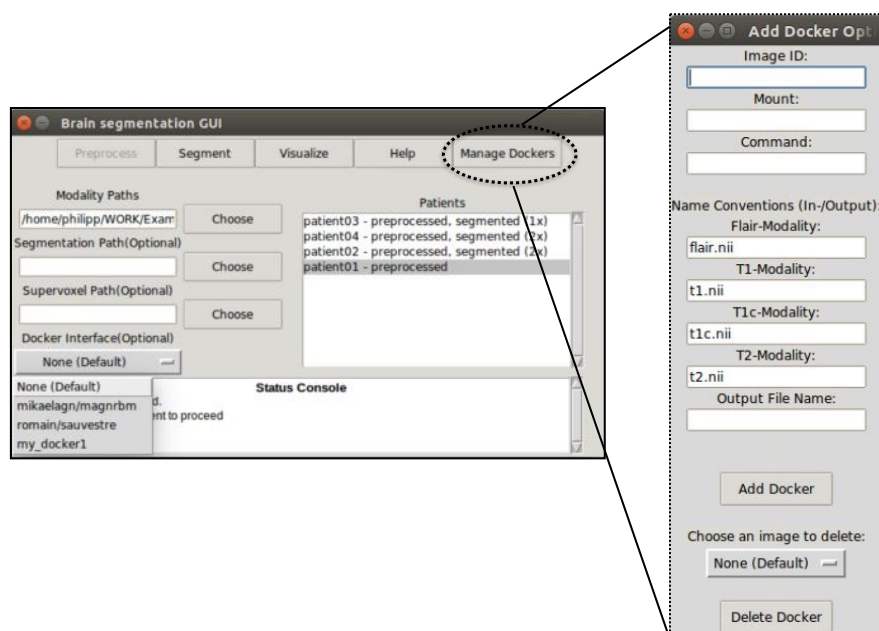


Figure 8.9: A snapshot of the segmentation GUI. The window named "Patients" shows data of four patients that have been already preprocessed by the first module. The data of the patient03 has been segmented by one method, while patient04 and patient02 have been segmented with two different methods. The lower left corner shows a list of available segmentations methods: the default one and three methods loaded from the docker library. The "Manage Dockers" button is used to load and unload the dockers.

Output

The pipeline provides the following outputs:

- registered multimodal MRI scans
- skull-stripped scans and brain mask
- brain tissue segmentations
- tumor segmentations (before and after correction)
- supervoxels

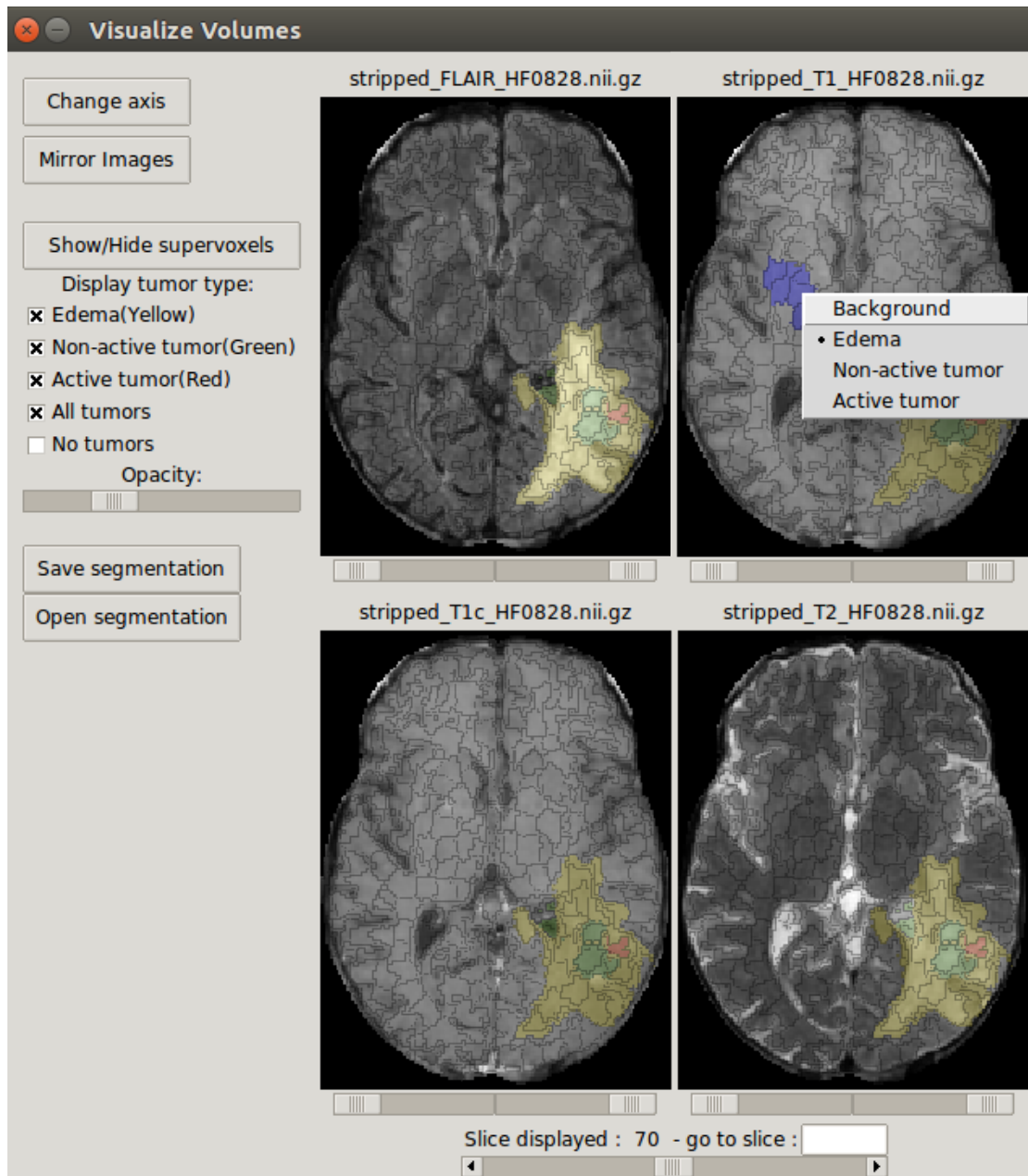


Figure 8.10: A snapshot of the interactive GUI for visualisation and segmentations corrections. Shown are skull-stripped and segmented MRI scans, together with the supervoxels grid. To correct a segmentation, the user can select one or multiple supervoxels, which get displayed in blue. The right-mouse click then displays a pop-up menu which allows to change the label of the selected supervoxels.

Modularity and extensibility

The pipeline consists of three main modules that can be used independently. The preprocessing module can be also applied to preprocess MRI scans of patients without brain lesion. The tissue segmentations can be deployed to estimate an extent of neurodegenerative diseases – such as Alzheimer – where the progression of the pathology is manifested by a decrease in the tissue volume over time. Since the postprocessing module allows to compute the supervoxels, it can be used even with segmentations computed outside of the pipeline. Finally, the segmentation module is the most flexible part, since it can be used with any method encapsulated in the docker container available on the BraTS docker library or even in the docker hub³.

Disclaimer:


- *The software presented in this section was written in a collaboration with Esther Alberts and several students that I had the pleasure to supervise. The first version of the pipeline was written by Stevica Bozhinoski, Yusuf Savran, and Abdurrahman Enes Senel – as part of their IDP project. Philipp Kaess, during his semester project, extended the pipeline to enable the usage of the segmentation methods from the docker containers. The IDP student, Mohak Chadha, translated the software to Python 3 and included the supervoxels computation into the visualization tool. Special thank goes to Christoph Berger for extending the BraTS docker library.*
- *The pipeline was deployed in the clinical study presented in Chapter 6. The first module of the pipeline was also used to preprocess data for the BraTS challenge (see Section 3.3.2).*

³<https://hub.docker.com/>

8.3 Stochastic simulation methods software

The stochastic simulation methods (SSMs) is a software for simulating networks of chemical reactions described by well-mixed continuous-time Markov chain models. The platform currently supports the following SSMs:

- the Gillespie SSA [55]
- the τ -leaping method [25]
- the R -leaping method [10]
- the S -leaping method [105]
- the Adaptive τ -leaping method [26]
- the Adaptive S -leaping method [105]

Description of all methods is presented in Chapter 7. The software is publicly available at : <https://github.com/JanaLipkova/SSM>. The repository contains also the installations instructions and several examples.

Architecture

The software is implemented in C++ language, using the C++11 random number generator library. Figure 8.11 shows the architecture of the software. The software takes as input an Extensible Markup Language (XML) file with the list of chemical reactions and the simulation specifications. The main function interprets the input file and launches the selected simulation. Each method is implemented as a separate C++ class, allowing an easy extension for new methods in the future. The software outputs two files containing: 1) mean trajectory of each chemical species and 2) the state of the system in the final time obtained from each sample; as shown in Fig. 8.11. Individual samples are simulated independently, allowing parallelization across the samples. The samples are distributed across the available processors using the platform-independent task parallelization library – called *torc* [65]. To ensure unique random numbers for each sample as well as reproducibility of the results, the random number generators are seeded with the unique index of each sample.

Input

The SSM software is using XML based input files utilizing the Systems Biology Markup Language (SBML) definition. The SBML is a standardized representation format for storing computational models in systems biology [44]. This ensures compatibility of the input file with most repositories of computational models, such as *BioModels Database* [30]. Examples of input XML files for several reactions systems can be found in the folder `SSM/ReactionSystemsXML`. Each input file consists of five parts:

1. <Header>
2. <AnnotationField>
3. <listOfCompartments>
4. <listOfSpecies>
5. <listOfReactions>

The 1.) <Header> contains standard SBML specifications and usually has the same structure as depicted in Fig. 8.12. 2.) The <AnnotationField> defines the simulation parameters such as: number of the samples, the simulation time, and the selected stochastic simulation method. 3.) <listOfCompartments> specifies the simulation domain, which is parametrized by its volume and number of compartments it constitutes of. Most simulations are performed in the unit volume domain with a single compartment. Multiple compartments are used to simulate stochastic reaction-diffusion processes, where the diffusion of molecules is modeled as a jump process between the neighboring compartments. For more information about the compartment-based stochastic methods see [23]. 4.) <listOfSpecies> prescribes the list of chemical species involved in the system and their initial amount. 5.) <listOfReactions> specifies the list of chemical reactions to be modeled, following the SBML standards. For the details about the input file and the parameters please see the provided examples in the repository folder SSM/ReactionSystemsXML.

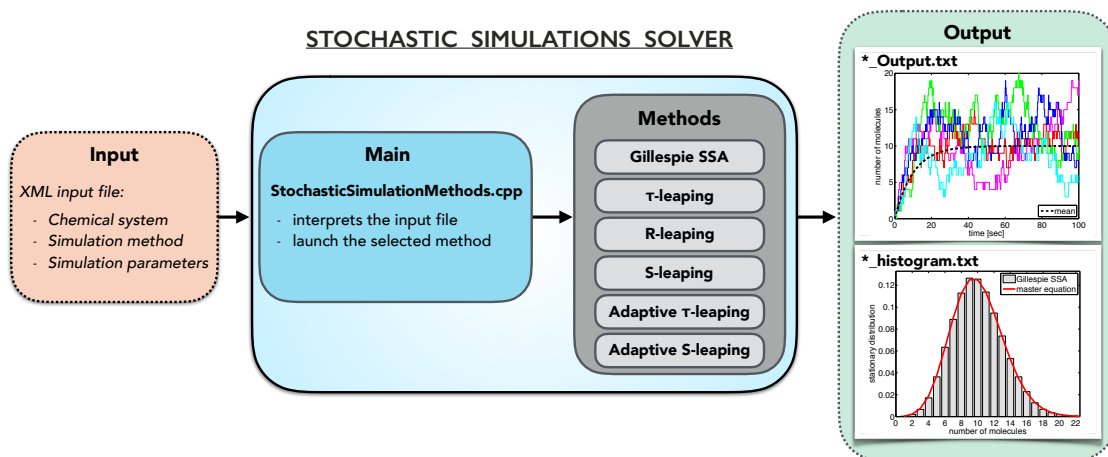


Figure 8.11: The architecture of SSM software. The input is provided in the form of XML file. The main function interprets the input and launches the selected simulation method. The currently supported SSMs are listed in the grey box. The software outputs two files, which content is visualized in the green box.

```
1 <?xml version="1.0" encoding="UTF-8"?>
2 <sbml xmlns:xsi="http://www.w3.org/2001/XMLSchema-instance"
3   xsi:schemaLocation="http://www.sbml.org/sbml/level1 http://www.sbml.org/sbml/level1"
4   xmlns="http://www.sbml.org/sbml/level1"
5   level="1"
6   version="2">
```

Figure 8.12: An illustration of the SBML header. The current implementation of the SSM software supports level 1 and 2 SBML files.

Output

Each simulation produces two output files with the extensions:

- **_Output.txt*
- **_histogram.txt*

while the prefix of the files contains the name of the selected simulation method. The first file stores a trajectory of each species computed as an average over the number of samples. Each column of the output file corresponds to one species and each line to one time point. The species are reported in the same order as they are initialized in the input file in `<listOfSpecies>` section. The number of time points in the output file is controlled by a parameter `stochSim:StoreInterval` in the `<AnnotationField>`. Figure 8.11 shows the mean trajectory as a dashed line while individual trajectories are shown in color. The second output file reports for each sample the number of each chemical species at the final time. Each line of the output file corresponds to one sample, while columns represent the individual species – reported in the same order as defined in the input file. This can be used to plot the histogram showing the distribution of the individual species at the final time, as shown in Fig. 8.11.

Modularity and extensibility

The software has been designed with modularity in mind and allows easy incorporation of new methods. To include a new method proceed as follows:

- Create a C++ class containing the new method.
- Link the class with the main function in `SSM/source/StochasticSimulationMethods.cpp`.

For consistency with the platform, please follow the design pattern of the existing methods. Please refer to the C++11 standards for random number generation.

Disclaimer:

- *The software presented in this section was written in collaboration with Basil Bayati, Gerardo Tauriello and George Arampatzis from the CSE Lab.*
- *The platform was publicly released in conjunction with the publication: Lipková, G. Arampatzis, P. Chatelain, B. Menze and P. Koumoutsakos: "S-Leaping: An adaptive, accelerated stochastic simulation algorithm, bridging τ -leaping and R-leaping ", published in *Bulletin of Mathematical Biology*, 80 (459) (2018).*
- *The SSM software was used to produce all the results presented in Chapter 7.*

GALLERY

Scientific visualizations play a significant role in understanding and analyzing results. This chapter presents a series of visualizations created within different projects during this Ph.D. work. The visualizations are performed with multiple rendering techniques and softwares; including Blender [151], Paraview [48], and Volume Perception [152]. Paraview is software for scientific visualizations, while Blender is used in computer graphics. Volume Perception – designed by Diego Rossinelli – is a rendering tool using a ray-casting technique. The main advantage of Volume Perception is its capability to visualize translucent iso-surfaces, which is often not possible with other softwares. In what follows, we present each visualization with a brief description of the used rendering method and the study behind it.

Sphere in a shear flow. Particle methods are a natural way of modeling flow problems. Particles can be seen as objects carrying a physical property of a system, following dynamics of a flow field. To assess the effectiveness and accuracy of a numerical method the following benchmark problem is considered. A sphere of a radius 0.15 and center at (0.35,0.35,0.35) is placed inside a unit cube. The sphere is then deformed by a divergent-free flow field; as proposed in [102]. The visualization in Fig. 9.1 shows three stages of the sphere’s deformation; with the initial state shown in the lower right corner, the intermediate state in the middle and the final state in the upper left corner. After reaching the final state, the flow deforms the interface back to the initial sphere, following the deformed states in reverse order. Since the deformation field is reversible, this simulation allows to evaluate the accuracy of a numerical method under complex conditions without knowing an analytical solution. For instance, incapability of the solver to reproduce the initial sphere indicates loss of the mass and dissipation of the method. The 3D visualization is used to identify sources and locations of such errors. The visualization is rendered with Volume Perception; the field is visualized as a translucent iso-surface obtained

with pre-integrated volume rendering. The visualization is accepted for a publication in a book *Beauty of Theoretical Biology*¹.

Pattern formation. Reaction and diffusion of chemical species can result in a variety of patterns, reminiscent of those observed in nature. The Gray-Scott equation [134] describes pattern formation caused by an interaction of two chemical species u and v which diffuse and react with each other. The reactions are controlled by reaction rates parameters, F and k . Different combination of these parameters results in significantly distinct patterns (see [134]). Here we present simulation of the Gray-Scott model inside a unit cube with parameters $F = 0.04$ and $k = 0.064$. Figure 9.2 shows the time evolution of the concentration of species u , initialized as a sphere with radius 0.1 in the center of a unit cube. The visualization is rendered with Volume Perception.

Brain tumor infiltration. As we saw in this thesis, medical imaging plays a central role in cancer therapy. However, the current imaging modalities cannot detect the full extent of infiltrative brain tumors, which in turns complicates radiotherapy planning. To tackle this issue, we calibrate a computational tumor growth model using the patient-specific structural and metabolic medical scans in a Bayesian inference framework to predict tumor cell infiltrations beyond those visible on the medical images (see Chapter 5). Figure 9.3 shows a visualization of a tumor infiltration inside the patient brain anatomy. Shown is the outline of the tumor visible on the medical scans in comparison with the predicted tumor infiltration. The brain anatomy is reconstructed from T1w MRI scan using the head processing software presented in Chapter 8. The visualization is rendered with Volume Perception and is accepted for a publication in a book *Beauty of Theoretical Biology*¹.

Bone mineral density. Increasing age is inevitable accompanied by a reduction in the bone mineral density. Medical images, such as CT scan, can be used to visualize such changes in the bone structure. Figure 9.4 shows a comparison of bone mineral density in two vertebrae – thoracic (T9) and lumbar (L5) – from 40 and 80 years old subjects. The decrease in the bone density is apparent mainly in the body and edges of the processes of the vertebrae. The vertebrae were segmented from the subject’s CT scans using the V-Net architecture; as presented in Section 3.2.4. The images are visualized with ParaView using volume rendering technique.

Human skull and brain anatomy. Figure 9.5 shows a visualization of the human skull, brain anatomy, and tumor, reconstructed from the MRI scan. The visualization is obtained with Blender, using surface rendering.

¹ <https://www.fias.science/de/lebenswissenschaften/gruppen/franziska-matthaeus/call/>

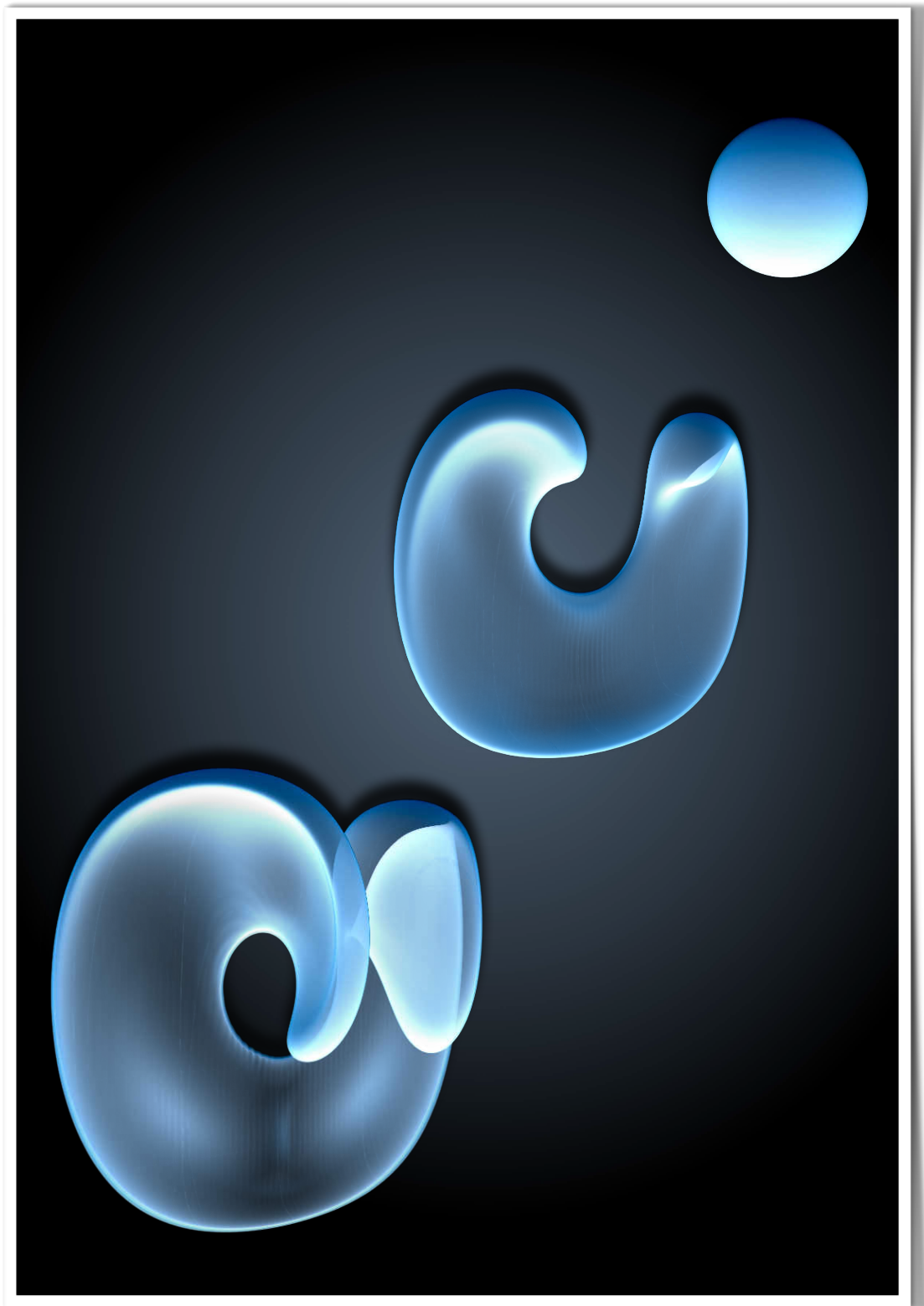


Figure 9.1: A sphere in a shear flow visualized as translucent iso-surface rendered by Volume Perception.

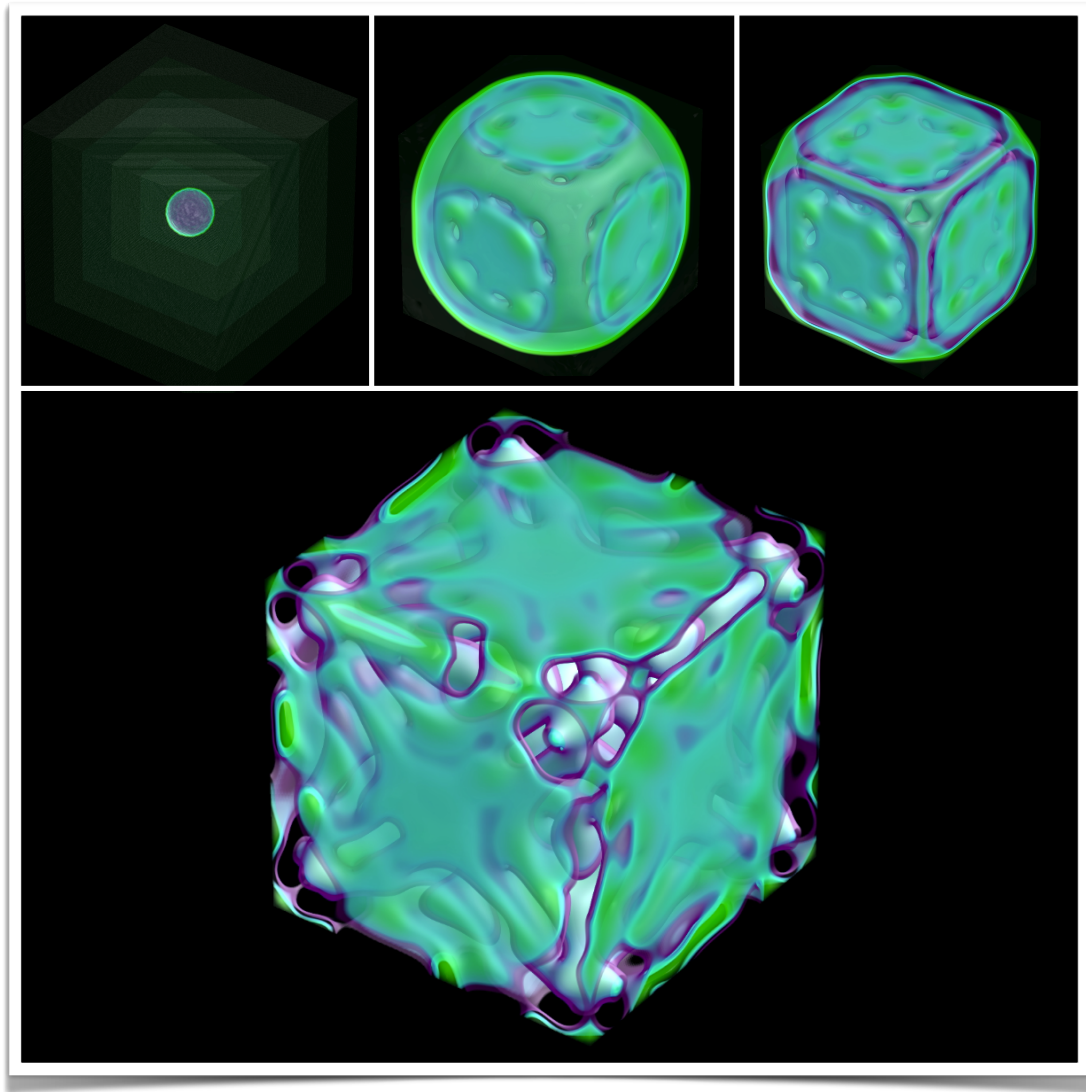


Figure 9.2: Simulation of the Gray-Scott system in a unit cube. The white/purple/green colors indicate high/medium/low concentration of u . The initial state is shown in the top right corner and the later states in middle and left in the top row. The final state – with the most resolved pattern – is shown at the bottom. The visualization is performed with Volume Perception.

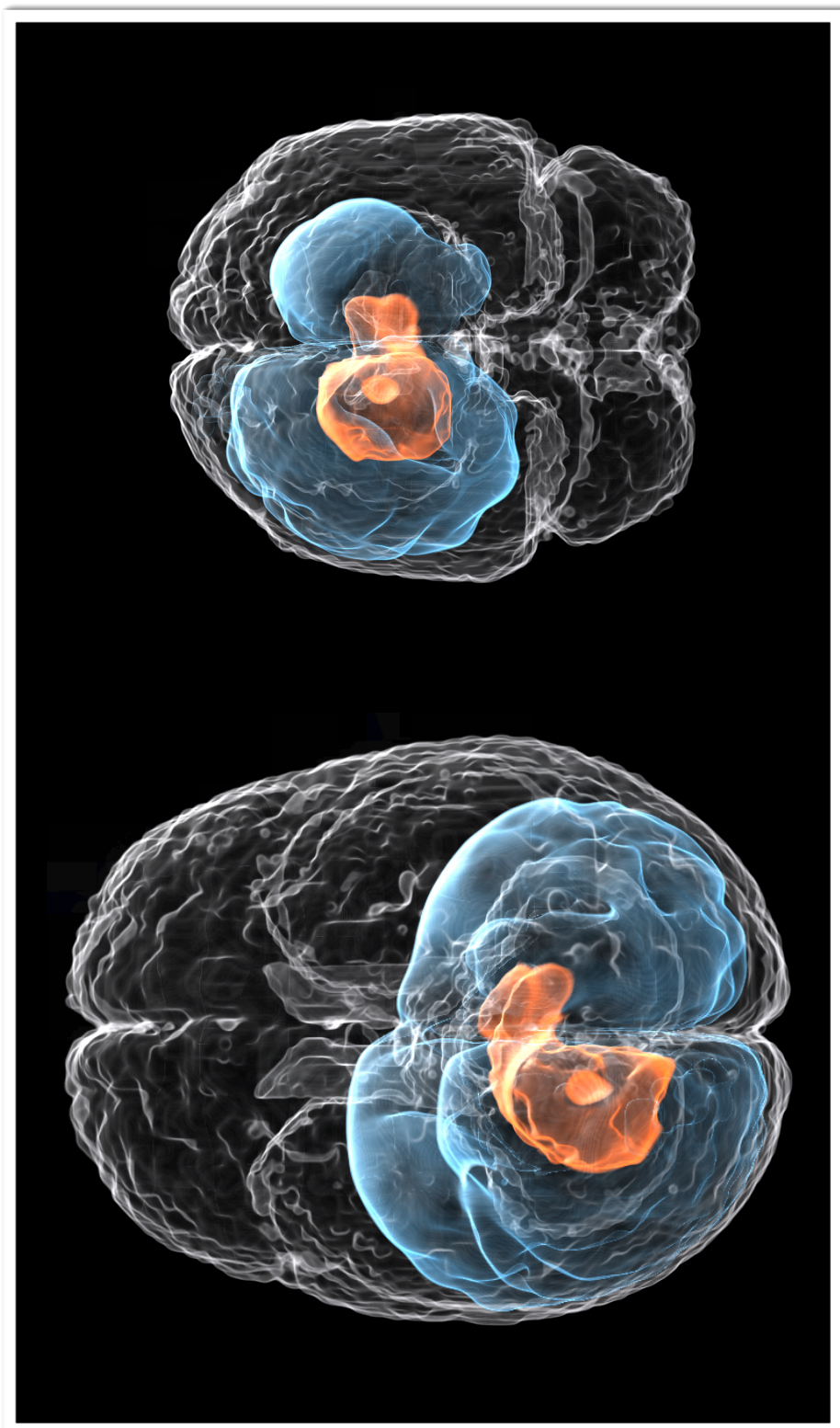


Figure 9.3: Visualization of tumor infiltration inside the patient brain anatomy. Translucent iso-surfaces, obtained by Volume Perception, are used to visualize the tumor outline visible on the patient's PET scans (orange) together with the outline of the predicted tumor cell infiltration (blue), inside the brain anatomy (white) reconstructed from the patient's medical scans.

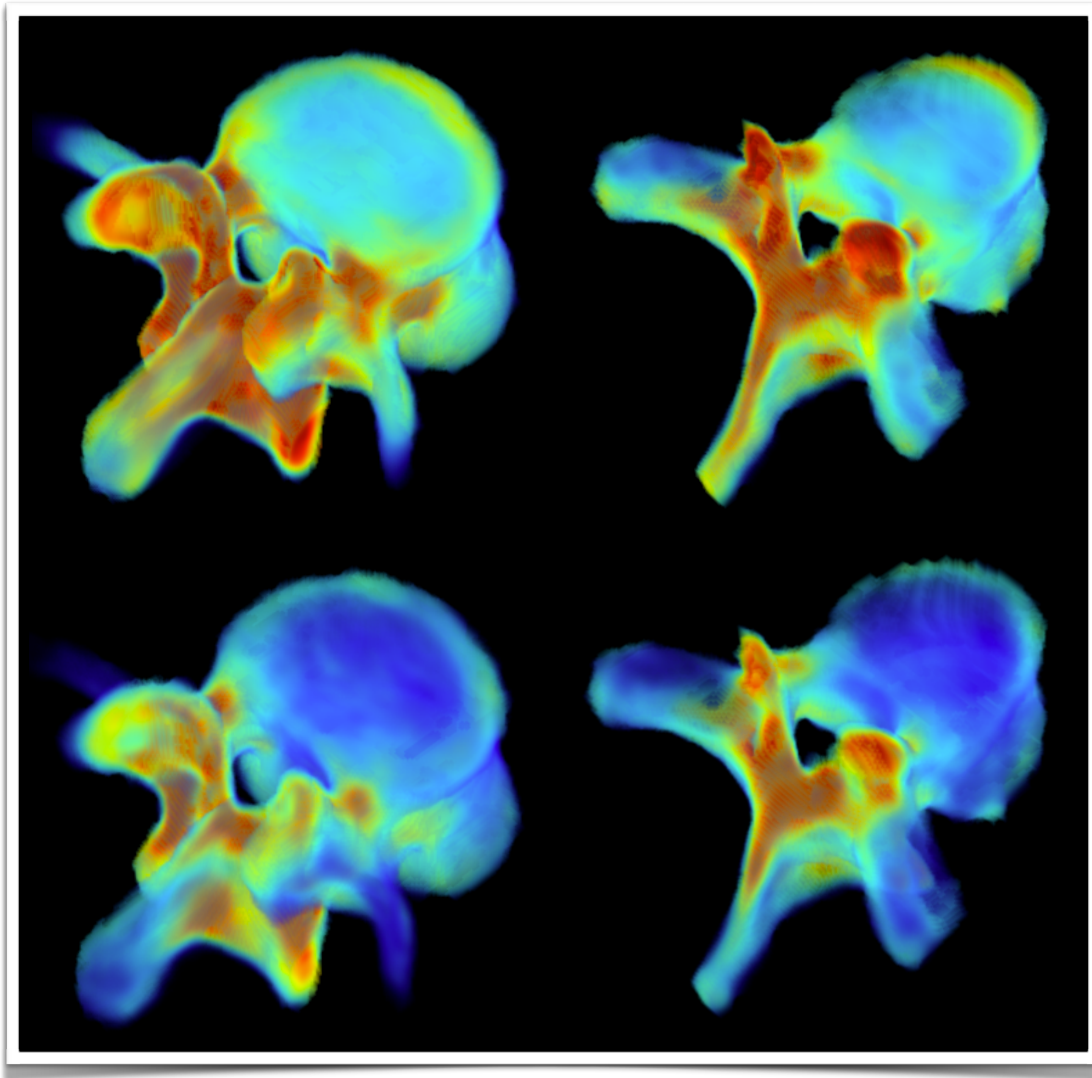


Figure 9.4: Visualization of changes in bone mineral density with increasing age. The top row shows thoracic (T9) and lumbar (L5) vertebrae of a 40 years old subject, while corresponding vertebrae from a 80 years old subject are shown at the bottom. The decrease in the bone density is apparent mainly in the body and edges of the processes of the vertebrae. The visualization was performed with ParaView using volume rendering technique.

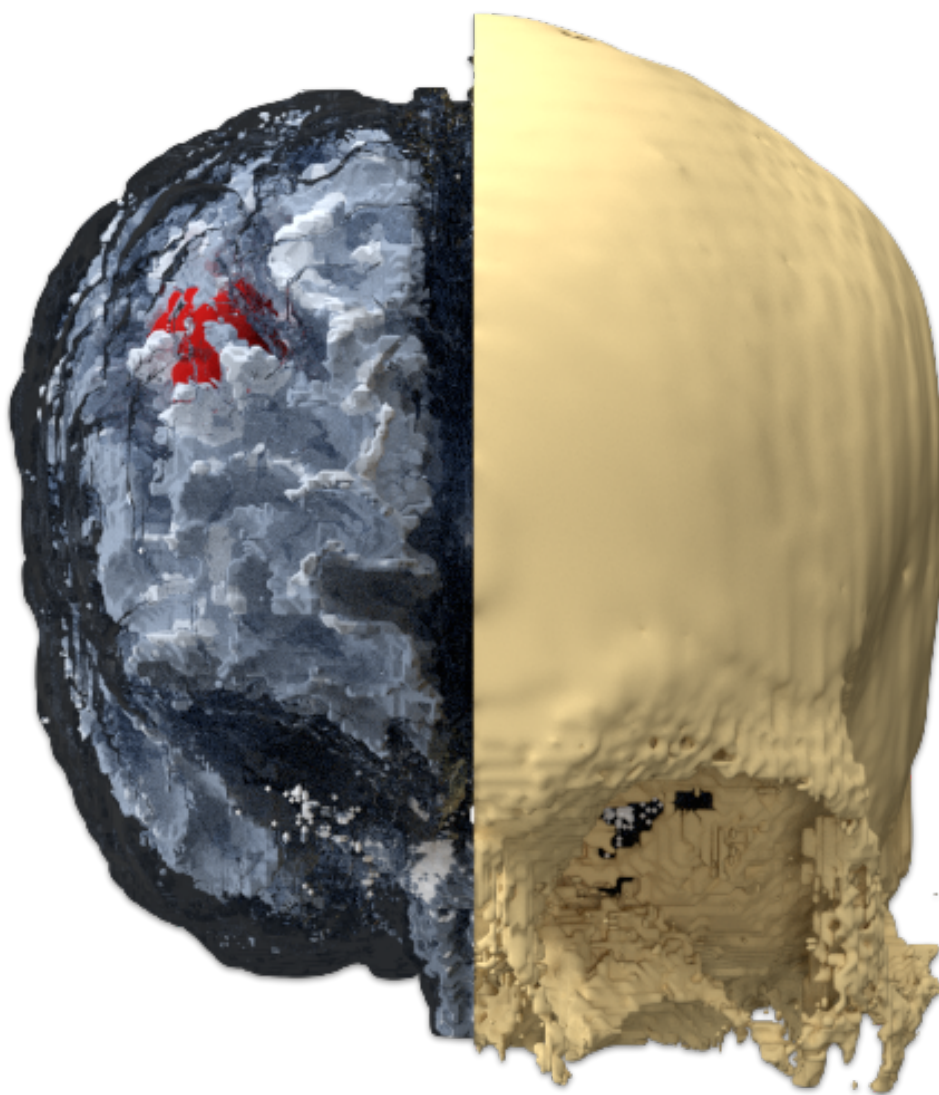


Figure 9.5: Visualization of human skull, brain, and tumor rendered with Blender. The skull, white matter and tumor are shown as non-transparent iso-surfaces, while the gray matter is visualized as opaque iso-surface.

CONCLUSION & OUTLOOK

The synergy of novel approaches from high-performance computing, computational modelling and medical imaging have paved a path to new possibilities in personalized medicine. This thesis has focussed on advances in the computational neurooncology and their application to clinical practice. This final chapter provides a brief summary of the main contributions of this work along with an outlook for the future research.

Contributions

In this thesis, we have presented new methods for automated detection and segmentation of lesions from patient medical scans as well as benchmarks for the unbiased evaluation of state-of-the-art segmentation methods (Chapter 3). We have developed a computational model of tumor progression in patient-specific anatomy, accounting for the most critical symptoms: tumor-induced brain deformations and intracranial pressure elevation (Chapter 4). A calibration strategy integrating information from the high-resolution MRI and highly-specific PET maps was developed to obtain patient-specific predictions about the tumor infiltration pathways (Chapter 5). The model predictions were deployed to design personalized radiotherapy plans. An initial clinical study showed that the personalized plans reduce radiation toxicity and identify radioresistant regions, while maintaining the accuracy of standard protocols. Next, we presented a pilot clinical study, which demonstrated the diagnostic potential of the CXCR4-directed PET imaging and suggested that it is able to predict the treatment response. Last but not least, an adaptive, accelerated stochastic simulation algorithm for modelling chemical reactions was developed (Chapter 7).

To facilitate the deployment of the presented contributions into scientific and clinical practice,

the developed algorithms were integrated into distributable software packages (Chapter 8). In particular, we have developed a scalable software for modelling tumor dynamics in patient-specific brain anatomies – called *GliomaSolver*. The software couples advanced numerical methods with a high-performance implementation, enabling efficient simulation of large, real world systems. Despite its name, the software is by no means restricted to brain tumors and can readily accommodate other types of malignancies and tumor models. Secondly, we designed a platform for processing and segmenting head scans of patients with brain lesions. To embrace the high pace with which new tumor segmentation methods are developed, the platform is designed in a modular way which allows the use of any segmentation method available in the BraTS docker library. The platform has already been employed to preprocess medical scans for the BraTS challenge and to assist in the CXCR4-directed PET clinical study. Thirdly, we presented a software for stochastic simulations of chemically reacting systems, which supports several of the state-of-the-art algorithms.

Application

Coming back to the vision presented in Chapter 1, how do these contributions come into play? Let us start with the medical scans that had to be manually processed by a radiologist. Now they can be processed and segmented automatically with the processing software developed herein. Since the accuracy of the automated methods is not yet at the level of manual segmentations – as we learned from the segmentation challenges – the automated segmentations have to be manually inspected and eventually corrected. Here, the postprocessing module offers a helping hand. Utilizing the supervoxels discretization, inspection and correction of multimodal patient scans takes approximately 5-10 minutes, which is a significant time reduction over manual approaches. Moreover, the time needed for the corrections will keep decreasing with the development of more advanced methods. Once the automated methods surpass the accuracy of the manual segmentations, the postprocessing module becomes redundant, but the rest of the platform remains usable thanks to its modular nature.

The processed scans can be further used as an input for the Bayesian calibration framework provided by the *GliomaSolver*. The software automatically calibrates the tumor model, estimates the tumor infiltration pathways, and computes personalized radiotherapy plans. Since the personalized plans were tested only on a small cohort so far, visual inspection is still needed. In the first phase of the process, a radiologist can fuse the hospital-specific and the personalized radiotherapy plans, taking into consideration the estimated tumor-free regions and radioresistant areas. After sufficient clinical evaluation, the personalized plan design can be fully automatised and embedded into mainstream healthcare. The *GliomaSolver* can be further applied to obtain predictions about the disease progression in the absence of treatment, accounting for the tumor-induced brain deformations and related critical conditions. Such prognosis can assist treatment

decision making; preventing invasive surgery in the case of elderly patients with estimated slow tumor progression and mild impairment.

If the patient is diagnosed with a brain lymphoma, the CXCR4-PET uptake values can be deployed to estimate patient's suitability and response to novel theranostic treatment procedures. Finally, the developed stochastic algorithms can assist the design of innovative imaging and treatment strategies by describing the delicate interaction between markers and cell receptors.

Future work

To truly reach the era of the *Medical Human Avatar*, the following elements should be targeted in the future work. First, the accuracy of the automated segmentation methods should be elevated (at least) at the level of the manual approach. This goal relies heavily on the segmentation benchmarks and their continuous effort in expanding the available datasets. Secondly, novel computational models describing the tumor heterogeneity, the interplay between macro- and microscopic processes, and the treatment response are needed. Advanced imaging modalities like spectroscopy, histology and novel PET markers can provide deeper insights into the complex tumor internal processes. This, in turn, allows calibration of more advanced tumor models and better predictions of disease progression and treatment response. Consequently, clinical trials evaluating the benefits and credibility of the computational models should be conducted. Machine learning methods trained to match suitable clinical trials to a given patient would provide additional help. Finally, we need software interconnecting all these components into a shiny mosaic of *Medical Human Avatar*.

PERSONALISED RADIOTHERAPY PLANNING

This appendix reports additional technical details to the personalized radiotherapy planning introduced in Chapter 5. First, we present the prior PDF used for the Bayesian model calibration, followed by an overview of the calibrated model parameters from the clinical study. Afterword, the role of complex brain anatomy on the tumor cell density at the lesion borders visible on the medical scans is discussed. We conclude with a description of the acquisition protocols and image processing techniques.

Prior PDF

The parameters $\theta = \{\theta_u, \theta_{\mathcal{F}T1Gd}, \theta_{\mathcal{F}FLAIR}, \theta_{\mathcal{F}FET}\}$ of the model $M = \{M_u, M_{\mathcal{J}}\}$ are assumed independent with uniform prior distribution: $\mathbb{P}(\theta|M) = \prod_{j=1}^{11} \mathbb{P}(\theta_j|M)$, where

$$\mathbb{P}(\theta_j|M) = \frac{1}{\log(\theta_j^{max}) - \log(\theta_j^{min})} \quad \text{for } \theta_j^{min} \leq \theta_j \leq \theta_j^{max}, \quad (\text{A.1})$$

and zero otherwise. The logarithm ensures a similar order of magnitude for the prior ranges of all considered parameters, which facilitates the sampling procedure. The prior ranges are chosen as follows: $D_w \in [0.013, 3.8] \text{ mm}^2/\text{day}$; $\rho \in [0.0027, 0.19] \text{ 1/day}$ as reported in [68]; $T \in [30, T^{max} + 365] \text{ day}$, where T^{max} is the maximum time that a propagation wave with velocity $v^{min} = 2\sqrt{\min(D_w \rho)}$ needs to travel a distance equal to the maximum radius of the visible tumor r^{max} . A prior for the initial location is taken as a cube with a side $2r^{max}$, centered at the tumor center of mass. The imaging model parameters are assumed to be $u_c^{T1Gd} \in [0.5, 0.85]$, $u_c^{FLAIR} \in [0.05, 0.5]$, $\sigma_\alpha^2 \in [0.05, 0.1]$, $\sigma \in [0.015, 0.2]$ and $b \in [0.5, 1.02]$. The lower bound for the scaling factor b comes from the fact the T1Gd and FET-PET scans usually do not enhance low grade gliomas, suggesting the same lower bound for both modalities.

Bayesian calibration

Table A.1 reports the results of the Bayesian calibration for the clinical data shown in Chapter 5.

Cases	D_w	ρ	T	ic_x	ic_y	ic_z	σ	b	u_c^{T1Gd}	u_c^{FLAIR}	σ_a^2
P1: MAP	0.188	0.029	273.130	169.293	177.075	141.235	0.111	0.959	0.693	0.521	0.051
P1: mean	0.334	0.054	192.649	169.242	177.101	140.851	0.109	0.951	0.712	0.516	0.053
P1: std	0.190	0.031	107.396	0.435	0.384	0.435	0.013	0.040	0.029	0.016	0.002
P2: MAP	0.060	0.024	337.582	108.186	158.182	173.926	0.160	0.846	0.559	0.436	0.051
P2: mean	0.090	0.036	407.101	108.262	157.978	173.850	0.161	0.859	0.577	0.448	0.053
P2: std	0.086	0.034	257.528	0.384	0.358	0.512	0.014	0.055	0.027	0.016	0.003
P3: MAP	0.846	0.010	1094.225	112.998	155.520	117.632	0.218	0.925	0.614	0.347	0.056
P3: mean	0.667	0.008	1468.721	111.821	154.035	118.298	0.214	0.884	0.627	0.352	0.061
P3: std	0.133	0.002	299.056	2.611	3.046	2.074	0.004	0.029	0.011	0.013	0.003
P4: MAP	0.223	0.010	848.498	163.405	162.944	183.347	0.149	1.011	0.796	0.416	0.050
P4: mean	0.227	0.010	1015.395	163.533	162.918	183.245	0.142	1.009	0.793	0.417	0.051
P4: std	0.167	0.007	403.933	0.333	0.410	0.307	0.010	0.009	0.005	0.007	0.000
P5: MAP	2.447	0.107	93.278	117.453	110.541	141.517	0.219	1.020	0.601	0.374	0.051
P5: mean	2.285	0.101	101.387	117.376	110.310	141.312	0.205	1.005	0.609	0.368	0.051
P5: std	0.312	0.014	17.692	0.691	0.486	0.333	0.008	0.013	0.006	0.008	0.001
P6: MAP	0.440	0.029	406.237	127.053	167.450	167.731	0.193	0.937	0.614	0.369	0.052
P6: mean	0.869	0.053	311.425	124.442	166.093	166.912	0.190	0.949	0.642	0.379	0.053
P6: std	0.557	0.033	262.315	1.024	0.947	0.870	0.014	0.040	0.021	0.010	0.002
P7: MAP	0.196	0.007	1580.353	162.867	98.509	121.088	0.218	0.837	0.604	0.362	0.052
P7: mean	0.282	0.010	1204.162	163.354	96.640	123.110	0.213	0.807	0.605	0.359	0.052
P7: std	0.079	0.003	340.776	0.486	1.408	1.024	0.004	0.020	0.004	0.009	0.001
P8: MAP	0.484	0.025	391.577	166.528	119.270	160.154	0.131	0.866	0.602	0.355	0.050
P8: mean	0.689	0.034	353.465	166.093	119.219	160.410	0.130	0.845	0.605	0.355	0.051
P8: std	0.399	0.020	190.028	0.256	0.205	0.256	0.003	0.017	0.003	0.005	0.001

Table A.1: Results of the Bayesian calibration for the patient data shown in Chapter 5. The maximum a posteriori (MAP) estimates, means and standard deviations (std) of the marginal distribution are shown for all parameters. The units are $D_w \sim mm^2/day$; $\rho \sim 1/day$; $T \sim day$; and $ic_x, ic_y, ic_z \sim mm$.

Effect of the brain anatomy on the tumor cell density

Several brain tumor modeling studies assume constant tumor cell density along the tumor borders visible on the medical scans. This assumption is valid in *in-vivo* experiments, however, it poses too strong simplification for real clinical cases. The complex patient-specific brain anatomy and anisotropic tumor growth often result in very diverse tumor cell density distribution at the outlines of the visible lesion – which is also consistent with our findings. Figure A.1 (A) shows the distribution of the inferred tumor cell densities across the tumor borders visible in T1Gd and FLAIR scans. The distributions vary significantly along the borders and among the patients. This is not surprising since in the regions of anatomical restrictions the outlines of the T1Gd and FLAIR tumor segmentations coincide. The effect of the anatomical restrictions can be alleviated by considering the tumor cell density only at the tumor segmentation outlines far from the ventricles and skull. In this case, the inferred tumor cell densities vary less and are

also more consistent among the patients, as shown in Fig. A.1 (B). This implies the importance of considering the imaging parameters patient-specific, especially when dealing with complex anatomies such as the brain.

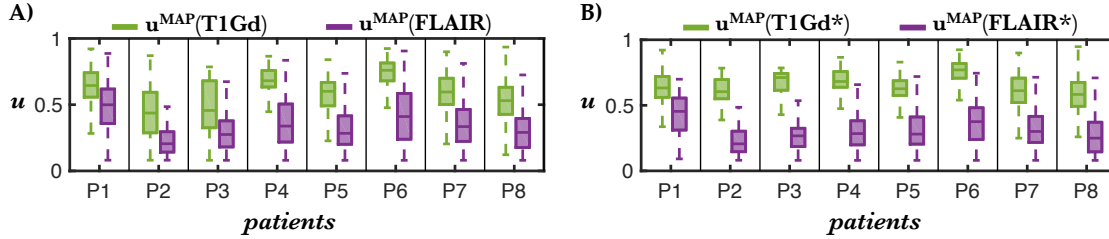


Figure A.1: The effect of brain anatomy on the tumor cell density. A) Distribution of the inferred tumor cell densities at the border of the T1Gd (green) and FLAIR (purple) tumor segmentations represented by box plots. B) Distribution of the tumor cell densities at segmentation borders far from anatomical restrictions. Boxplot whiskers demarcate the 95% percentiles.

Acquisition protocol

The MRI scans were conducted with 3T mMR Biograph scanner (Siemens Medical Solutions, Germany). FET-PET scans were acquired on a SIEMENS Biograph 64 PET/CT scanner. For standardized metabolic conditions, patients were asked to fast for a minimum of 6h before the PET scan. Intravenous administration of 190 MBq of FET was performed, and low-dose CT (24–26 mAs, 120 kV) for attenuation correction was acquired. Ten-minute PET acquisitions were performed 30 to 40 min post-injection. PET data were reconstructed by filtered back-projection using a Hann filter with corrections for attenuation, scatter, and radioactive decay. All patients provided informed written consent. The study was approved by the ethics committee of the TU Munich and carried out in accordance with the approved guidelines.

Image processing

The scans of each patient were registered to preoperative T1Gd scans using affine ANTs registration [11]. The white matter, gray matter, and cerebrospinal fluid were segmented from T1w MRI scan using the S3 method presented in Section 3.2.2. In this way, the brain atlas is deformed to reach a spatial consistency with the visible brain tissue of the patient, while the tissue underneath the tumor is described by the anatomy of the deformed atlas. The tumors were segmented with a generative EM algorithm [121]. All segmentations were manually inspected and corrected – if needed. All aforementioned image processing was performed with the head scan processing pipeline presented in Section 8.2.

CAHN-HILLIARD IMAGE FILTERING

Performance of image processing methods is strongly influenced by the quality of the input images. Medical scans often exhibit strong artifacts such as high levels of noise, low contrast, large variations in the image intensities, and the mixed interface between the image components caused, for instance, by infiltrative tumors invading the surrounding tissue (see Fig. 3.21). Image filtering algorithms can be applied to reduce such artifacts, which in turn increase the performance of the detection and segmentation methods.

Herein, we present a novel image filtering method based on the Cahn-Hilliard separation. The benefits of the proposed method over standard image filtering algorithms are first demonstrated on synthetic data. Afterward, the method is tested on clinical CT scans of livers with lesions, provided by the LiTS challenge (see Section 3.3.1). The Cahn-Hilliard image filtering significantly simplifies detection and segmentation of the liver pathologies, as demonstrated by the presented qualitative and quantitative results. To obtain the quantitative measurements, the liver lesions were segmented by simple thresholding of the Cahn-Hilliard solution. The segmentations were tested on the LiTS challenge during the ISBI conference, where the proposed algorithm scored as the best unsupervised method and the 6th best segmentation method in the overall ranking. We wish to point out, that the aim of this work is image filtering and not tumor segmentation. The presented segmentations are used to demonstrate the importance of robust image filtering and its effect on the subsequent image processing methods.

Motivation

Image filtering methods can be utilized to improve the detection and segmentation of pathologies. Popular filtering methods include bilateral filtering [181], image-guided filtering [72], total variation [154], and anisotropic diffusion filtering [61, 137, 189]. These methods can be applied

iteratively to suppress various levels of noise. However, the required number of iterations is not known a priori and depends on the noise level. This complicates the application of such methods in an automated fashion especially in the case of medical scans which often display large noise variations. In such cases, it can be difficult to find the optimal trade-off between the denoising of the artifacts and preservation of the pathologies with small volume or infiltrative interface.

Here, we propose a novel image filtering method based on phase separation. In chemistry, phase separation is a process describing a spontaneous separation of mixed chemical components into distinct components with a well-defined interface. The separation process can be mathematically described by the Cahn-Hilliard equation [22]. We propose to interpret image structures (e.g. healthy tissue, pathologies) as different chemical components represented by different image intensities. The noise or regions with the infiltrative interface are interpreted as mixing between the components. The Cahn-Hilliard equation is used to remove the noise and separate the image into the components with a well-defined interface while preserving volumes of the individual structures.

The proposed Cahn-Hilliard separation (CHS) method is similar to popular anisotropic diffusion (AD) filtering, however, it offers three main advantages: A1) CHS is a well-posed problem [101], while AD is ill-posed and requires additional regularization [61, 156, 189], which likely introduces unwanted blurring effect. A2) The CHS is an energy minimization problem, which allows to identify the optimal number of iterations in an automated fashion. Moreover, an increased number of iterations does not deteriorate the image quality. The reason is that once the system approaches its energy minimum, changes caused by additional image filtering become negligible. A3) The CHS preserves the interface even of infiltrative pathologies, which might be too smooth to be detected by the edge-preserving mechanism of the AD filtering. These factors make the CHS promising method for denoising of the CT scans with intra-organ pathologies, where large variations in noise levels, image intensities, and interface thickness are presented.

Cahn-Hilliard Separation

Background: Phase separation is a process describing a spontaneous separation of a system of finely mixed components into distinct components. For simplicity, consider first a system with two chemical components: A and B . The state of the system is characterized by so-called *phase field function* $\psi(x, y, z, t) \in [0, 1]$, which describes the concentration of component A at location $(x, y, z) \in \Omega$ and time t (same as in Section 4.2). The state of component B is then given as $1 - \psi(x, y, z, t)$. The regions where $\psi = 1$ and $\psi = 0$ are the domains where the components have completely separated, while the mixed state is characterized by the regions where $\psi \in (0, 1)$. The free energy of this system can be described as [22]:

$$E_\epsilon(\psi) = \int_{\Omega} f(\psi) + \frac{\epsilon^2}{2} |\nabla \psi|^2 dV, \quad (\text{B.1})$$

with Ω being the domain of the system, $f(\psi)$ the free-energy density inside the components, $\frac{\varepsilon^2}{2}|\nabla\psi|^2$ the free-energy density at the interfaces and ε the interface thickness. The free energy $f(\psi)$ is modeled as a double-well potential whose minima corresponds to the separated components, e.g., $f(\psi) = \frac{1}{4}\psi^2(1-\psi)^2$. If the system is perturbed from its equilibrium state, the components will spontaneously separate to minimize the energy ultimately yielding distinct components with diffuse interfaces whose width is proportional to ε . The separation is driven by differences in the chemical potential and can be modeled by the Cahn-Hilliard equation [22]:

$$\frac{\partial\psi}{\partial t} = \nabla \cdot (M(\psi)\nabla\mu) \quad \text{in } \Omega, \quad (\text{B.2})$$

$$\mu = \frac{\delta E_\varepsilon(\psi)}{\delta\psi} := \frac{df(\psi)}{d\psi} - \varepsilon^2\Delta\psi, \quad (\text{B.3})$$

with no flux boundary conditions $\vec{n} \cdot \nabla\psi = 0$ on $\partial\Omega$, where \vec{n} is outward unit normal to $\partial\Omega$. The term μ is the chemical potential of the system, defined as the variational derivation of the systems free energy. The mobility term $M(\psi) = \sqrt{4f(\psi)}$ inhibits long-range diffusion and tends to preserve the volumes of the individual components.

The Cahn-Hilliard dynamics contains two stages, each appearing at very distinct time scales [135]. In the first stage, which occurs at $O(\varepsilon^2)$, high frequencies are removed and the internal structure of interfaces separating different domains is established but the interfaces do not move. The second stage occurs at the scales $O(1/\varepsilon)$ and includes coarsening of the components and eventually also movement of the interfaces. However, this happens at a significantly different time scale than the first stage. For instance, in the system with 128 grid points per dimension (i.e. 128 voxels per dimension) and interface thickness $\varepsilon = 3h$, where $h = 1/128$ is the size of the simulated grid point, the difference between the two scales is nine orders of magnitude.

Application to images: We exploit the first stage of the Cahn-Hilliard dynamics to remove the noise from the images while preserving the separation of the image components. We will consider the image as the simulation domain Ω , where each voxel is represented by one grid point in the Ω . We define ψ as normalized image intensity, which takes values between 0 and 1. The different image intensities represent different components of the system, while the noise and infiltrative interface can be seen as mixing between the components. The Cahn-Hilliard equation is iteratively solved within the time scale of the first stage until the changes in the system energy drop below a certain threshold (i.e. energy minimization). Moreover, since the first stage mainly suppresses high frequencies, the Cahn-Hilliard denoising can be applied in the same way to images with multiple components, where ψ is defined as normalized image intensity – same as before.

The CHS is similar to AD filtering, which filters the normalized input image ψ by solving the diffusion equation [137]:

$$\frac{\partial\psi}{\partial t} = \nabla \cdot \left(\frac{1}{1 + (\|\nabla\psi\|/K)^2} \nabla\psi \right) \quad \text{in } \Omega, \quad (\text{B.4})$$

with no flux boundary conditions $\vec{n} \cdot \nabla \psi = 0$ on $\partial\Omega$. The AD identifies the edges in the image by computing gradient of the image intensities (i.e. $\|\nabla \psi\|$). The smoothing effect is then reduced in these regions to preserve the edges. The parameter K is used to control the sensitivity to the edges and is chosen experimentally. Despite the wide use of the AD method, the Eq. (B.4) is an ill-posed problem. On the other hand, existence and uniqueness of the Cahn-Hilliard solution are guaranteed by the existence of the free energy (Lyapunov) functional in Eq. (B.1). In the next section, we use synthetic data to illustrate the advantages of the CHS over the AD filtering.

Results

To illustrate the capability of the CHS filtering to suppress noise in an automated fashion and to preserve infiltrative mixed interface, the method is tested on synthetic data together with the AD [137]. The CHS is then applied to clinical CT scans of liver with lesions.

Synthetic data.

Figure B.1 **A**) shows a slice across the 3D ground truth image with resolution $[128, 128, 128]$. This can be seen as a synthetic representation of a CT scan of an organ and infiltrative lesions, each characterized by different image intensities. The outer sphere has intensity 1.0, while the inner spheres have intensity 0.8. The interface between the inner and the outer spheres has thickness 6 voxels. For the testing purposes, the GT image is polluted by additive Gaussian noise with zero mean and $\sigma = 0.05$. The resulting normalized image, shown in Fig. B.1 **B**), is used as input for the denoising methods.

For comparison purposes, both AD and CHS equation are discretized by finite differences in space and by explicit Euler in time. The AD is assumed with the parameter $K = 1$ to emphasize the edge preservation. The CHS is used with the interface parameter $\varepsilon = 3h$ and the stopping criteria $\tau = 5e - 05$. The energy of the system is computed every 50 iterations to check for the convergence to the energy minimum.

Figure B.1 **(C,E)** shows the best results of both methods. The number of suitable iterations for AD was found manually, while in the CHS it is estimated by the changes in the system's energy, shown in **G**). Both methods successfully suppressed the noise and preserved all lesions. The results of additional image filtering of both methods are shown in **(D,F)**. It can be seen that the CHS preserves all the lesions even with the increasing number of iterations, whereas the AD smooths out the smallest lesions. This makes CHS a promising method for automated preprocessing of noisy CT scans with diverse pathologies.

Clinical data.

To demonstrate the potential of the CHS filtering on clinical data, the method is tested on CT scans of livers with lesions.

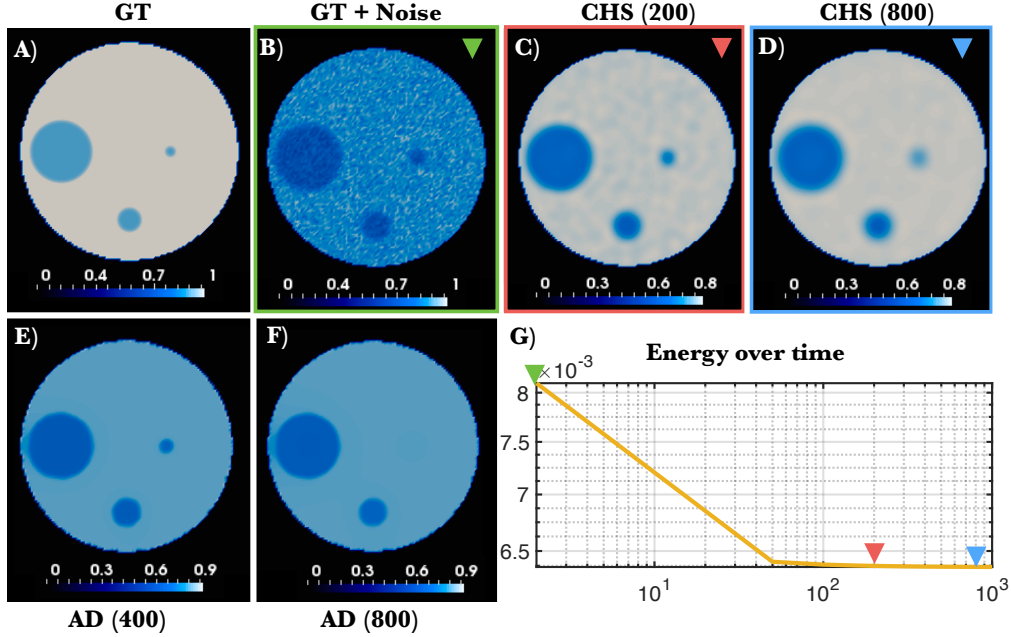


Figure B.1: Comparison of the CHS and AD filleting on the synthetic data. **A)** The ground truth (GT) image contains two different components (white and blue) with smooth infiltrative interface between them. The GT image, polluted by additive noise, shown **B)**, is used as input for the filtering methods. The results of the AD are shown in **E-F**. Subplot **C-D** shows results of CHS filtering, while the system's energy (in log-log scale) is shown in **G)**. The colored triangles in **G)** mark the energy states corresponding to the system states shown in **B,C,D**. In contrast to the AD, the CHS preserves the interface between the components even with the increasing number of iterations.

Data and data preprocessing: The experiments are conducted on CT scans of liver with lesions obtained from LiTS challenge dataset [17]. The test dataset consists of 70 volumes acquired at multiple centers with different acquisition protocols and resolution, resulting in data with various image intensities, noise levels, contrast, and types of lesions (see Section 3.3.1). All data are preprocessed in the following way. First, the liver tissue is segmented using the cascaded fully convolutional neural networks [34]. The liver intensities I_{Liver} are then clipped to $[0, 200]$ HU, to exclude atypical liver values like metal implants. The outliers are further removed by clipping the liver intensities to a 95% credibility interval (CI). The phase field function is then initialized as $\psi = \frac{1}{C} \left[\left(I_{Liver} \Big|_{[0, 200]} \right) \Big|_{95\% CI} \right]$, where C is a normalisation constant.

Phase separation: The Cahn-Hilliard equation, with the interface parameter $\varepsilon = 3h$, is evolved in time until the system approaches its energy minimum. Results of the CHS and the corresponding input CT scans are shown in Fig. B.2 (**A-B**) and Fig. B.3 (the first two columns). The CHS removes the noise and enhances the image contrast while preserving the liver-lesion

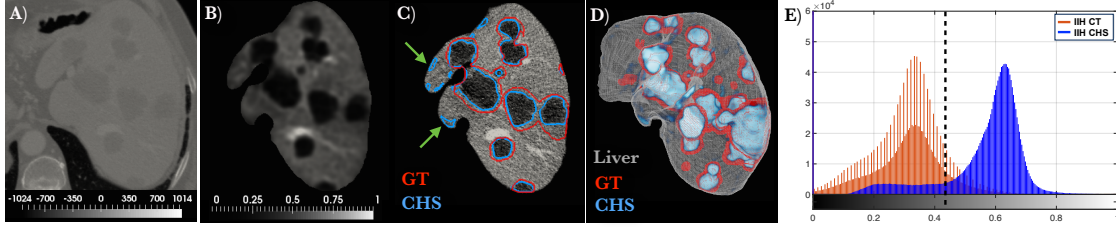


Figure B.2: An illustration of the CHS image filtering in the CT scan of the liver with lesions. The input CT scan is shown in **A)** while the results of the CHS filtering are depicted in **B)**. Outlines of the lesions segmentation obtained by thresholding of the Cahn-Hilliard solution (blue) are shown in comparison with the manual ground truth (GT) segmentation (red) in **C)**. The subplot **D)** shows 3D visualization of the GT segmentations (red) and CHS soft segmentations (white-blue colormap) inside the liver anatomy (white). The IIH of the normalized liver CT before (red) and after (blue) Cahn-Hilliard separation is depicted in **E)**. The dashed line indicates the separation between liver and lesions image intensities computed by the triangle method.

interface. The contrast enhancement is also evident from the image intensity histogram (IIH) of the normalized liver CT before and after CHS, shown in Fig. B.2 **E)**. The histogram is divided into 255 bins corresponding to the grayscale levels. The spikes visible on the original liver CT histogram are caused by the noise in the data. After the CHS filtering, the originally unimodal histogram separates into two modes, healthy liver and lesions, allowing simple lesions detection.

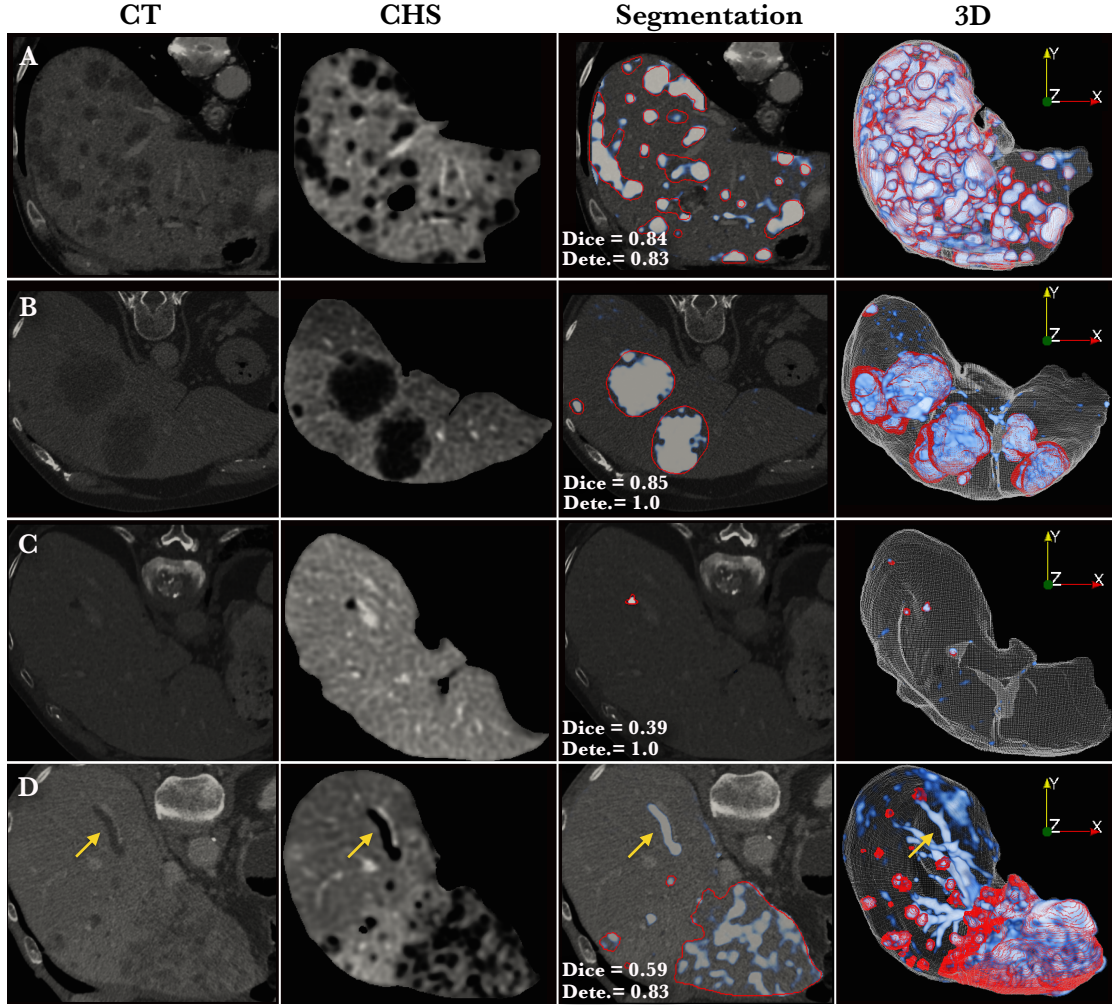


Figure B.3: Qualitative results of CHS filtering in four CT cases marked as (A-D) of livers with lesions. The first column shows the original CT scans, second the results of the CHS method, while the comparison of the ground truth (red) and Cahn-Hilliard segmentation (white-blue) is shown in the third and fourth column. Dice score and detection rate are reported for each case. The yellow arrows indicate the segmentation artifacts.

Lesions segmentation: To illustrate the benefits of the CHS on the lesions detection and segmentation task, the liver lesions are here segmented by simple thresholding. The intensity I_0 , separating the healthy liver from lesions is computed by thresholding of the IIH using the triangle method [197]. The identified threshold is shown as the dashed line in Fig. B.2 E) and as blue lines in Fig. B.2 C). The Cahn-Hilliard formulation allows to further approximate the hard interface between the components by hyperbolic tangent [22], allowing to translate the hard

binary segmentations into soft probabilistic segmentations as:

$$\psi_{soft}(I) = \frac{1}{2} \left[1 + \tanh \left(\frac{(I_0 - I)}{2\sqrt{2}\varepsilon} \right) \right]. \quad (\text{B.5})$$

The soft lesions segmentations are shown in Fig. B.2 **D**) and in Fig. B.3 (last two columns), together with the manual segmentations (shown in red). Figure B.3 demonstrates that the CHS method preserves even small lesions, as shown in **(A-C)**, as well as the lesion with infiltrative interface of various width – shown in **B**). In Fig. B.3 **(A,B,D)**, the CHS delineates the liver-lesion interface with more precision than manual segmentations which tends to approximate complex lesion structures with simplified geometries.

Figure B.3 reports the detection rate and Dice score for each case while the scores from the LiTS test dataset are presented in Section 3.3.1. We wish to emphasize that the aim of this work is the image filtering and not the segmentation task. The presented lesions segmentations are used to demonstrate the importance of robust image filtering provided by the presented CHS method.

Conclusion

Herein, we have presented CHS, a novel image filtering method with the advantages (A1-A3). We showed that the CHS method can be applied in an automated way to remove the noise and enhance contrast while preserving small lesions as well as lesions with the infiltrative mixed interface. This makes the proposed method particularly suitable for preprocessing of CT scans with infiltrative lesions commonly encountered in liver, spleen, bones or stroke lesions.

Disclaimer: This section is partly reproduced from the article "J. Lipková, M. Rempfler, P. Christ, Patrick, J. Lowengrub and B. Menze : Automated Unsupervised Segmentation of Liver Lesions in CT scans via Cahn-Hilliard Phase Separation", available as arXiv preprint arXiv:1704.02348.

LIST OF PUBLICATIONS

Published or accepted articles:

1. J. **Lipková**, P. ANGELIKOPOULOS, S. WU, E. ALBERTS, B. WIESTLER, C. DIEHL, C. PREIBISCH, T. PYKA, S. COMBS, P. HADJIDOUKAS, ET AL., *Personalized Radiotherapy Design for Glioblastoma: Integrating Mathematical Tumor Models, Multimodal Scans and Bayesian Inference.*, IEEE transactions on medical imaging, (2019)
2. I. EZHOV, J. **Lipkova**, S. SHIT, F. KOFLER, N. COLLOMB, B. LEMASSON, E. BARBIER, AND B. MENZE, *Neural parameters estimation for brain tumor growth modeling*, accepted for MICCAI 2019, preprint at arXiv:1907.00973, (2019)
3. J. **Lipková**, G. ARAMPATZIS, P. CHATELAIN, B. MENZE, AND P. KOUMOUTSAKOS, *S-Leaping: An Adaptive, Accelerated Stochastic Simulation Algorithm, Bridging tau-Leaping and R-Leaping*, Bulletin of mathematical biology, (2018), pp. 1–23
4. L. XU, G. TETTEH, J. **Lipková**, Y. ZHAO, H. LI, P. CHRIST, M. PIRAUD, A. BUCK, K. SHI, AND B. H. MENZE, *Automated Whole-Body Bone Lesion Detection for Multiple Myeloma on ^{68}Ga -Pentixafor PET/CT Imaging Using Deep Learning Methods*, Contrast media & molecular imaging, (2018)
5. L. XU, G. TETTEH, M. MUSTAFA, J. **Lipková**, Y. ZHAO, M. BIETH, P. CHRIST, M. PIRAUD, B. MENZE, AND K. SHI, *W-Net for Whole-Body Bone Lesion Detection on ^{68}Ga -Pentixafor PET/CT Imaging of Multiple Myeloma Patients*, in Molecular Imaging, Reconstruction and Analysis of Moving Body Organs, and Stroke Imaging and Treatment, Springer, (2017), pp. 23–30
6. J. **Lipková**, D. ROSSINELLI, J. LOWENGRUB, P. KOUMOUTSAKOS, AND B. MENZE, *Visualisation of a brain tumor infiltration*, accepted for publication in the Springer, Beauty of theoretical biology, (2019)
7. J. **Lipková**, D. ROSSINELLI, P. KOUMOUTSAKOS, AND B. MENZE, *Visualisation of a sphere in the shear flow*, accepted for publication in the Springer, Beauty of theoretical biology, (2019)

8. J. **Lipková**, K. C. ZYGALAKIS, S. J. CHAPMAN, AND R. ERBAN, *Analysis of Brownian dynamics simulations of reversible bimolecular reactions*, SIAM Journal on Applied Mathematics, 71 (2011), pp. 714–730

Manuscripts under revision:

1. P. HERHAUS, J. **Lipková**, T. VAG, A. S.-H. J. LAMMER, FELICITAS, C. LAPA, B. MENZE, T. PUKROP, I. IAKUCHEV, D. HELLWIG, A. K. BUCK, M. DECKERT, B. WIESTLER, H.-J. EZHOV, IVAN WESTER, M. SCHWEIGER, AND U. KELLER, *CXCR4-targeted positron emission tomography imaging of central nervous system B-cell lymphoma*, submitted to American Society of Hematology, (2019)
2. M. METZ, M. MOLINA, J. **Lipkova**, F. LIESCHE, B. MENZE, S. COMBS, C. ZIMMER, AND B. WIESTLER, *Prediction of glioblastoma recurrence from preoperative MR scans through fractional anisotropy maps with free water suppression*, submitted to RSNA, (2019)
3. G. TETTEH, L. XU, A. GAFITA, J. **Lipková**, A. ZELDIN, K. SHI, AND B. MENZE, *Lesion Detection of Recurrent Prostate Cancer on Hybrid 68Ga-PSMA PET/CT Imaging*, (Under double blind revision), (2019)
4. P. BILIC, P. F. CHRIST, E. VORONTSOV, G. CHLEBUS, H. CHEN, Q. DOU, C.-W. FU, X. HAN, P.-A. HENG, J. HESSER, ET AL., *The Liver Tumor Segmentation Benchmark (LiTS)*, arXiv preprint arXiv:1901.04056, (2019)
5. S. BAKAS, M. REYES, A. JAKAB, S. BAUER, M. REMPFLE, A. CRIMI, R. T. SHINOHARA, C. BERGER, S. M. HA, M. ROZYCKI, ET AL., *Identifying the Best Machine Learning Algorithms for Brain Tumor Segmentation, Progression Assessment, and Overall Survival Prediction in the BRATS Challenge*, arXiv preprint arXiv:1811.02629, (2018)
6. P. F. CHRIST, F. ETTLINGER, F. GRÜN, M. E. A. ELSHAERA, J. **Lipková**, S. SCHLECHT, F. AHMADDY, S. TATAVARTY, M. BICKEL, P. BILIC, ET AL., *Automatic liver and tumor segmentation of CT and MRI volumes using cascaded fully convolutional neural networks*, arXiv preprint arXiv:1702.05970, (2017)
7. J. **Lipková**, M. REMPFLE, P. CHRIST, J. LOWENGRUB, AND B. H. MENZE, *Automated Un-supervised Segmentation of Liver Lesions in CT scans via Cahn-Hilliard Phase Separation*, arXiv preprint arXiv:1704.02348, (2017)

Manuscripts in preparation:

1. F. KOFLER, J. **Lipkova**, B. WIESTLER, AND B. MENZE, *The BRATS preprocessing software: Translating state-of-the-art brain tumor segmentation methods into clinical and scientific practice*, in preparation for BRATS special issue, (2019)

-
2. **J. Lipkova**, B. MENZE, P. KOUMOUTSAKOS, AND J. LOWENGRUB, *Tumor-induced brain deformations*, in preparation, (2019)

LIST OF TABLES

3.1	Results of the V-Net and W-Net for MM bone lesion detection and segmentation in clinical cases. The best results are shown in yellow.	55
4.1	A relation between the intracranial pressure values and the corresponding pathological conditions.	80
4.2	An overview of the model parameters and their units. The parameters $T[day]$, $L[cm]$ and $M[g]$ denote the characteristic time, length and mass, respectively.	83
5.1	Results of the Bayesian calibration for the synthetic case generated with the ground truth (GT) values.	100
6.1	Patients characteristics in the CXCR4-directed PET study.	111
7.1	The reaction network for the dimerization system studied in Sections 7.3.1 and 7.3.2.	130
7.2	The reaction network for the <i>Bacillus subtilis</i> system studied in Section 7.3.3.	133
7.3	The averaged number of simulation steps and the execution time for the <i>Bacillus subtilis</i> system with the $\varepsilon = 0.05$ presented in Section 7.3.3.	133
7.4	The reaction network for the LacZ/LacY system discussed in Section 7.3.4.	135
A.1	Results of the Bayesian calibration for the patient data shown in Chapter 5.	172

TABLE

Page

LIST OF FIGURES

1.1	An illustration of <i>Medical Human Avatar</i>	3
2.1	An illustration of the hallmarks of cancer.	12
2.2	A schematic representation of a CT scanner and a slice from an abdominal CT scan.	17

2.3	Approximate Hounsfield values of tissues commonly found in a CT scan.	17
2.4	A 3D rendering of anatomies reconstructed from a CT scan.	18
2.5	Positron emission and antimatter annihilation.	19
2.6	A schematic representation of a PET scanner and a slice from a FDG-PET scan. . . .	20
2.7	A hybrid PSMA-PET/CT scan.	21
2.8	The principle of MRI physics inside a voxel.	22
2.9	Polarization and excitation of protons in a magnetic field	23
2.10	T1 and T2 relaxation.	24
2.11	A slice of a brain scan acquired with four different MRI modalities.	24
2.12	The multimodal scans of a patient diagnosed with glioblastoma.	29
2.13	The multimodal scans of a patient with brain lymphoma.	29
3.1	Illustration of the image segmentation task.	32
3.2	Illustration of two binary tumor segmentations.	33
3.3	Illustration of the partial volume effect.	35
3.4	An illustration of brain MRI atlas construction.	36
3.5	The T1w and T2w MRI atlas of the healthy adult human brain together with tissue probability maps provided by [50].	37
3.6	An illustration of a rigid registration of an atlas to a subject scan.	37
3.7	An overview of the S3 algorithm.	40
3.8	A comparison of the brain masks computed by S3, ROBEX, and BET method on a brain scan without a pathology.	41
3.9	Results of the skull-stripping methods on the scans with brain lesions	42
3.10	Results of the skull-stripping methods on the scans with resection cavities.	43
3.11	A comparison of brain tissue segmentations computed by S3 (orange box) and EM (blue box) on five scans (A-E) with brain lesions.	44
3.12	An illustration of an artificial neuron.	46
3.13	An illustration of a deep neural network	47
3.14	An illustration of CNN.	49
3.15	An illustration of a max-pooling operation.	49
3.16	An illustration of U-Net architecture.	51
3.17	A distribution of MM lesions within a patient with ^{68}Ga -Pentixafor PET/CT imaging	53
3.18	A simplified illustration of the W-Net architecture for the whole-body MM lesions detections from the hybrid PET/CT scan.	54
3.19	Convergence curves of W-Net and V-Net architectures.	54
3.20	Qualitative results of the V-Net and W-Net for the MM lesion detection.	56
3.21	Abdominal CT scans of three patients with liver lesions and corresponding image intensity histogram of lesions and healthy liver tissue.	60

3.22	Results of the lesions segmentations obtained by the six best methods from the ISBI challenge.	61
3.23	Dispersion of Dice scores for liver segmentation task from individual algorithms submitted to LiTS and the fused methods.	62
3.24	Dispersion of Dice scores for liver lesions segmentation task from individual algorithms submitted to LiTS and the fused methods.	63
3.25	A relation between the tumor properties and the performance of the best method from the MICCAI 2017.	63
3.26	Glioma sub-regions considered in the BraTS segmentation challenge.	66
3.27	An illustration of pipeline used for predicting patient overall survival in the BraTS challenge.	67
3.28	Ranking of overall survival prediction task of all teams participating in BraTS 2018.	68
3.29	The patient-wise distribution of ranking for the segmentation task for all teams participating in BraTS 2018.	69
4.1	An illustration of different spatio-temporal scales of the tumor mechanisms.	74
4.2	The brain anatomy used for the tumor growth simulation.	76
4.3	Simulation of tumor growth over a period of 600 days.	76
4.4	A distribution of proliferation (ρ) and infiltration (D_w) for LGG and HGG, as reported in [68].	77
4.5	An overview of the simulation domain and phase-field function.	85
4.6	Results of the tumor-induced brain deformation model in the synthetic case.	87
4.7	Visualisation of the brain midline shift in the synthetic case.	87
4.8	Tumor induced-brain deformations in two patients with HGG lesions.	89
4.9	Tumor progression from LGG to HGG.	90
5.1	An illustration of a standard RT plan for a glioblastoma patient.	94
5.2	Overview of the inference framework.	97
5.3	Synthetic test case.	101
5.4	The results of the Bayesian calibration for the synthetic case.	102
5.5	Insensitivity of the tumor cell density to the speed of the growth.	103
5.6	Results of the Bayesian calibration for patients <i>P1-P8</i>	105
5.7	A comparison of the RT plan based on the RTOG protocol and MAP estimates.	106
6.1	Ex-vivo CXCR4 expression within lymphoma lesions.	111
6.2	Specificity of the CXCR4-directed PET imaging for CNSLs.	112
6.3	Tumor dynamics upon treatment determined by MRI (T1c and FLAIR) in 7 patients with available follow-up scans.	114
6.4	Correlation between the treatment efficiency η and the tumor properties extracted from the pretreatment scans.	115

7.1	An illustration of a well-stirred chemically reacting system.	119
7.2	Convergence of the approximate leap solutions to the exact SSA solution with decreasing values of the accuracy parameter ε for the non-stiff dimerization system of Section 7.3.1.	131
7.3	Errors and speed-up for non-stiff dimerization system of Section 7.3.1.	131
7.4	Errors and efficiency for stiff dimerization system discussed in Section 7.3.2.	132
7.5	Error of the leap methods (left) and a single trajectory of the <i>Bacillus subtilis</i> computed with SSA (right).	133
7.6	Errors and efficiency for the LacZ/LacY system discussed in Section 7.3.4, with small initial population.	136
7.7	Errors and efficiency for the LacZ/LacY system discussed in Section 7.3.4, with large initial population.	136
8.1	The architecture of the Glioma solver.	141
8.2	The simulation domain in the <i>Glioma solver</i>	142
8.3	The adaptive grid refinement and compression.	142
8.4	The results of the reaction-diffusion tumor growth model visualized with <i>ParaView</i>	143
8.5	The report file created by the Bayesian calibration framework for the personalized RT planning.	145
8.6	The architecture of the brain tumor processing pipeline.	148
8.7	An illustration of the required folder structure with the input patient data in <i>nifty</i> (A) and <i>dicom</i> (B) format.	149
8.8	The central window of the GUI with imported data from multiple patients.	149
8.9	A snapshot of the segmentation GUI.	151
8.10	A snapshot of the interactive GUI for visualisation and segmentations corrections.	152
8.11	The architecture of SSM software.	155
8.12	An illustration of the SBML header.	156
9.1	A sphere in a shear flow visualized as translucent iso-surface rendered by Volume Perception.	161
9.2	Simulation of the Gray-Scott system in a unit cube rendered by Volume Perception.	162
9.3	Visualization of tumor infiltration inside the patient brain anatomy rendered by Volume Perception.	163
9.4	Visualization of changes in bone mineral density with increasing age rendered by ParaView.	164
9.5	Visualization of human skull, brain, and tumor rendered with Blender.	165
A.1	The effect of brain anatomy on the tumor cell density.	173
B.1	Comparison of the CHS and AD filleting on the synthetic data.	179

LIST OF FIGURES

B.2 An illustration of the CHS image filtering in the CT scan of the liver with lesions. . .	180
B.3 Qualitative results of CHS filtering in CT scans of liver with lesions.	181
FIGURE	Page

LIST OF ACRONYMS

^{68}Ga -Pentixafor	^{68}Ga -Pentixafor.
2D	two-dimensional.
3D	three-dimensional.
AD	anisotropic diffusion.
ANN	artificial neural network.
AT	active tumor.
BET	Brain Extraction Tool.
BraTS	Brain Tumor Segmentation.
CHS	Cahn-Hilliard separation.
CNN	convolutional neural network.
CNS	central nervous system.
CNSL	central nervous system lymphoma.
CSF	cerebrospinal fluid.
CT	computed tomography.
CTV	clinical target volume.
CXCR4	C-X-C motif receptor 4.
DDM	diffuse domain method.
DL	Deep Learning.
EM	Expectation-Maximization.
EORTC	European Organization for Research and Treatment of Cancer.
FCNN	fully convolutional neural network.
FDG	^{18}F -fluorodeoxyglucose.
FET	^{18}F -fluoro-ethyl-tyrosine.
FK	Fisher-Kolmogorov.

LIST OF ACRONYMS

GBM	glioblastoma.
GT	ground-truth.
GTR	gross total resection.
GTV	gross tumor volume.
GUI	graphical user interface.
HGG	high grade glioma.
HU	Hounsfield units.
ICP	intracranial pressure.
IIH	image intensity histogram.
ISBI	International Symposium on Biomedical Imaging.
LGG	low grade glioma.
LiTS	Liver Tumor Segmentation.
MAP	maximum a posteriori.
MICCAI	Medical Image Computing & Computer Assisted Intervention.
ML	Machine Learning.
MM	Multiple Myeloma.
MPI	Message Passing Interface.
MRAG	Multi-Resolution-Adaptive-Grid.
MRI	magnetic resonance imaging.
NABTT	New Approaches to Brain Tumor Therapy.
OpenMP	Open Multi-Processing.
OS	overall survival.
PCNSL	primary central nervous system lymphoma.
PDE	partial differential equation.
PDF	probability distribution function.
PET	positron-emission tomography.
PFF	phase-field function.
PSMA	Prostate-Specific Membrane Antigen.

PTV	planning target volume.
RF	radio frequency.
ROBEX	Robust Learning-based Brain Extraction System.
RT	radiotherapy.
RTOG	Radiation Therapy Oncology Group.
S3	simple skull stripping.
SBML	Systems Biology Markup Language.
SCNSL	secondary central nervous system lymphoma.
SSA	stochastic simulation algorithm.
SSM	stochastic simulation method.
T1c	T1-contrast enhanced.
T1w	T1-weighted.
T2w	T2-weighted.
TBB	Thread Building Blocks.
TC	tumor core.
TMCMC	Transitional Markov Chain Monte Carlo.
VEGF	vascular endothelial growth factor.
WT	whole tumor.
XML	Extensible Markup Language.

BIBLIOGRAPHY

- [1] B. P. ABBOTT, R. ABBOTT, T. ABBOTT, M. ABERNATHY, F. ACERNESE, K. ACKLEY, C. ADAMS, T. ADAMS, P. ADDESSO, R. ADHIKARI, ET AL., *Observation of gravitational waves from a binary black hole merger*, Physical review letters, 116 (2016), p. 061102.
- [2] R. ACHANTA, A. SHAJI, K. SMITH, A. LUCCHI, P. FUA, AND S. SÜSSTRUNK, *Slic super-pixels*, tech. rep., 2010.
- [3] S. ALBELWI AND A. MAHMOOD, *A framework for designing the architectures of deep convolutional neural networks*, Entropy, 19 (2017), p. 242.
- [4] E. ALBERTS, *Multi-modal Multi-temporal Brain Tumor Segmentation, Growth Analysis and Texture-based Classification*.
- [5] P. ALJABAR, R. A. HECKEMANN, A. HAMMERS, J. V. HAJNAL, AND D. RUECKERT, *Multi-atlas based segmentation of brain images: atlas selection and its effect on accuracy*, Neuroimage, 46 (2009), pp. 726–738.
- [6] K. ALLERS, G. HÜTTER, J. HOFMANN, C. LODDENKEMPER, K. RIEGER, E. THIEL, AND T. SCHNEIDER, *Evidence for the cure of HIV infection by CCR5 Δ 32/ Δ 32 stem cell transplantation*, Blood, 117 (2011), pp. 2791–2799.
- [7] F. AMATO, A. LÓPEZ, E. M. PEÑA-MÉNDEZ, P. VAÑHARA, A. HAMPL, AND J. HAVEL, *Artificial neural networks in medical diagnosis*, 2013.
- [8] D. F. ANDERSON AND T. G. KURTZ, *Continuous Time Markov Chain Models for Chemical Reaction Networks*, Springer New York, New York, NY, 2011, pp. 3–42.
- [9] A. ARBEY, M. BATTAGLIA, A. DJOUADI, AND F. MAHMOUDI, *The Higgs sector of the phenomenological MSSM in the light of the Higgs boson discovery*, Journal of High Energy Physics, 2012 (2012), p. 107.
- [10] A. AUGER, P. CHATELAIN, AND P. KOUMOUTSAKOS, *R-leaping: accelerating the stochastic simulation algorithm by reaction leaps*, J Chem Phys, 125 (2006), p. 084103.
- [11] B. B. AVANTS, N. TUSTISON, AND G. SONG, *Advanced normalization tools (ANTS)*, Insight j, 2 (2009), pp. 1–35.

BIBLIOGRAPHY

- [12] U. AYACHIT, *The paraview guide: a parallel visualization application*, Kitware, Inc., 2015.
- [13] S. BAKAS, M. REYES, A. JAKAB, S. BAUER, M. REMPFER, A. CRIMI, R. T. SHINOHARA, C. BERGER, S. M. HA, M. ROZYCKI, ET AL., *Identifying the Best Machine Learning Algorithms for Brain Tumor Segmentation, Progression Assessment, and Overall Survival Prediction in the BRATS Challenge*, arXiv preprint arXiv:1811.02629, (2018).
- [14] A. BARANISKIN, M. DECKERT, G. SCHULTE-ALTEDORNEBURG, U. SCHLEGEL, AND R. SCHROERS, *Current strategies in the diagnosis of diffuse large B-cell lymphoma of the central nervous system*, British journal of haematology, 156 (2012), pp. 421–432.
- [15] E. BELLON ET AL., *Evaluation of manual vs semi-automated delineation of liver lesions on CT images*, European Radiology, 7 (1997), pp. 432–438.
- [16] A. BELTON, S. SAINI, K. LIEBERMANN, G. BOLAND, AND E. F. HALPERN, *Tumour size measurement in an oncology clinical trial: comparison between off-site and on-site measurements*, Clinical radiology, 58 (2003), pp. 311–314.
- [17] P. BILIC, P. F. CHRIST, E. VORONTSOV, G. CHLEBUS, H. CHEN, Q. DOU, C.-W. FU, X. HAN, P.-A. HENG, J. HESSER, ET AL., *The Liver Tumor Segmentation Benchmark (LiTS)*, arXiv preprint arXiv:1901.04056, (2019).
- [18] K. BOUCHELOUCHE AND J. CAPALA, *“Image and treat”—an individualized approach to urological tumors*, Current opinion in oncology, 22 (2010), p. 274.
- [19] K. BOUCHELOUCHE AND P. L. CHOYKE, *PSMA PET in prostate cancer—a step towards personalized medicine*, Current opinion in oncology, 28 (2016), p. 216.
- [20] A. BRUNN, M. MONTESINOS-RONGEN, A. STRACK, G. REIFENBERGER, C. MAWRIN, C. SCHALLER, AND M. DECKERT, *Expression pattern and cellular sources of chemokines in primary central nervous system lymphoma*, Acta neuropathologica, 114 (2007), pp. 271–276.
- [21] M. CABEZAS, A. OLIVER, X. LLADÓ, J. FREIXENET, AND M. B. CUADRA, *A review of atlas-based segmentation for magnetic resonance brain images*, Computer methods and programs in biomedicine, 104 (2011), pp. e158–e177.
- [22] J. W. CAHN AND J. E. HILLIARD, *Free energy of a nonuniform system. I. Interfacial free energy*, The Journal of chemical physics, 28 (1958), pp. 258–267.
- [23] Y. CAO AND R. ERBAN, *Stochastic Turing patterns: Analysis of compartment-based approaches*, Bulletin of mathematical biology, 76 (2014), pp. 3051–3069.
- [24] Y. CAO, D. GILLESPIE, AND L. PETZOLD, *Efficient step size selection for the tau-leaping simulation method*, Journal of Chemical Physics, 124 (2006), p. 044109.

-
- [25] Y. CAO, D. T. GILLESPIE, AND L. R. PETZOLD, *Avoiding negative populations in explicit Poisson tau-leaping*, J Chem Phys, 123 (2005), p. 054104.
- [26] Y. CAO, D. T. GILLESPIE, AND L. R. PETZOLD, *Adaptive explicit-implicit tau-leaping method with automatic tau selection*, J. of Chemical Physics, 126 (2007), p. 224101.
- [27] Y. CAO AND L. PETZOLD, *Accuracy limitations and the measurement of errors in the stochastic simulation of chemically reacting systems*, Journal of Computational Physics, 212 (2006), pp. 6–24.
- [28] S. CHA, *Update on brain tumor imaging: from anatomy to physiology*, American Journal of Neuroradiology, 27 (2006), pp. 475–487.
- [29] I. CHATTOPADHYAY, A. KUCHINA, G. M. SÜEL, AND H. LIPSON, *Inverse Gillespie for inferring stochastic reaction mechanisms from intermittent samples*, Proceedings of the National Academy of Sciences, 110 (2013), pp. 12990–12995.
- [30] V. CHELLIAH, C. LAIBE, AND N. L. NOVÈRE, *BioModels database: a repository of mathematical models of biological processes*, Encyclopedia of Systems Biology, (2013), pp. 134–138.
- [31] M. CHEN, A. ELAZAB, F. JIA, J. WU, G. LI, X. LI, AND Q. HU, *Automatic estimation of midline shift in patients with cerebral glioma based on enhanced voigt model and local symmetry*, Australasian physical & engineering sciences in medicine, 38 (2015), pp. 627–641.
- [32] J. CHING AND Y.-C. CHEN, *Transitional Markov chain Monte Carlo method for Bayesian model updating, model class selection, and model averaging*, Journal of engineering mechanics, (2007).
- [33] P. CHRIST, F. ETTLINGER, F. GRÜN, J. LIPKOVA, AND G. KAISSIS, *Lits-liver tumor segmentation challenge*, ISBI and MICCAI, (2017).
- [34] P. F. CHRIST, F. ETTLINGER, F. GRÜN, M. E. A. ELSHAERA, J. **Lipková**, S. SCHLECHT, F. AHMADDY, S. TATAVARTY, M. BICKEL, P. BILIC, ET AL., *Automatic liver and tumor segmentation of CT and MRI volumes using cascaded fully convolutional neural networks*, arXiv preprint arXiv:1702.05970, (2017).
- [35] O. CLATZ, M. SERMESANT, P.-Y. BONDIAU, H. DELINGETTE, S. K. WARFIELD, G. MALLANDAIN, AND N. AYACHE, *Realistic simulation of the 3-D growth of brain tumors in MR images coupling diffusion with biomechanical deformation*, Medical Imaging, IEEE Transactions on, 24 (2005), pp. 1334–1346.

BIBLIOGRAPHY

- [36] D. CLOWE, M. BRADAČ, A. H. GONZALEZ, M. MARKEVITCH, S. W. RANDALL, C. JONES, AND D. ZARITSKY, *A direct empirical proof of the existence of dark matter*, The Astrophysical Journal Letters, 648 (2006), p. L109.
- [37] C. A. COCOSCO, V. KOLLOKIAN, R. K.-S. KWAN, G. B. PIKE, ET AL., *Brainweb: Online interface to a 3D MRI simulated brain database*, in NeuroImage, Citeseer, 1997.
- [38] M. COJOC, C. PEITZSCH, F. TRAUTMANN, L. POLISHCHUK, G. D. TELEGEEV, AND A. DUBROVSKA, *Emerging targets in cancer management: role of the CXCL12/CXCR4 axis*, OncoTargets and therapy, 6 (2013), p. 1347.
- [39] S. E. COMBS, I. BURKHOLDER, L. EDLER, S. RIEKEN, D. HABERMEHL, O. JÄKEL, ET AL., *Randomised phase I/II study to evaluate carbonion radiotherapy versus fractionated stereotactic radiotherapy in patients with recurrent or progressive gliomas: The CIN-DERELLA trial*, BMC cancer, (2010).
- [40] F. A. COSMINA HOGEA, GEORGE BIROS AND C. DAVATZIKOS, *A robust framework for soft tissue simulations with application to modeling brain tumor mass effect in 3D MR images*, PHYSICS IN MEDICINE AND BIOLOGY, 52 (2007).
- [41] H. DADGAR, *Diagnostic of FET PET in Patients with Recurrent Glioma: Case Series*, J Nucl Med Radiat Ther, 9 (2018), p. 2.
- [42] I. DESPOTOVIĆ, B. GOOSSENS, AND W. PHILIPS, *MRI segmentation of the human brain: challenges, methods, and applications*, Computational and mathematical methods in medicine, 2015 (2015).
- [43] A. DREVELEGAS AND N. PAPANIKOLAOU, *Imaging modalities in brain tumors*, in Imaging of Brain Tumors with Histological Correlations, Springer, 2011, pp. 13–33.
- [44] W. DUBITZKY, O. WOLKENHAUER, H. YOKOTA, AND K.-H. CHO, *Encyclopedia of systems biology*, Springer Publishing Company, Incorporated, 2013.
- [45] R. ERBAN, J. CHAPMAN, AND P. MAINI, *A practical guide to stochastic simulations of reaction-diffusion processes*, <https://arxiv.org/abs/0704.1908>, (2007).
- [46] R. ERBAN AND S. J. CHAPMAN, *Stochastic modelling of reaction–diffusion processes: algorithms for bimolecular reactions*, Physical biology, 6 (2009), p. 046001.
- [47] I. EZHOV, J. **Lipkova**, S. SHIT, F. KOFLER, N. COLLOMB, B. LEMASSON, E. BARBIER, AND B. MENZE, *Neural parameters estimation for brain tumor growth modeling*, accepted for MICCAI 2019, preprint at arXiv:1907.00973, (2019).

-
- [48] N. FABIAN, K. MORELAND, D. THOMPSON, A. C. BAUER, P. MARION, B. GEVECIK, M. RASQUIN, AND K. E. JANSEN, *The paraview coprocessing library: A scalable, general purpose in situ visualization library*, in 2011 IEEE Symposium on Large Data Analysis and Visualization, IEEE, 2011, pp. 89–96.
- [49] R. D. FALGOUT AND U. M. YANG, *hypre: A library of high performance preconditioners*, in International Conference on Computational Science, Springer, 2002, pp. 632–641.
- [50] V. FONOV, A. C. EVANS, K. BOTTERON, C. R. ALMLI, R. C. MCKINSTRY, D. L. COLLINS, B. D. C. GROUP, ET AL., *Unbiased average age-appropriate atlases for pediatric studies*, Neuroimage, 54 (2011), pp. 313–327.
- [51] G. P. C. GEORGE, F. PISANESCHI, Q.-D. NGUYEN, AND E. O. ABOAGYE, *Positron emission tomographic imaging of CXCR4 in cancer: challenges and promises*, Molecular imaging, 14 (2015), pp. 7290–2014.
- [52] A. GHOSE, G. LIM, AND S. HUSAIN, *Treatment for glioblastoma multiforme: current guidelines and Canadian practice*, Current oncology, 17 (2010), p. 52.
- [53] L. GILLES, C. R. VOGEL, AND B. L. ELLERBROEK, *Multigrid preconditioned conjugate-gradient method for large-scale wave-front reconstruction*, JOSA A, 19 (2002), pp. 1817–1822.
- [54] D. T. GILLESPIE, *A general method for numerically simulating the stochastic time evolution of coupled chemical reactions*, J. of Computational Physics, 22 (1976), pp. 403–434.
- [55] ———, *Exact stochastic simulation of coupled chemical reactions*, J. of physical chemistry, 81 (1977), pp. 2340–2361.
- [56] ———, *Approximate accelerated stochastic simulation of chemically reacting systems*, J. of Chemical Physics, 115 (2001), p. 1716.
- [57] D. T. GILLESPIE AND L. R. PETZOLD, *Improved leap-size selection for accelerated stochastic simulation*, J. of Chemical Physics, 119 (2003), p. 8229.
- [58] I. GOODFELLOW, Y. BENGIO, AND A. COURVILLE, *Deep learning*, MIT press, 2016.
- [59] A. GRAVES, A.-R. MOHAMED, AND G. HINTON, *Speech recognition with deep recurrent neural networks*, in 2013 IEEE international conference on acoustics, speech and signal processing, IEEE, 2013, pp. 6645–6649.
- [60] J. P. GROTZINGER, *Analysis of surface materials by the Curiosity Mars rover*, 2013.
- [61] P. GUIDOTTI, *Anisotropic diffusions of image processing from Perona-Malik on*, Advanced Studies in Pure Mathematics, 99 (2015), p. 20XX.

- [62] R. K. GUPTA, S. ABDUL-JAWAD, L. E. MCCOY, H. P. MOK, D. PEPPA, M. SALGADO, J. MARTINEZ-PICADO, M. NIJHUIS, A. M. WENSING, H. LEE, ET AL., *HIV-1 remission following CCR5 Δ 32/ Δ 32 haematopoietic stem-cell transplantation*, *Nature*, (2019), p. 1.
- [63] S. HABRINGER, C. LAPA, P. HERHAUS, M. SCHOTTELIUS, R. ISTVANFFY, K. STEIGER, J. SLOTTA-HUSPENINA, A. SCHIRBEL, H. HÄNSCHEID, S. KIRCHER, ET AL., *Dual targeting of acute leukemia and supporting niche by CXCR4-directed theranostics*, *Theranostics*, 8 (2018), p. 369.
- [64] P. E. HADJIDOUKAS, P. ANGELIKOPOULOS, C. PAPADIMITRIOU, AND P. KOUMOUTSAKOS, *$\Pi 4U$: A high performance computing framework for Bayesian uncertainty quantification of complex models*, *Journal of Computational Physics*, (2015).
- [65] P. E. HADJIDOUKAS, E. LAPPAS, AND V. V. DIMAKOPOULOS, *A runtime library for platform-independent task parallelism*, in 2012 20th Euromicro International Conference on Parallel, Distributed and Network-based Processing, IEEE, 2012, pp. 229–236.
- [66] M. HADZIAHMETOVIC, K. SHIRAI, AND A. CHAKRAVARTI, *Recent advancements in multi-modality treatment of gliomas*, *Future oncology*, 7 (2011), pp. 1169–1183.
- [67] E. C. HALPERIN, G. BENTEL, E. R. HEINZ, AND P. C. BURGER, *Radiation therapy treatment planning in supratentorial glioblastoma multiforme: an analysis based on post mortem topographic anatomy with CT correlations*, *International Journal of Radiation Oncology* Biology* Physics*, 17 (1989), pp. 1347–1350.
- [68] K. R. S. HANA L.P. HARPOLD, ELLSWORTH C. ALVORD, *The Evolution of Mathematical Modeling of Glioma Proliferation and Invasion*, *J Neuropathol Exp Neurol*, (2007).
- [69] D. HANAHAN AND R. A. WEINBERG, *The hallmarks of cancer*, *cell*, 100 (2000), pp. 57–70.
- [70] ———, *Hallmarks of cancer: the next generation*, *cell*, 144 (2011), pp. 646–674.
- [71] A. HAWKINS-DAARUD, S. K. JOHNSTON, AND K. R. SWANSON, *Quantifying Uncertainty and Robustness in a Biomathematical Model Based Patient-Specific Response Metric for Glioblastoma*, *bioRxiv*, (2018).
- [72] K. HE, J. SUN, AND X. TANG, *Guided image filtering*, *IEEE transactions on pattern analysis and machine intelligence*, 35 (2013), pp. 1397–1409.
- [73] A. K. HENRICK, T. D. ASLAM, AND J. M. POWERS, *Mapped weighted essentially non-oscillatory schemes: achieving optimal order near critical points*, *Journal of Computational Physics*, 207 (2005), pp. 542–567.

-
- [74] P. HERHAUS, S. HABRINGER, T. VAG, K. STEIGER, J. SLOTTA-HUSPENINA, C. GERN-GROSS, B. WIESTLER, H.-J. WESTER, M. SCHWAIGER, AND U. KELLER, *Response assessment with the CXCR4-directed positron emission tomography tracer [68 Ga] Pentixafor in a patient with extranodal marginal zone lymphoma of the orbital cavities*, EJNMMI research, 7 (2017), p. 51.
- [75] P. HERHAUS, J. **Lipková**, T. VAG, A. S.-H. J. LAMMER, FELICITAS, C. LAPA, B. MENZE, T. PUKROP, I. IAKUCHEV, D. HELLWIG, A. K. BUCK, M. DECKERT, B. WIESTLER, H.-J. EZHOV, IVAN WESTER, M. SCHWEIGER, AND U. KELLER, *CXCR4-targeted positron emission tomography imaging of central nervous system B-cell lymphoma*, submitted to American Society of Hematology, (2019).
- [76] K. HERRMANN, M. SCHOTTELIUS, C. LAPA, T. OSL, A. POSCHENRIEDER, H. HÄNSCHIED, K. LÜCKERATH, M. SCHREDER, C. BLUEMEL, M. KNOTT, ET AL., *First-in-human experience of CXCR4-directed endoradiotherapy with 177Lu-and 90Y-labeled pentixather in advanced-stage multiple myeloma with extensive intra-and extramedullary disease*, Journal of nuclear medicine, 57 (2016), pp. 248–251.
- [77] M. HINGORANI, W. P. COLLEY, S. DIXIT, AND A. M. BEAVIS, *Hypofractionated radiotherapy for glioblastoma: strategy for poor-risk patients or hope for the future?*, The British Journal of Radiology, (2012).
- [78] K. HOANG-XUAN, E. BESSELL, J. BROMBERG, A. F. HOTTINGER, M. PREUSSER, R. RUDÀ, U. SCHLEGEL, T. SIEGAL, C. SOUSSAIN, U. ABACIOGLU, ET AL., *Diagnosis and treatment of primary CNS lymphoma in immunocompetent patients: guidelines from the European Association for Neuro-Oncology*, The Lancet Oncology, 16 (2015), pp. e322–e332.
- [79] C. HOGEA, F. ABRAHAM, G. BIROS, AND C. DAVATZIKOS, *A framework for soft tissue simulations with applications to modeling brain tumor mass-effect in 3-d images*, COMPUTATIONAL BIOMECHANICS FOR MEDICINE, (2006), p. 24.
- [80] C. HOGEA, C. DAVATZIKOS, AND G. BIROS, *Modeling glioma growth and mass effect in 3D MR images of the brain*, in International Conference on Medical Image Computing and Computer-Assisted Intervention, Springer, 2007, pp. 642–650.
- [81] A. F. HOTTINGER, L. M. DEANGELIS, J. YAHALOM, AND L. E. ABREY, *Salvage whole brain radiotherapy for recurrent or refractory primary CNS lymphoma*, Neurology, 69 (2007), pp. 1178–1182.
- [82] D. H. HUBEL AND T. N. WIESEL, *Receptive fields of single neurones in the cat's striate cortex*, The Journal of physiology, 148 (1959), pp. 574–591.

BIBLIOGRAPHY

- [83] M. HUTTERER, M. NOWOSIELSKI, D. PUTZER, N. L. JANSEN, M. SEIZ, M. SCHOCKE, M. MCCOY, G. GÖBEL, C. LA FOUGÈRE, I. J. VIRGOLINI, ET AL., *[18F]-fluoro-ethyl-L-tyrosine PET: a valuable diagnostic tool in neuro-oncology, but not all that glitters is glioma*, *Neuro-oncology*, 15 (2013), pp. 341–351.
- [84] J. E. IGLESIAS, C.-Y. LIU, P. M. THOMPSON, AND Z. TU, *Robust brain extraction across datasets and comparison with publicly available methods*, *IEEE transactions on medical imaging*, 30 (2011), pp. 1617–1634.
- [85] J. E. IGLESIAS AND M. R. SABUNCU, *Multi-atlas segmentation of biomedical images: a survey*, *Medical image analysis*, 24 (2015), pp. 205–219.
- [86] P. R. JACKSON, J. JULIANO, A. HAWKINS-DAARUD, R. C. ROCKNE, K. R. SWANSON, ET AL., *Patient-specific mathematical neuro-oncology: using a simple proliferation and invasion tumor model to inform clinical practice*, *Bulletin of mathematical biology*, (2015).
- [87] P. KALAVATHI AND V. S. PRASATH, *Methods on skull stripping of MRI head scan images—a review*, *Journal of digital imaging*, 29 (2016), pp. 365–379.
- [88] A. M. KIERZEK, *STOCKS: STOChastic Kinetic Simulations of biochemical systems with Gillespie algorithm.*, *Bioinformatics* (Oxford, England), 18 (2002), pp. 470–81.
- [89] D. P. KINGMA AND J. BA, *Adam: A method for stochastic optimization*, *arXiv preprint arXiv:1412.6980*, (2014).
- [90] M. KIRCHER, P. HERHAUS, M. SCHOTTELIUS, A. K. BUCK, R. A. WERNER, H.-J. WESTER, U. KELLER, AND C. LAPA, *CXCR4-directed theranostics in oncology and inflammation*, *Annals of nuclear medicine*, 32 (2018), pp. 503–511.
- [91] F. KOFLER, J. **Lipkova**, B. WIESTLER, AND B. MENZE, *The BRATS preprocessing software: Translating state-of-the-art brain tumor segmentation methods into clinical and scientific practice*, in preparation for BRATS special issue, (2019).
- [92] E. KONUKOGLU, O. CLATZ, H. DELINGETTE, AND N. AYACHE, *Personalization of reaction-diffusion tumor growth models in MR images: application to brain gliomas characterization and radiotherapy planning*, 2010.
- [93] A. KORFEL AND U. SCHLEGEL, *Diagnosis and treatment of primary CNS lymphoma*, *Nature Reviews Neurology*, 9 (2013), p. 317.
- [94] A. KRIZHEVSKY, I. SUTSKEVER, AND G. E. HINTON, *Imagenet classification with deep convolutional neural networks*, in *Advances in neural information processing systems*, 2012, pp. 1097–1105.

-
- [95] M. KUNZ, N. THON, S. EIGENBROD, C. HARTMANN, R. EGENSEPERGER, J. HERMS, J. GEISLER, C. LA FOUGERE, J. LUTZ, J. LINN, ET AL., *Hot spots in dynamic¹⁸FET-PET delineate malignant tumor parts within suspected WHO grade II gliomas*, *Neuro-oncology*, 13 (2011), pp. 307–316.
- [96] C. LAPA, K. HERRMANN, A. SCHIRBEL, H. HÄNSCHEID, K. LÜCKERATH, M. SCHOTTELIUS, M. KIRCHER, R. A. WERNER, M. SCHREDER, S. SAMNICK, ET AL., *CXCR4-directed endoradiotherapy induces high response rates in extramedullary relapsed Multiple Myeloma*, *Theranostics*, 7 (2017), p. 1589.
- [97] C. LAPA, K. LÜCKERATH, I. KLEINLEIN, C. M. MONORANU, T. LINSENMANN, A. F. KESSLER, M. RUDELIUS, S. KROPF, A. K. BUCK, R.-I. ERNESTUS, ET AL., *⁶⁸Ga-pentixafor-PET/CT for imaging of chemokine receptor 4 expression in glioblastoma*, *Theranostics*, 6 (2016), p. 428.
- [98] C. LAPA, M. SCHREDER, A. SCHIRBEL, S. SAMNICK, K. M. KORTÜM, K. HERRMANN, S. KROPF, H. EINSELE, A. K. BUCK, H.-J. WESTER, ET AL., *[⁶⁸Ga] Pentixafor-PET/CT for imaging of chemokine receptor CXCR4 expression in multiple myeloma-Comparison to [¹⁸F] FDG and laboratory values*, *Theranostics*, 7 (2017), p. 205.
- [99] M. LÊ, H. DELINGETTE, J. KALPATHY-CRAMER, E. R. GERSTNER, ET AL., *Bayesian personalization of brain tumor growth model*, in *International Conference on Medical Image Computing and Computer-Assisted Intervention*, Springer, 2015.
- [100] Y. LECUN, B. E. BOSER, J. S. DENKER, D. HENDERSON, R. E. HOWARD, W. E. HUBBARD, AND L. D. JACKEL, *Handwritten digit recognition with a back-propagation network*, in *Advances in neural information processing systems*, 1990, pp. 396–404.
- [101] D. LEE ET AL., *Physical, mathematical, and numerical derivations of the Cahn–Hilliard equation*, *Computational Materials Science*, 81 (2014), pp. 216–225.
- [102] R. J. LEVEQUE, *High-resolution conservative algorithms for advection in incompressible flow*, *SIAM Journal on Numerical Analysis*, 33 (1996), pp. 627–665.
- [103] X. LI, J. LOWENGRUB, A. RÄTZ, AND A. VOIGT, *Solving PDEs in complex geometries: a diffuse domain approach*, *Communications in mathematical sciences*, 7 (2009), p. 81.
- [104] J. **Lipková**, P. ANGELIKOPOULOS, S. WU, E. ALBERTS, B. WIESTLER, C. DIEHL, C. PREIBISCH, T. PYKA, S. COMBS, P. HADJIDOUKAS, ET AL., *Personalized Radiotherapy Design for Glioblastoma: Integrating Mathematical Tumor Models, Multimodal Scans and Bayesian Inference.*, *IEEE transactions on medical imaging*, (2019).

- [105] J. **Lipková**, G. ARAMPATZIS, P. CHATELAIN, B. MENZE, AND P. KOUMOUTSAKOS, *S-Leaping: An Adaptive, Accelerated Stochastic Simulation Algorithm, Bridging tau-Leaping and R-Leaping*, Bulletin of mathematical biology, (2018), pp. 1–23.
- [106] J. **Lipkova**, B. MENZE, P. KOUMOUTSAKOS, AND J. LOWENGRUB, *Tumor-induced brain deformations*, in preparation, (2019).
- [107] J. **Lipková**, M. REMPFLE, P. CHRIST, J. LOWENGRUB, AND B. H. MENZE, *Automated Unsupervised Segmentation of Liver Lesions in CT scans via Cahn-Hilliard Phase Separation*, arXiv preprint arXiv:1704.02348, (2017).
- [108] J. **Lipková**, D. ROSSINELLI, P. KOUMOUTSAKOS, AND B. MENZE, *Visualisation of a sphere in the shear flow*, accepted for publication in the Springer, Beauty of theoretical biology, (2019).
- [109] J. **Lipková**, D. ROSSINELLI, J. LOWENGRUB, P. KOUMOUTSAKOS, AND B. MENZE, *Visualisation of a brain tumor infiltration*, accepted for publication in the Springer, Beauty of theoretical biology, (2019).
- [110] J. **Lipková**, K. C. ZYGALAKIS, S. J. CHAPMAN, AND R. ERBAN, *Analysis of Brownian dynamics simulations of reversible bimolecular reactions*, SIAM Journal on Applied Mathematics, 71 (2011), pp. 714–730.
- [111] J. M. LÖTJÖNEN, R. WOLZ, J. R. KOIKKALAINEN, L. THURFJELL, G. WALDEMAR, H. SOININEN, D. RUECKERT, A. D. N. INITIATIVE, ET AL., *Fast and robust multi-atlas segmentation of brain magnetic resonance images*, Neuroimage, 49 (2010), pp. 2352–2365.
- [112] D. N. LOUIS, A. PERRY, G. REIFENBERGER, A. VON DEIMLING, D. FIGARELLA-BRANGER, W. K. CAVENEE, H. OHGAKI, O. D. WIESTLER, P. KLEIHUES, AND D. W. ELLISON, *The 2016 World Health Organization classification of tumors of the central nervous system: a summary*, Acta neuropathologica, 131 (2016), pp. 803–820.
- [113] H. MAAMAR, A. RAJ, AND D. DUBNAU, *Noise in gene expression determines cell fate in Bacillus subtilis*, Science, 317 (2007), pp. 526–529.
- [114] M. C. MABRAY, R. F. BARAJAS, AND S. CHA, *Modern brain tumor imaging*, Brain tumor research and treatment, 3 (2015), pp. 8–23.
- [115] F. MARTÍNEZ-MARTÍNEZ, J. KYBIC, L. LAMBERT, AND Z. MECKOVÁ, *Fully automated classification of bone marrow infiltration in low-dose CT of patients with multiple myeloma based on probabilistic density model and supervised learning*, Computers in biology and medicine, 71 (2016), pp. 57–66.

-
- [116] J. MAZZIOTTA, A. TOGA, A. EVANS, P. FOX, J. LANCASTER, K. ZILLES, R. WOODS, T. PAUS, G. SIMPSON, B. PIKE, ET AL., *A probabilistic atlas and reference system for the human brain: International Consortium for Brain Mapping (ICBM)*, Philosophical Transactions of the Royal Society of London. Series B: Biological Sciences, 356 (2001), pp. 1293–1322.
- [117] M. W. McDONALD, H.-K. G. SHU, W. J. CURRAN JR, AND I. R. CROCKER, *Pattern of failure after limited margin radiotherapy and temozolomide for glioblastoma*, International Journal of Radiation Oncology* Biology* Physics, 79 (2011), pp. 130–136.
- [118] J. S. MENDEZ, Q. T. OSTROM, H. GITTLEMAN, C. KRUCHKO, L. M. DEANGELIS, J. S. BARNHOLTZ-SLOAN, AND C. GROMMES, *The elderly left behind—changes in survival trends of primary central nervous system lymphoma over the past 4 decades*, Neuro-oncology, 20 (2017), pp. 687–694.
- [119] B. MENZE, K. VAN LEEMPUT, A. HONKELA, E. KONUKOGLU, M.-A. WEBER, ET AL., *A generative approach for image-based modeling of tumor growth*, in Information Processing in Medical Imaging, Springer, 2011.
- [120] B. H. MENZE, A. JAKAB, S. BAUER, J. KALPATHY-CRAMER, K. FARAHANI, J. KIRBY, Y. BURREN, N. PORZ, J. SLOTBOOM, R. WIEST, ET AL., *The multimodal brain tumor image segmentation benchmark (BRATS)*, IEEE transactions on medical imaging, 34 (2015), p. 1993.
- [121] B. H. MENZE, K. VAN LEEMPUT, D. LASHKARI, T. RIKLIN-RAVIV, E. GEREMIA, E. ALBERTS, P. GRUBER, S. WEGENER, M.-A. WEBER, G. SZÉKELY, ET AL., *A generative probabilistic model and discriminative extensions for brain lesion segmentation—with application to tumor and stroke*, IEEE transactions on medical imaging, 35 (2016), pp. 933–946.
- [122] B. H. MENZE, K. VAN LEEMPUT, D. LASHKARI, M.-A. WEBER, N. AYACHE, AND P. GOLAND, *A generative model for brain tumor segmentation in multi-modal images*, in Medical Image Computing and Computer-Assisted Intervention—MICCAI 2010, Springer, 2010, pp. 151–159.
- [123] M. METZ, M. MOLINA, J. **Lipkova**, F. LIESCHE, B. MENZE, S. COMBS, C. ZIMMER, AND B. WIESTLER, *Prediction of glioblastoma recurrence from preoperative MR scans through fractional anisotropy maps with free water suppression*, submitted to RSNA, (2019).
- [124] J. METZCAR, Y. WANG, R. HEILAND, AND P. MACKLIN, *A Review of Cell-Based Computational Modeling in Cancer Biology*, JCO clinical cancer informatics, 2 (2019), pp. 1–13.

BIBLIOGRAPHY

- [125] F. MILLETARI, N. NAVAB, AND S.-A. AHMADI, *V-net: Fully convolutional neural networks for volumetric medical image segmentation*, in 2016 Fourth International Conference on 3D Vision (3DV), IEEE, 2016, pp. 565–571.
- [126] A. MOHAMED AND C. DAVATZIKOS, *Finite element modeling of brain tumor mass-effect from 3D medical images*, in International Conference on Medical Image Computing and Computer-Assisted Intervention, Springer, 2005, pp. 400–408.
- [127] M. MURGASOVA, *Tutorial on Expectation-Maximization: Application to Segmentation of Brain MRI*, 2007.
- [128] T. NAGASAWA, *CXC chemokine ligand 12 (CXCL12) and its receptor CXCR4*, Journal of Molecular Medicine, 92 (2014), pp. 433–439.
- [129] P. L. NGUYEN, A. CHAKRAVARTI, D. M. FINKELSTEIN, F. H. HOCHBERG, T. T. BATCHELOR, AND J. S. LOEFFLER, *Results of whole-brain radiation as salvage of methotrexate failure for immunocompetent patients with primary CNS lymphoma*, Journal of Clinical Oncology, 23 (2005), pp. 1507–1513.
- [130] M. A. NIELSEN, *Neural networks and deep learning*, vol. 25, Determination press USA, 2015.
- [131] Q. T. OSTROM, H. GITTLEMAN, G. TRUITT, A. BOSCIA, C. KRUCHKO, AND J. S. BARNHOLTZ-SLOAN, *CBTRUS statistical report: primary brain and other central nervous system tumors diagnosed in the United States in 2011–2015*, Neuro-oncology, 20 (2018), pp. iv1–iv86.
- [132] H. PARK, P. H. BLAND, AND C. R. MEYER, *Construction of an abdominal probabilistic atlas and its application in segmentation*, IEEE Transactions on medical imaging, 22 (2003), pp. 483–492.
- [133] A. K. PAULSSON, K. P. MCMULLEN, A. M. PEIFFER, W. H. HINSON, W. T. KEARNS, A. J. JOHNSON, G. J. LESSER, ET AL., *Limited margins using modern radiotherapy techniques does not increase marginal failure rate of glioblastoma*, American journal of clinical oncology, (2014).
- [134] J. E. PEARSON, *Complex patterns in a simple system*, Science, 261 (1993), pp. 189–192.
- [135] R. L. PEGO, *Front migration in the nonlinear Cahn-Hilliard equation*, in Proceedings of the Royal Society of London A: Mathematical, Physical and Engineering Sciences, vol. 422, The Royal Society, 1989, pp. 261–278.
- [136] R. PERNICK AND C. WILDER, *The clean tech revolution*, The next big growth and investment opportunity. New York, (2007).

-
- [137] P. PERONA AND J. MALIK, *Scale-space and edge detection using anisotropic diffusion*, IEEE Transactions on pattern analysis and machine intelligence, (1990), pp. 629–639.
 - [138] D. L. PHAM, C. XU, AND J. L. PRINCE, *Current methods in medical image segmentation*, Annual review of biomedical engineering, 2 (2000), pp. 315–337.
 - [139] K. PHILIPP-ABBREDERIS, K. HERRMANN, S. KNOP, M. SCHOTTELIUS, M. EIBER, K. LÜCKERATH, E. PIETSCHMANN, S. HABRINGER, C. GERNGROSS, K. FRANKE, ET AL., *In vivo molecular imaging of chemokine receptor CXCR4 expression in patients with advanced multiple myeloma*, EMBO molecular medicine, 7 (2015), pp. 477–487.
 - [140] ———, *In vivo molecular imaging of chemokine receptor CXCR4 expression in patients with advanced multiple myeloma*, EMBO molecular medicine, 7 (2015), pp. 477–487.
 - [141] M. PIROTH, M. PINKAWA, R. HOLY, J. KLOTZ, S. SCHAAR, G. STOFFELS, ET AL., *Integrated boost IMRT with FET-PET-adapted local dose escalation in glioblastomas*, Strahlentherapie und Onkologie, (2012).
 - [142] M. D. PIROTH, M. PINKAWA, R. HOLY, J. KLOTZ, S. NUSSEN, G. STOFFELS, H. H. COENEN, H. J. KAISER, K. J. LANGEN, AND M. J. EBLE, *Prognostic value of early [18F] fluoroethyltyrosine positron emission tomography after radiochemotherapy in glioblastoma multiforme*, International Journal of Radiation Oncology* Biology* Physics, 80 (2011), pp. 176–184.
 - [143] P. RABOEL, J. BARTEK, M. ANDRESEN, B. BELLANDER, AND B. ROMNER, *Intracranial pressure monitoring: invasive versus non-invasive methods—a review*, Critical care research and practice, 2012 (2012).
 - [144] W. RACHINGER, C. GOETZ, G. PÖPPERL, F. J. GILDEHAUS, F. W. KRETH, M. HOLT-MANNSPÖTTER, J. HERMS, W. KOCH, K. TATSCH, AND J.-C. TONN, *Positron emission tomography with O-(2-[18F] fluoroethyl)-l-tyrosine versus magnetic resonance imaging in the diagnosis of recurrent gliomas*, Neurosurgery, 57 (2005), pp. 505–511.
 - [145] M. RATHINAM, L. R. PETZOLD, Y. CAO, AND D. T. GILLESPIE, *Stiffness in stochastic chemically reacting systems: The implicit tau-leaping method*, J. of Chemical Physics, 119 (2003), p. 12784.
 - [146] S. RIEKEN, D. HABERMEHL, F. L. GIESEL, C. HOFFMANN, ET AL., *Analysis of FET-PET imaging for target volume definition in patients with gliomas treated with conformal radiotherapy*, Radiotherapy and Oncology, (2013).
 - [147] R. C. ROCKNE, A. D. TRISTER, J. JACOBS, A. J. HAWKINS-DAARUD, ET AL., *A patient-specific computational model of hypoxia-modulated radiation resistance in glioblastoma using 18 F-FMISO-PET*, Journal of the Royal Society Interface, (2015).

- [148] S. ROCKWELL, I. T. DOBRUCKI, E. Y. KIM, S. T. MARRISON, AND V. T. VU, *Hypoxia and radiation therapy: past history, ongoing research, and future promise*, Current molecular medicine, 9 (2009).
- [149] T. ROHLFING, N. M. ZAHR, E. V. SULLIVAN, AND A. PFEFFERBAUM, *The SRI24 multi-channel atlas of normal adult human brain structure*, Human brain mapping, 31 (2010), pp. 798–819.
- [150] O. RONNEBERGER, P. FISCHER, AND T. BROX, *U-net: Convolutional networks for biomedical image segmentation*, in International Conference on Medical image computing and computer-assisted intervention, Springer, 2015, pp. 234–241.
- [151] T. ROOSENDAL AND S. SELLER, *The Official Blender 2.3 guide: free 3D creation suite for modeling, animation, and rendering*, vol. 3, No Starch Press San Francisco, 2004.
- [152] D. ROSSINELLI, *Multiresolution flow simulations on multi / many-core architectures*, PhD thesis, ETH Zurich, 2011.
- [153] D. ROSSINELLI, B. HEJAZIALHOSSEINI, W. VAN REES, M. GAZZOLA, ET AL., *MRAG-I2D: Multi-resolution adapted grids for remeshed vortex methods on multicore architectures*, Journal of Computational Physics, (2015).
- [154] L. I. RUDIN, S. OSHER, AND E. FATEMI, *Nonlinear total variation based noise removal algorithms*, Physica D: nonlinear phenomena, 60 (1992), pp. 259–268.
- [155] W. SANDMANN, *Exposition and streamlined formulation of adaptive explicitimplicit tau-leaping*, tech. rep., Citeseer, 2009.
- [156] O. SCHERZER AND J. WEICKERT, *Relations between regularization and diffusion filtering*, Journal of Mathematical Imaging and Vision, 12 (2000), pp. 43–63.
- [157] J. G. SCHNEIDER, S. R. AMEND, AND K. N. WEILBAECHER, *Integrins and bone metastasis: integrating tumor cell and stromal cell interactions*, Bone, 48 (2011), pp. 54–65.
- [158] J. R. SHEWCHUK, *Sweep algorithms for constructing higher-dimensional constrained delaunay triangulations*, in Annual Symposium on Computational Geometry: Proceedings of the sixteenth annual symposium on Computational geometry, vol. 12, 2000, pp. 350–359.
- [159] M. S. SHIELS, R. M. PFEIFFER, C. BESSON, C. A. CLARKE, L. M. MORTON, L. NOGUEIRA, K. PAWLISH, E. L. YANIK, G. SUNEJA, AND E. A. ENGELS, *Trends in primary central nervous system lymphoma incidence and survival in the US*, British journal of haematology, 174 (2016), pp. 417–424.

- [160] D. SILVER, A. HUANG, C. J. MADDISON, A. GUEZ, L. SIFRE, G. VAN DEN DRIESSCHE, J. SCHRITTWIESER, I. ANTONOGLOU, V. PANNEERSHELVAM, M. LANCTOT, ET AL., *Mastering the game of Go with deep neural networks and tree search*, *nature*, 529 (2016), p. 484.
- [161] E. SMISTAD, T. L. FALCH, M. BOZORGI, A. C. ELSTER, AND F. LINDSETH, *Medical image segmentation on GPUs—A comprehensive review*, *Medical image analysis*, 20 (2015), pp. 1–18.
- [162] S. M. SMITH, *Fast robust automated brain extraction*, *Human brain mapping*, 17 (2002), pp. 143–155.
- [163] L. SOUAMI, W. SEIFERHELD, D. BRACHMAN, E. B. PODGORSK, M. WERNER-WASIK, R. LUSTIG, ET AL., *Randomized comparison of stereotactic radiosurgery followed by conventional radiotherapy with carmustine to conventional radiotherapy with carmustine for patients with glioblastoma multiforme: report of Radiation Therapy Oncology Group 93-05 protocol*, *International Journal of Radiation Oncology* Biology* Physics*, (2004).
- [164] N. SPAETH, M. T. WYSS, B. WEBER, S. SCHEIDEGGER, A. LUTZ, J. VERWEY, I. RADOVANOVIC, J. PAHNKE, D. WILD, G. WESTERA, ET AL., *Uptake of 18F-fluorocholine, 18F-fluoroethyl-L-tyrosine, and 18F-FDG in acute cerebral radiation injury in the rat: implications for separation of radiation necrosis from tumor recurrence*, *Journal of Nuclear Medicine*, 45 (2004), pp. 1931–1938.
- [165] A. C. SPOO, M. LÜBBERT, W. G. WIERDA, AND J. A. BURGER, *CXCR4 is a prognostic marker in acute myelogenous leukemia*, *Blood*, 109 (2007), pp. 786–791.
- [166] M. B. SPORN, *The war on cancer*, *The lancet*, 347 (1996), pp. 1377–1381.
- [167] F. STOCKHAMMER, M. PLOTKIN, H. AMTHAUER, F. K. VAN LANDEGHEM, AND C. WOICIECHOWSKY, *Correlation of F-18-fluoro-ethyl-tyrosin uptake with vascular and cell density in non-contrast-enhancing gliomas*, *Journal of neuro-oncology*, 88 (2008), pp. 205–210.
- [168] M. R. STRATTON, P. J. CAMPBELL, AND P. A. FUTREAL, *The cancer genome*, *Nature*, 458 (2009), p. 719.
- [169] R. STUPP, M. BRADA, M. VAN DEN BENT, J.-C. TONN, AND G. PENTHEROUDAKIS, *High-grade glioma: ESMO Clinical Practice Guidelines for diagnosis, treatment and follow-up*, *Annals of oncology*, 25 (2014), pp. iii93–iii101.

BIBLIOGRAPHY

- [170] R. STUPP, W. P. MASON, M. J. VAN DEN BENT, M. WELLER, B. FISHER, M. J. TAPHOORN, K. BELANGER, A. A. BRANDES, C. MAROSI, U. BOGDHORN, ET AL., *Radiotherapy plus concomitant and adjuvant temozolomide for glioblastoma*, New England Journal of Medicine, 352 (2005), pp. 987–996.
- [171] G. M. SÜEL, J. GARCIA-OJALVO, L. M. LIBERMAN, AND M. B. ELOWITZ, *An excitable gene regulatory circuit induces transient cellular differentiation*, Nature, 440 (2006), pp. 545–550.
- [172] P. SUETENS, *Fundamentals of medical imaging*, Cambridge university press, 2002.
- [173] E. A. SWABB, J. WEI, AND P. M. GULLINO, *Diffusion and convection in normal and neoplastic tissues*, Cancer research, 34 (1974), pp. 2814–2822.
- [174] A. SWAN, T. HILLEN, J. C. BOWMAN, AND A. D. MURTHA, *A patient-specific anisotropic diffusion model for brain tumour spread*, Bulletin of mathematical biology, (2018).
- [175] K. R. SWANSON, E. C. ALVORD JR, AND J. MURRAY, *Virtual brain tumours (gliomas) enhance the reality of medical imaging and highlight inadequacies of current therapy*, British journal of cancer, 86 (2002), p. 14.
- [176] A. A. TAHA AND A. HANBURY, *Metrics for evaluating 3D medical image segmentation: analysis, selection, and tool*, BMC medical imaging, 15 (2015), p. 29.
- [177] I. TARIQ, T. CHEN, N. F. KIRKBY, AND R. JENA, *Modelling and Bayesian adaptive prediction of individual patients’ tumour volume change during radiotherapy*, Physics in Medicine & Biology, 61 (2016), p. 2145.
- [178] K. E. TEIGEN, X. LI, J. LOWENGRUB, F. WANG, AND A. VOIGT, *A diffuse-interface approach for modeling transport, diffusion and adsorption/desorption of material quantities on a deformable interface*, Communications in mathematical sciences, 4 (2009), p. 1009.
- [179] G. TETTEH, L. XU, A. GAFITA, J. **Lipková**, A. ZELDIN, K. SHI, AND B. MENZE, *Lesion Detection of Recurrent Prostate Cancer on Hybrid 68Ga-PSMA PET/CT Imaging*, (Under double blind revision), (2019).
- [180] C. THOMAS, C. SCHABEL, B. KRAUSS, K. WEISEL, M. BONGERS, C. D. CLAUSSEN, AND M. HORGER, *Dual-energy CT: virtual calcium subtraction for assessment of bone marrow involvement of the spine in multiple myeloma*, American Journal of Roentgenology, 204 (2015), pp. W324–W331.
- [181] C. TOMASI AND R. MANDUCHI, *Bilateral filtering for gray and color images*, in Computer Vision, 1998. Sixth International Conference on, IEEE, 1998, pp. 839–846.

- [182] C. TSIEN, J. MOUGHAN, J. M. MICHALSKI, M. GILBERT, ET AL., *Phase I three-dimensional conformal radiation dose escalation study in newly diagnosed glioblastoma: Radiation Therapy Oncology Group Trial 98-03*, International Journal of Radiation Oncology* Biology* Physics, (2009).
- [183] J. UNKELBACH, B. MENZE, E. KONUKOGLU, F. DITTMANN, ET AL., *Radiotherapy planning for glioblastoma based on a tumor growth model: improving target volume delineation*, Physics in medicine and biology, (2014).
- [184] T. VAG, C. GERNGROSS, P. HERHAUS, M. EIBER, K. PHILIPP-ABBREDERIS, F.-P. GRANER, J. ETTL, U. KELLER, H.-J. WESTER, AND M. SCHWAIGER, *First experience with chemokine receptor CXCR4-targeted PET imaging of patients with solid cancers*, Journal of Nuclear Medicine, 57 (2016), pp. 741–746.
- [185] J. E. VILLANUEVA-MEYER, M. C. MABRAY, AND S. CHA, *Current clinical brain tumor imaging*, Neurosurgery, 81 (2017), pp. 397–415.
- [186] C. WANJEK, *Exciting New Cancer Treatments Emerge Amid Persistent Myths*, Retrieved 2009, (2009).
- [187] S. K. WARFIELD, K. H. ZOU, AND W. M. WELLS, *Simultaneous truth and performance level estimation (STAPLE): an algorithm for the validation of image segmentation*, IEEE transactions on medical imaging, 23 (2004), p. 903.
- [188] J. WEICKENMEIER, M. KURT, E. OZKAYA, R. DE ROOIJ, T. OVAERT, R. EHMAN, K. B. PAULY, AND E. KUHLE, *Brain stiffens post mortem*, Journal of the mechanical behavior of biomedical materials, 84 (2018), pp. 88–98.
- [189] J. WEICKERT, *Anisotropic diffusion in image processing*, Teubner Stuttgart, 1998.
- [190] R. A. WEINBERG AND R. A. WEINBERG, *The biology of cancer*, vol. 1, Garland science New York, 2007.
- [191] N. M. WOODY AND G. M. VIDETIC, *Handbook of treatment planning in radiation oncology*, Demos Medical Publishing, 2014.
- [192] L. XU, G. TETTEH, J. **Lipková**, Y. ZHAO, H. LI, P. CHRIST, M. PIRAUD, A. BUCK, K. SHI, AND B. H. MENZE, *Automated Whole-Body Bone Lesion Detection for Multiple Myeloma on 68Ga-Pentixafor PET/CT Imaging Using Deep Learning Methods*, Contrast media & molecular imaging, (2018).
- [193] L. XU, G. TETTEH, M. MUSTAFA, J. **Lipková**, Y. ZHAO, M. BIETH, P. CHRIST, M. PIRAUD, B. MENZE, AND K. SHI, *W-Net for Whole-Body Bone Lesion Detection on ⁶⁸*

- Ga-Pentixafor PET/CT Imaging of Multiple Myeloma Patients*, in Molecular Imaging, Reconstruction and Analysis of Moving Body Organs, and Stroke Imaging and Treatment, Springer, (2017), pp. 23–30.
- [194] H. YAN, A. KONSTORUM, AND J. S. LOWENGRUB, *Three-dimensional spatiotemporal modeling of colon cancer organoids reveals that multimodal control of stem cell self-renewal is a critical determinant of size and shape in early stages of tumor growth*, Bulletin of mathematical biology, 80 (2018), pp. 1404–1433.
- [195] H. YAN, M. ROMERO-LÓPEZ, L. I. BENITEZ, K. DI, ET AL., *3D mathematical modeling of glioblastoma suggests that transdifferentiated vascular endothelial cells mediate resistance to current standard-of-care therapy*, Cancer research, (2017).
- [196] J. YU, M. A. VODYANIK, K. SMUGA-OTTO, J. ANTOSIEWICZ-BOURGET, J. L. FRANE, S. TIAN, J. NIE, G. A. JONSDOTTIR, V. RUOTTI, R. STEWART, ET AL., *Induced pluripotent stem cell lines derived from human somatic cells*, science, 318 (2007), pp. 1917–1920.
- [197] G. ZACK, W. ROGERS, AND S. LATT, *Automatic measurement of sister chromatid exchange frequency*, Journal of Histochemistry & Cytochemistry, (1977), pp. 741–753.
- [198] H. ZHAO, L. GUO, H. ZHAO, J. ZHAO, H. WENG, AND B. ZHAO, *CXCR4 over-expression and survival in cancer: a system review and meta-analysis*, Oncotarget, 6 (2015), p. 5022.
- [199] Y.-R. ZOU, A. H. KOTTMANN, M. KURODA, I. TANIUCHI, AND D. R. LITTMAN, *Function of the chemokine receptor CXCR4 in haematopoiesis and in cerebellar development*, Nature, 393 (1998), p. 595.